ETH IPP
Institute for Particle Physics

Diss. ETH No. 14480
ETHZ–IPP Internal Report 2001-10
November 2001

A Measurement of the Beauty Production Cross Section via $B \to J/\psi X$ at HERA

A dissertation submitted to the

Swiss Federal Institute of Technology Zurich

for the degree of

Doctor of Natural Sciences

presented by

Stefan Lüders
dipl. phys. University of Hamburg
born October 24th 1971 in Hamburg / Germany

accepted on the recommendation of
Prof. Dr. Ralph A. Eichler, examiner and
Prof. Dr. André Rubbia, co–examiner

November 2001

Diss. ETH No. 14480

A Measurement of the Beauty Production Cross Section via $B \rightarrow J/\psi X$ at HERA

A dissertation submitted to the

Swiss Federal Institute of Technology Zurich

for the degree of

Doctor of Natural Sciences

presented by

Stefan Lüders

dipl. phys. University of Hamburg

born October 24th 1971 in Hamburg / Germany

accepted on the recommendation of

Prof. Dr. Ralph A. Eichler, examiner and

Prof. Dr. André Rubbia, co–examiner

November 2001

Abstract

For the first time at HERA, the decay of beauty–flavoured hadrons into J/ψ mesons has been exploited to extract the beauty production cross section in photoproduction. The measurement presented here is based on an integrated luminosity of $56\,\mathrm{pb}^{-1}$ taken during the e^+p running conditions of the years 1997, 1999 and 2000 by the H1 experiment. Utilizing a lifetime tag, the fraction of J/ψ mesons originating from beauty–flavoured events is determined to be $\left[52.0 \pm 26.2(\mathrm{stat.}) \pm 7.7(\mathrm{syst.})\right]\%$ at low inelasticities $0.1 < z < 0.5$. This is converted into a visible beauty production cross section in photoproduction of $\sigma_{\mathrm{vis}}(ep \to b\bar{b}X \to J/\psi X' \to \mu^+\mu^- X'') = \left[13.0 \pm 6.2(\mathrm{stat.}) \pm 2.5(\mathrm{syst.})\right]\,\mathrm{pb}$ at an ep center–of–mass energy of $\sqrt{s} \approx 318\,\mathrm{GeV}$. The visible range is defined by the inelasticity interval $0.1 < z < 0.5$, photon–proton center–of–mass energies $W_{\gamma p} > 100\,\mathrm{GeV}$ and two muons within the polar angular range $20^\circ < \theta_\mu < 160^\circ$. The extrapolation to the full phase–space gives a total beauty production cross section in photoproduction of $\sigma(ep \to b\bar{b}X) = \left[19.5 \pm 9.3(\mathrm{stat.}) \pm 3.7(\mathrm{syst.}) \pm 1.8(\mathrm{ext.})\right]\,\mathrm{nb}$ and $\langle\sigma(\gamma p \to b\bar{b}X)\rangle = \left[310 \pm 150(\mathrm{stat.}) \pm 60(\mathrm{syst.}) \pm 40(\mathrm{ext.})\right]\,\mathrm{nb}$ for the total γp cross section at an average photon–proton center–of–mass energy of $\langle W_{\gamma p}\rangle = 168\,\mathrm{GeV}$. The central values for both visible and total beauty production cross sections exceed current theoretical predictions in NLO QCD by about a factor 3.5 — in agreement with previous measurements performed at HERA. Due to the large statistical errors, these differences correspond, however, to only about 1.35 standard deviations. In addition, the contribution from the decay of beauty–flavoured hadrons into J/ψ mesons to the inclusive J/ψ production cross section is discussed. The beauty–subtracted, direct J/ψ meson production cross section in photoproduction is measured to be $\sigma(ep \to c\bar{c}X \to J/\psi X') = \left[950 \pm 540(\mathrm{stat.}) \pm 180(\mathrm{syst.}) \pm 50(\mathrm{ext.})\right]\,\mathrm{pb}$.

Zusammenfassung

Erstmalig bei HERA wurde der Zerfall von Beauty Hadronen in J/ψ Mesonen benutzt, um den Beauty Produktionswirkungsquerschnitt in Photoproduktion zu extrahieren. Etwa $56\,\mathrm{pb}^{-1}$ integrierte Luminosität aus den e^+p Datennahmeperioden 1997, 1999 und 2000 wurde mit dem H1 Experiment aufgenommen. Basierend auf der Lebensdauer–Information der Beauty Hadronen konnte der Anteil an Ereignissen mit Beauty–Flavour im Inelastizitäts–Intervall $0.1 < z < 0.5$ zu $\left[52.0 \pm 26.2(\mathrm{stat.}) \pm 7.7(\mathrm{syst.})\right]\,\%$ bestimmt werden. Dieser Anteil ergab einen sichtbaren Beauty–Produktionswirkungsquerschnitt von $\sigma_{\mathrm{vis}}(ep \to b\bar{b}X \to J/\psi X' \to \mu^+\mu^- X'') = \left[13.0 \pm 6.2(\mathrm{stat.}) \pm 2.5(\mathrm{syst.})\right]$ pb bei einer ep Schwerpunktsenergie von $\sqrt{s} \approx 318\,\mathrm{GeV}$. Der sichtbare Bereich ist definiert durch das Inelatizitäts–Intervall $0.1 < z < 0.5$, Photon–Proton Schwerpunktsenergien von $W_{\gamma p} > 100\,\mathrm{GeV}$ und durch zwei Myonen innerhalb des Polarwinkelbereiches $20^\circ < \theta_\mu < 160^\circ$. Die Extrapolation auf den gesamten Phasenraum ergibt den totalen Beauty–Produktionswirkungsquerschnitt in Photoproduktion zu $\sigma(ep \to b\bar{b}X) = \left[19.5 \pm 9.3(\mathrm{stat.}) \pm 3.7(\mathrm{syst.}) \pm 1.8(\mathrm{ext.})\right]$ nb und $\langle\sigma(\gamma p \to b\bar{b}X)\rangle = \left[310 \pm 150(\mathrm{stat.}) \pm 60(\mathrm{syst.}) \pm 40(\mathrm{ext.})\right]$ nb für den totalen γp–Produktionswirkungsquerschnitt bei einer durchschnittlichen Photon–Proton Schwerpunktsenergie von $\langle W_{\gamma p}\rangle = 168\,\mathrm{GeV}$. Die Zentralwerte für den sichtbaren und totalen Beauty–Produktionswirkungsquerschnitt liegen um etwa einen Faktor 3.5 über den aktuellen theoretische Vorhersagen in NLO QCD. Dies ist in Übereinstimmung mit vorangehenden HERA Messungen. Jedoch entsprechen diese Differenzen aufgrund der grossen statistischen Unsicherheit nur etwa 1.35 Standardabweichungen. Des weiteren wurde der Einfluss des Zerfalls von Beauty Hadronen in J/ψ Mesonen auf den inklusiven J/ψ Meson Produktionswirkungsquerschnitt diskutiert. Der beauty–subtrahierte, direkte J/ψ Meson Produktionswirkungsquerschnitt wurde in Photoproduktion zu $\sigma(ep \to c\bar{c}X \to J/\psi X') = \left[950 \pm 540(\mathrm{stat.}) \pm 180(\mathrm{syst.}) \pm 50(\mathrm{ext.})\right]$ pb gemessen.

Contents

Introduction

Over the last decade measurements in photon–photon, photon–hadron and hadron–hadron collisions have revealed that theoretical predictions in next–to–leading order QCD underestimate the beauty production cross section by a factor of two to three. This discrepancy is rather puzzling, because the beauty quark mass is sufficiently large such that perturbative NLO QCD calculations are expected to be accurate. Apparently large NNLO corrections are needed, since even extreme choices of the free parameters (e.g. parton densities, scales or quark masses) can only barely bridge the difference between measurements and prediction.

All the measurements performed previously at HERA utilized the beauty quark's semi–leptonic decay. In this thesis, for the first time at HERA, the decay $B \to J/\psi X$ is used to determine the beauty production cross section in photoproduction at HERA. Since beauty–flavoured hadrons decay weakly, and thus much more slowly, than J/ψ mesons, a lifetime–based tag is used to separate the J/ψ mesons from b–flavoured hadron decays and directly produced J/ψ mesons. The pair of muons from the subsequent J/ψ meson decay gives a clean signature at the H1 experiment for reconstruction and triggering. The b–flavoured hadron's (and thus the J/ψ meson's) decay vertex can be accurately reconstructed using the central silicon detector (CST). The CST is precise enough to reconstruct decay lengths — distances between production and decay vertices — of approximately $150\,\mu$m.

The intrinsic decay length resolution leads to a symmetric distribution for directly produced or wrongly reconstructed J/ψ mesons. An excess at positive values, where the sign is defined by the decay topology, indicates exclusively events with beauty–flavour. The fraction of b–flavoured events is extracted by means of a log–likelihood method and converted into a beauty production cross section. The resolution function and the description of the background are directly determined from data.

The measurement performed in this thesis will also make a valuable contribution to inelastic J/ψ meson production analyses. J/ψ mesons from beauty–flavoured hadron decays are predominantly found at small inelasticities z. In this régime the resolved and direct photoproduction of J/ψ mesons are used to compare so–called Colour Octet contributions to the Colour–Singlet Model. In this context, b–flavoured events are considered as background and are usually modelled by Monte Carlo simulations. Due to the aforementioned uncertainty in the beauty production cross section, the uncertainty in the background induces large systematic errors. The measurement presented in this thesis will constrain the beauty–flavoured contribution at low z.

An introduction to HERA kinematics is given in Chapter 1, where also the beauty and the direct J/ψ meson production processes are explained. After describing briefly HERA and the H1 experiment (Chapter 2), the basic selection criteria are presented (Chapter 3). J/ψ meson candidates are reconstructed from two identified muon candidates. Chapter 4 explains how the three–dimensional decay vertex of heavy hadrons is reconstructed from both muon candidates using the precision of the central silicon detector and a newly introduced linking procedure. An excess at positive decay lengths determines the fraction of J/ψ mesons from b–flavoured decays, from which the beauty production cross section is calculated (Chapter 5). Chapter 6 contains a summary and an outlook towards HERA II.

Chapter 1

Theoretical Framework

Measurements in photon–photon, photon–hadron and hadron–hadron collisions demonstrate that the theoretical prediction in next–to–leading order QCD underestimates the cross section for the production of the second heaviest quark, the beauty quark, by some factor of two to three. Even extreme choices of the free parameters (e.g. beauty quark mass, the gluon density function, renormalization and factorization scales) can barely cancel this discrepancy.

The J/ψ meson provides a beautiful — in the most literal sense of the word — possibility to extract beauty–flavoured events. Since the b–flavoured hadron decays weakly into a J/ψ meson, large time scales are involved, whereas the dominating directly produced J/ψ mesons decay "promptly" by means of negligible inherent lifetime. Consequently the open beauty production cross section can be determined by means of a lifetime–based tag.

The basic aspects of the ep scattering process at HERA are discussed in Section 1.1. Heavy quarks are produced dominantly in boson–gluon–fusion. The production mechanisms and the hadronization into a final state are discussed in Section 1.2. The decay channel $B \to J/\psi X$ is to be used here to perform a lifetime tag on b–flavoured events. The main background sources (e.g. inelastic J/ψ meson production) are described in Section 1.3. Finally, Section 1.4 discusses the Monte Carlo models used for this measurement.

1.1 Kinematics of Positron–Proton Scattering

At the storage ring HERA, positrons[1] and protons are collided together at high energies. The incoming positron can emit an electroweak gauge boson (γ, Z^0 or $W^\pm$), which can then be used to probe the structure of the proton. Depending on the exchanged particle, two basic processes can be distinguished (Figure 1.1). In *neutral current* (NC) processes a photon γ or a neutral Z^0 boson is exchanged, whereas in *charged current* (CC) processes a charged $W^\pm$ boson is mediated. Both can be distinguished by their final state lepton, either a positron or an electron–(anti)neutrino.

[1]In fact, both charge conjugates of the electron can be stored in HERA. This thesis will focus on e^+p data, but the term "positron" can be used interchangeably to label positrons *and* electrons.

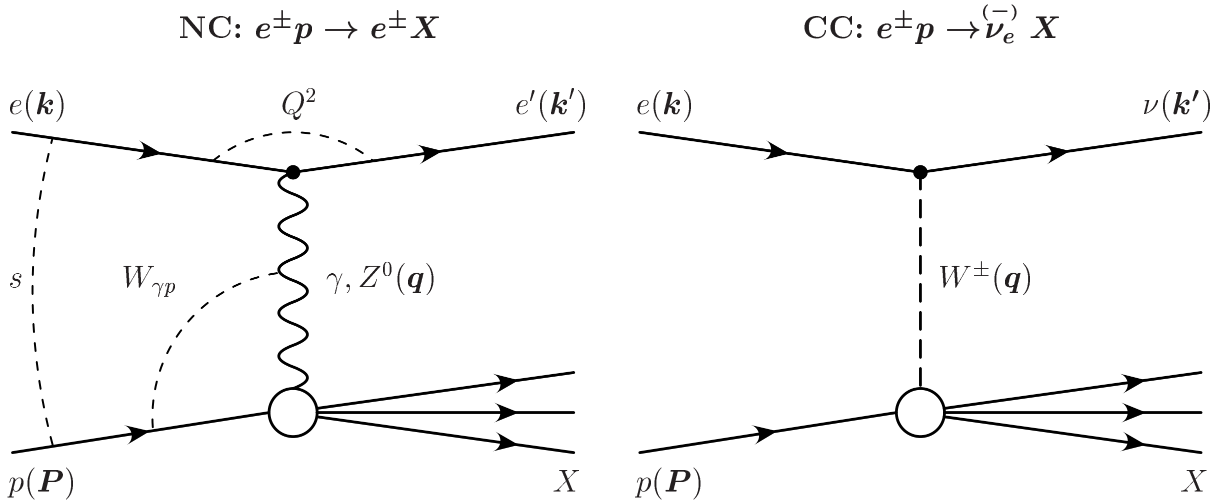

Figure 1.1: *Generic Feynman diagrams in lowest order for ep collisions: neutral current process (left) and charged current process (right). The basic kinematical variables and the particle momenta are annotated.*

The negative square of the four–momentum of the gauge boson is given by

$$Q^2 \equiv -\boldsymbol{q}^2 = -(\boldsymbol{k} - \boldsymbol{k}')^2 \tag{1.1}$$
$$= 2 \cdot E_e \cdot E'_e \cdot (1 + \cos\theta_e), \tag{1.2}$$

where θ_e is the lepton scattering angle and $\boldsymbol{k} = (E_e, \vec{p}_e)$ and $\boldsymbol{k}' = (E'_e, \vec{p}'_e)$ are the four–momenta of the incoming and the scattered leptons respectively. For "not too high" values of Q^2 the ep interaction is predominantly mediated by a photon since in the matrix element Z^0 boson exchange is suppressed by a factor $1/(Q^2 + M^2_{Z^0})$, where M_{Z^0} is the mass of the Z^0 boson. Due to the corresponding propagator term for the $W^{\pm}$ boson, the charged current contributions are also negligible at low Q^2 values. The momentum transfer Q^2 is therefore then a measure of the virtuality of the photon which is quasi–real at $Q^2 \simeq 0$. In the following, only the pure photon exchange will be considered.

The ep center–of–mass energy squared of the initial ep system is given by

$$s = (\boldsymbol{P} + \boldsymbol{k})^2 \simeq 4 \cdot E_e \cdot E_p, \tag{1.3}$$

where $\boldsymbol{P}$ represents the four–momentum of the initial proton and E_p is the energy of the incoming proton. The masses of the positron m_e and proton m_p are negligible in comparison to their energies and are neglected here and in the following. At fixed center–of–mass energies $\sqrt{s}$ the kinematics of the scattering process can be completely described in terms of two dimensionless Lorentz scalars, Bjorken–x and the relative energy transfer y, which are defined as follows;

$$x \equiv -\frac{1}{2} \cdot \frac{\boldsymbol{q} \cdot \boldsymbol{q}}{\boldsymbol{q} \cdot \boldsymbol{P}} \qquad 0 \leq x \leq 1 \tag{1.4}$$
$$y \equiv \frac{\boldsymbol{q} \cdot \boldsymbol{P}}{\boldsymbol{k} \cdot \boldsymbol{P}} \qquad 0 \leq y \leq 1. \tag{1.5}$$

In the naïve quark–parton model [1] x denotes the fraction of the proton's momentum carried by the struck parton and y is the relative energy loss of the positron in the proton's rest frame. Both variables are related to Q^2 via the relationship $Q^2 = s \cdot x \cdot y$. The photon–proton (γp) center–of–mass energy squared $W^2_{\gamma p}$ is given by

$$\begin{aligned} W^2_{\gamma p} &\equiv (\boldsymbol{P} + \boldsymbol{q})^2 \\ &= Q^2 \cdot \frac{1-x}{x} = y \cdot s - Q^2 = M_X^2 \end{aligned} \tag{1.6}$$

and corresponds to the square of the invariant mass of the hadronic final state M_X^2.

1.1.1 Inclusive Cross Section and Structure Functions

The inclusive cross section for the neutral current process $ep \to eX$ can be calculated to lowest order in *Quantum Electrodynamics* (*QED*) and is proportional to the product of the leptonic tensor $L_{\mu\nu}$ and the hadronic tensor $W^{\mu\nu}$;

$$\sigma_{ep} \propto L_{\mu\nu} W^{\mu\nu}. \tag{1.7}$$

The leptonic tensor describes the interaction between the positron and the exchanged photon and is exactly calculable in QED. The hadronic tensor describes the interaction between the photon and the proton. Since the proton structure is a–priori unknown, the hadronic tensor is not calculable and must be extracted using experimental measurements. The requirement of Lorentz invariance and current conservation leads to an expression for the corresponding inclusive double differential cross section or *Born* cross section

$$\frac{d^2\sigma_{ep}(x, Q^2)}{dx\, dQ^2} = \frac{4\pi\alpha^2}{x \cdot Q^4} \cdot \Big[y^2 \cdot x \cdot F_1(x, Q^2) + (1-y) \cdot F_2(x, Q^2) \Big], \tag{1.8}$$

where α is the electromagnetic coupling constant and $F_1(x, Q^2)$ and $F_2(x, Q^2)$ are two structure functions depending on Bjorken–x and the virtuality Q^2. Both describe the dynamics of the process.

The Quark Parton Model

In the naïve quark parton model (QPM) the proton is considered to be composed of *non–interacting* point–like constituents (*partons*) [1]. If the interaction time with the photon is short compared to that for the hadronization into a final state, e.g. due to the presence of a hard scale like $Q^2 \gg m_\rho^2$ or in the case of *heavy quark* production, the inelastic ep scattering process reduces to an incoherent sum of elastic positron–parton scatterings. The probability of finding a parton or antiparton of type i with a momentum fraction x inside the proton is given by the *parton density functions* $q_i(x)$ and $\bar{q}_i(x)$ respectively. These are related to the structure functions as follows;

$$F_1(x) = \frac{1}{2} \cdot \sum_{\text{partons } q_i} e^2_{q_i} \cdot \Big[q_i(x) + \bar{q}_i(x) \Big] \tag{1.9}$$

and

$$F_2(x) = x \cdot \sum_{\text{partons } q_i} e_{q_i}^2 \cdot \Big[q_i(x) + \bar{q}_i(x)\Big]. \tag{1.10}$$

Here e_{q_i} denotes the charge of the parton. The QPM implies that both structure functions do not depend on Q^2 for fixed values of x, thus $F_1(x)$ and $F_2(x)$ are *scaling invariant* [2]. Equations (1.9) and (1.10) are connected by the Callan–Gross relation, $F_2 = 2 \cdot x \cdot F_1$ [3], which is valid under the assumption that partons have spin $\frac{1}{2}$ and a normal (Dirac) magnetic moment.

The partons can be identified with the "quark" constituents proposed by M. Gell–Mann and G. Zweig [4]. In this model the proton, like all baryons, consists of three fractionally charged *valence* quarks (in the case of the proton *uud*, where u and d denote the *flavours* "up" and "down", respectively) and which determine the quantum numbers of the proton (baryon). *Mesons* consist of quark–antiquark pairs. This quark model led to Gell–Mann being awarded the 1969 Nobel Prize for Physics.

Based on the initial assumptions of the QPM, the sum of the momenta of all valence quarks should equal that of the proton:

$$\sum_{\text{quarks } q_i} \int_0^1 dx\, x \cdot \Big[q_i(x) + \bar{q}_i(x)\Big] = 1 \tag{1.11}$$

Measurements, however, have demonstrated that the total momentum carried by the quarks amounts to approximately only half the momentum of the proton [5]. This is a strong indication that quarks cannot be the only constituents of the proton. Furthermore, the measurement of $F_2(x, Q^2)$ shows a logarithmic dependence on Q^2. The scaling invariance is violated [6].

Quantum Chromodynamics

The strong interaction, the predominant interaction between quarks, is described within the framework of *Quantum Chromodynamics* (QCD). In addition to its valence quarks, the proton contains a *sea* of quark–antiquark pairs. The quark density functions depend also on the virtuality, i.e. $q_i(x, Q^2)$. The quarks carry an additional quantum number under the strong interaction, the *colour charge* [7]. Colour is exchanged by eight *gluons*, which carry different combinations of colour doublets. Gluons are massless, electrically neutral and have spin one. In contrast to photons gluons are able to couple to each other. The self–coupling of the colour field leads to a specific dependence of the strong coupling constant α_s on Q^2;

$$\alpha_s(Q^2) = \frac{12\pi}{(33 - 2 \cdot N_f) \cdot \ln\left(Q^2/\Lambda_{\mathrm{QCD}}^2\right)}, \tag{1.12}$$

where N_f is the number of quark flavours and Λ_{QCD} a parameter that has to be determined from experiments and is of the order $\mathcal{O}(200\,\mathrm{MeV})$ [8]. At low Q^2 the coupling strength approaches unity and the quarks are strongly bounded together (*confinement*). At higher virtualities α_s is much smaller than unity (*asymptotic freedom*).

If α_s is sufficiently below unity, perturbative QCD (*pQCD*) calculations are applicable. In the framework of pQCD the parton densities cannot be calculated from first principles. Their parameterization has to be deduced from measurements. However predictions for the dynamic evolution of quarks and gluons can be calculated in a perturbative expansion within the framework of the DGLAP evolution equations [9]. In leading order, these equations are calculated for the quark densities $q_i(x, Q^2)$

$$\frac{dq_i(x,Q^2)}{d\ \ln Q^2} = \frac{\alpha_s(Q^2)}{2\pi} \cdot \int_x^1 \frac{dz}{z} \left[q_i(x,Q^2) \cdot P_{qq}\left(\frac{x}{z}\right) + g(x,Q^2) \cdot P_{qg}\left(\frac{x}{z}\right) \right] \tag{1.13}$$

and for the gluon densities $g(x, Q^2)$

$$\frac{dg(x,Q^2)}{d\ \ln Q^2} = \frac{\alpha_s(Q^2)}{2\pi} \cdot \int_x^1 \frac{dz}{z} \left[\sum_{q_i,\bar{q}_i} q_i(x,Q^2) \cdot P_{gq}\left(\frac{x}{z}\right) + g(x,Q^2) \cdot P_{gg}\left(\frac{x}{z}\right) \right]. \tag{1.14}$$

where $q_i \in \{u, d, s\}$ denote the *light quarks*[2]. The *spitting functions* P_{qq}, P_{qg}, P_{gq} and P_{gg} give the probability for the processes $q \to q(z)\ g(1-z)$, $g \to q(z)\ q(1-z)$, $q \to g(z)\ q(1-z)$, and $g \to g(z)\ g(1-z)$ as a function of the fraction z of the initial parton's momentum, respectively. The parton densities can be extrapolated to any large value of Q^2, if the parameterization of the parton densities $q_i(x, Q_0^2)$ and $g(x, Q_0^2)$ are known at a specific starting scale Q_0^2. This initial parameterization fixes also the dependence on x.

An introduction to QCD can be found in [10].

1.1.2 Deep Inelastic Scattering and Photoproduction

Two different kinematical regions in virtuality Q^2 are usually distinguished at HERA. For $Q^2 \to 0$, where quasi–real photons are emitted by the incoming positron, the *photoproduction* region is defined, whilst in the region $Q^2 \gg 1\,\mathrm{GeV}^2$, processes are referred to as *Deep Inelastic Scattering* (DIS) processes with virtual photons γ^* radiated off the positron. Due to the $1/Q^2$ dependence of the neutral current matrix element, the photoproduction process is dominant.

Some theorists define the boundary between the two domains to be at the squared mass of the lightest vector meson, i.e. the ρ meson which has a mass of $m_\rho = 770\,\mathrm{MeV/c^2}$. This boundary corresponds approximately to the acceptance of the H1 main detector for the scattered positron. In DIS, for virtualities of at least $Q^2 \approx 1\,\mathrm{GeV}^2$ the positron can be measured in the main detector. Otherwise, the positron escapes under small scattering angles from the main detector into the beam pipe and might be measured in one of the electron taggers (*tagged* photoproduction for $Q^2 < 0.01\,\mathrm{GeV}^2$).

Within the scope of this thesis, it will be sufficient to consider only untagged photoproduction.

[2]The s labels the flavour "*strange*".

The Weizsäcker–Williams Approximation

The photon–proton cross section $\sigma(\gamma p \to e'X)$ can be extracted from the ep scattering cross section using the photon flux factor which describes the probability of the emission of a photon [11], $e \to e'\gamma$, viz.

$$\frac{d^2\sigma_{ep}}{dydQ^2} = f^T_{\gamma/e}(y,Q^2)\cdot\sigma^T_{\gamma p}(W^2_{\gamma p},Q^2) + f^L_{\gamma/e}(y,Q^2)\cdot\sigma^L_{\gamma p}(W^2_{\gamma p},Q^2). \tag{1.15}$$

Here $f^T_{\gamma/e}$ and $f^L_{\gamma/e}$ denote the flux factors for transversely and longitudinally polarized photons respectively and $\sigma^T_{\gamma p}$ and $\sigma^L_{\gamma p}$ are the corresponding cross sections.

In the photoproduction limit, the emitted photon is quasi–real and consequently predominantly transverse polarized. The flux factor can be calculated in the extended Weizsäcker–Williams Approximation (or *equivalent photon approximation*) [12, 13] according to

$$f_{\gamma/e}(y,Q^2) \approx f^T_{\gamma/e}(y,Q^2) = \frac{\alpha}{2\pi y Q^2}\cdot\left(1+(1-y)^2-\frac{2m_e^2y^2}{Q^2}\right). \tag{1.16}$$

The first two terms on the right hand side of Equation (1.16) come from the original Weizsäcker–Williams Approximation [12], whilst the last term arises only in ep collisions. This correction is of order $\mathcal{O}(\,7\%)$ [13].

An integration over fixed ranges in Q^2 and y relates the total ep cross section to the average photoproduction cross section $\langle\sigma_{\gamma p}\rangle$;

$$\begin{aligned}\sigma_{ep} &= \mathcal{F}_{\gamma/e}\cdot\underbrace{\frac{1}{\mathcal{F}_{\gamma/e}}\cdot\int_{y_{\min}}^{y_{\max}}dy\int_{Q^2_{\min}(y)}^{Q^2_{\max}}dQ^2\; f_{\gamma/e}(y,Q^2)\cdot\sigma_{\gamma p}\left(W^2_{\gamma p},Q^2\right)} && (1.17)\\ &= \mathcal{F}_{\gamma/e}\cdot\qquad\qquad\langle\sigma_{\gamma p}\rangle, && (1.18)\end{aligned}$$

where the integrated photon flux is given by

$$\mathcal{F}_{\gamma/e} = \int_{y_{\min}}^{y_{\max}}dy\int_{Q^2_{\min}(y)}^{Q^2_{\max}}dQ^2\; f_{\gamma/e}(y,Q^2). \tag{1.19}$$

The minimum virtuality of the photon $Q^2_{\min}$ is constrained by y according to $Q^2_{\min}(y) = m_e^2y^2/(1-y)$, while $Q^2_{\max}$ is usually constrained by the upper boundary for the photoproduction domain, i.e. $1\,\mathrm{GeV}^2$ (cf. above).

The average value of the γp cross section is equal to the total photoproduction cross section at some values $W^2_{\gamma p,0}$ and Q^2_0;

$$\sigma_{\gamma p}\left(W^2_{\gamma p,0},Q^2_0\right) = \langle\sigma_{\gamma p}\rangle, \tag{1.20}$$

which can be approximated by the mean values, $W^2_{\gamma p,0}\approx\langle W^2_{\gamma p}\rangle$ and $Q^2_0\approx\langle Q^2_0\rangle$.

1.2 Production of Beauty Quarks

Heavy quark production at HERA provides a valuable tool for probing the structure of the proton, especially the direct extraction of its gluon density and the study of the mechanisms of the hard subprocesses underlying *ep* interactions [14, 15]. The term "heavy quark" is used to denote quarks with flavour *charm* or *beauty* and will be abbreviated with "Q".

Since the mass of the beauty quark ($m_b \approx 4.75\,\mathrm{GeV/c^2}$) is large, it provides a "hard scale" ($m_\mathrm{b} \gg \Lambda_\mathrm{QCD}$), which justifies the use of perturbative calculations in QCD. Consequently, theoretical calculations are expected to describe measurements of b–quark production. Measurements at HERA [16]–[20], however, as well as in hadron–hadron collisions [21]–[30] and recently also in two photon interactions [31, 32] have observed that the NLO expectations underestimate the beauty production cross section.

In the analysis described in this thesis the decay of a b–flavoured meson (B^+, B^0 or B^0_s) or baryon into a J/ψ meson ($B^+/B^0/B^0_s/b$–baryon $\to J/\psi\ X$) followed by the subsequent decay of the $J/\psi \to \mu^+\mu^-$, is to be used to determine the beauty production cross section in photoproduction. Although the total branching ratio for this process is small, i.e. $\mathcal{O}(10^{-3})$, the decay of the J/ψ meson into two muons provides a clean signature for triggering and reconstruction.

Beauty production mechanisms and the formation of the hadronic final state together with the b–flavoured hadron's decay into a J/ψ meson are now described together with NLO predictions and recent measurements.

1.2.1 Photon–Gluon–Fusion

The creation of b–flavoured mesons and baryons can be factorized into the product of the beauty quark production process and the formation of the hadronic final state [33]. The former *hard* process proceeds within time scales of order $\mathcal{O}(m_\mathrm{Q}^{-1})$, which are short in comparison to time scales needed for the binding and recombination of the partons to hadrons. Since $\alpha_s(m_b) \approx 0.2$ [34] is small enough, the hard process can be calculated using pQCD, whereas the latter "soft" process cannot and must be parameterized using *fragmentation* models.

The dominant process for heavy quark production in *ep* scattering at low virtualities Q^2 is *photon–gluon–fusion*[3], where the photon couples to a gluon in the proton to create a heavy quark–antiquark pair $\mathrm{Q\bar{Q}}$ (Figure 1.2, left). Contributions from photon–photon processes have been predicted to be negligible, i.e. $\mathcal{O}(100\,\mathrm{pb})$ and $\mathcal{O}(1\,\mathrm{pb})$ for charm and beauty production respectively [35] (cf. Table 1.1).

The γp cross section can be considered as a convolution of the gluon density $g(x_g, \mu_f)$ and the photon–gluon cross section [36, 37]. This gives an ansatz for a direct measurement of the gluon density in the proton:

$$\sigma_{\gamma p} = \int dx_g\ g(x_g, \mu_f) \cdot \sigma_{\gamma g}(\hat{s}, m^2_\mathrm{Q}, \mu^2_f, \mu^2_r), \tag{1.21}$$

[3] With inclusion of the Z^0 boson exchange, this is labeled as *boson–gluon–fusion*.

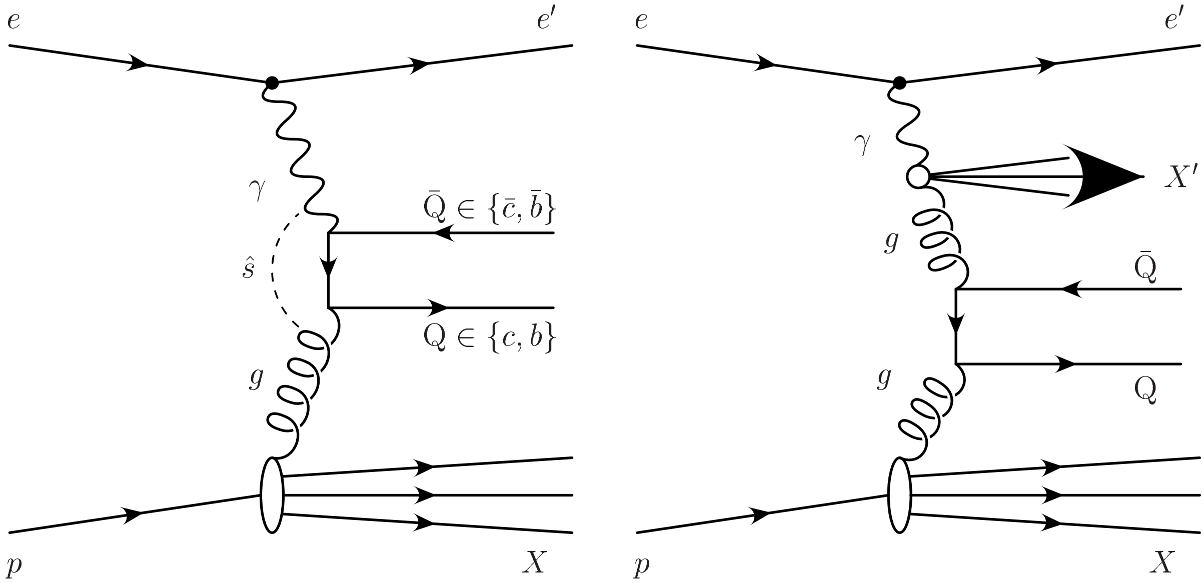

Figure 1.2: *Feynman diagrams for the direct photon–gluon–fusion in lowest order $\mathcal{O}(\alpha\alpha_s)$ (left) and in the resolved process (gluon–gluon–fusion, right).*

where x_g denotes the relative proton momentum carried by the gluon, $\hat{s} = (\boldsymbol{P}_{\mathrm{Q}} + \boldsymbol{P}_{\bar{\mathrm{Q}}})^2$ the squared center–of–mass energy of the heavy quark pair and m_{Q} is the mass of the heavy quark. The gluon density is determined at the factorization scale μ_f and the renormalization scale μ_r is needed for the calculation of the genuine photon–parton interaction. The scales are not fixed and not necessarily equal. In photoproduction $\mu_r = m_{\mathrm{Q}}$ and $\mu_f = 2\mu_r$ or $\mu_r = \sqrt{m_{\mathrm{Q}}^2 + p_t^2}$ and $\mu_f = \mu_r$ are usual choices, where p_t is the transverse momentum of the heavy quark. The total photon–gluon cross section can be written in leading order [38] as

$$\sigma_{\gamma g} = \frac{\pi e_{\mathrm{Q}}^2 \alpha \alpha_s}{\hat{s}} \cdot \left[\left(2 + 2\xi - \xi^2 \right) \cdot \ln \left(\frac{1+\chi}{1-\chi} \right) - 2\chi(1+\xi) \right], \tag{1.22}$$

where $\xi = 4m_{\mathrm{Q}}^2/\hat{s}$ and $\chi = \sqrt{1-\xi}$.

Resolved Processes

In addition to the *direct* photon–gluon–fusion process, which dominates the beauty production cross section [39], *resolved* processes also contribute. In resolved processes, the incoming photon first fluctuates — within the time allowed by the Heisenberg uncertainty principle — into a quark–antiquark pair with the same quantum numbers as the photon. Thus the photon is viewed as a quantum mechanical superposition of a bare QED photon and a hadronic state

$$|\gamma\rangle = N_1 |\gamma_{\mathrm{QED}}\rangle + N_2 |h\rangle, \tag{1.23}$$

where N_1 and N_2 are normalization factors. At small relative momenta between both quarks, $p_\perp \lesssim 1\,\mathrm{GeV/c}$, the pair is considered as a bound state — the *vector meson* — as described within the framework of the Vector Meson Dominance Model [40]. The scattering between the vector meson and the proton proceeds via the exchange of a colourless object (the "pomeron") in QCD comprised of at least two gluons. For larger $p_\perp$, the quark pair is treated to be unbound (the so–called "anomalous" component of the photon [41]). This partonic content of the photon interacts directly with a parton from the proton.

With the presence of a hard scale, e.g. due to the large beauty quark mass, the partonic structure of the photon can be evolved in analogy to the proton structure functions using the DGLAP equations. In addition to the hadronic parton splitting terms of Equation (1.13), however, the process $\gamma \to q\bar{q}$ must be considered as an extra term [42, 43], i.e.

$$\frac{dq_i(x,Q^2)}{d\,\ln Q^2} = \left.\frac{dq_i(x,Q^2)}{d\,\ln Q^2}\right|_{\text{hadronic}} + \frac{\alpha}{2\pi}\int_x^1 \frac{dz}{z} P_{q\gamma}\Big(\frac{x}{z}\Big). \tag{1.24}$$

Depending on the parameterization of the photon structure function (taking LAC1 [44] as an extreme choice[4]) resolved processes contribute a maximum 40 % to the total beauty production cross section in photoproduction [46].

In the resolved process heavy quarks are produced predominantly in gluon–gluon–fusion (cf. Figure 1.2, right). Due to the small photon virtuality the photon remnant X' propagates in the direction of the scattered positron. Quark–antiquark annihilation $q\bar{q} \to \mathrm{Q}\bar{\mathrm{Q}}$ contributes approximately 10 % of the gluon–gluon–fusion contribution. Larger contributions to the resolved process are expected due to *heavy flavour excitation* [47], where the photon fluctuates into a heavy quark pair. Hard scattering occurs then between one of the heavy quarks and a parton in the proton. The Feynman diagram for this process is equivalent to that of photon–gluon–fusion, with $\hat{s} = (\boldsymbol{P}_{\mathrm{Q}(\bar{\mathrm{Q}})} + \boldsymbol{P}_X)^2$ defining the hard scale instead of $\hat{s} = (\boldsymbol{P}_{\mathrm{Q}} + \boldsymbol{P}_{\bar{\mathrm{Q}}})^2$.

1.2.2 Higher Order Processes

Th first measurements of the beauty production cross section (in gluon–gluon–fusion at CERN's Sp$\bar{\text{p}}$S storage ring [48, 49]) showed that LO QCD predictions are not sufficient to reproduce the total $b\bar{b}$ cross section. A comparison to the full theoretical calculations to order $\mathcal{O}(\alpha_s^3)$ [50, 51] established that NLO QCD contributions account for 30 % to 40 % of the overall cross section [52].

Similarly next–to–leading order QCD calculations for hadroproduction have been performed for photoproduction at HERA for all $2 \to 2$ and $2 \to 3$ processes [53] and completed to order $\mathcal{O}(\alpha\alpha_s^2)$ [37, 54]. Five contributing Feynman diagrams are shown in Figure 1.3. The resulting predictions for the total beauty cross section in photoproduction are listed in Table 1.1, where *all* free parameters have been varied to maximize (minimize) the cross section. The direct and resolved photon–gluon–fusion cross sections have uncertainties of factors 2 and 3 [43]. The largest contributing uncertainties are due to the value of the beauty quark mass, the knowledge of the gluon density in the

[4] This choice has in the meantime been disfavoured by measurements (e.g. [45]).

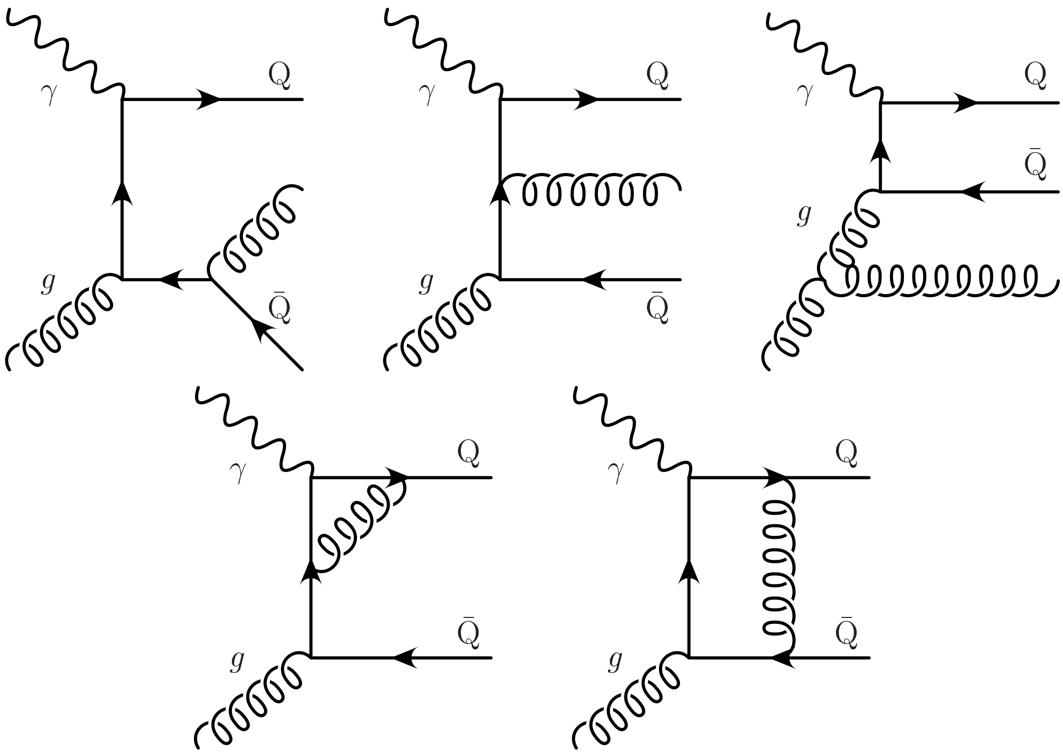

Figure 1.3: *Feynman Diagrams contributing to NLO QCD photon–gluon–fusion in $\mathcal{O}(\alpha\alpha_s^2)$. The upper row shows processes of final (left and middle) and initial state radiation (right). The vertex correction graphs in the lower row are of higher order but interfere with the leading order diagram because of the same final state and, therefore, contribute to $\mathcal{O}(\alpha\alpha_s^2)$. More graphs can be obtained by reversing the quark lines.*

Reference	σ_{tot} [nb]	μ_f	Scheme	μ_r	m_b [GeV/c^2]
R.K. Ellis and P. Nason [37]	min. 4.9	$2m_b$	$\overline{\text{MS}}$	$2m_b$	5.0
	max. 7.1	$m_b/2$	$\overline{\text{MS}}$	$m_b/2$	4.5
S. Frixione et al. (FMNR) [46]	min. 4.81	m_b	$\overline{\text{MS}}$	m_b	5.0
	max. 9.91	m_b	$\overline{\text{MS}}$	m_b	4.5
R.A. Eichler and Z. Kunzst [53]	8.0	$\frac{1}{2}\sqrt{\hat{s}}$	—		5.27
J. Smith and W.L. van Neerven	min. 6.12	$2m_b$	$\overline{\text{MS}}$	$2m_b$	4.75
[54]	max. 8.77	$m_b/2$	DIS	$m_b/2$	4.75
`AROMA 2.2` $b\bar{b}$ LO QCD [55]	3.53	$\sqrt{\hat{s}}$	—		5.0

Table 1.1: *Upper and lower boundaries for predictions of the total beauty production cross section in NLO QCD. The boundaries are obtained by varying all parameters, especially the renormalization scheme ("$\overline{MS}$" [56], "DIS" [57]) and scale μ_r, factorization scale μ_f and beauty quark mass m_b, in a direction that maximizes (minimizes) the cross section. For the sake of completeness, the last row gives the prediction of the* `AROMA` *$b\bar{b}$ Monte Carlo simulation which is to be used (cf. Section 1.4.1).*

proton and photon (thus also the knowledge of the photon structure function) and the renormalization and factorization scales [46].

In addition, radiative effects at small x_g induce large NLO corrections. These are proportional to the expansion parameter $\alpha\alpha_s^2 \ln(W_{\gamma p}^2/4m_Q^2)$, where $W_{\gamma p}^2 = Q^2 \cdot \frac{1-x_g}{x_g}$ (cf. Equation 1.6). For small values of x_g and at fixed Q^2 the parameter approaches unity, thereby spoiling the convergence of the perturbative expansion. Because of the large mass of the beauty quark, the resummation of all *small–x effects* leads to an increase in the NLO QCD result by approximately 5 % [43]. In charm production at HERA and in hadroproduction this increase is much larger.

1.2.3 Parton Showers and Fragmentation

Since beauty quark production at HERA dominates near threshold, i.e. $\hat{s} \approx 4 \cdot m_{\mathrm{Q}}^2$, the transverse momenta of the $b\bar{b}$ pair are small. Therefore, the heavy quarks are only of moderate virtuality. This virtuality decreases due to final state radiation and the heavy quarks approach their mass shell. The emitted gluons can subsequently radiate partons, where the probability of the emission of a specific parton and the decrease in the virtuality can be deduced from the splitting functions P_{qq}, P_{qg}, P_{gq} and P_{gg} (cf. Section 1.1.1). A *parton shower* develops [58]. Similarly initial state radiation can initiate a parton shower.

The contribution to heavy quark production due to parton showers (i.e. gluon splitting, $g \to \mathrm{Q\bar{Q}}$) has been measured for charm quarks and is approximately 2 % [15]. Since the beauty quark is more massive than the c–quark, the contribution to beauty production should be negligible.

String Fragmentation

With decreasing virtualities, the effective coupling α_s approaches unity. The partons, including the heavy quarks, enter the régime of confinement. The transition of all coloured quarks, including those from the proton remnant, to colourless mesons and baryons is described by the process of *fragmentation* (sometimes referred to as *hadronization*). Fragmentation is not yet understood from first principles, but can be modelled phenomenologically using for example the Lund string fragmentation model [59].

In the Lund string fragmentation model, confinement is implemented by stretching colour flux tubes (*strings*) between colour triplet states (a quark from either the parton showers or proton remnant). Di–quarks are considered to be in an anti–colour triplet state and are thus treated like antiquarks. The string topology can be derived from the colour flow of the hard process [60].

Strings correspond to a description of a linear confinement potential with string tension $\kappa \approx 1\,\mathrm{GeV/fm}$. As the triplets move apart, the potential energy in the flux tube increases and at a specific threshold the string breaks producing a new quark–antiquark pair out of the vacuum. The creation obeys the selection rule $u\bar{u} : d\bar{d} : s\bar{s} : c\bar{c} \approx 1 : 1 : 0.3 : 10^{-11}$. Thus the production of heavy quarks through fragmentation is highly suppressed. The new $q\bar{q}$ pair attaches to the ends of the split string. If the invariant mass of either of the string pieces is large enough, further breaks occur. The string splitting process proceeds until only on–shell mesons and baryons remain. These constitute the hadronic final state.

1.2.4 The b–Flavoured Hadron Decay into J/ψ Mesons

In a first approximation of b–flavoured hadron decays, only the single constituent beauty quark participates in the transition, with the other light quark(s) "spectating". The beauty quark can only decay weakly into a c– or a u–quark via the emission of a W^- boson (Figure 1.4). The width Γ of a heavy quark weak decay $\mathrm{Q}^a \to \mathrm{Q}^b X$ is proportional to the

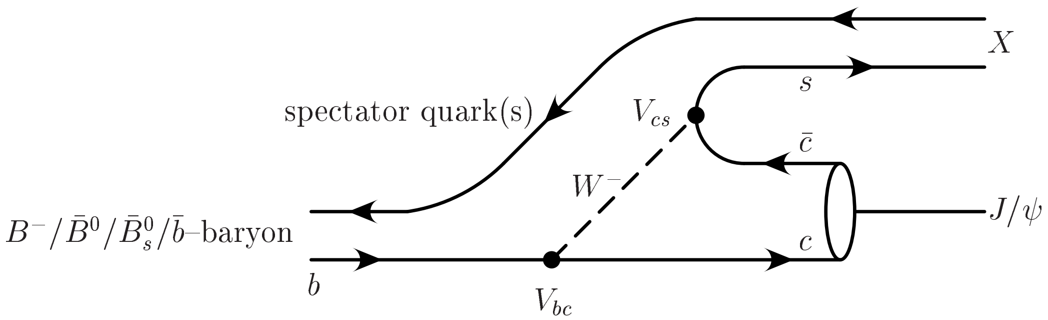

Figure 1.4: *Feynman diagram of the weak decay of the b–quark and the successive production of a J/ψ meson. The $c\bar{c}$ pair forms a colour singlet state and hadronizes into the J/ψ meson. The spectator quark and the remaining light quark fragmentate into a final state X, which is most likely a kaon.*

corresponding squared elements of the Cabbibo–Kobayashi–Maskawa (CKM) matrix [61]:

$$\Gamma(\mathrm{Q}^a \to \mathrm{Q}^b X) \propto |V_{\mathrm{Q}^a\mathrm{Q}^b}|^2 \tag{1.25}$$

Measurements of the semi–leptonic decays of B mesons at LEP and at CLEO have shown that the matrix elements relevant for b–quark decay are very small compared to other elements: $|V_{ub}| = [4.00 \pm 0.65(\text{stat.})^{+0.67}_{-0.76}(\text{syst.}) \pm 0.19(\text{theory})] \cdot 10^{-3}$ [62] and $|V_{cb}| = 0.0402 \pm 0.0019$ [34]. Consequently the b–quark decay is highly suppressed, i.e. it has a relatively large *lifetime*. Since the matrix element for the decay $b \to cW^-$ dominates ($|V_{bu}/V_{bc}| = 0.090 \pm 0.025$ [34]), beauty quarks prefer to decay into a charm quark than into an up quark.

Subsequently, the $W^\pm$ boson decays either semi–leptonically or hadronically. In the work described here, the decays $W^- \to s\bar{c}$ and $W^- \to d\bar{c}$ (and charge conjugates) are of specific interest. If the colour assignments of the anticharm quark and of the charm quark — the b–quark's remnant — can be combined to a colour singlet state, both can form a bound $c\bar{c}$ state, e.g. a J/ψ meson (cf. Section 1.3). The measured branching ratio for the b–flavoured hadronic decays into a J/ψ meson, $B^+/B^0/B_s^0/b$–baryon $\to J/\psi X$, is [34]

$$BR(B^+/B^0/B_s^0/b\text{–baryon} \to J/\psi X) = (1.16 \pm 0.10)\,\%. \tag{1.26}$$

The remaining light quark and the spectator quark participate in the fragmentation into a hadronic final state X. Since $|V_{cd}|/|V_{cs}| = 0.215 \pm 0.037$ [34], the $s\bar{c}$ combination is preferred. The hadronic final state which is produced is therefore most likely to contain a strange quark, for example inside a kaon.

In this thesis, this decay channel $B^+/B^0/B_s^0/b$–baryon $\rightarrow J/\psi X$ will be used for the first time at HERA to determine the beauty cross section in photoproduction. The total cross section for J/ψ meson production from b–flavoured hadron decays has been predicted to be 180 pb [53] (i.e. 90 pb per beauty quark). Together with the leptonic decay modes of the J/ψ meson, $J/\psi \rightarrow e^+e^-$ and $J/\psi \rightarrow \mu^+\mu^-$ (cf. Section 1.3), the total branching ratio $B^+/B^0/B_s^0/b$–baryon $\rightarrow J/\psi X \rightarrow l^+l^-X$ is (0.068 ± 0.006) % for each leptonic decay channel.

Lifetime

The typical time scale of weak decays is of the order $\mathcal{O}(M_W^{-1}) \approx \mathcal{O}(10^{-12}\,\mathrm{s})$. This is much longer than the lifetime of the J/ψ meson (cf. Section 1.3). Therefore the J/ψ meson is considered to decay immediately after creation, i.e. to decay *promptly*. Under the assumption that a B meson and a J/ψ meson were produced, a J/ψ meson resulting from the b–flavoured hadron's decay is delayed compared to prompt J/ψ meson background.

The b–flavoured hadron's *lifetime* $c\tau$ is related to a decay length l,

$$l = \beta\gamma \cdot c\tau = \frac{p(B)}{m(B)} \cdot c\tau, \tag{1.27}$$

where $m(B)$, $\beta\gamma$ and $p(B)$ and are the particle's mass, boost and momentum respectively. The probability for an unstable particle to decay at some length L is given by

$$\mathcal{P}(L) = 1 - \exp\left(-\frac{L}{\beta\gamma c\tau}\right). \tag{1.28}$$

This length L can be viewed as the distance between the $b\bar{b}$ production vertex, i.e. the ep interaction point, and the location of the subsequent J/ψ meson's decay. The mean lifetimes of b–flavoured hadrons have been measured at LEP [34] to be

$$c\tau(B^+) = 496\,\mu\mathrm{m} \tag{1.29}$$
$$c\tau(B^0) = 464\,\mu\mathrm{m} \tag{1.30}$$
$$c\tau(B_s^0) = 448\,\mu\mathrm{m} \tag{1.31}$$
$$c\tau(\Lambda_b^0) = 368\,\mu\mathrm{m}. \tag{1.32}$$

The weighted average is 466 μm, where the weights are given by the production fractions $B(\bar{b} \rightarrow B^+, B^0) = 2 \times (38.9 \pm 1.3)$ %, $B(\bar{b} \rightarrow B_s^0) = (10.7 \pm 1.4)$ % and $B(\bar{b} \rightarrow b\text{–baryon}) = (11.6 \pm 2.0)$ % [34]. The average boost $\beta_t\gamma$ at HERA[5], however, is only about 0.7 and increases slowly with virtuality Q^2 (Figure 1.5). Thus the average decay length is ap-

[5] Here the subset "t" denotes transverse components with respect to the initial proton's flight direction. The H1 experiment is more sensitive in the transverse plane as will be described in Chapter 2.

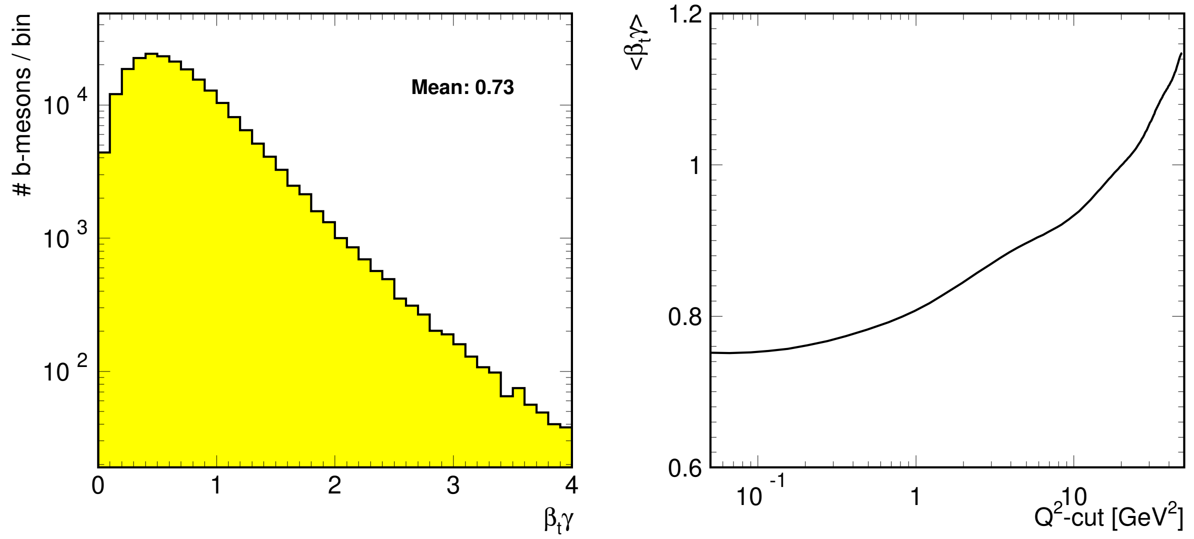

Figure 1.5: *$\beta_t\gamma$ distribution for beauty–flavoured hadrons (left) and its mean value as a function of the photon virtuality Q^2 (right). After a steep rise at very low Q^2 values, the distribution reaches a mean of unity for $Q^2 \gtrsim 23$ GeV^2. The properties have been calculated using the* `AROMA` *$b\bar{b}$ Monte Carlo simulation (cf. Section 1.4.1)*

proximately 326 μm. An identification of b–flavoured events through a lifetime based tag and their separation from the prompt J/ψ meson background should still be feasible if the production and decay vertices of the B meson are known with high precision, i.e. $\mathcal{O}(100\mu m)$.

1.2.5 Measurements of the Beauty Production Cross Section

The first measurement of the beauty production cross section at HERA was based on the semi–muonic decay of the beauty quark [16]. Since the beauty quark is heavier than the charm quark this leads to the expectation that the muon shows a relatively high transverse momenta $p_\perp^{\mathrm{rel}}$ with respect to the direction of flight of the decaying particle. Since b–flavoured hadrons can only be poorly reconstructed at HERA, their direction is approximated by the thrust axis of the jet associated with the muon. The observed $p_\perp^{\mathrm{rel}}$ distribution of the muon can be described using contributions from beauty– and charm–flavoured Monte Carlo events as well as events with mis–identified muons (cf. Figure 1.6, left). The simultaneous fit gives the visible b–quark cross section in photoproduction at H1, $\sigma_{\mathrm{vis}}(ep \to b\bar{b}X \to \mu X') = [176 \pm 16(\mathrm{stat.})^{+26}_{-17}(\mathrm{syst.})]$ pb [17]. This has been compared to NLO QCD calculations by Frixione et al. (FMNR) [46] with $m_b = 4.75\,\mathrm{GeV/c^2}$ and the MRS(G) [63] and GRV-HO [64] structure functions for the proton and photon respectively. The prediction for the visible cross section of 54 ± 9 pb [65] underestimates the measurement by a factor of about 3.25. The visible cross section has also been extrapolated to the available full phase–space. The total photoproduction cross section is $\sigma(ep \to eb\bar{b}X) = [14.8 \pm 1.3(\mathrm{stat.})^{+3.3}_{-2.8}(\mathrm{syst.})]$ nb at $\sqrt{s} \approx 300\,\mathrm{GeV}$.

A similar analysis performed by the ZEUS collaboration used the semi–leptonic decay into an electron, $ep \to b\bar{b}X \to e + \mathrm{dijet} + e^- X$ and qualifies the observed deviation. The

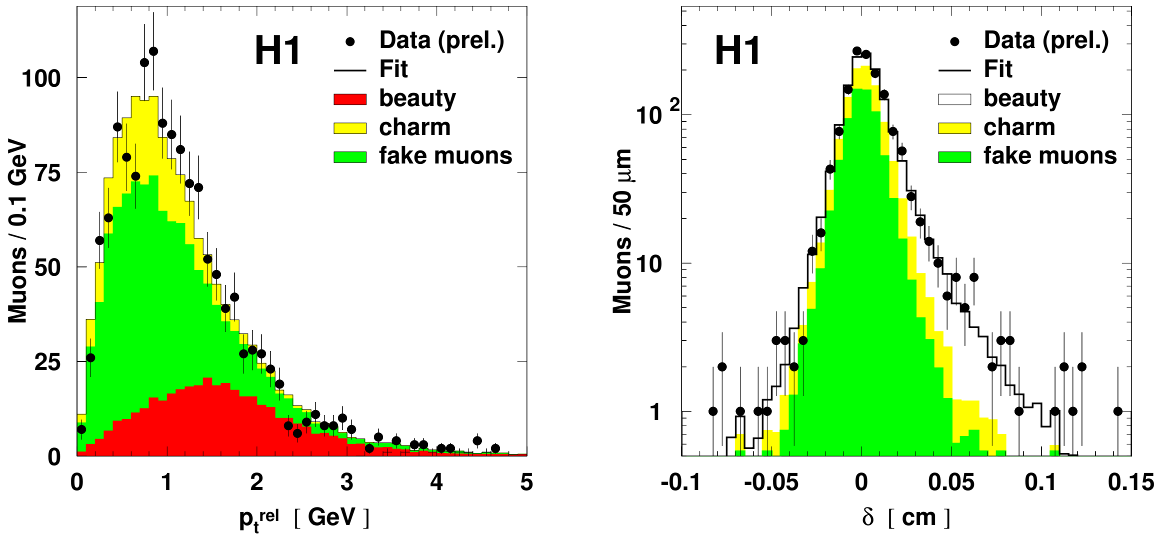

Figure 1.6: *Measurement of the beauty production cross section in photoproduction [19]. Contributions from beauty– and charm–flavoured Monte Carlo events as well as from wrongly identified ("fake") muons are fitted to the $p_\perp^{\rm rel}$ (left) and the impact parameter distributions (right).*

visible cross section is within errors in agreement with the prediction, while the cross section extrapolated to the full phase–space lies "somewhat above" [18] the central NLO predictions.

An extension of the H1 measurement uses in addition the lifetime information from the weak decay of the beauty quark [19]. This measurement exploited, in addition to the relative transverse momentum $p_\perp^{\rm rel}$ (cf. above), the impact parameter δ of the muon relative to the ep interaction vertex. The cross section has been determined from a combined two–dimensional $(\delta, p_\perp^{\rm rel})$ likelihood fit (Figure 1.6) and leads to a visible cross section $\sigma_{\rm vis}(ep \to b\bar{b}X \to \mu X) = [160 \pm 16({\rm stat.}) \pm 29({\rm syst.})]$ pb. This is, within errors, in agreement with the first H1 measurement.

Using the same two–dimensional method, recent preliminary results establish an excess with respect to the expectation in the deep inelastic scattering régime [20]. The measured cross section $\sigma_{\rm vis}(ep \to b\bar{b}e'X \to \mu e'X) = [39 \pm 8({\rm stat.}) \pm 10({\rm syst.})]$ pb may be compared with (11 ± 2) pb from a NLO QCD prediction [66]. As observed in photoproduction, the theoretical prediction is about a factor of 3.5 below measurement.

Measurements of the semi–leptonic decay of b–flavoured hadrons in photon–photon collisions at LEP also reveal that NLO QCD predictions underestimate the inclusive b–quark cross section. The production cross sections have been determined to be about three [31] and two standard deviations [32] higher than expected from NLO QCD calculations respectively.

More exclusive measurements have been performed at the Tevatron [21]–[25], e.g. using the exclusive decay $B \to J/\psi K$ [26]–[30]. Measurements of the integrated cross section for b–quarks with a transverse momentum above a given limit $p_t^{\rm min}$ are shown for several

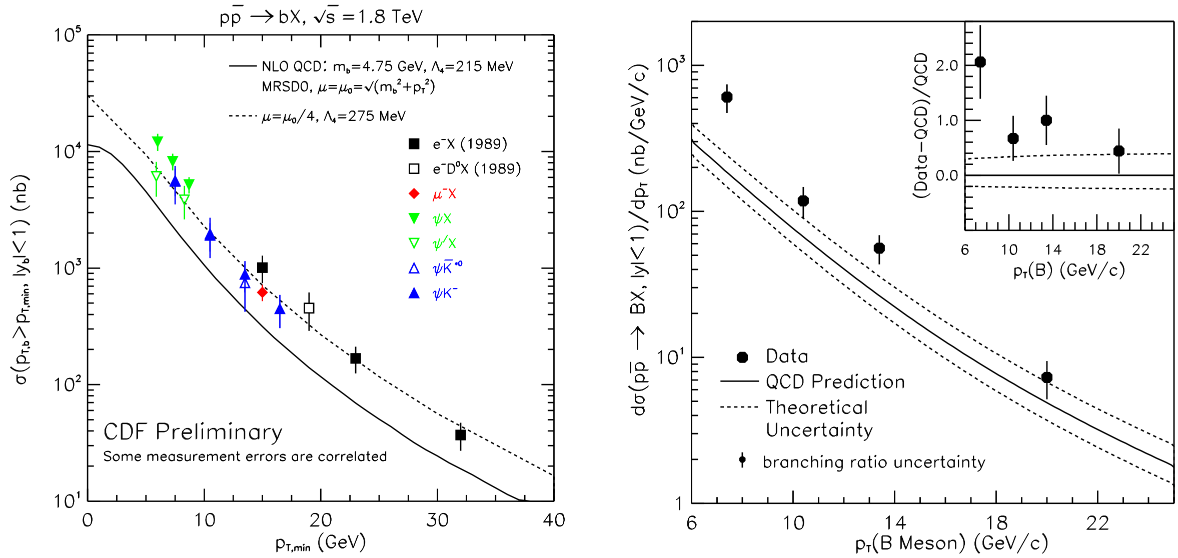

Figure 1.7: *Measurements of the beauty production cross section in hadroproduction at CDF. The integrated cross section for $p_t(b) > p_t^{\min}$, using several decay modes, is shown on the left [21, 26, 27]. The observations agree over a wide range in transverse momentum with the upper band of the NLO QCD prediction [51]. On the right, the average B meson differential cross section [29] is compared to NLO QCD [51, 67]. The inset graph shows the ratio (data − QCD)/QCD on a linear scale. Figures from [68].*

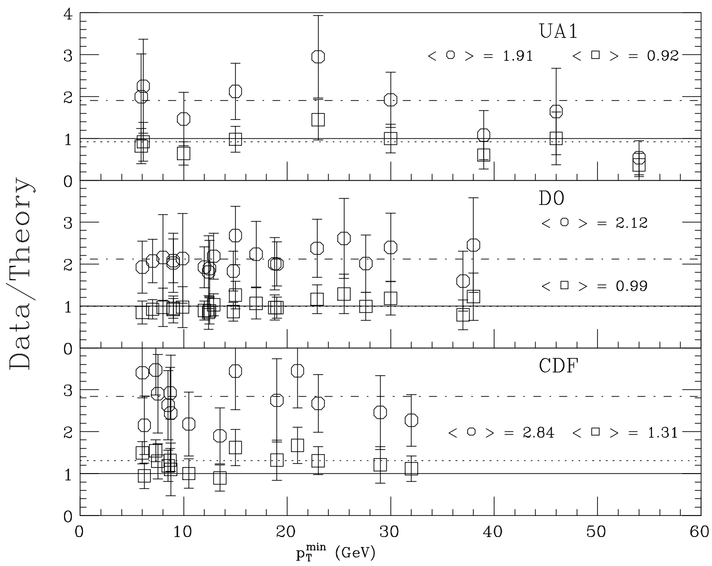

Figure 1.8: *Comparison between theory and data [21, 22, 26, 27, 49] for the beauty production cross section for $p_t(b) > p_t^{\min}$ in $p\bar{p}$ collisions. The open circles have been obtained in using default parameters for the theory prediction ($m_b = 4.75$ GeV/c^2, $\mu_r = \mu_f = \mu_0$, where $\mu_0 = \sqrt{p_t^2 + m_b^2}$ and $\Lambda_5^{\overline{MS}} = 152$ MeV). The boxes represent an extreme choice of the parameters, namely $m_b = 4.5$ GeV/c^2, $\mu_r = \mu_f = \mu_0/2$ and $\Lambda_5^{\overline{MS}} = 300$ MeV. Figure from [69].*

different decay modes in Figure 1.7 (left). Although the shape of the distribution is very well described by NLO QCD predictions, the absolute value is only consistent with the upper edge of the NLO QCD band. This discrepancy becomes smaller for higher transverse momenta [24]. Furthermore, the exclusive decay $B \to J/\psi K$ can be used to determine the differential cross section $d\sigma(p\bar{p} \to bX)/dp_t$. The theoretical prediction is an overall scale factor $1.9 \pm 0.2(\text{stat.}) \pm 0.2(\text{syst.})$ below the measurement [29] (Figure 1.7, right). A comparison between theory and data in hadroproduction is shown in Figure 1.8.

1.2.6 Conclusions

The present–day NLO QCD calculations of the beauty production cross section underestimate various recent measurements by a factor of order two to three in electroproduction as well as in hadroproduction. Large corrections to the prediction are expected due to NNLO QCD contributions and from the uncertainty in the beauty mass, the scales and renormalization schemes involved and in the gluon density in the proton.

Since the Tevatron runs at higher center–of–mass energies than HERA, larger influences on the NLO calculations due to the parameterization of the gluon density at low values of x and the previously mentioned other small–x effect are expected in hadroproduction [70] than in photoproduction. The difference between the theory and the Tevatron measurements is expected to be larger than those determined at H1. This is, however, not observed.

A recent approach [71] is to extract the unintegrated gluon density from HERA F_2 measurements using CCFM evolution equations [72] rather than DGLAP. The CCFM equations reproduce the correct small–x leading logarithms for the total cross section. These calculations give a good simultaneous description of the Tevatron and ZEUS measurements, but still underestimate the H1 measurements by a factor of about 2.6 [73]. The larger discrepancy between this theoretical prediction and the measurements of the H1 collaboration is still being discussed.

1.3 Direct J/ψ Vector Meson Production

The hadronization of a b– or $\bar{b}$–quark into a final state containing a J/ψ vector meson is used in this thesis to tag beauty events. Due to the low beauty production cross section, this contribution is expected to be smaller than the main direct J/ψ meson production mechanisms, which are here sources of background.

The production of the J/ψ meson can be divided into two mechanisms, *diffractive* and *inelastic* J/ψ meson production. Diffractive production is described using the exchange of a colourless "pomeron", whereas in the inelastic case photon–gluon–fusion is the dominant process. Both mechanisms are *prompt* in the sense that the production and the formation of the J/ψ meson happen within much smaller time scales than b–flavoured hadron production followed by a subsequent weak decay into a J/ψ meson.

Both J/ψ meson production mechanisms are described in Sections 1.3.2 and 1.3.3.

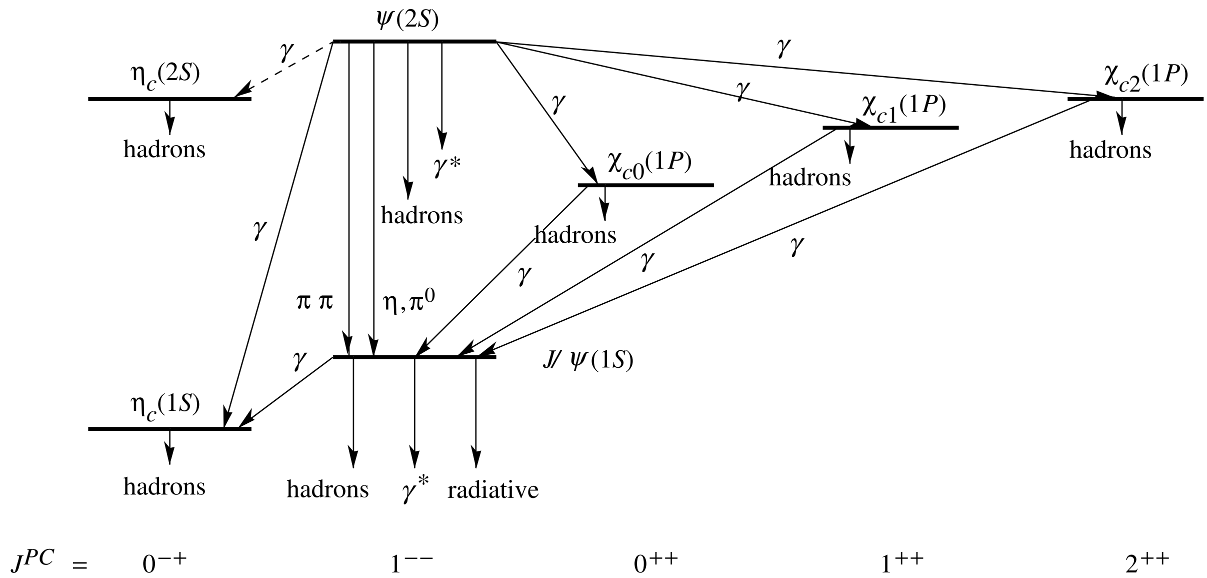

Figure 1.9: *Level diagram of the established members of the charmonium family. Figure from [76].*

1.3.1 Charmonia

In November 1974, in what was later to be referred to as the November Revolution of particle physics, two groups discovered almost simultaneously the particle today referred to as the J/ψ meson. At BNL an enhancement in the e^+e^- mass spectrum was observed in the reaction $pBe \to (J \to e^+e^-)\,X$, naming it "$J$" [74]. At SLAC, a narrow resonance "ψ" was discovered in the total e^+e^- annihilation cross section [75]. These discoveries led to S.C.C. Ting and B. Richter being awarded the 1976 Nobel Prize in physics.

The J/ψ particle is identified as a member of the *charmonium* family consisting of a bound *charm–anticharm* ($c\bar{c}$) state with the quantum numbers $n^{2s+1}L_J = 1^3S_1$. Here n denotes the radial quantum number, s the intrinsic spin and L and J the orbital and total angular momenta respectively. The J/ψ particle translates under charge conjugation C and parity transformation P in the same way as the photon, $J^{PC} = 1^{--}$. Consequently the J/ψ particle is a vector meson. The current world average measurement of its mass is [34]

$$m_{J/\psi} = 3.09687 \pm 0.00004\,\mathrm{GeV/c^2}. \tag{1.33}$$

With the exception of the pseudo–scalar η_c particle ($J^{PC} = 0^{-+}$) which has a mass $m_{\eta_c} = 2.98\,\mathrm{GeV/c^2}$, the J/ψ vector meson is the lightest meson in the charmonium family (Figure 1.9).

The J/ψ meson produces a very narrow resonance of width

$$\Gamma_{J/\psi} = (87 \pm 5)\ \mathrm{keV}, \quad \text{i.e. a lifetime of} \quad \tau = \frac{\hbar}{\Gamma} = (7.6 \pm 0.1) \cdot 10^{-21}\,\mathrm{s}. \tag{1.34}$$

This decay width is about three orders of magnitude below that typical of strong decays, e.g. ρ meson decays. The extremely small value is a consequence of the fact that charm conserving J/ψ meson decays, e.g. the decay of the J/ψ meson into a pair of charmed $D\bar{D}$ mesons, are energetically forbidden, since the J/ψ meson has a mass below threshold[6]. All other strong decay modes can only proceed via diagrams in which the $c\bar{c}$ pair annihilates and these are strongly suppressed as described by the Okubo–Zweig–Iizuka rule [77]. Decays via single or two gluon exchange do not preserve simultaneously colour conservation and the Landau–Yang theorem. The Landau–Yang theorem states that two massless spin–one particles cannot couple to a state with an angular momentum of one (like the J/ψ meson) [78]. Thus at least three gluons are needed for the hadronic decay of the J/ψ meson (Figure 1.10, left).

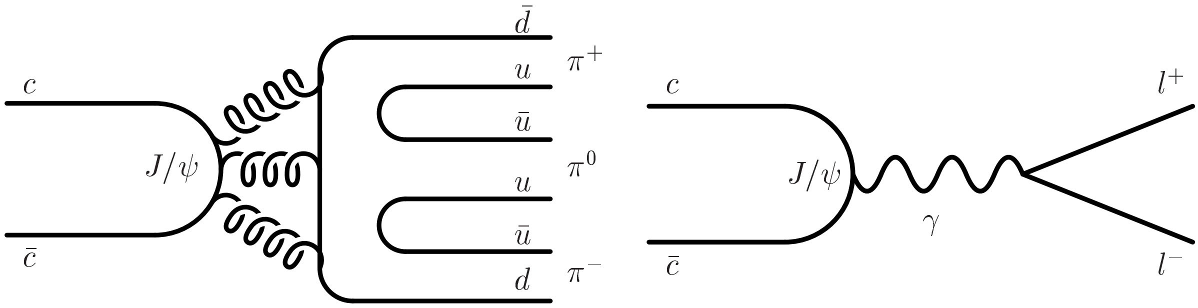

Figure 1.10: *Strong decay of the J/ψ meson into three light mesons (left) and electromagnetic decay into two leptons (right).*

The J/ψ meson's electromagnetic decays, e.g. $J/\psi \to \mu^+\mu^-$, therefore dominate (cf. Figure 1.10, right). The electronic width is $\Gamma_{ee} = (5.26 \pm 0.37)$ keV [34], which corresponds to a lifetime of $\tau = (1.25 \pm 0.09) \cdot 10^{-19}$ s. Lepton universality implies identical branching ratios for the decay into e^+e^- and $\mu^+\mu^-$. The branching ratios have been measured to be [34]

$$BR(J/\psi \to e^+e^-) = (5.93 \pm 0.10)\,\% \qquad (1.35)$$

$$BR(J/\psi \to \mu^+\mu^-) = (5.88 \pm 0.10)\,\%. \qquad (1.36)$$

The Inelasticity z

A powerful variable which can be used to discriminate the different J/ψ production mechanisms in *ep* scattering from the decay of b–flavoured hadrons, is the Lorentz invariant inelasticity

$$z \equiv \frac{\boldsymbol{P} \cdot \boldsymbol{P}_{J/\psi}}{\boldsymbol{P} \cdot \boldsymbol{q}} = \frac{y_{J/\psi}}{y}, \qquad (1.37)$$

where $\boldsymbol{P}_{J/\psi}$ is the four–momentum of the J/ψ meson and $\boldsymbol{P}$, $\boldsymbol{q}$ and y are as defined in Section 1.1. In the proton rest frame, the *inelasticity* is the fraction of the photon's energy transferred to the J/ψ meson, $z = E_{J/\psi}/E_{\gamma^*}$. Since beauty quarks are always produced in pairs, the inelasticity z of an event in which a J/ψ meson is created in a b–flavoured decay cannot exceed 0.5 (Figure 1.11). Slightly higher values can occur, if the heavy quarks' transverse momenta are not exactly balanced.

[6]This holds for all charmonia below the 3^3S_1 ψ'' state.

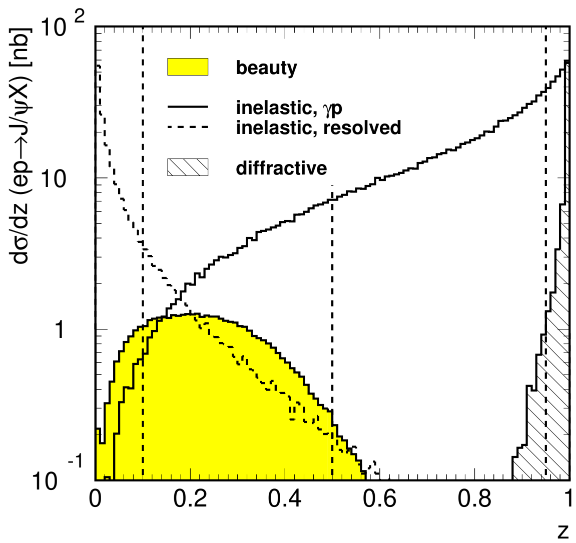

Figure 1.11: *Distributions for the inelasticity z separately for the direct inelastic (solid line), resolved inelastic (dashed line) and diffractive (hatched) J/ψ production. The shaded histogram marks the region for J/ψ mesons from b–flavoured hadron decays, where its contribution is normalized to the cross section measured at H1 [17, 65]. The vertical lines represent the domain borders (at $z = 0.1$, 0.5 and 0.95) used in this thesis. The inelastic (diffractive) distributions have been calculated with the* `EPJPSI` *(*`DIFFVM`*) $c\bar{c}$ Monte Carlo simulation; the b–flavoured contribution with the* `AROMA` *$b\bar{b}$ Monte Carlo simulation (cf. Section 1.4).*

1.3.2 Diffractive J/ψ Meson Production

Diffractive processes characteristically produce a large *rapidity gap*[7] between the hadronic final state, e.g. the J/ψ meson, and the proton. This is interpreted as arising from the exchange of a colourless object between the vector meson and the proton.

In the framework of the Vector Meson Dominance Model [40] the initial photon is (as in the resolved processes mentioned in Section 1.2.1) a superposition of a bare QED photon and a hadronic state. In this context, the photon is assumed to fluctuate into a J/ψ meson. The subsequent interaction of this virtual hadron and the proton puts the J/ψ meson on mass shell (Figure 1.12). Diffractive hadron–hadron scattering is assumed to proceed via the exchange of a colourless object with the quantum numbers of the vacuum, e.g. at high energies the “pomeron” trajectory (*Regge theory* [79]). Perturbative QCD simulates the exchange of the pomeron using a minimum of two gluons [80].

In diffractive scattering events the proton can remain intact (*elastic*) or break–up (*proton–dissociative*). The inelasticity of the former process is $z \approx 1$ and in the latter case $z \gtrsim 0.95$. Due to these high inelasticity values, diffractive J/ψ production is not a background source

[7] The rapidity is defined as

$$\eta \equiv \frac{1}{2} \ln \frac{E + p_z}{E - p_z} \tag{1.38}$$

and is equal to the pseudo–rapidity $\eta^* \equiv -\ln(\tan\theta/2)$ if the particle mass is neglected. Except for an additional constant, the rapidity difference is invariant under Lorentz transformation along the z–axis.

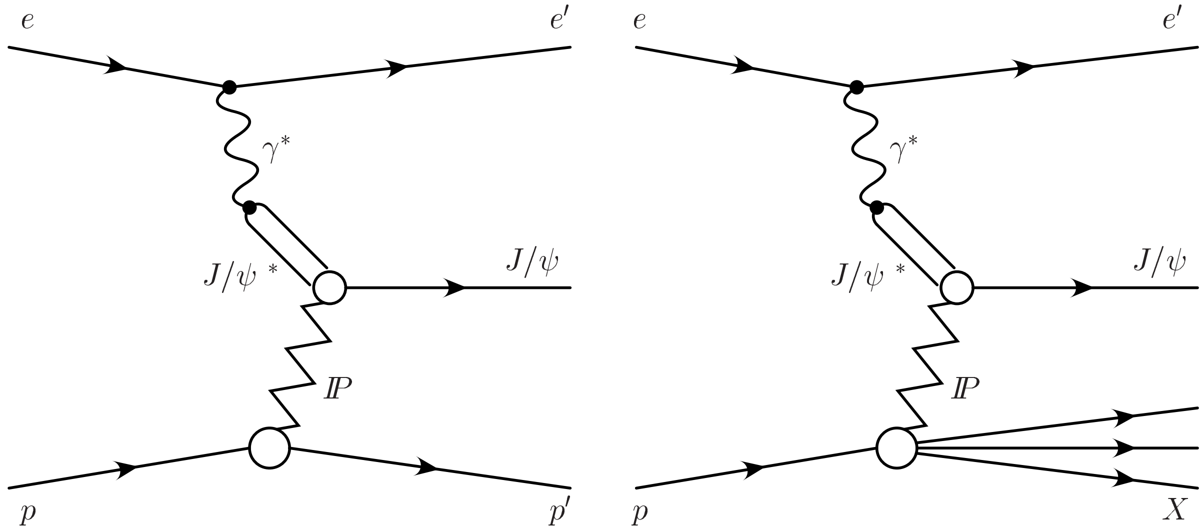

Figure 1.12: *Feynman diagrams for elastic (left) and proton–dissociative (right) J/ψ meson production. The photon fluctuates into a virtual J/ψ meson which becomes real in the subsequent pomeron exchange with the proton.*

in the analysis described in this thesis (cf. Figure 1.11), but is used for systematical cross–checks.

1.3.3 Inelastic J/ψ Meson Production

For inelasticities $z \lesssim 0.95$, the description of J/ψ production due to photon–gluon–fusion becomes appropriate. In this process $c\bar{c}$ pairs produced in photon–gluon–fusion fluctuate into a bound state with the same quantum numbers as a charmonium state, e.g. the J/ψ meson $ep \to c\bar{c}X \to J/\psi X$ [81]. The quark–pair is produced over short time scales $\mathcal{O}(m_c^{-2})$ compared to the time needed for the formation of a colourless bound charmonium state. The former process can be calculated in pQCD whilst the latter is a non–perturbative long distance process. Several models exist to describe the transition from a coloured $c\bar{c}$ pair into a colourless J/ψ meson.

Direct photon–gluon–fusion dominates J/ψ production at medium z values. Resolved processes contribute significantly at $z < 0.3$ (cf. Figure 1.11). Consequently inelastic J/ψ production is expected to be *the* main background source.

A overview of inelastic J/ψ production can be found in [82].

The **Colour–Singlet Model** (*CSM*) describes the transition of a coloured $c\bar{c}$ pair into a J/ψ meson via the emission of one *hard gluon* [81, 83] (Figure 1.13). The $c\bar{c}$ pair acquires the same quantum numbers (colour, spin, angular momentum, C–parity) as the final charmonium state. The cross section can be factorized into the short–time hard process of creating a $c\bar{c}$ pair in a colour singlet state, and the long–time process describing the transition into a bound state, $c\bar{c} \to J/\psi$;

$$d\sigma(\gamma g \to J/\psi g) \propto d\hat{\sigma}(\gamma g \to c\bar{c}[n]\; g) \cdot \langle \mathcal{O}^{J/\psi}[n] \rangle. \tag{1.39}$$

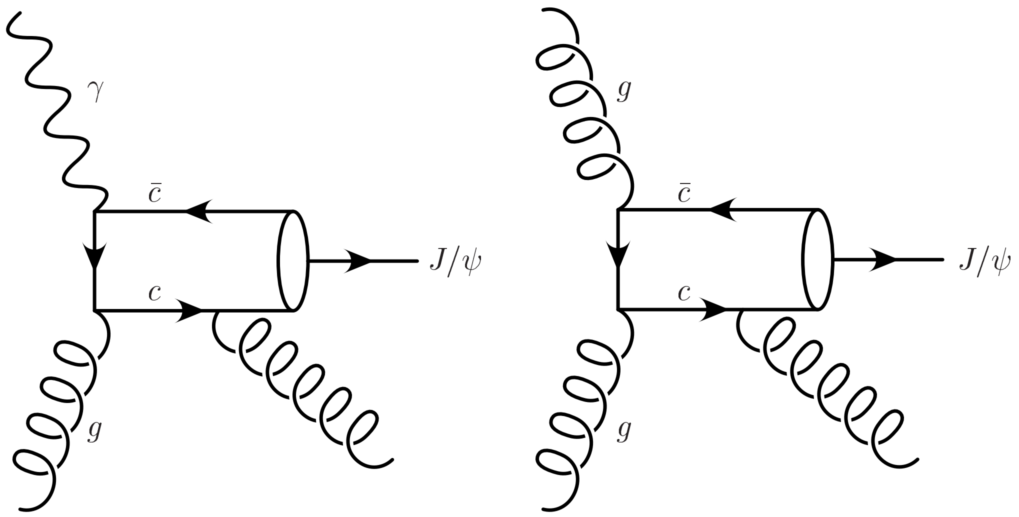

Figure 1.13: *Feynman diagrams for inelastic J/ψ meson production in the Colour–Singlet Model. The $c\bar{c}$ pair is produced via photon–gluon–fusion (direct photon process, left) or gluon–gluon–fusion (resolved photon process, right).*

Here $[n]$ denotes the $c\bar{c}$ state, e.g. $n = (\text{col},{}^{2S+1}L_J) = (\underline{1},{}^3S_1)$ where $\underline{1}$ labels a colour singlet state. The matrix element $\langle \mathcal{O}^{J/\psi}[n] \rangle$ is proportional to the squared radial wavefunction of the J/ψ meson at the origin and is related to the leptonic decay width Γ_{ee};

$$\langle \mathcal{O}^{J/\psi}[\underline{1},{}^3S_1] \rangle \propto |R_{J/\psi}(0)|^2 = \frac{m^2_{J/\psi}}{4e_c^2\alpha^2} \cdot \Gamma_{ee} \cdot \left(1 - \frac{16\alpha_s}{3\pi}\right)^{-1}. \tag{1.40}$$

The QCD correction to the leptonic decay width (term in brackets) leads to an increase of $|R_{J/\psi}(0)|$ by approximately a factor two [84].

The perturbative expansion requires a hard gluon, so the CSM is only reliable in the region $z \lesssim 0.9$ (Figure 1.14, left). In photoproduction, NLO QCD contributions of order $\mathcal{O}(\alpha_s^3)$ to the hard process give high correction factors at higher transverse momenta, $p_t^2(J/\psi) \gtrsim 2\,\mathrm{GeV}^2/\mathrm{c}^2$ [88, 89] (Figure 1.14, right).

The CSM depends only on one non–perturbative parameter, $\langle \mathcal{O}^{J/\psi}[\underline{1},{}^3S_1] \rangle$, for any high energy process. It, therefore, has enormous predictive power, but lacks a general factorization theorem for higher orders in pQCD. Despite the discrepancy with $p\bar{p}$ measurements at the Tevatron [27, 30, 90], the CSM successfully describes inelastic J/ψ production at HERA [85, 86] (cf. Figure 1.14) and muon production at fixed target experiments (NMC, EMC) [91].

Colour–Octet (*CO*) calculations generalize the Colour–Singlet Model by including colour octet matrix elements $\langle \mathcal{O}^{J/\psi}[\underline{8},{}^1S_0] \rangle$, $\langle \mathcal{O}^{J/\psi}[\underline{8},{}^3S_1] \rangle$ and $\langle \mathcal{O}^{J/\psi}[\underline{8},{}^3P_{0,1,2}] \rangle$:

$$d\sigma(ep \to J/\psi X) = \sum_{c\bar{c}\text{ states }n} C_n(ep \to c\bar{c}[n] + X) \cdot \langle \mathcal{O}^{J/\psi}[n] \rangle \tag{1.41}$$

The factors C_n are once again perturbatively calculable parton cross sections describing the production of a $c\bar{c}$ pair with vanishing relative momentum. The non–perturbative factor $\langle \mathcal{O}^{J/\psi}[n] \rangle$ describes the formation of a bound state by the emission of soft gluons.

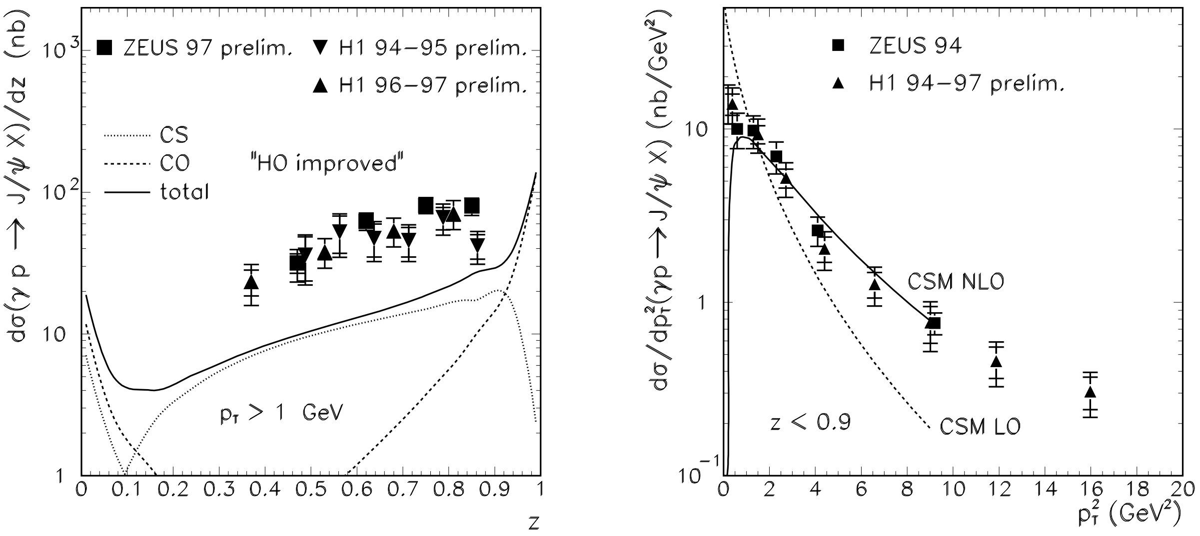

Figure 1.14: *Measurements of inelastic J/ψ meson production at HERA [85, 86]. The differential cross section in leading order as a function of the inelasticity z is shown on the left. A good agreement with Colour–Singlet (dotted line) and Colour–Octet (dashed line) calculations [87] is achieved if a normalization of approximately $k = 3$ is applied to the predictions. This k–factor accounts for the missing NLO QCD contributions. The trends at low–z are the corresponding resolved contributions. On the right, the cross section as a function of the transverse momentum of the J/ψ meson $p_t(J/\psi)$ is compared with leading order and NLO calculations in the Colour–Singlet Model [88]. No k–factor has been applied.*

The Colour–Octet calculations are based on a general factorization formalism [92] based on non–relativistic QCD (*NRQCD*) velocity scaling rules. NRQCD is an effective field theory in which the heavy quarks are treated non–relativistically. If the relative velocity of the charm quarks in the J/ψ meson is of the order $v^2 \approx 0.25$ the infinite expansion in Equation (1.41) can be truncated to a low order in v. Colour–Octet contributions are suppressed by a factor v^4 compared to J/ψ production in a colour singlet state. In the limit $v \to 0$ the CSM is restored. The leading–order process contributes at values of $z \approx 1 - v^2 \gtrsim 0.8$ and $p_t(J/\psi) \to 0$.

Measurements at HERA [93]–[95] have so far not been able to determine whether Colour–Octet contributions are necessary to describe inelastic J/ψ meson production (cf. Figure 1.14). A separation is most likely possible at low z, in a régime, where J/ψ mesons from b–flavoured hadron decays contribute as background. This contribution is usually modelled by Monte Carlo simulations. Due to the aforementioned uncertainty in the beauty production cross section, the simulation of the b–flavoured background will induce large systematic errors. The measurement presented in this thesis will constrain the fraction of J/ψ mesons originating from beauty–flavoured hadron decays at low z.

$\psi(2S)$ Production

$\psi(2S)$ mesons ($m_{\psi(2S)} = 3.686\,\mathrm{GeV/c^2}$, $J^{PC} = 1^{--}$) can also be produced in photon–gluon–fusion. Their branching ratio $BR(\psi(2S) \to J/\psi X)$ is $(55 \pm 5)\%$ [34]. QCD calculations have determined the $\psi(2S)$ production cross section to be about one quarter of the J/ψ production cross section. The inclusive J/ψ production cross section is, therefore, enhanced by approximately 15 %.

J/ψ meson production via the decay of other charmonia states are negligible.

1.4 Monte Carlo Simulations

The *Monte Carlo simulation* of physics processes is used to study detector acceptances and efficiencies, to correct the data for detector effects and to estimate contributions from background processes. According to the theoretical calculations of a specific process, e.g. beauty or J/ψ meson production, including parton showers and the subsequent hadronization, Monte Carlo (*MC*) generators deliver the four–momenta of all stable particles, i.e. particles with a lifetime longer than typically 8 ns. For most particles the origin of these four–vectors correspond to the nominal interaction region of the initial colliding beams. The detector response to all generated stable particles is simulated in a second step, thus the theoretical prediction can be compared to measurement. The H1 experiment, its detector components and their response to particles crossing them will be described in Chapter 2.

Two different Monte Carlo generators are used in this thesis: `AROMA 2.2` for the simulation of J/ψ meson production from beauty–flavoured hadron decays and `EPJPSI 3.3` for the description of the prompt inelastic J/ψ meson background. Table 1.2 gives a summary of their production processes, the corresponding cross sections and the generated integrated luminosities.

Throughout this thesis, the statistics of both years (1997 and 1999) are combined, unless explicitly stated otherwise. In the case of the `EPJPSI` $c\bar{c}$ MC simulation the direct and

Process		Cross Section [pb]	Int. Lumi. [pb^{-1}]	Events	Year
`AROMA 2.2`					
$b\bar{b} \to J/\psi X$	direct BGF	3442.7 ± 1.7	9 880	$34 \cdot 10^6$	1997
$b\bar{b} \to J/\psi X$	direct BGF	3608.4 ± 1.8	9 426	$34 \cdot 10^6$	1999
`EPJPSI 3.3`					
$c\bar{c} \to J/\psi$	direct BGF	11324.3 ± 203.3	153.1	$1.7 \cdot 10^6$	1997
$c\bar{c} \to J/\psi$	resolved BGF	1822.2 ± 38.0	469.5	86 000	1997
$c\bar{c} \to J/\psi$	direct BGF	11544.8 ± 142.2	150.0	$1.7 \cdot 10^6$	1999
$c\bar{c} \to J/\psi$	resolved BGF	1945.9 ± 35.2	439.8	86 000	1999

Table 1.2: *Listing of the used Monte Carlo generators. The columns label the production process, the underlying cross section, the generated integrated luminosity and number of events. The year refers to the corresponding detector simulation and beam energies (cf. Chapter 2).*

resolved processes are also merged and weighted according to the corresponding generated luminosities.

1.4.1 AROMA 2.2

The AROMA 2.2 Monte Carlo program [55] describes the heavy quark production processes $ep \to e\mathrm{Q}\bar{\mathrm{Q}}X$ via the photon–gluon–fusion mechanism in photoproduction as well as in DIS. Resolved photon processes are not included.

The beauty production cross section is given by a convolution of the gluon density $g(x_g, \mu_f^2)$ and the QCD hard subprocess $\hat{\sigma}(y, Q^2, x_g, z, \Phi)$:

$$\sigma(ep \to eb\bar{b}'X) = \int dy \int dQ^2 \int dx_g \int dz \int d\Phi \;\; g(x_g, \mu_f^2) \cdot \hat{\sigma}(y, Q^2, x_g, z, \Phi), \tag{1.42}$$

where Φ measures in the photon–gluon rest frame the azimuthal angle around the photon axis between a plane spanned by the three–vectors of the incoming and scattered positron and a plane containing the heavy quark pair. The gluon density of the proton $g(x_g, \mu_f^2)$ is evaluated at the factorization scale given by the center–of–mass energy of the partonic interaction $\mu_f^2 = \hat{s}$. The proton density function used is the leading order parameterization provided in GRV94-LO [96].

The hard subprocess $\gamma p \to b\bar{b}$ is calculated in leading order QCD (order $\mathcal{O}(\alpha^2\alpha_s)$) taking into account the heavy quark mass ($m_b = 5.0\,\mathrm{GeV/c^2}$) and the complete electroweak structure for the NC processes. At lowest order the $\mathrm{Q}\bar{\mathrm{Q}}$–quark pair recoils in an essentially back–to–back topology in the photon–proton center–of–mass system with low overall transverse momentum. Small deviations from this can arise from a non–vanishing primordial transverse momentum k_t of the initial gluon. This is generated according to a Gaussian distribution. Larger deviations arise from initial state radiation off the incoming gluon. Starting with the hard process, the shower is reconstructed in "backward evolution" according to the DGLAP equations. Higher order QCD radiation off the heavy quark (i.e. gluon bremsstrahlung) is treated by using final state parton showers. Only the leading logarithm corrections are considered in this approach [59].

In photoproduction, NLO QCD corrections to the inclusive heavy quark distributions (i.e. η and p_t, Figure 1.15) have been found to be similar in shape to the LO ones [55]. NLO QCD corrections are, therefore, applied using a simple constant k–factor multiplied to the LO distributions. Since NLO corrections contribute significantly to the beauty production cross section (cf. Section 1.2), the prediction of the AROMA 2.2 LO Monte Carlo is expected to underestimate the cross section (cf. Table 1.1), but the shape of the inclusive distributions should still give a reasonable description.

Parton showers and fragmentation are performed by the JETSET 7.4 package which uses the Lund string model [59]. The decay of the heavy meson, e.g. $B \to J/\psi X$, is generated according to the CKM matrix elements. The J/ψ meson is emitted almost co–linearly with the direction of the initial B–meson, $\sigma(\Delta\phi) \approx 13°$, and carries approximately 67 % of the B–meson's transverse momentum (Figure 1.16).

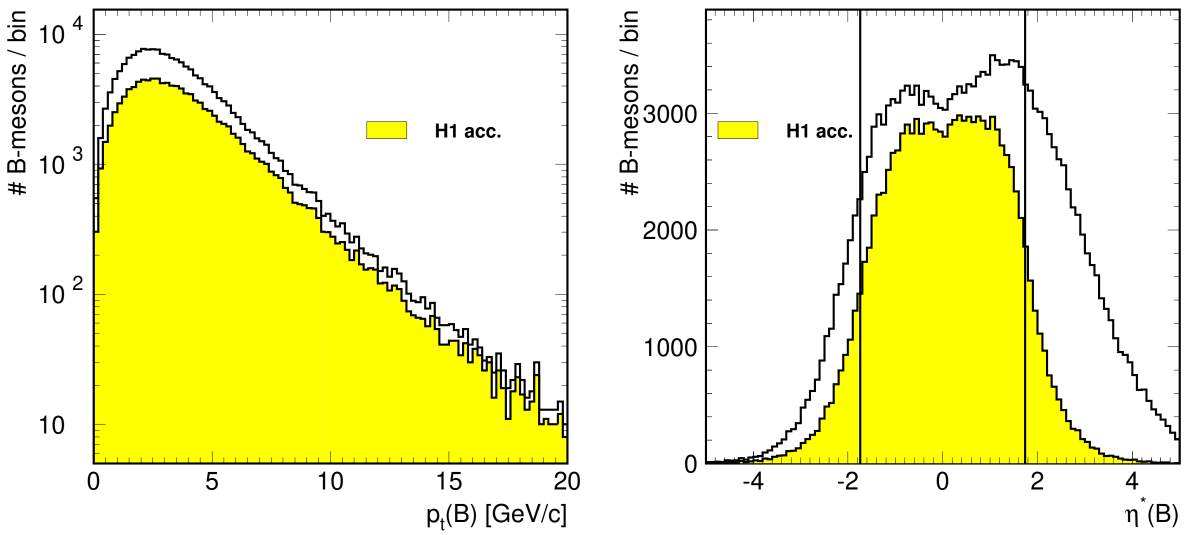

Figure 1.15: *Kinematical properties of the B–mesons as generated with the* `AROMA` *$b\bar{b}$ Monte Carlo simulation: transverse momenta p_t (left) and pseudo–rapidity η^* (right) distributions. The two vertical lines indicate the geometrical acceptance of the H1 experiment for each decay muon, i.e. $20^\circ \lesssim \theta \lesssim 160^\circ$ (cf. Section 1.4.3). The shaded histogram displays the distributions after this acceptance requirement.*

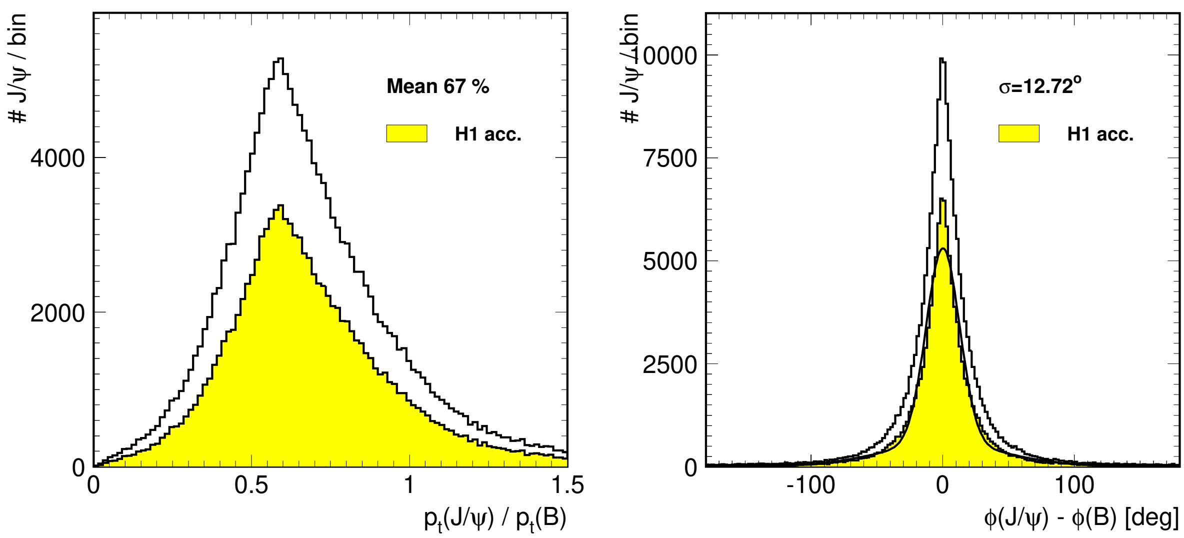

Figure 1.16: *Kinematical properties of the J/ψ meson compared to its preceding B–meson (generated with the* `AROMA` *$b\bar{b}$ Monte Carlo simulation). The fraction of the B–mesons's transverse momentum carried by the J/ψ meson, $p_t(J/\psi)/p_t(B)$, is about 67 % (left). The J/ψ meson follows quite closely the B–meson (right). The difference in the azimuthal angle $\phi(J/\psi) - \phi(B)$ is only about 13°. As in Figure 1.15 the shaded histogram displays the distributions after the geometrical acceptance requirement (cf. Section 1.4.3).*

1.4.2 EPJPSI 3.3

The `EPJPSI 3.3` Monte Carlo program [97] can generate J/ψ mesons in high energy γp, ep, μp, $p\bar{p}$ and pp collisions. The interaction between positrons and protons is described via photon exchange in the Weizsäcker–Williams Approximation (cf. Section 1.1.2). The relevant production mechanisms are direct photon–gluon–fusion as well as gluon–gluon–fusion, which is the dominant process for resolved photons.

In both processes, the calculation of the J/ψ production cross section is performed according to the Colour–Singlet Model (cf. Section 1.3.3). Relativistic corrections to the relative motion of the bound $c\bar{c}$ state are taken into account [98]. This can be used up to high values of inelasticity z. In the resolved process, two subprocesses dominate: $gg \to J/\psi g$ and $gg \to J/\psi\gamma$. The generated cross section for the latter is about a factor 5 lower than the former one.

The parton density functions used are MRS(A') [63] and GRV-G(LO) [64] for the proton and photon respectively. The scale for the evolution of the parton densities is chosen to be $\mu = m_{J/\psi}$ and $\alpha_s(\mu)$ is fixed to 0.29. Higher order QCD effects are simulated by initial and final parton showers using the leading logarithm approach (cf. Section 1.4.1). Parton showers and fragmentation are performed by the `JETSET 7.4` package which uses the Lund string model [59].

1.4.3 Definition of the Visible Range

To ensure a good detection efficiency for the decay muons using the H1 detector, the Monte Carlo event samples have been restricted to a *visible range* of $20° < \theta(\mu_{1,2}) < 160°$, where $\theta(\mu_{1,2})$ is the polar angle of each muon. The resulting acceptance for each Monte Carlo simulation is displayed in Figure 1.17. The acceptances as a function of the inelasticity z are nearly constant above $z > 0.1$ and are 49.2 % for the `AROMA` $b\bar{b}$ Monte Carlo simulation and 36.2 % for the `EPJPSI` $c\bar{c}$ MC. The statistics provided by the `AROMA` $b\bar{b}$ MC fade out at higher z, where, however, no J/ψ mesons originating from beauty–flavoured hadron decays are expected to contribute (cf. Figure 1.11).

The distributions for the photon–proton center–of mass energy $W_{\gamma p}$ depend strongly on the underlying hard process. In the `EPJPSI` $c\bar{c}$ direct process, small energy transfers from the photon lead to low values of $W_{\gamma p}$. The J/ψ meson, therefore, follows closely the boost of the proton and the decay muons are not detected (as for $W_{\gamma p} \lesssim 50\,\mathrm{GeV}$). High values of $W_{\gamma p}$, however, are needed to produce a J/ψ meson in the resolved process. This results in the plateau in the acceptance at high $W_{\gamma p}$. Since for beauty production $\hat{s} \gtrsim 4 \cdot m_b^2$, the photon–proton center–of mass energy must be higher than in the prompt J/ψ meson production process to achieve similar results.

In the final measurement of the beauty production cross section, a global acceptance value will be used to extrapolate the measured, or *visible* cross section to the full kinematical range. The acceptance, therefore, should be sufficiently constant. Thus two additional constraints are made on the event kinematics in the case of the `AROMA` $b\bar{b}$ Monte Carlo simulation. The inelasticity must be within $0.1 < z < 0.5$ (cf. Figure 1.11) and for

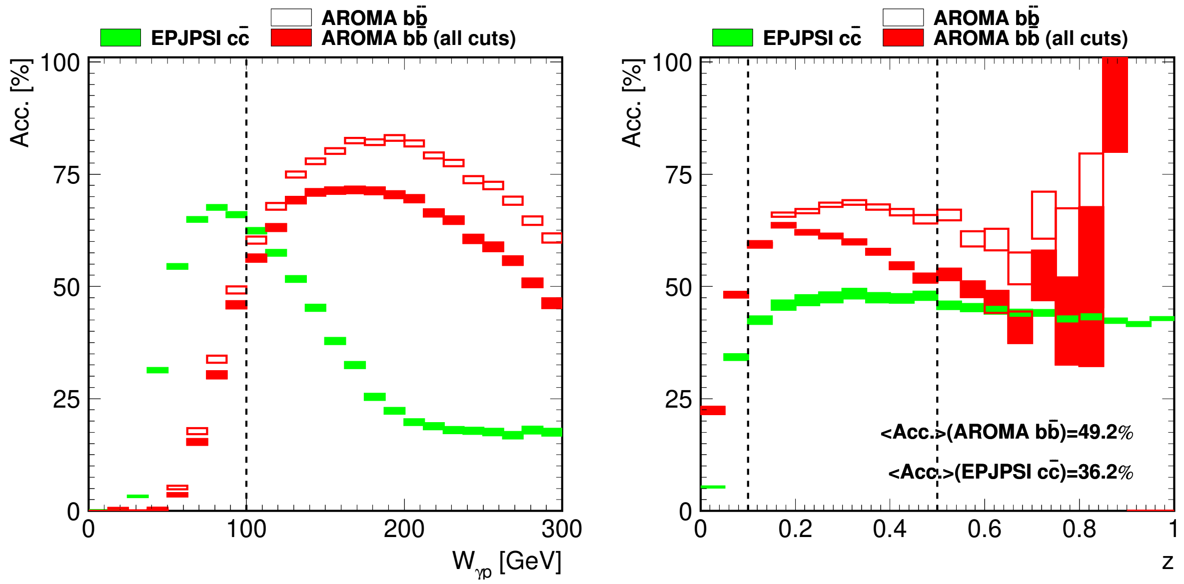

Figure 1.17: *Acceptances of the Monte Carlo simulations in the visible range $20^\circ < \theta(\mu_{1,2}) < 160^\circ$ as a function of the photon–proton center–of mass energy $W_{\gamma p}$ (left) and the inelasticity z (right). The dark shaded rectangles correspond to the* `AROMA` *$b\bar{b}$ Monte Carlo simulation, while the light shaded rectangles are the* `EPJPSI` *$c\bar{c}$ MC. In addition, the* `AROMA` *$b\bar{b}$ MC distributions before the application of the kinematical cuts $0.1 < z < 0.5$ and $W_{\gamma p} > 100$ GeV are shown (open histogram). These cuts are indicated by the vertical lines. The size of the rectangles corresponds to the one–sigma statistical uncertainty.*

the photon–proton center–of–mass energy $W_{\gamma p} > 100$ GeV is required. The dependence of this extrapolation on the choice of the `AROMA` $b\bar{b}$ Monte Carlo simulation will then be considered in the systematic error. Since the direct J/ψ meson production cross section will be determined in fixed z and $W_{\gamma p}$ ranges, only the muons' polar angles must be extrapolated.

From now on only events generated within the (Monte Carlo generator specific) visible range are considered.

1.4.4 Comparison of the Decay Muon Kinematics

The muonic J/ψ meson decay is used in this thesis to identify beauty–flavoured events. At low inelasticities $0.1 < z < 0.5$, i.e. in the region where J/ψ mesons from beauty–flavoured hadron decays contribute, the decay muons are typically produced with smaller opening angles and with higher transverse momenta than the muons from prompt J/ψ meson decays (Figure 1.18). These kinematical properties are not enough to separate b–flavoured events from the prompt J/ψ meson background, since the beauty production cross section is too low. Other methods — e.g. using lifetime information — must be considered to achieve this.

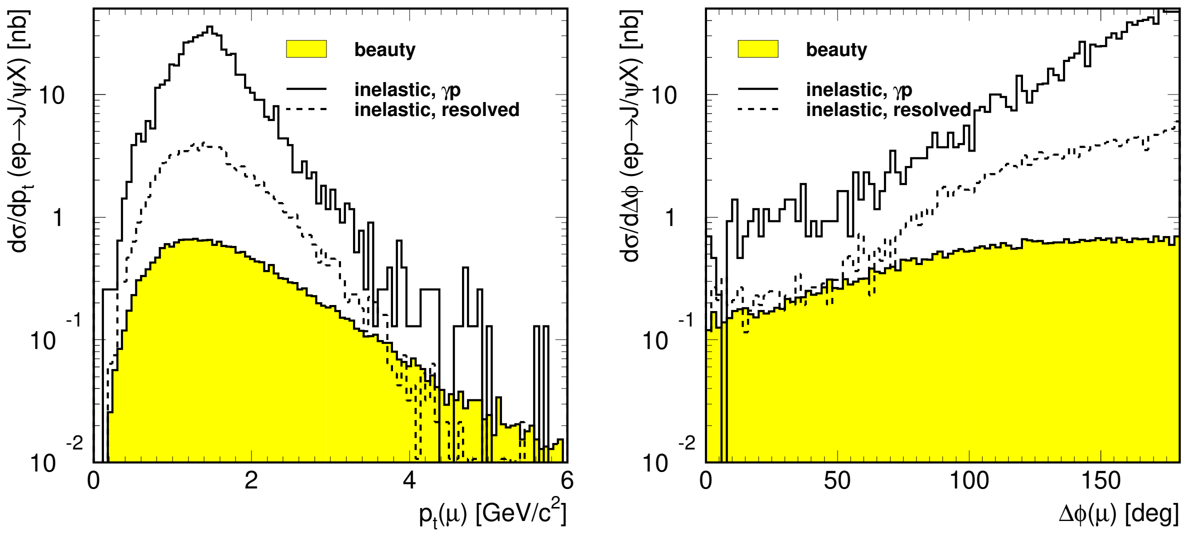

Figure 1.18: *Kinematical properties of the muons from a J/ψ decay for small inelasticities $0.1 < z < 0.5$. The transverse momentum of the muons (left) and the opening angle between both muons (right) are shown. The contribution from b–flavoured hadron decays (shaded) shows a harder transverse momentum and a smaller opening angle than in the direct inelastic (solid line) and resolved inelastic (dashed line) J/ψ production mechanisms. The beauty cross section is normalized to the cross section measured at H1 [17, 65].*

Chapter 2

The H1 Experiment at HERA

This thesis is based on data from positron–proton collisions in the Hadron Electron Ring Accelerator (*HERA*) at the Deutsches Elektronen Synchrotron (*DESY*) laboratory in Hamburg, Germany. The data were collected with the H1 experiment.

A short overview of HERA is given in Section 2.1. Afterwards Section 2.2 briefly explains the H1 experiment and focuses on those components relevant for this thesis. The simulation of the experiment in Monte Carlo events is described in Section 2.3.

2.1 The HERA Positron–Proton Collider

Unique in its configuration, the HERA positron–proton collider is the world's largest electron microscope, probing the structure of the proton and testing the standard model of particle physics.

After passing a chain of pre–accelerators, positrons and protons are stored in two separate rings of 6.4 km circumference some ten metres below ground level (Figure 2.1). The HERA–e and HERA–p rings are used to accelerate the particles to their final energies of 27.5 GeV and 820 GeV respectively. Synchrotron radiation of the positron beam increases strongly with the beam energy and is the limiting factor for the positron beam. The high energy of the proton beam requires high magnetic fields to keep the beam in its circular orbit. The limit of superconducting magnets constrains the proton energy. In 1998 the limit was improved, therefore the proton beam energy could be raised to 920 GeV.

Once the beams have reached their final energies, they are adjusted to collide at zero crossing angle in the interaction regions of the H1 and ZEUS experiments. The center–of–mass energy of $\sqrt{s} \approx 318\,\text{GeV}$ ($\sqrt{s} \approx 300\,\text{GeV}$ until 1997) is one order of magnitude larger than the energies achieved in fixed–target lepton–nucleon scattering experiments.

The beams consist of bunches 96 ns apart, corresponding to a collision rate of 10.4 MHz. A small number of non–colliding bunches (*pilot bunches*) are used to study background induced by interactions of the beam with the residual gas within the beam pipe or with the beam pipe's wall.

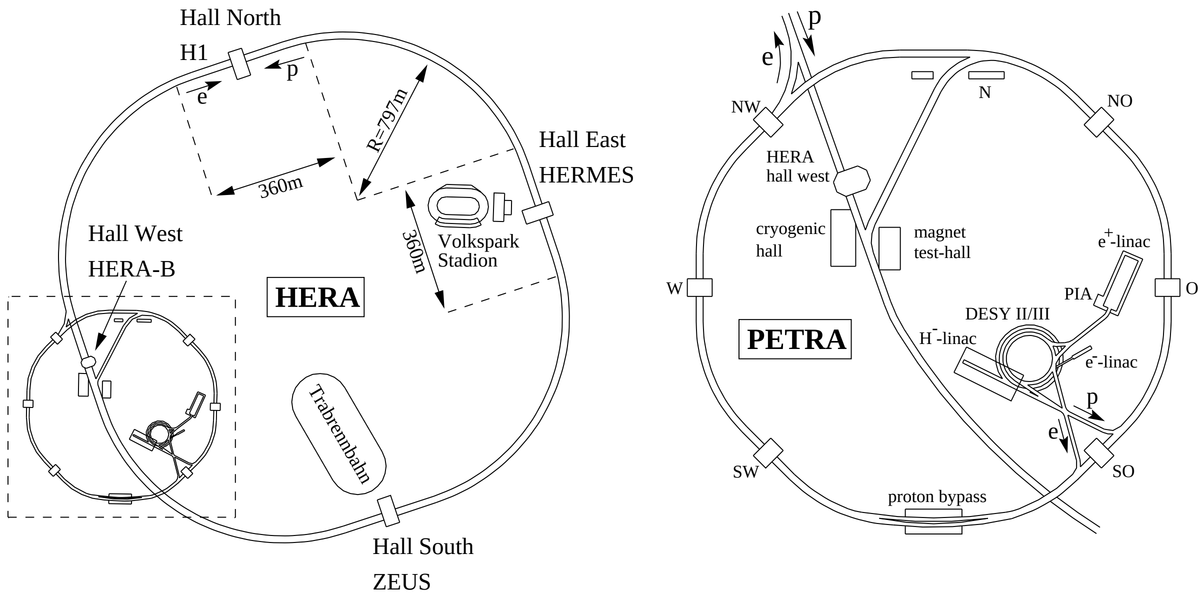

Figure 2.1: *The HERA collider (left) and its pre–accelerators (right) at DESY. The experiments H1, ZEUS, HERA–B and HERMES are each located at one of the four interaction regions.*

The lateral dimensions of the proton and positron beams are $190\,\mu\text{m}\times 50\,\mu\text{m}$ and $200\,\mu\text{m}\times 53\,\mu\text{m}$ respectively [99]. Correspondingly the interaction region or the *beam spot* is $138\,\mu\text{m}\times 36\,\mu\text{m}$ (all values given are the corresponding one–sigma contours). In 1997, the beam spot size was $145\,\mu\text{m}\times 39\,\mu\text{m}$, in agreement with a H1 measurement which used the central silicon detector [100]. The longitudinal extension of the interaction region is constrained by the average length (FWHM) of the proton bunches of 45 cm (positrons: 8 mm). The width of the interaction region is, therefore, $\sigma(z) = 113\,\text{mm}$.

2.2 The H1 Experiment

Located in the North hall of HERA, the H1 experiment is a general purpose detector with almost full coverage of the 4π solid angle surrounding the nominal ep interaction point. The apparatus is a composition of several detector components which are optimized for the measurement of various physical quantities. Due to the different beam energies, the center–of–mass system is highly boosted along the proton direction. Consequently the *forward region* of H1 experiment is more densely instrumented. The symmetry axis of the H1 experiment defines the z–axis of a right handed coordinate system and points in the proton beam direction[1]. With the origin at the nominal interaction point, the x–axis points towards the center of the HERA ring and the y–axis is directed upward. The polar angle θ is measured with respect to the proton beam direction, whilst the azimuthal angle ϕ extends clockwise from the x–axis to the upper half. The projection *transverse* to the z–axis is labeled the $r\phi$–plane and the projection along the z–axis the rz–plane.

[1]The beams are slightly ($\mathcal{O}(\,\text{mrad})$) tilted with respect to the symmetry axis.

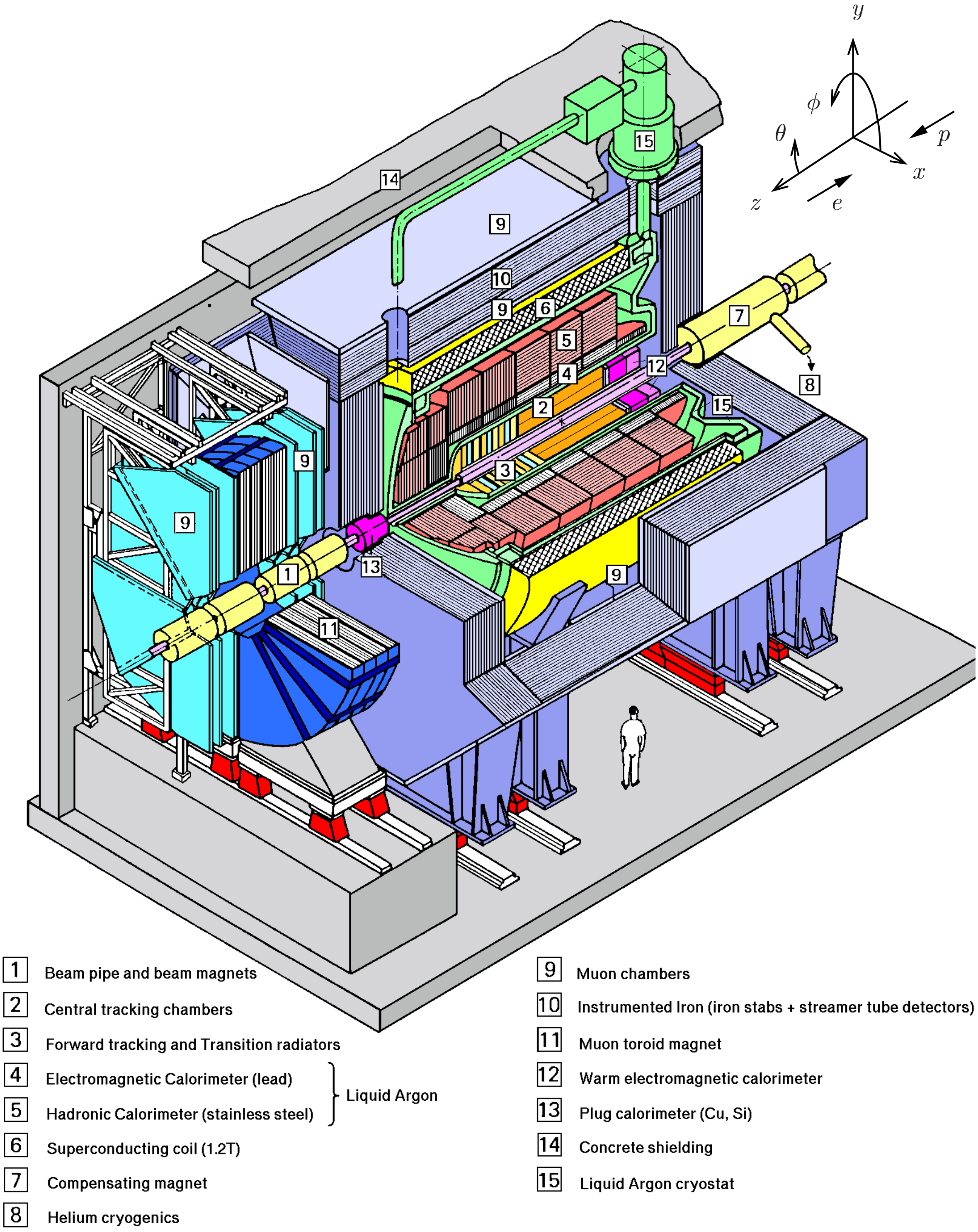

Figure 2.2: *Overview of the H1 experiment. The coordinate system is defined in the top right corner.*

Figure 2.2 gives a three–dimensional schematic overview of the H1 experiment. The protons enter through the beam pipe $\boxed{1}$ from the right, the positrons from the left. The beam pipe is surrounded by the central $\boxed{2}$ and forward $\boxed{3}$ tracking detectors, consisting of silicon detectors, multiwire proportional chambers and drift chambers. The liquid argon calorimeter is made up of electromagnetic $\boxed{4}$ and hadronic $\boxed{5}$ sections and encloses the tracking detectors. The backward region is covered by a drift chamber and a scintillating fiber calorimeter $\boxed{12}$. Both are used mainly for tagging the scattered positron. The tracking detectors and calorimeters are surrounded by a super–conducting solenoid $\boxed{6}$ which provides a magnetic field of 1.16 T parallel to the z–axis. The iron return yoke $\boxed{10}$ for the magnetic field is instrumented with layers of streamer tubes $\boxed{9}$. Together they form the central muon system, which provides the identification and track recognition for muons as well as a measurement of energy leakage out of the liquid argon calorimeter. In the forward region a copper / plastic scintillator calorimeter (*PLUG*) $\boxed{13}$ is embedded in the iron yoke. Three layers of drift chambers $\boxed{9}$ on each side of a 1.5 to 1.75 T toroid magnet $\boxed{11}$ perform muon detection in the forward region. Not shown in the schematic view are the scintillator walls of the Time-of–Flight system at both ends of the experiment, which are for suppression of beam–induced background, the forward proton and neutron detectors located far in front of the detector along the outgoing proton beam pipe and the electron taggers and luminosity system positioned far behind the experiment near the positron beam pipe.

In the following the detector components relevant for this thesis are presented in more detail. A complete description of the H1 experiment can be found in [101, 102].

2.2.1 The Central Tracking System

The central tracking system is a cylinder symmetrical arrangement of different detectors centered around the nominal interaction point (Figure 2.3). Working outwards, the central silicon detector (*CST*, cf. Section 2.2.2) encloses the CFK–beam pipe[2] and is followed by a multiwire proportional chamber (*CIP*) and an inner z–chamber (*CIZ*). These are surrounded by the central jet chamber, which is divided into two parts (*CJC1* and *CJC2*) by the outer z–chamber (*COZ*) and the outer multiwire proportional chamber (*CIP*). Their acceptances are listed in Table 2.1.

Central Jet Chamber

Of major importance for track reconstruction is the *central jet chamber*, designed to measure the transverse momenta of charged particles with high precision. It consists of two cylindrical, coaxial volumes (CJC1 and CJC2), with sense wires strung parallel to the z–axis. In the azimuthal direction, the *CJC1* (*CJC2*) is subdivided in 30 (60) identical *drift cells*. Each drift cell contains one wire plane with 24 (32) anode sense wires accompanied by two adjacent cathode planes shaping the drift field (Figure 2.4). Due

[2] CFK: Carbon Fiber Komposites. Until 1997 an aluminum beam pipe was used.

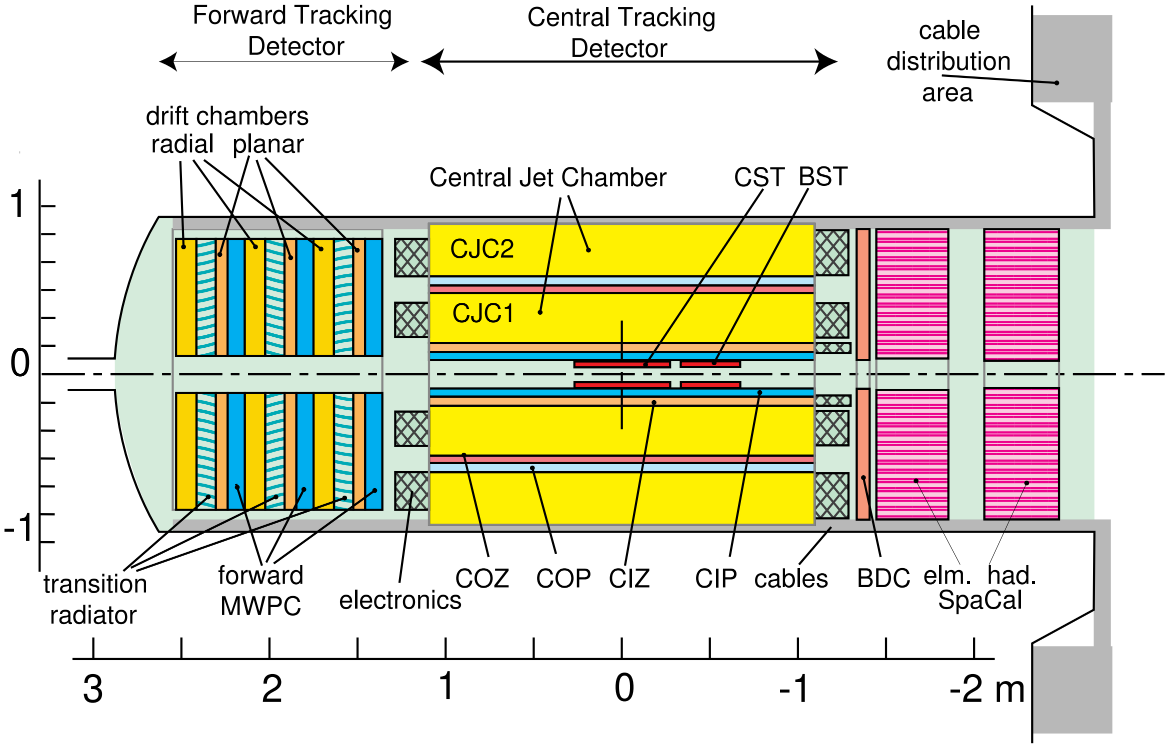

Figure 2.3: *Schematic side view of the tracking system. In addition to the forward and central tracking detectors, the backward drift chamber BDC and the calorimeter SpaCal are shown.*

	radial [mm]		z [mm]		θ [°]	
	min	max	min	max	min	max
CST	58	98	-178	178	29	151
CIP	150	173	-1125	1065	8	172
CIZ	174	200	-1080	720	16	170
CJC1	203	451	-1125	1075	11	170
COZ	460	485	-1105	1055	25	156
COP	493	523	-1107	1065	25	156
CJC2	530	844	-1125	1075	26	154

Table 2.1: *Active regions of the central tracking detectors.*

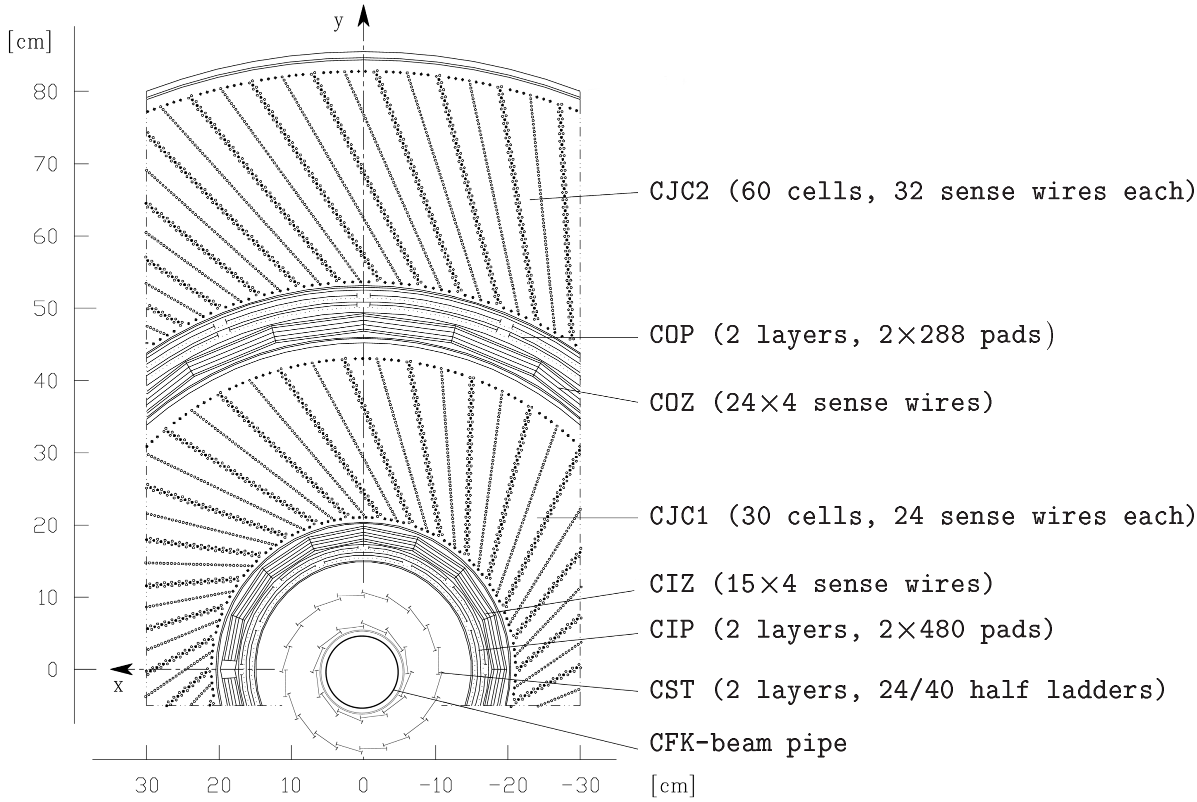

Figure 2.4: *Radial view of the central tracking system.*

to the presence of a magnetic field, the ionization electrons do not drift parallel to the electric field. The cells, therefore, are tilted by about 30°. The drift direction for a high momentum particle originating from the interaction region is almost perpendicular to the particle's flight direction. This improves the track resolution and resolves ambiguities by matching track segments from neighbouring cells. A further advantage is that high momentum tracks cross at least one sense wire plane in CJC1 and CJC2.

The jet chamber has a single hit resolution in the $r\phi$–plane of $\sigma_{r\phi} \approx 140\,\mu$m and a transverse momentum resolution of $\sigma(p_t)/p_t^2 \approx 0.5\,\mathrm{GeV}^{-1}$ [103]. The energy loss dE/dx can be used for particle identification and is measured to a precision of $\sigma(dE/dx) \simeq 7\%$ for "long" tracks. The passing time of a particle can be determined to an accuracy of approximately 0.5 ns. Thus tracks from different bunch crossings and from cosmic ray showers can be separated. The sense wires are read out at both ends so that a measurement of the z–coordinate can be made by the means of charge division. The resolution is about 6 cm [104], depending on the polar angle and the energy loss. The double track resolution is about 2 mm.

Central Proportional Chambers

The inner and outer *multiwire proportional chambers* (*CIP* and *COP*, respectively) [105] deliver a fast timing signal with a better time resolution than the bunch crossing interval of 96 ns. Each is built of a double layer. In the azimuthal angle, each layer is equally subdivided into eight (CIP) and 16 segments (COP), respectively. In the case of the CIP, both layers are rotated by 22.5° against each other in order to achieve an effective 16–fold segmentation. Each segment of CIP and COP consist of 60 and 18 separate pad cathodes along the z–axis respectively. The signals are used for a fast level one and level two trigger decision (cf. Section 2.2.5).

z–Chambers

Since the z–resolution of the CJC is moderately low, additional thin drift chambers with sense wires perpendicular to the beam axis are installed [106]. In the case of the *inner z–chamber* (*CIZ*), these wires form a 16–edge polygon concentrically around the beam axis. A 24–edge polygon is used for the *outer z–chamber* (*COZ*). The CIZ (COZ) consists of 15 (24) identical rings along the z–axis, each with four sense wires stacked on top of each other. The single z–resolution is 380 μm, two orders of magnitude better than for the CJC alone.

2.2.2 The Central Silicon Tracker

The *central silicon tracker* (*CST*) was installed to provide vertex information by performing precision measurements of charged particle tracks close to the interaction point [100]. This makes it possible to identify heavy flavour particles with decay lengths of a few hundred micrometers and establishes the basis for this thesis. The CST has been fully operational since the middle of 1997. In the backward region it is complemented by the backward silicon tracker.

The CST consists of two layers composed from 12 and 20 faces (*ladders*) at radii of 57.5 mm and 97.5 mm respectively. One *half ladder* threads three silicon sensors and an aluminum nitride hybrid carrying the front–end electronics (Figure 2.5). The positions of the ladders are shifted tangentially to ensure an overlap of adjacent active areas in the $r\phi$–plane, which amounts to 1.5% (2.1%) in the inner (outer) layer (cf. Figure 2.4). The detector is centered around the nominal interaction point and has an active length of 356 mm in the z–direction.

The double–sided silicon strip sensors allow precise measurements to be made in the $r\phi$–plane as well as in the z–direction. The high resolution in the azimuthal angle is delivered by p^+–acceptor strip implants on one side (*p–side*) of the sensor. The strips are positioned parallel to the z–axis with 25 μm pitch and every second strip is read out. On the *n–side*, n^+–donator strip implants of 88 μm pitch are oriented perpendicular to the z–axis. This determinates the z–coordinate. Every n–side strip is read out via a second metal layer which has readout lines perpendicular to the n^+–donator strips. The n–side readout lines of the three sensors of a half ladder are daisy–chained and, therefore, produce a threefold ambiguity along the z–direction.

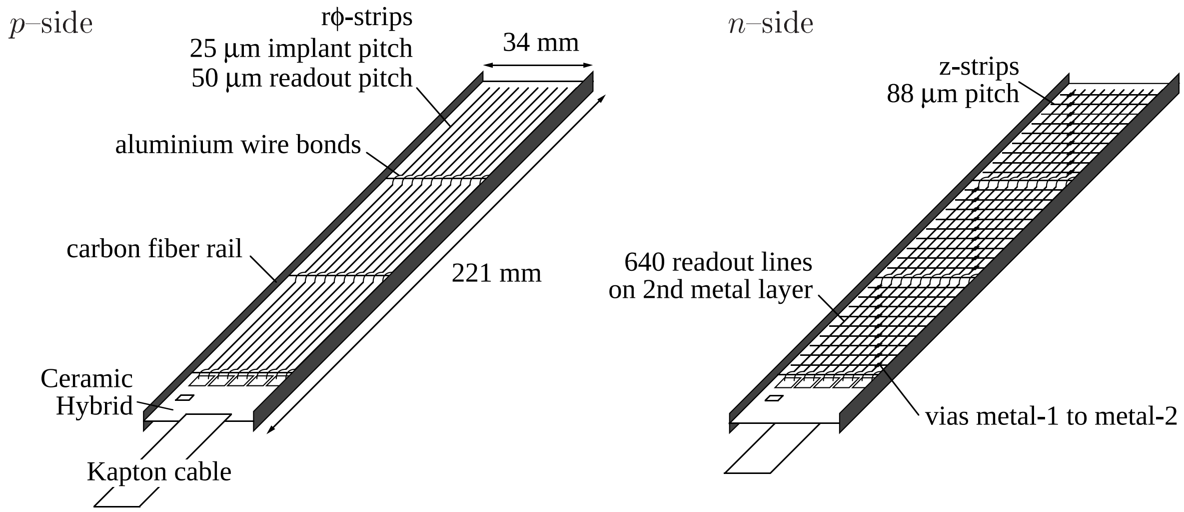

Figure 2.5: *Schematic view of a CST half ladder. The p–side is shown on the left, the n–side on the right.*

Hit Finding

A hit finding algorithm is applied [107]; groups of contiguous strips with a signal above noise threshold define a *cluster*. The total signal–to–noise ratio of the cluster must exceed five for the p–side and four for the n–side. Due to the presence of the second metal layer the larger capacitance on the n–side harms the signal–to–noise ratio which is only about ten compared to approximately 20 for the p–side (Figure 2.6). The center–of–gravity of

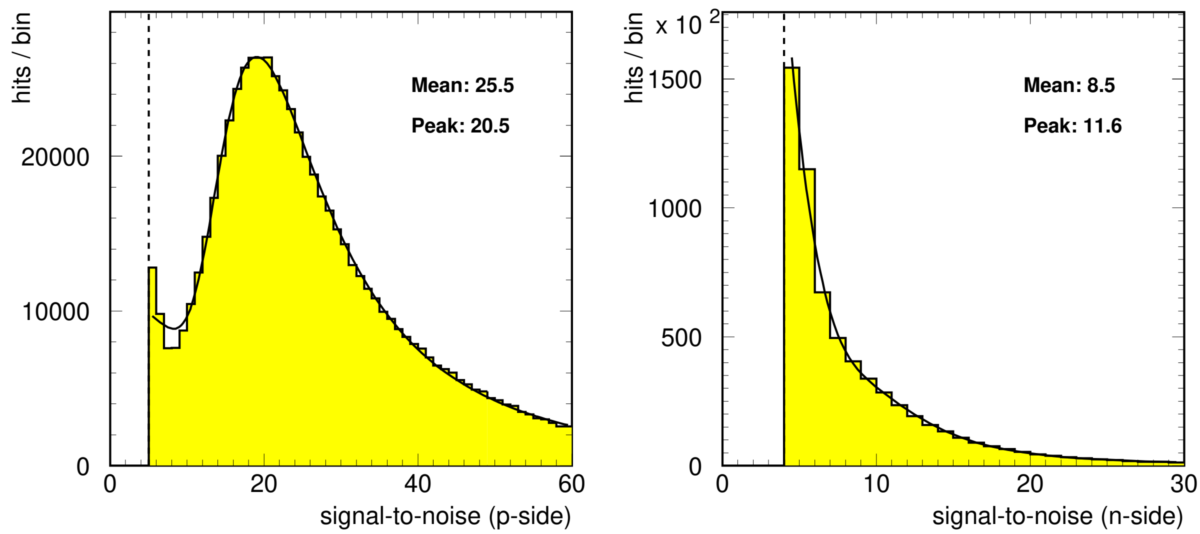

Figure 2.6: *Signal–to–noise ratio distributions for the p–side (left) and n–side (right). The dashed line marks the cuts made in the hit finding. The peak and mean values are from a best–fit Landau (signal) plus exponential (noise) curve as indicated by the solid line. The n–side suffers from the low signal–to–noise ratio (the noise distribution dominates over the landau peak).*

the cluster determines the hit position. The combination of p– and n–side clusters form three–dimensional *spacepoints*.

The intrinsic hit resolution in the $r\phi$–projection is $12\,\mu$m and can be derived from *overlap residuals*, i.e. the difference between hits and tracks in the overlap regions. In the z–direction, the resolution is parabolically correlated with the incidence angle ($\lambda = 90^\circ - \theta$) and reaches a minimum of $22\,\mu$m at about 15° from normal incidence [108].

Alignment

In order to profit from the high intrinsic position resolution of the CST the position of each sensor must be known with comparable precision. The positions of the three sensors on each half ladder have been measured by an optical survey. The *local software alignment* determines the position of the 64 half ladders relative to each other. The *global* software alignment fixes the entire CST with respect to the H1 coordinate system. All hits are corrected accordingly to the alignment parameters.

Three different data sets, cosmic ray shower data, a data set with particles passing the overlap regions and high track multiplicity events from genuine *ep* collisions, are used for the local alignment. A common least–squares fit with respect to the 384 local alignment parameters[3] is performed using these three sets simultaneously. The resulting parameters have a RMS value of $6\,\mu$m and 0.1 mrad. In the global alignment three displacements and three tilts of the CST are determined by minimizing the differences between CST and CJC / CIZ / COZ tracks, using genuine *ep* events and cosmic ray shower data. The alignment constants are determined offline periodically during a year and then written to the H1 database.

2.2.3 Calorimetry

To obtain a high position and energy resolution of (un)charged particles, a highly segmented *liquid argon (LAr) calorimeter* surrounds the forward and central tracker [109]. Altogether 45 000 cells cover the polar angular range $4^\circ \lesssim \theta \lesssim 154^\circ$. These are shared by an inner, *electromagnetic* part (*EMC*), dedicated to the identification of electrons and photons, and an outer, *hadronic* part (*HAC*) for the measurement of charged and neutral hadrons (Figure 2.7).

The electromagnetic (hadronic) calorimeter is built of stacks of lead (stainless steel) absorber plates as ionizing material, with gaps in between which are filled with liquid argon for charge collection. The thickness of the electromagnetic part varies between 20 and 30 radiation lengths X_0 with polar angle, whilst the total thickness of the LAr calorimeter is 4 to 8 nuclear interaction lengths λ. The achieved energy resolution for electrons is $\sigma(E_e)/E_e \approx 12\%/\sqrt{E\,[\,\mathrm{GeV}]} \oplus 1\%$ and for pions $\sigma(E_\pi)/E_\pi \approx 50\%/\sqrt{E\,[\,\mathrm{GeV}]} \oplus 2\%$ [110]. The calorimeter is non–compensating, i.e. the energy deposition of pions is on average 30% to 40% lower than those from electrons at the same initial energy. The absolute energy scales are known to 3% and 4% for the electromagnetic and hadronic part respectively [111].

[3]Three displacements and three tilts are needed for each of the 64 half ladders.

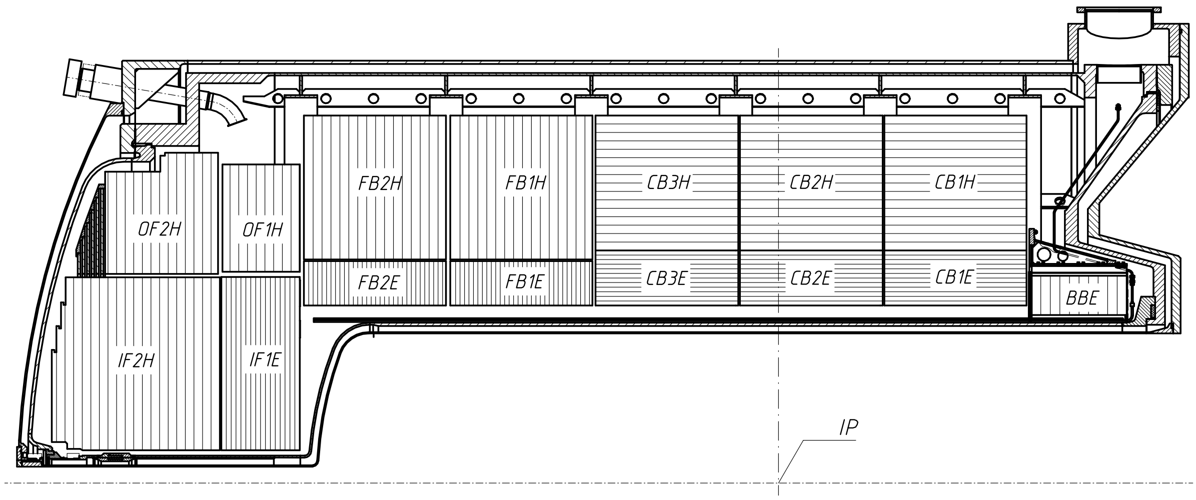

Figure 2.7: *Side view of the upper half of the LAr calorimeter divided into the electromagnetic (dark shaded) and the hadronic section (light shaded). The nominal interaction point is labeled with "IP".*

The Spaghetti Calorimeter

In the backward direction the LAr calorimeter is complemented by the "spaghetti" type lead / scintillating fiber calorimeter *SpaCal* [111, 112]. It is split into an electromagnetic section with a radiation length of $X_0 = 0.91\,\mathrm{cm}$ and a hadronic section with an interaction length of $\lambda = 25\,\mathrm{cm}$. The electromagnetic part consists of 1192 cells and the hadronic part of 136 cells with an active depth of 25 cm for each section. The small cell size of $4.5 \times 4.5\,\mathrm{cm}^2$ in the electromagnetic part guarantees a good spatial resolution and a good positron–pion separation. The cell size of the hadronic section is $11.93 \times 11.90\,\mathrm{cm}^2$. A small ring of four cells around the beam pipe serves as a veto counter. The electromagnetic (hadronic) energy resolution achieved is about $\sigma(E)/E \approx 7.5\,\%/\sqrt{E[\,\mathrm{GeV}]} \oplus 1\,\%$ $(30\,\%/\sqrt{E[\,\mathrm{GeV}]} \oplus 7\,\%)$. The polar angular acceptance for the scattered positron is $153^\circ \lesssim \theta \lesssim 178^\circ$, which corresponds to the kinematical range $1\,\mathrm{GeV}^2 \lesssim Q^2 \lesssim 100\,\mathrm{GeV}^2$.

2.2.4 The Central Muon System

The instrumented iron yoke of the H1 experiment, besides being the return yoke for the magnetic flux, is also used for the identification of minimal ionizing particles and the measurement of hadronic energy leaking out of the LAr calorimeter. In the *central muon system* the iron yoke is instrumented with streamer tubes put in between iron sheets of 75 mm thickness [113]. An additional three streamer tube layers (*muon boxes*) are mounted inside and outside the total ten sheets of iron (Figure 2.8). The gas filled tubes have a cross section $10 \times 10\,\mathrm{mm}^2$ and a single copper–beryllium sense wire strung in the center. The single layer efficiency reaches about 80% [114].

The central muon system is divided into four regions: the forward inner and outer end–caps (*FIEC* and *FOEC*, respectively) covering the polar angle of $4^\circ \lesssim \theta \lesssim 34^\circ$, the

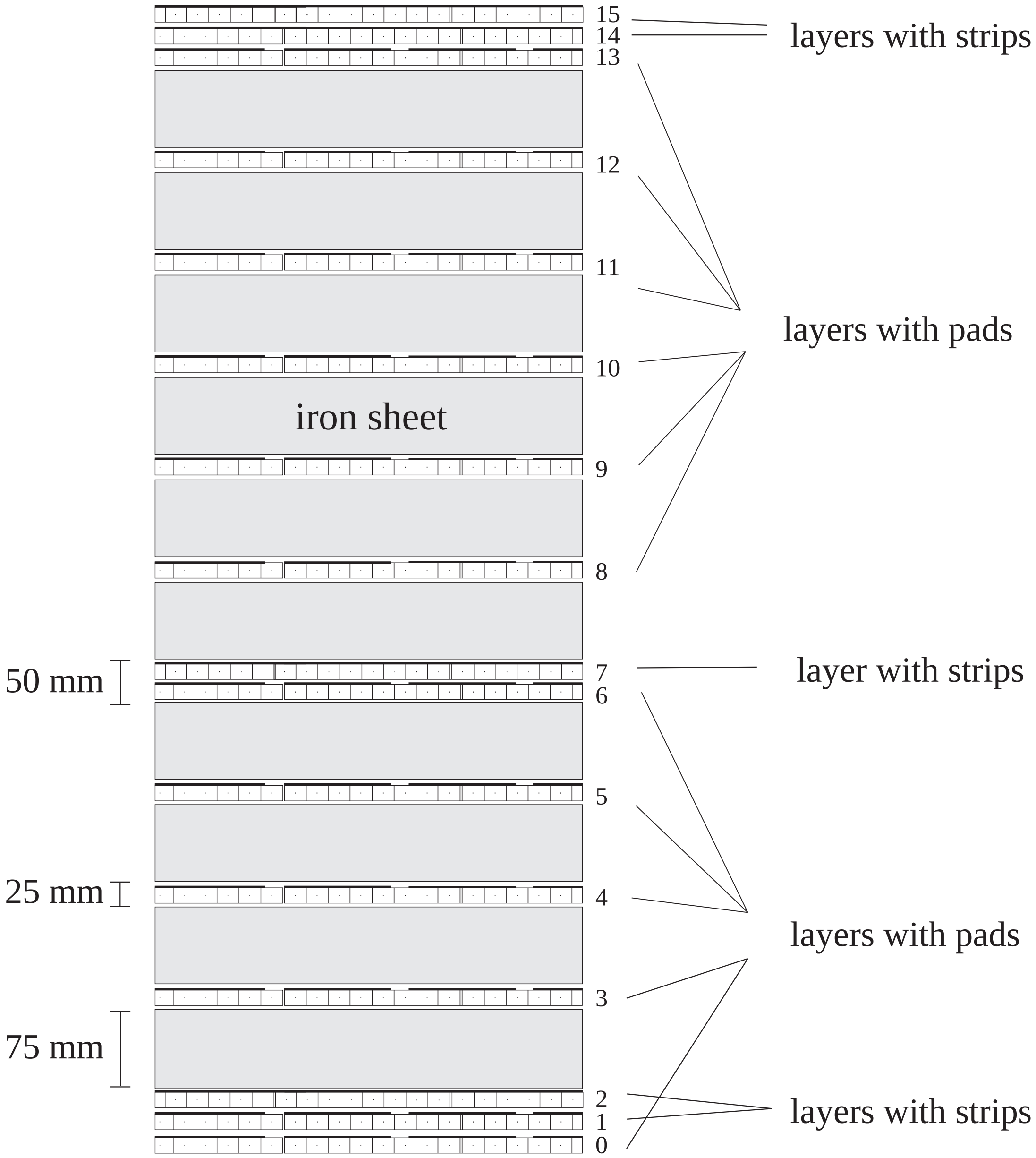

Figure 2.8: *Cross section of the instrumented iron.*

forward and backward barrel ($34° \lesssim \theta \lesssim 127°$) and the backward inner and outer end–cap (*BIEC* and *BOEC*, respectively) with $127° \lesssim \theta \lesssim 175°$. Each region is segmented into 16 modules. In the barrel region, the streamer tubes are oriented parallel to the z–axis, whilst in the end–caps they are oriented along the x–direction. The top sides of the layers are equipped with either strip or pad cathodes. The strip cathodes are glued perpendicular to the sense wires in order to allow a two–dimensional local measurement. A spatial resolution of about 3 to 4 mm for the sense wires and 10 to 15 mm for the strip cathodes is achieved. The maximum charge–over–momentum resolution is 30% for particles traversing the barrel, but lower in the end–caps. The pad cathodes are used to resolve ambiguities and to measure hadronic energy leaking out of the LAr calorimeter.

Further Detector Components

Further detector components of relevance for this thesis are listed here:

Two **Electron Taggers** located along the positron beam pipe at $z = -33\,\mathrm{m}$ and $z = -44\,\mathrm{m}$ are used to measure the scattered positron in photoproduction. Each consists of a total absorbing Čerenkov calorimeter with 21.5 radiation lengths thickness and an energy resolution of $\sigma(E)/E \approx 10\%\sqrt{E} \oplus 1\%$. Their acceptances depend on the kinematical variables y and Q^2 and on the tilt of the positron beam. Positrons are detected if their scattering angle is smaller than 5 mrad and their energy is within the region of $5.5\,\mathrm{GeV} < E'_e < 22\,\mathrm{GeV}$. This corresponds to photon virtualities $Q^2 < 0.01\,\mathrm{GeV}^2$ and event inelasticities of $0.3 \lesssim y \lesssim 0.7$ at $-33\,\mathrm{m}$ and $0.08 \lesssim y \lesssim 0.18$ at $-44\,\mathrm{m}$.

Several **Time–of–Flight** detectors are used to distinguish beam–induced background from genuine ep interactions. Several scintillator walls perpendicular to the z–axis have been installed [115]; the forward ToF at $z = 7.0\,\mathrm{m}$, the Plug ToF at $z = 5.3\,\mathrm{m}$ and the backward ToF at $z = -3.2\,\mathrm{m}$. The time resolution is 1 to 1.5 ns. Coincidences in time measure particles, where timing windows make it possible to distinguish between genuine and background interactions. The coincidences are used in the trigger scheme.

The **Veto Wall** consists of two pairs of scintillator walls at $z = -6.5\,\mathrm{m}$ and $z = -8.1\,\mathrm{m}$, each with an inner and an outer wall. The outer veto wall covers the smaller inner wall and the full radial extension of the LAr calorimeter. The time resolution of the inner (outer) veto wall is 3 ns (8 ns). Thus the z–coordinate of the ep collision can be determined online with an accuracy of 0.3 m.

2.2.5 Data Acquisition and Trigger Scheme

The H1 trigger system was designed to discriminate genuine ep interactions from background events and to filter out interesting physics events [116]. The main background sources are interactions of the proton beam with the residual gas inside the beam pipe or with the beam pipe itself. Typical rates are approximately 50 kHz and 1 kHz respectively. In addition, events due to synchrotron radiation contribute. Signatures from cosmic ray shower muons occur at a rate of 1 kHz, in coincidence with a genuine ep event at a trigger rate of 0.1 Hz.

A four level trigger scheme, L1 to L5[4], is used to cope with the high bunch crossing frequency and to minimize deadtime. The trigger levels L1 and L2 are hardware triggers, whilst L4 is a software trigger. The fifth trigger level L5 runs offline and uses the full detector information for an event classification (Figure 2.9). The individual trigger levels are described in more detail below:

[4]The L3 trigger has not yet been implemented.

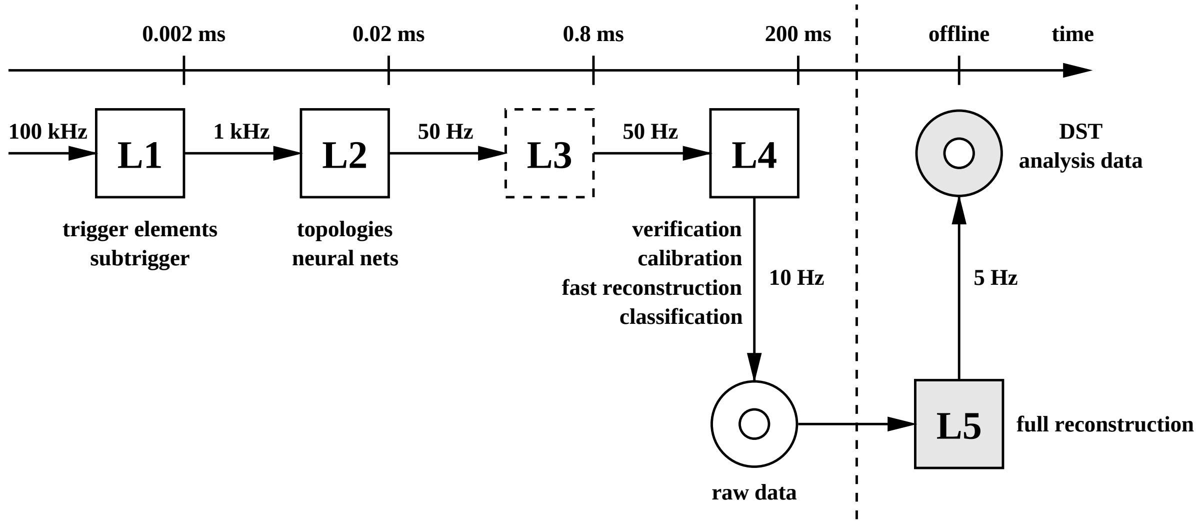

Figure 2.9: *Sketch of the multi–level trigger scheme and data acquisition. Shown are typical event rates and decision times for each level.*

L1 combines the trigger information, i.e. *trigger elements* provided by various subdetectors, logically to *subtriggers* [117]. In order to have a deadtime–free first level trigger, the information from the subdetectors is stored in front–end buffers. These *pipelines* have a depth of 24 bunch crossings. The depth corresponds to the L1 decision time of 2.3 μs. If an event is triggered by one (or more) of the 128 subtriggers a *L1 keep* signal is sent to all subsystems and the pipelines are frozen. From this moment on the dead–time is relevant. The L1 trigger reduces the typical acquisition rate of 100 kHz by roughly a factor of 100. In order to control the output rate, subtriggers might be *prescaled*, i.e. subtriggers with a prescale of n are considered only every n^{th} positive trigger decision.

The trigger elements used in this thesis are discussed in the next section.

L2 validates the decision of the L1 trigger level. L2 is based on artificial neural networks [118] and topological correlations [119]. Within a fixed latency of 20 μs, the input rate of approximately 1 kHz is reduced to about 50 Hz. Every L2 trigger element is associated to one or more L1 subtriggers. If an event is accepted by a L2 trigger decision (*L2 keep*) all components of the experiment are read out. The readout lasts typically 1 to 2 ms per event. The termination of the readout or an *L2 reject* decision resets the pipelines and restarts the data acquisition.

L4 is a multi processor farm made up of 30 Power PC boards working in parallel. The L4 input rate of approximately 50 Hz is reduced to 10 Hz, which is limited by the bandwidth of recorded events to tape. With the full detector information available, the lower level trigger decisions are verified, a fast event reconstruction is performed and calibration constants are determined. The latter are written to the H1 database.

Selection algorithms examine each event according to *hard–scales*, such as a track with high transverse momentum or a high energy deposition in the calorimeter, and *final–state finders*. Depending on the signature, the event is assigned to certain physics *classes*[5]. If none of the hard–scales are fulfilled or none of the finders recognize the event, the event enters a prescale scheme by which it is scaled down according to a Q^2–dependent factor. This leaves bandwidth available for more rare physics processes. Due to the high delivered luminosity by HERA since 1997, a fraction of processes with high rates, e.g. inclusive photoproduction events, were also scaled down. The performance of these finders is monitored using a fraction 1% of the rejected events, which are retained for this purpose.

L5 is a dedicated computing farm. Using the calibration data taken on L4, all recorded events are fully reconstructed and stored on *data summary tapes* (DSTs) which are the basis of physics analyses.

Selected L1 Trigger Elements

The level one trigger scheme consists of 256 trigger elements (192 elements until 1998). These are provided by various subdetectors and combined to subtriggers for the triggering of specific physics processes. Those elements which are relevant for this thesis are briefly explained here and listed in Table 2.2.

The ***z*–Vertex Trigger** [120] provides a rough determination of the z–position of the ep interaction vertex. The trigger elements are based on the combination of the pad signals of the central multiwire proportional chambers (CIP and COP) and the first double–layer of the forward proportional chamber (*FPC*). A *ray* is defined as the

[5]Until 1998, this has been done by L5.

Trigger Element	Condition
`zVtx_sig`	peak significance of at least one
`zVtx_sig>1`	peak significance of at least two
`DCRPh_Tc`	at least three validated masks
`DCRPh_THig`	at least one validated mask with $p_t > 800\,\mathrm{MeV/c}$
`DCRPh_TNeg`	at least one validated mask for negative charges
`Mu_Bar`	at least one muon candidate in the barrel region
`Mu_FOEC`	at least one muon candidate in the FOEC
`Mu_BOEC`	at least one muon candidate in the BOEC
`Mu_2_BIoOEC`	at least two muon candidates in the BIEC or BOEC

Table 2.2: *The trigger elements used in this thesis. Veto conditions have been omitted.*

"three out of four" coincidence of hit pads that can be connected by a straight line in the rz–plane. Thus the direction of a track can be inferred from the pad pattern. The rays are extrapolated to the z–axis, where the position of crossings enter a 16 bin–wide histogram. Sixteen histograms (one for each ϕ sector) are combined to give the z–vertex histogram. It covers a range $z = \pm 44$ cm around the nominal interaction point. For genuine ep collisions the histogram will show a significant peak which is not expected for background events (Figure 2.10).

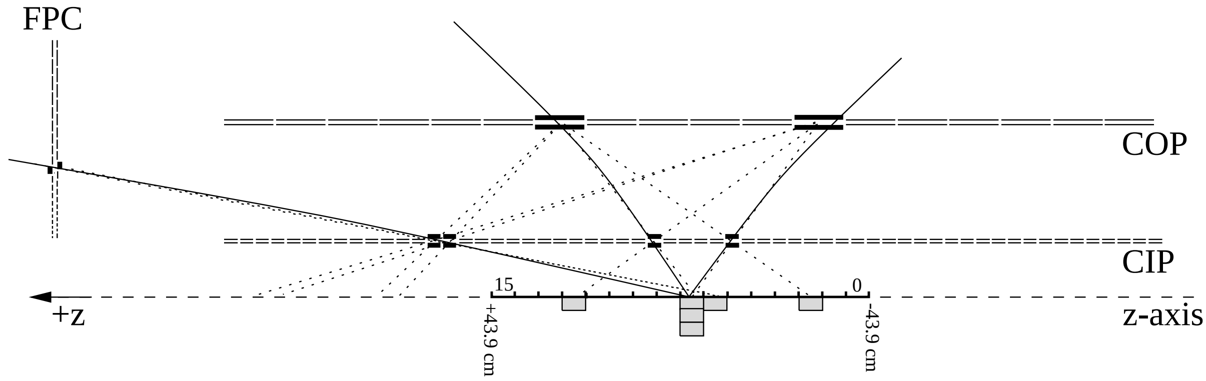

Figure 2.10: *The z–vertex histogram in the rz–view for one ϕ sector is shown. Rays originating from genuine particles are indicated by solid lines, whilst dotted lines indicate the wrong combinations.*

The z–vertex trigger logic provides a large variety of significance and multiplicity conditions. The most important one is the `zVtx_T0` trigger element which is set when at least one ray is found. It is used by most subtriggers to measure the time of the bunch crossing. Multiplicity trigger elements (`zVtx_mul`) require a certain number of entries in the z–vertex histogram, whilst significance conditions (`zVtx_sig`) compare the number of entries in a potential peak with the average number of entries in the remaining bins and, therefore, measure a possible maximum.

The **Central Drift Chamber (*DCrϕ*) Trigger** [121] complements the z–vertex trigger. It is able to find charged tracks in the $r\phi$ projection. Drift–time patterns from the digitized hits of ten of the 54 wire layers of the CJC (seven in the CJC1 and three in inner part of the CJC2) are compared to a total of 10 000 predefined masks. In the case of a match, at least one mask is *validated.* Four different types of masks account for track candidates of low (400 MeV/c $\lesssim p_t \lesssim$ 800 MeV/c) and high ($p_t \gtrsim$ 800 MeV/c) transverse momenta separately for negative and positive charges. Depending on the type of the validated mask(s), different trigger conditions are fulfilled, e.g. `DCRPh_THig` and `DCRPh_TNeg`. Since the masks are suitable only for tracks which originate from the interaction region, the DC$r\phi$ trigger efficiently rejects background due to beam–wall interactions and from cosmic ray particles.

The **Muon Trigger Elements** are based on five of the 16 streamer tube layers, namely the layers 3, 4, 5, 8 and 12. Different coincidences are required for the four iron regions to trigger a muon candidate. In the barrel region hits in two out of the innermost four trigger layers are demanded to fulfill the trigger condition `Mu_Bar`. In the BIEC, BOEC and FOEC three out of four layers are required (for the trigger elements `Mu_BIEC`, `Mu_BOEC` and `Mu_FOEC` respectively).

Veto Conditions against beam–induced background are mainly deduced from timing coincidences in different subdetectors, e.g. the veto walls or the time–of–flight detectors. In addition, timing information from the z–vertex (i.e. `zVtx_T0`), DC$r\phi$ (i.e. `DCRPh_T0`) and SpaCal triggers is used. Because of the large variety, the veto conditions have been omitted from Table 2.2.

2.2.6 Luminosity Measurement

The luminosity is determined from the rate of Bethe–Heitler bremsstrahlung events $ep \to ep\gamma$ [122]. The cross section for this process can be calculated in QED with a precision of 0.3 %. The scattered positron as well as the outgoing photon are measured in coincidence in the electron tagger (ET) at $z = -33\,\mathrm{m}$ and the photon detector (PD) at $z = -103\,\mathrm{m}$ respectively (Figure 2.11). The main source of background, bremsstrahlung of the positron

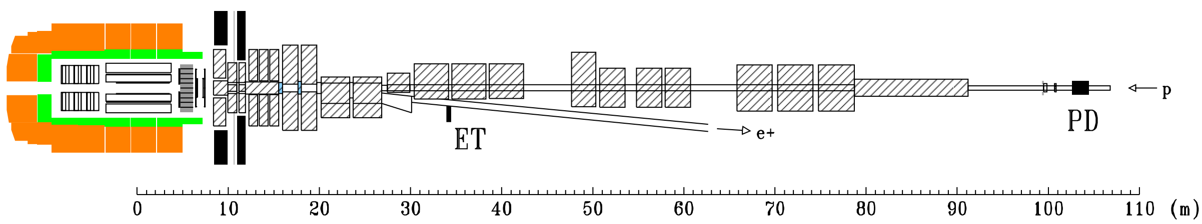

Figure 2.11: *The H1 luminosity system.*

interacting with the residual gas inside the beam pipe $eA \to eA\gamma$, can be subtracted on a statistical basis using positron pilot bunches. The luminosity is calculated according to

$$\mathcal{L} = \frac{R_{\mathrm{tot}} - (I_{\mathrm{tot}}/I_0)R_0}{\sigma_{\mathrm{vis}}}, \tag{2.1}$$

where R_{tot} is the total rate of the bremsstrahlung processes, R_0 is the rate of the positron pilot bunches, I_{tot} and I_0 are the corresponding beam currents and σ_{vis} the visible part of the Bethe–Heitler cross section. The integrated luminosity is calculated offline from the single photon rate only. This gives a slightly lower systematic error than the coincidence method.

2.3 Detector Simulation

Events generated by Monte Carlo programs are used to study the detector response in terms of acceptances and efficiencies (cf. Section 1.4).

Based on the specific physics production mechanisms, the four–vectors of particles are generated and propagated through a virtual H1 experiment. The interaction with each detector volume passed is simulated within the `GEANT` framework [123] and includes a parameterization of the development of electromagnetic and hadronic showers in the LAr calorimeter [124]. Afterwards the response of each detector component and the trigger response is deduced. Detector noise is taken into account by means of randomly triggered events from special runs. Finally, the same reconstruction algorithm as that used for real data is applied to the simulated Monte Carlo events.

The `AROMA` $b\bar{b}$ and the `EPJPSI` $c\bar{c}$ Monte Carlo events have been simulated according to the experimental setup of the H1 experiment and the beam energies of the years 1997 and 1999. Since the conditions have been reasonably stable since 1999 no additional simulation for 2000 has been performed.

Chapter 3

Data Selection

In this chapter, a data set which contains J/ψ meson candidates is selected. Divided into three inelasticity regions, the data provides a beauty–enriched sample at low inelasticities z and two control samples at higher values of z. The decay length calculated with the CST makes it possible to separate events with beauty origin from prompt J/ψ meson production events (cf. Chapters 4 and 5).

The integrated luminosity is determined in Section 3.1. Only photoproduction events are selected (Section 3.2). The J/ψ meson is reconstructed via its decay into a pair of muons, i.e. $J/\psi \rightarrow \mu^+\mu^-$. The decay muons are identified using their signatures in the LAr calorimeter or in the central muon detector (Section 3.3). The J/ψ meson candidates are classified according to their inelasticity z. Additional requirements suppress cosmic ray shower background (Section 3.4). The selection efficiency is deduced in Section 3.5 and the analysis triggers of this basic selection are discussed in Section 3.6.

3.1 Luminosity

The CST is the essential detector component used in this thesis and has been fully commissioned since mid–1997. The basic data sample is taken from the positron–proton running years 1997, 1999 and 2000 corresponding to a total integrated luminosity of $112\,\mathrm{pb}^{-1}$ (Figure 3.1). Due to the bad beam conditions of the electron–proton running years 1998 and 1999 (until May), the central tracking detector suffered from high background rates. Due to an unacceptably low tracking efficiency, this period has not been taken into account. Run periods[1] with special trigger settings (e.g. minimum bias runs) or with a systematically shifted vertex position have also been excluded.

A fraction of events is produced in collisions of positrons with protons originating from so–called *satellite bunches*. Protons can migrate and accumulate into satellite bunches separated by about 5 ns from the main bunches and hence collide with the positron beam

[1] The term *run* is used for data acquisition periods, where the detector performance, the trigger settings and the background conditions are roughly constant. A typical duration of a run is about 30 minutes.

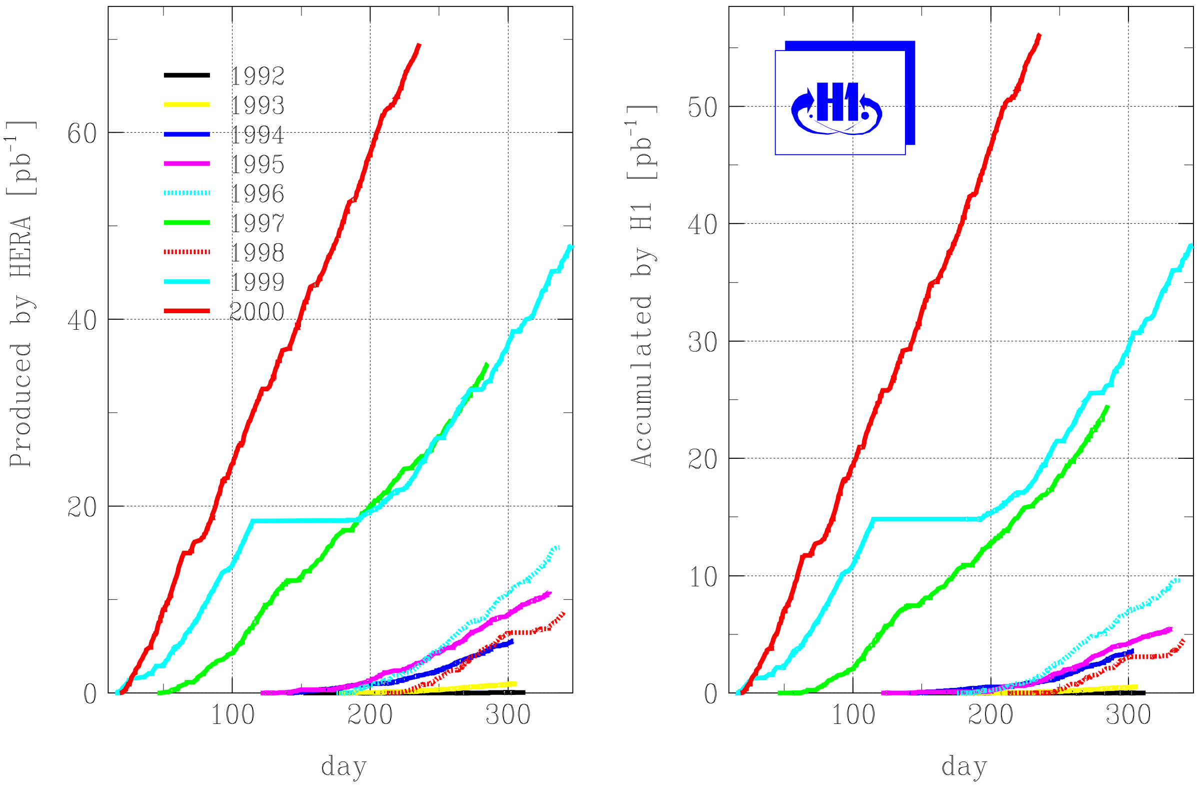

Figure 3.1: *Integrated luminosity produced by HERA and measured in H1 for the years 1992 to 2000 [125]. The accumulated luminosity corresponds to the luminosity of good and medium runs.*

at distances greater than about 70 cm away from the nominal interaction point. In order to discard these events, the *ep* collision is required to occur within ±35 cm around the nominal interaction point. This requirement also suppresses background from beam–wall or beam–gas interactions and from cosmic ray showers. The luminosity was corrected according to the fraction of events rejected by this requirement.

To ensure a properly working data acquisition and trigger system, the major components of the H1 experiment and the components essential for this thesis are required to have been fully operational in terms of their high voltage (*HV*) condition and read–out chain. These relevant components are the CST, the CJC, the LAr calorimeter, the SpaCal and the central muon system as well as the luminosity system and the time–of–flight system. Only runs with *good* or *medium* quality[2] are chosen and stable trigger conditions (the so–called *trigger phases* 2 to 4) are required. The luminosity has been corrected according to these HV conditions.

For a part of the 2000 data sample, the local and global alignment parameters were replaced on the database and became inconsistent with the CST improved short term run vertex. Since this change is irrecoverable, runs after run 273798 have been discarded.

The underlying integrated luminosities from positron–proton running during the years

[2]A run is classified as *poor* when one of more essential detector components, e.g. the LAr calorimeter or the CJC were not operational.

		1997 e^+p	1999 e^+p	2000 e^+p	$\sum$
$\int \mathcal{L}\,dt$ delivered by HERA	[nb^{-1}]	33360	27626	67889	127875
$\int \mathcal{L}\,dt$ H1 on tape	[nb^{-1}]	28220	24780	59260	112261
$\int \mathcal{L}\,dt$ H1 good / medium runs	[nb^{-1}]	24530	23360	56080	103970
Average satellite correction	[%]	6.8	3.9	4.4	
Run ranges selected		185631–200443	244963–259486	262144–273798	
$\int \mathcal{L}\,dt$ after run selection	[nb^{-1}]	16259	17544	33253	67056
$\int \mathcal{L}\,dt$ after HV conditions	[nb^{-1}]	13159	13760	29156	56075
Total absolute error on $\int \mathcal{L}\,dt$	[nb^{-1}]	197	206	437	841
Relative error on $\int \mathcal{L}\,dt$	[%]	1.5	1.5	1.5	1.5

Table 3.1: *Integrated luminosities of the e^+p data of the years 1997, 1999 and 2000 [125]. The luminosity finally used in this thesis is (56.1 ± 0.8) pb^{-1}.*

1997, 1999 and 2000 and the reduction due to corrections are listed in Table 3.1. The luminosity finally used for this thesis is $(56.1 \pm 0.8)\,\mathrm{pb}^{-1}$.

3.2 The Photoproduction Régime

The present analysis is restricted to the photoproduction domain, i.e. $Q^2 < 1\,\mathrm{GeV}^2$. Only those events are selected, in which no scattered positron was detected in the SpaCal or in the LAr calorimeter. For this it is sufficient to reject events with an electromagnetic cluster with an energy above $E_{\mathrm{clu}} > 8\,\mathrm{GeV}$. In addition, the energy E_{veto} deposited in the veto ring of the electromagnetic part of the SpaCal is required to be less than 1 GeV. This excludes events, where the scattered positron only "streaks" the SpaCal and its energy is only partially measured. The efficiency of these requirements has been determined with the `EPJPSI` $c\bar{c}$ direct photon–gluon–fusion MC, which contains both photoproduction and DIS events. Only events with the scattered positron inside the H1 main detector are considered. At an energy E_{clu} of 8 GeV, the number of events from both domains are equal (Figure 3.2, left). After the application of $E_{\mathrm{clu}} < 8\,\mathrm{GeV}$ and $E_{\mathrm{veto}} < 1\,\mathrm{GeV}$ almost all DIS events are removed, whilst photoproduction events are almost entirely kept (Figure 3.2, right). The efficiency for correctly tagging a photoproduction event is about 97.8 %, while the purity is 99.9 %.

3.3 Decay Muon Identification

The decay products of the J/ψ meson are measured in the central tracking detector and identified in the LAr calorimeter or in the central muon system. A track selection is

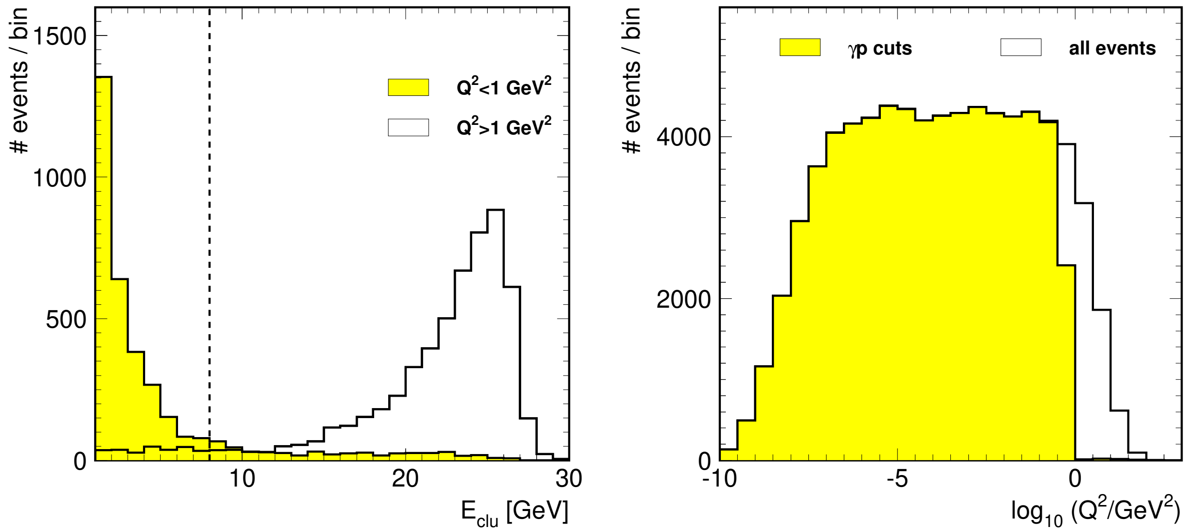

Figure 3.2: *Separation between photoproduction and DIS in the* EPJPSI $c\bar{c}$ *direct BGF MC. The distributions of the measured cluster energy in the SpaCal* $E_{\rm clu}$ *(left) for events with* $Q^2 > 1$ *GeV*^{2} *(open histogram) and* $Q^2 < 1$ *GeV*^{2} *(shaded histogram) are equal at* 8 *GeV. A corresponding cut removes the majority of DIS events. If no depositions with* $E_{\rm clu} > 8$ *GeV or* $E_{\rm veto} > 1$ *GeV have been measured, the sample consists nearly purely of photoproduction events (right).*

applied to all tracks within the event to ensure proper momenta and angular measurement. Afterwards, these tracks are examined for distinct muon signatures in the LAr calorimeter or central muon system. If a track appears to have originated from a muon, tighter track selection criteria are applied to this *muon candidate*.

3.3.1 Track Selection

Essential for the determination of the decay length is the central silicon tracker. Both muon candidates have to be in the geometrical acceptance of the CST. Since the CJC covers the full CST acceptance (cf. Table 2.1), only tracks measured in the CJC, i.e. *central tracks*, are selected.

In the following, some aspects of the standard track reconstruction will be explained. A detailed description can be found in [102].

Standard Track Reconstruction

A charged particle is bent by the solenoidal magnetic field in a way that the particle's trajectory can be described by a helix. Since the magnetic field is parallel to the z–axis the projection on the $r\phi$–plane is a circle. The circle equation is expressed as

$$\frac{1}{2} \cdot \kappa \cdot (r_i^2 + d_{ca}^2) + (1 - \kappa \cdot d_{ca}) \cdot r_i \cdot \sin(\phi_i - \phi_0) - d_{ca} = 0. \tag{3.1}$$

Appropriately the measured hits i of the CJC are defined in cylindrical polar coordinates $(r, \phi, z)^i$. At least three hits are needed to obtain the curvature (or inverse radius) $\kappa\,[\,\mathrm{cm}^{-1}] = \pm r^{-1}$, the distance of closest approach to the primary vertex $d_{ca}\,[\,\mathrm{cm}]$, and the azimuthal angle $\phi_0\,[\,\mathrm{rad}]$ using a non–iterative method [126] on Equation (3.1). Hence the arc length $S^i_{r\phi}$ in the $r\phi$–projection is calculated, with $S^i_{r\phi} = 0$ at the point of closest approach. A linear least–squares fit in the Sz–plane,

$$z^i = z_0 + S^i_{r\phi} \cdot \frac{dz}{dS} \quad \text{and} \quad \frac{dz}{dS} = \tan(90^\circ - \theta_0), \tag{3.2}$$

determines the polar angle $\theta_0\,[\,\mathrm{rad}]$ and the z–axis intercept $z_0\,[\,\mathrm{cm}]$ at the point of closest approach. The transverse momentum of the track is given by the equation $p_t\,[\,\mathrm{GeV}] = 0.003 \cdot B\,[\,\mathrm{T}]/|\kappa|\,[\,\mathrm{cm}^{-1}]$. The inhomogeneities of the magnetic field along the helix are corrected for.

In an extension of the standard track reconstruction, all these *non–vertex fitted* tracks are combined with hits in the CST. The result is an extended, non–standard set of *CST improved* tracks. Because this has no influence on the basic data selection done here, the CST track reconstruction will be explained in Chapter 4.

Vertex Determination

The interaction region in the $r\phi$–plane extends over a few hundred micrometers with a rather stable mean position for a sequence of runs. Initially, the coordinates of the *run vertex* (x_{beam} and y_{beam}, defined at $z = 0$, and the beam tilts α_x and α_y) are determined by a least–squares fit minimizing the overall distances of closest approach. Only well measured non–vertex fitted tracks with high transverse momentum as selected from all events of a run are considered in the minimization. The run vertex position is written to the database.

In a combined fit, all non–vertex fitted tracks in an event are constrained to a *primary vertex* (1$^{\mathrm{st}}$ vertex, sometimes also referred to as the *event vertex*) using the run vertex as seed. The hit information of the CIZ / COZ is also considered. The primary vertex constraint together with integration of the CIZ / COZ information improves significantly the resolution of the track parameters. The re–parameterized track parameters (p_t, ϕ', θ'), i.e. the transverse momenta and two angles describing the flight direction at the vertex, define the *vertex fitted* tracks. Finally, a search for vertices caused by the decays of long–lived particles, e.g. $K^0_s \to \pi^+\pi^-$ or $\Lambda^0 \to p\pi^-$, is performed.

Track Requirements

The track selection is based on (CST improved) non–vertex fitted tracks. For a reliable determination of the track parameters, a minimum track length in the $r\phi$–plane of 15 cm is required with the trajectory starting in the volume of CJC1, i.e. at $R_{\mathrm{start}} < 50\,\mathrm{cm}$. A minimum transverse momentum of $p_t > 200\,\mathrm{MeV/c}$ is required for all tracks. For muon candidates the transverse momenta must exceed $p_t > 800\,\mathrm{MeV/c}$ to justify a proper muon identification. All tracks must come from the region around the primary vertex, i.e. have a distance of closest approach $|d_{ca}| < 5\,\mathrm{mm}$. This discards tracks of bad quality or from cosmic ray shower particles and considerably reduces the background originating from tracks from kaon decays.

All requirements are listed in Table 3.2.

Start radius	R_{start}	$<$	50 cm
Track length	l	$>$	15 cm
Transverse momentum	p_t	$>$	200 MeV/c
Distance–of–closest approach	d_{ca}	$<$	5 mm

Table 3.2: *Basic track selection cuts.*

3.3.2 Muon Identification in the Liquid Argon Calorimeter

Particles traversing the LAr calorimeter loose a certain amount of their energy. In the case of the muon, this energy deposition should be compatible with that of a minimal ionizing particle, whereas hadrons and electrons produce an extended particle shower leaving large energy depositions. It is, therefore, possible to separate muons from electrons and hadrons according to their signature [127, 128].

Each central track is extrapolated as a helix across the LAr calorimeter, taking into account energy loss due to ionization. Two concentric tubes with radii $r_a = 150\,\mathrm{mm}$ and $r_b = 300\,\mathrm{mm}$ are defined around the extrapolated track (Figure 3.3). These radii are optimized such that the inner tube contains all the energy of the minimum ionizing muons, whereas hadronic showers initiated by pions (which constitute the majority of

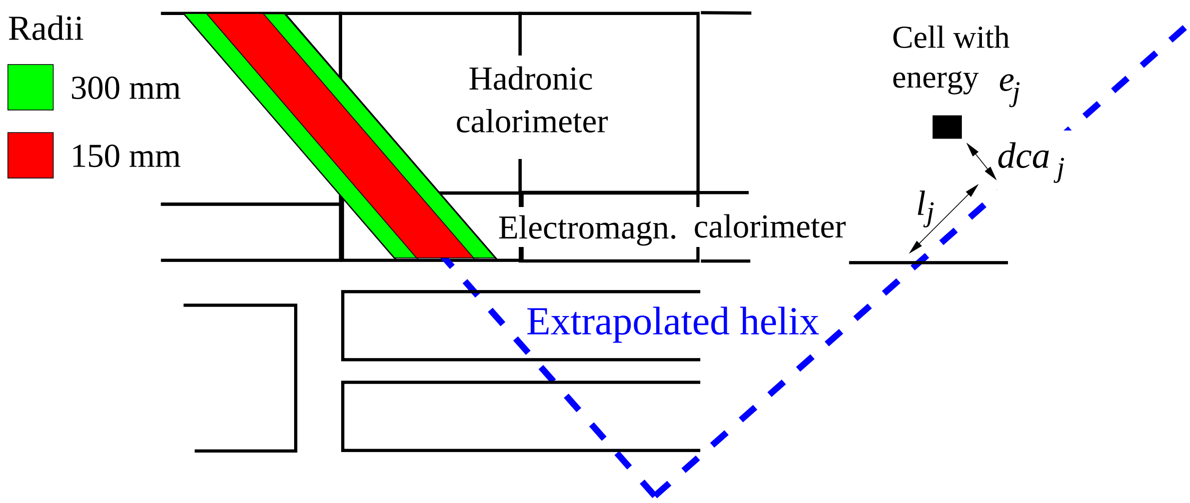

Figure 3.3: *Schematic illustration of muon identification in the LAr calorimeter.*

the background) are contained within the outer tube. All energies have been evaluated at the "final" scale, which contains dead material correction, topological noise suppression and reweighting of hadronic energy deposits to correct for the non–compensating characteristics of the LAr calorimeter.

Four estimators are defined for each track to discriminate muon signatures from pion signatures:

E_{EMC}: summed energy in the electromagnetic part of the LAr calorimeter and inside the inner tube

E_{tot}: summed energy in both parts of the LAr calorimeter and inside the outer tube

L_{max}: maximum longitudinal distance l_j between the entry point of the helix and a cell (j) inside the inner tube (Figure 3.3)

L_{HAC}: sum of the distances of all cells in the hadronic part of the LAr calorimeter and inside the inner tube

Taking their correlations into account, cut values are defined on each estimator. These depend on the track momentum and polar angle, since the energy deposition of a muon candidate in the LAr calorimeter does (Table 3.3). A weighted sum of all individual

Estimator	lower cut value	upper cut value
E_{EMC}	100 MeV	800 MeV
E_{tot}	400 MeV	2.4 GeV
L_{max}	0.8 m	
L_{HAC}	1.5 m	

Table 3.3: *Cut values for the identification of muons in the LAr calorimeter. The mean values for the central region are given.*

deviations of the estimators from the cut values defines how well a particle is identified as a muon: well identified (*good quality*), medium, badly identified or not a muon. The probability of mis–identifying a pion or kaon as a muon of good or medium quality is lower than 2% and 5% respectively [128]. In this analysis only good quality muons are used.

3.3.3 Muon Identification in the Central Muon System

Muon identification in the central muon system proceeds in two stages. A pattern recognition algorithm searches for tracks in the instrumented iron. These so–called *iron tracks* are then linked to tracks reconstructed in the central tracking detectors.

The iron track reconstruction [114] uses the method of conformal mapping [129] to search for simple hit patterns in the wire and pad layers. An *association* is required to have at least three wires hit and a minimum length of 150 mm. Tracks crossing from the barrel into one of the end–caps are not recognized and are typically lost due to their short length within each subdetector. This leads to a significant decrease in the efficiency in the overlap regions. On the basis of least–squares fitting method, a track reconstruction is performed for each association.

The following quality criteria for matching iron tracks and CJC tracks have to be fulfilled. The curvature has to be small enough to ensure that the particle can geometrically reach the instrumented iron, i.e. $|\kappa_{\mathrm{CJC}}| < 0.003\,\mathrm{cm}^{-1}/\sin\theta_{\mathrm{CJC}}$. Furthermore, central and iron tracks must match in polar angle, $|\theta_{\mathrm{CJC}} - \theta_{\mathrm{iron}}| < 12^\circ$, and azimuthal angle, $-90^\circ < Q\cdot\sin(\phi_{\mathrm{CJC}} - \phi_{\mathrm{iron}}) < 12^\circ$, where Q denotes here the charge (± 1) of the muon. Bending due to the magnetic field is taken into account by the asymmetric requirement. The angles θ_{iron} and ϕ_{iron} are defined by a straight line between the first measured point in the instrumented iron and the event vertex.

For all combinations passing these criteria, the central tracks are extrapolated to the inner edge of the instrumented iron taking into account multiple scattering and energy loss in between. The iron track parameters $\vec{T}_{\mathrm{iron}}$ and the extrapolated track parameters $\vec{T}_{\mathrm{CJC}}$ are tested for their compatibility by calculating the chi–squared probability for a common track fit. Only combinations with $\mathcal{P} > 10^{-4}$ are considered as muon candidates. If there are several link hypotheses, the one with the highest probability is chosen. Due to the geometrical acceptance of the instrumented iron, i.e. uncovered holes for cryogenic supply and support structures, the reconstruction efficiency is limited to about 90%.

In the present analysis, the muon candidate must fulfill some additional conditions. At least two iron sheets must have been crossed and a minimum of two layers of streamer tubes must have been hit in the barrel region and 6 (3) layers in the forward (backward) end–cap respectively.

The muon identification criteria are summarized in Table 3.4.

Transverse momentum	$p_t(\mu)\ >\ 800\,\mathrm{MeV/c}$
LAr calorimeter	
quality	good
Central Muon System	
iron sheets crossed	$N_{\mathrm{iron}}\ \geq\ 2$
streamer tubes hit	$N_{\mathrm{hit}}\ \geq\ 2$ (barrel)
	$N_{\mathrm{hit}}\ \geq\ 6$ (forward end–cap)
	$N_{\mathrm{hit}}\ \geq\ 3$ (backward end–cap)
link probability	$\mathcal{P}\ >\ 10^{-4}$

Table 3.4: *Summary of the muon identification criteria.*

3.4 Reconstruction of J/ψ Meson Candidates

For each pair of muon candidates which passed the aforementioned requirements, i.e. a good quality LAr muon or an iron muon, the invariant mass is calculated. A coarse mass window of $\pm 1\,\mathrm{GeV/c^2}$ around the nominal J/ψ meson mass selects a sample of J/ψ meson candidates. In addition, the J/ψ meson candidate's transverse momentum $p_t(\mu\mu)$, polar angle $\theta(\mu\mu)$ and azimuthal angle $\phi(\mu\mu)$ are determined from the muon pair.

3.4.1 Rejection of Muons from Cosmic Ray Showers

One major source of background originates from cosmic ray shower muons (*cosmics*) detected in the active volumes of the H1 experiment. In this analysis cosmic ray shower muons would severely spoil the determination of a decay length by producing outlayers.

A discriminating feature of cosmic muons is their back–to–back topology. Cosmics passing the tracking volume are reconstructed under the assumption that they originate from the nominal interaction point. This yields two muon tracks with polar and azimuthal opening angles of $\Delta\theta = |\theta(\mu_1) + \theta(\mu_2)| \simeq 180^\circ$ and $\Delta\phi = |\phi(\mu_1) - \phi(\mu_2)| \simeq 180^\circ$ respectively (Figure 3.4). Since in photoproduction vector mesons have dominantly low transverse momenta, the decay muons leave in opposite directions in the $r\phi$–plane (cf. Figure 1.18, right). Both muons, however, follow the boost of the center–of–mass system. When J/ψ mesons originate from beauty–flavoured meson decays, the additional boost from the B meson decreases the azimuthal opening angle.

Topologies which fulfill the distance requirement

$$R \equiv \sqrt{\left(\frac{\Delta\phi - 180^\circ}{3^\circ}\right)^2 + \left(\frac{\Delta\theta - 180^\circ}{15^\circ}\right)^2} < 1 \tag{3.3}$$

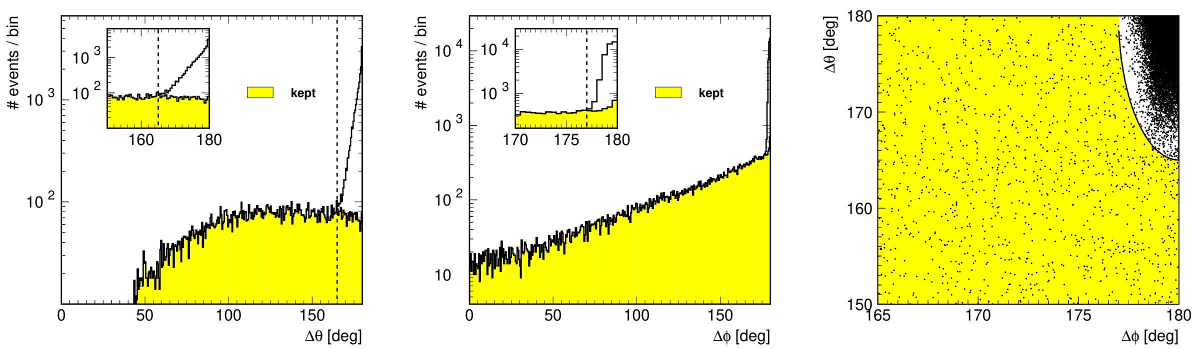

Figure 3.4: *Cosmic muon signatures in topological distributions. From left to right: difference in the polar angle $\Delta\theta$, the azimuthal angle $\Delta\phi$ and their correlation. The weights, 3° and 15° respectively, and the distance requirement (cf. Equation 3.3) are marked with lines. A clear excess at large angle differences, $\Delta\theta$ and $\Delta\phi$, indicates the cosmic muon population. The remaining events after the distance requirement $R > 1$ are shaded.*

are, therefore, discarded. The weights 3° and 15° take into account the different resolutions of the central drift chamber in the azimuthal and polar angles respectively and have been determined from the one–dimensional distributions (cf. insets of Figure 3.4).

With this distance requirement cosmics can be safely discarded, while the continuous trend of the distributions of the remaining events is nearly undisturbed. This distance requirement, therefore, has a high separation power.

3.4.2 Reconstruction of the Inelasticity z

A signal from beauty–flavoured hadron decays is expected for low inelasticities z, i.e. $0.1 < z < 0.5$ (cf. Figure 1.11). Below $z = 0.1$ the H1 acceptance tends towards zero (cf. Section 1.4.3). The J/ψ meson candidates with medium–z and high–z, $0.5 < z < 0.95$ and $0.95 < z$, will serve as cross–check samples and should not contain any b–flavour.

Experimentally, the inelasticity z is reconstructed via

$$z = \frac{(E - p_z)_{J/\psi}}{2 \cdot E_e \cdot y_{\mathrm{JB}}}, \tag{3.4}$$

where $E^2 = p^2 + m^2$ is the J/ψ meson candidate's energy and p, m and p_z are its momentum, mass and longitudinal momentum respectively.

The photon–proton center–of–mass energy $W_{\gamma p}$ and the relative energy transfer y can be approximately determined from the hadronic final state only (*method of Jacquet–Blondel*) [130] by summation over the energy E_h and longitudinal momenta $p_{z,h}$ of the final state particles:

$$y_{\mathrm{JB}} = \frac{\sum\limits_{\text{hadrons } h} (E - p_z)_h}{2 \cdot E_e} \tag{3.5}$$

$$W_{\gamma p} \simeq \sqrt{y_{\mathrm{JB}} \cdot s} \qquad \text{(in photoproduction)}, \tag{3.6}$$

where s is the ep center–of–mass energy squared (i.e. $\sqrt{s} \approx 300\,\mathrm{GeV}$ for 1997 and $\sqrt{s} \approx 318\,\mathrm{GeV}$ afterwards) and $E_e = 27.5\,\mathrm{GeV}$ is the positron beam energy.

For charged particles the measurement in the tracking detectors is usually more accurate than in the calorimeters. Neutral particles, however, are only detected in the calorimeters. Both systems are used and — to avoid double counting — the region in the calorimeters behind a charged track is excluded from the sum.

Since $(E - p_z)_h$ is negligible for particles at small polar angles, this reconstruction method is rather insensitive to particle losses through the beam pipe in proton beam direction. In the positron beam direction the scattered positron is assumed to escape detection and does not belong to the hadronic final state. Possible contributions in the SpaCal from the photon remnant of resolved photon processes are considered since these are needed for a good reconstruction of y_{JB} [131].

The determination of the inelasticity z has been checked using the `EPJPSI` $c\bar{c}$ Monte Carlo simulation (Figure 3.5). The resolution is deduced from a best–fit Gaussian curve and

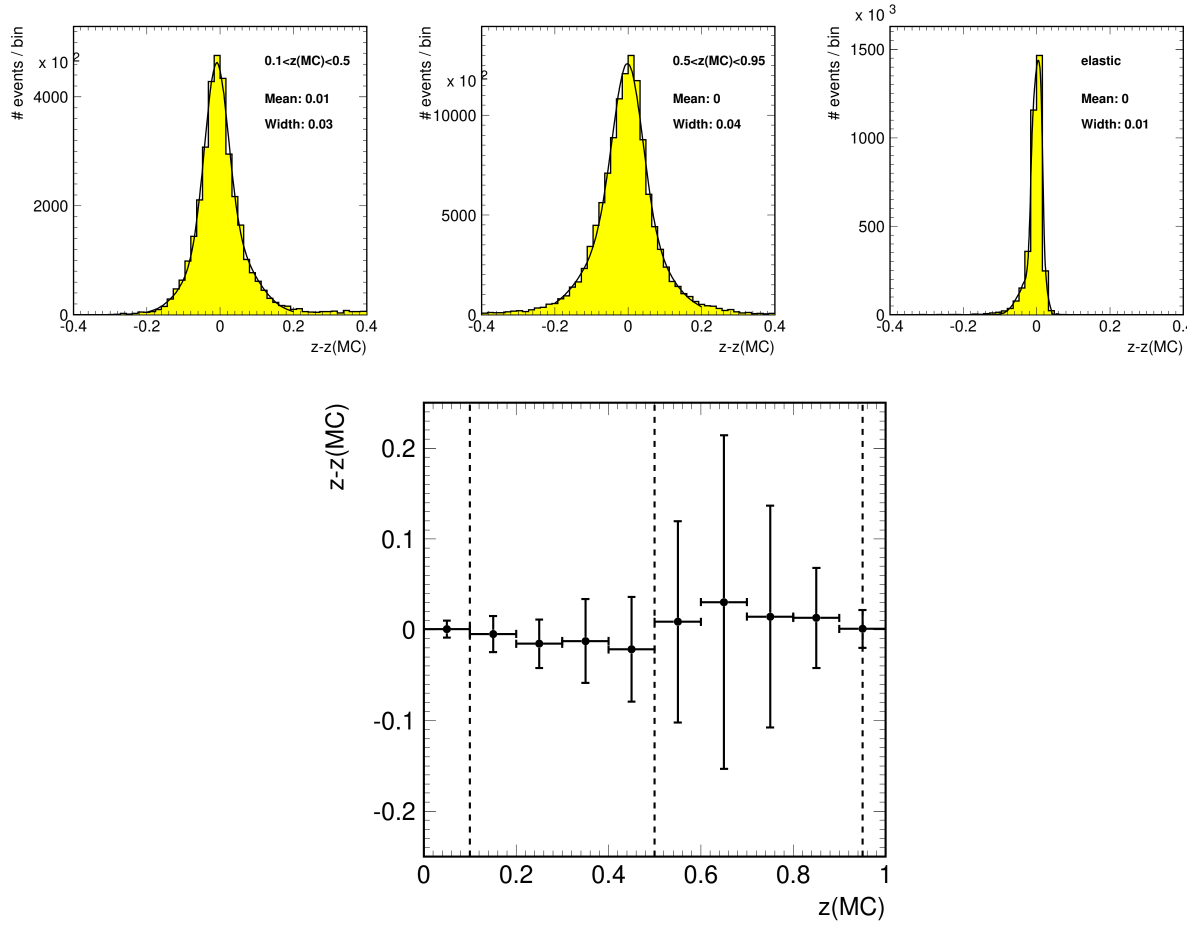

Figure 3.5: *Reconstructed inelasticity z compared to the generated value $z(MC)$ in the* EPJPSI *$c\bar{c}$ Monte Carlo simulation separately for the low–z, medium–z and high–z régimes (top row, left to right). A best–fit of a Gaussian curve gives the indicated means and resolutions (points and error bars). The resolution as a function of $z(MC)$ is shown in the lower plot.*

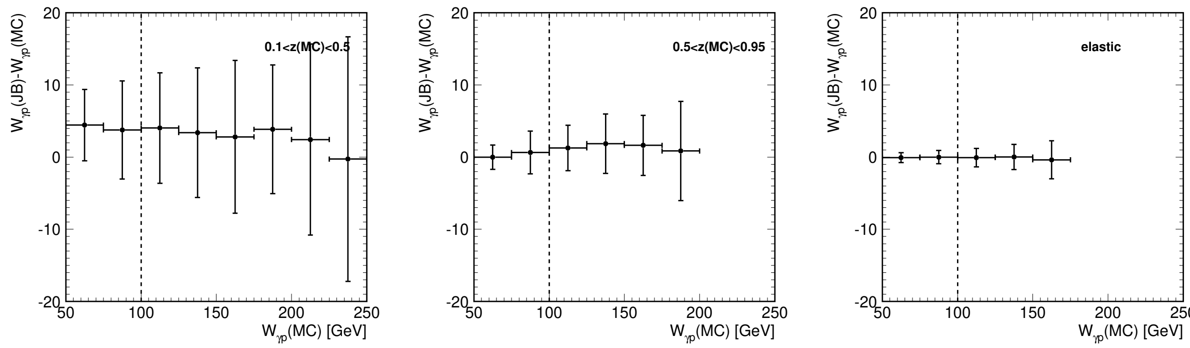

Figure 3.6: *Reconstructed photon–proton center–of–mass energy $W_{\gamma p}$ compared to the generated value $W_{\gamma p}(MC)$ in the* EPJPSI *$c\bar{c}$ Monte Carlo simulation. Separately for low–z, medium–z and the elastic régime (left to right), a best-fit Gaussian curve gives the indicated means and resolutions (points and error bars). Due to lack of statistics, some points at higher $W_{\gamma p}(MC)$ have been omitted. The dashed line indicates the visible range $W_{\gamma p}(MC) > 100\ GeV$.*

varies between approximately 0.03 at low z and to 0.06 at higher inelasticities. These values agree with those obtained using the AROMA $b\bar{b}$ MC simulation (giving a resolution of 0.03 and a mean of 0.01). Generally, z can be reconstructed with sufficient precision.

Depending on the inelasticity value, the resolution of the photon–proton center–of–mass energy $W_{\gamma p}$ has been calculated using Equation (3.6). The resulting resolution, as a function of z, is shown in Figure 3.6. At medium and high inelasticities, the resolution is 5 GeV and better, whilst at low z the resolution is 10 GeV with a slight bias of about 3 GeV towards higher reconstructed values.

3.4.3 J/ψ Meson Candidates at Low Inelasticities z

The invariant mass distributions for the low–, medium– and high–z régimes are shown in Figure 3.7. The unlike–sign combinations show a significant peak at the nominal J/ψ meson's mass. The width of the mass peak, as determined from a best–fit Gaussian curve, is about 66 MeV/c^2. The background has been parameterized by a straight line and is reasonably described by the muon combinations with equal charge. An excess over the background parameterization at $m(\mu\mu) \approx 3.7\,\mathrm{GeV/c^2}$ shows a clear indication of the $\psi(2S)$ meson. Its width has been fixed to that of the J/ψ meson. Due to the very low statistics and that this is only present at higher z no suppressive cut is applied.

Although the probability that a hadron is mis–identified as a good LAr calorimeter muon is low (2 %), the overwhelming number of produced hadrons leads to many wrongly reconstructed J/ψ meson candidates. At low inelasticities — corresponding to high track multiplicities — the background from wrongly assigned ("fake") muons dominates the invariant mass distribution of the J/ψ meson candidates. Since the mis–identification probability decreases with increasing hadron momenta, the background is lower at higher invariant masses. This mis–identification background is essentially independent of the charge combination of the muon pair and can be estimated from like–sign muon candidate combinations.

The remaining difference between like–sign and unlike–sign combination background can be explained by non–resonant pion pair production and by open–charm contributions. In open–charm processes, two charmed mesons are produced. These prefer to decay directly into muons or into kaons accompanied by some pions. A kaon can subsequently decay into a muon, into pions or can itself fake a muon. At higher inelasticities, $z > 0.5$, contributions from muon pair production due to QED two–photon processes, $ep \to \gamma\gamma \to \mu^+\mu^-$, dominate the background.

3.5 Selection Efficiency

The selection efficiency ϵ_{sel} is deduced from the Monte Carlo simulations only, whereby the basic J/ψ meson selection described in this chapter is considered. An additional efficiency factor ϵ_{CST} results from the selection of CST improved tracks and their combination into a common decay vertex. This efficiency is determined in Chapter 4.

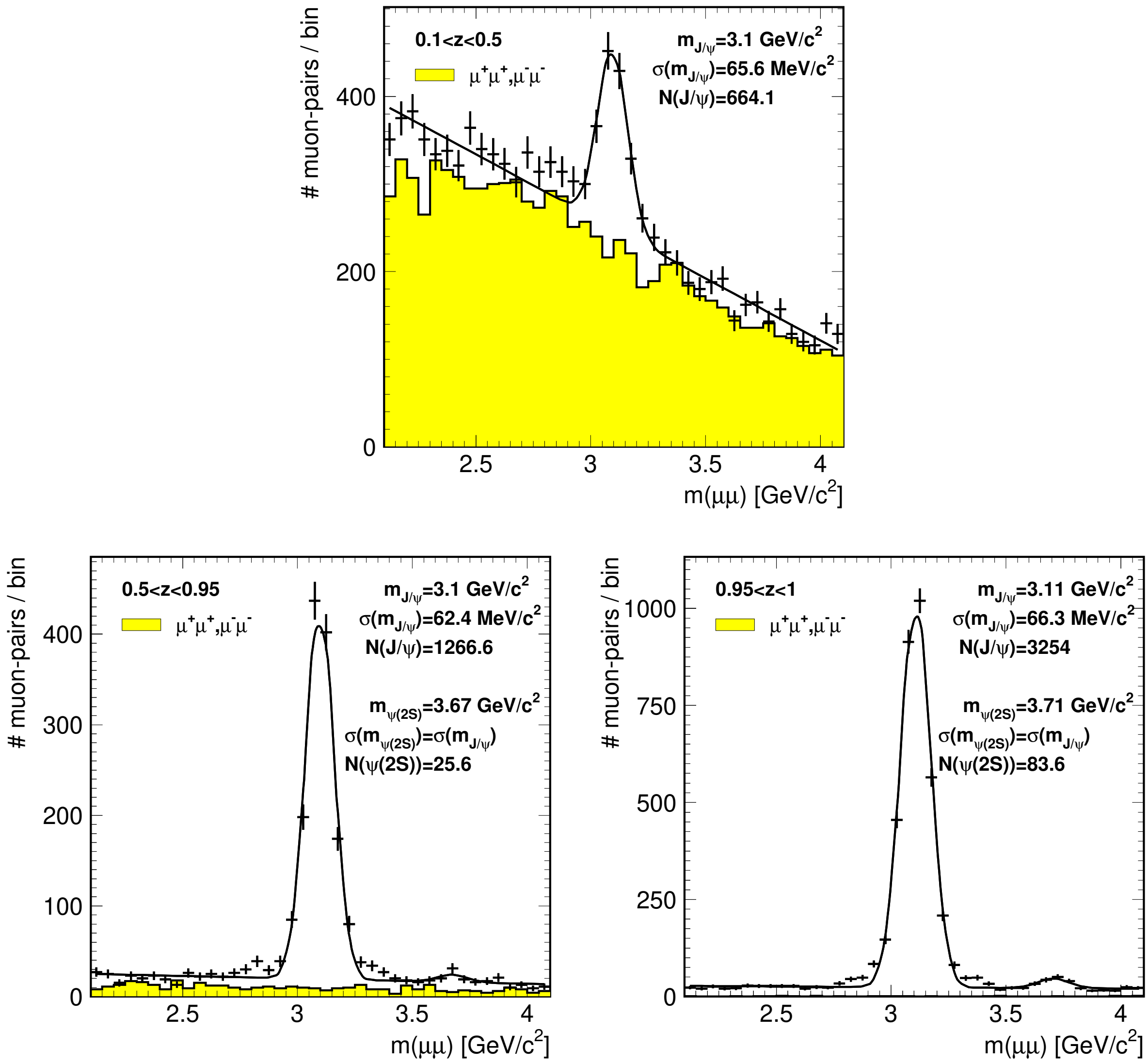

Figure 3.7: *Invariant mass distribution of the J/ψ meson candidates (1997, 1999 and 2000 e^+p data, without trigger requirements) in the low–z region,* $0.1 < z < 0.5$ *(top). The cross–check samples with candidates in the medium–z* $(0.5 < z < 0.95)$ *and high–z regions* $(0.95 < z)$ *are shown in the lower row, left and right, respectively. A best–fit curve of a Gaussian plus a straight line describes the mass distributions very well. Like–sign muon combinations are indicated by the shaded histograms.*

Since a major inefficiency, however, is expected to come from the muon identification, the muon identification efficiency in data must be adequately described by the Monte Carlo simulations. This is verified in the following section.

3.5.1 Efficiency of the Muon Identification

The efficiency of muon identification in data is deduced from two–prong event samples for the years 1997 and 1999. *Two–prong events* consist of two tracks only, e.g. two muons from the decay of an elastically produced J/ψ meson. The efficiency is determined from events with *at least one* identified muon by studying the other particle. Both particles must have opposite charges and have passed the aforementioned track requirements (cf. Section 3.3.1). In addition the tagged muon must be identified in the central muon system or in the LAr calorimeter (cf. Table 3.4). Only those events are selected, which are triggered by at least one subtrigger without any muon trigger elements.

The resulting data samples show clean J/ψ meson signals in the invariant mass distribution of the two tracks. By requiring an invariant mass within a window of about three standard deviations $3 \cdot \sigma(m_{\mu\mu})$ around the nominal J/ψ meson mass, i.e. $2.9\,\mathrm{GeV/c^2} < m_{\mu\mu} < 3.3\,\mathrm{GeV/c^2}$, each sample consists mainly of quasi–elastic J/ψ meson candidates. This implies that the particle to be studied is most probably a true muon[3]. The identification efficiency is determined from the probability of having measured this muon candidate in the central muon system or in the LAr calorimeter.

Adjusting of the Two–Prong Data Sample

The kinematics of these muon candidates differ, however, from those of candidates from inelastically produced J/ψ mesons or from J/ψ mesons produced in beauty–flavoured hadron decays. The identification efficiency is assumed to depend only on the transverse momentum $p_t(\mu)$ and the polar angle $\theta(\mu)$ of the muon candidate. Therefore the two–dimensional kinematical distribution $(p_t(\mu), \theta(\mu))$ of the candidates of the two–prong sample is weighted according to the reconstructed distribution in the AROMA $b\bar{b}$ Monte Carlo simulation (and separately according to the EPJPSI $c\bar{c}$ MC). Since the efficiencies of the weighted (and unweighted) two–prong samples for 1997 and 1999 do not differ, both have been combined and the weights have been re–adjusted.

The efficiency for muon identification in the LAr calorimeter and the central muon system is compared for the weighted two–prong sample and the AROMA $b\bar{b}$ Monte Carlo simulation (Figure 3.8) and to the EPJPSI $c\bar{c}$ Monte Carlo simulation (Figure 3.9). The efficiency in the central muon system is nicely described in the simulation. Since the identification is mostly efficient at higher transverse momenta, $p_t(\mu) \gtrsim 2\,\mathrm{GeV/c}$, but the average transverse momentum of the muons is only approximately $1\,\mathrm{GeV/c}$ (cf. Figure 1.18, left), the efficiency in the barrel region is rather low ($\sim 25\,\%$). In the backward region the instrumented iron is not shadowed by the LAr calorimeter leading to high efficiency values for the backward end–cap. As in previous analyses the calorimeter identification efficiency in Monte Carlo simulations is found to be overestimated [93, 94, 128]. Therefore this efficiency is weighted in the simulations to match the data as functions of $p_t(\mu)$ and $\theta(\mu)$.

Muons which have been identified in the calorimeter are quite complementary to those identified in the central muon system. Their combination significantly improves the total average efficiency to about $76\,\%$.

[3]This method will fail for inelastically produced J/ψ candidates due to the high background contribution (cf. Figure 3.7). Since the track multiplicity increases with lower values of z, the "other" muon candidate cannot be uniquely determined anymore.

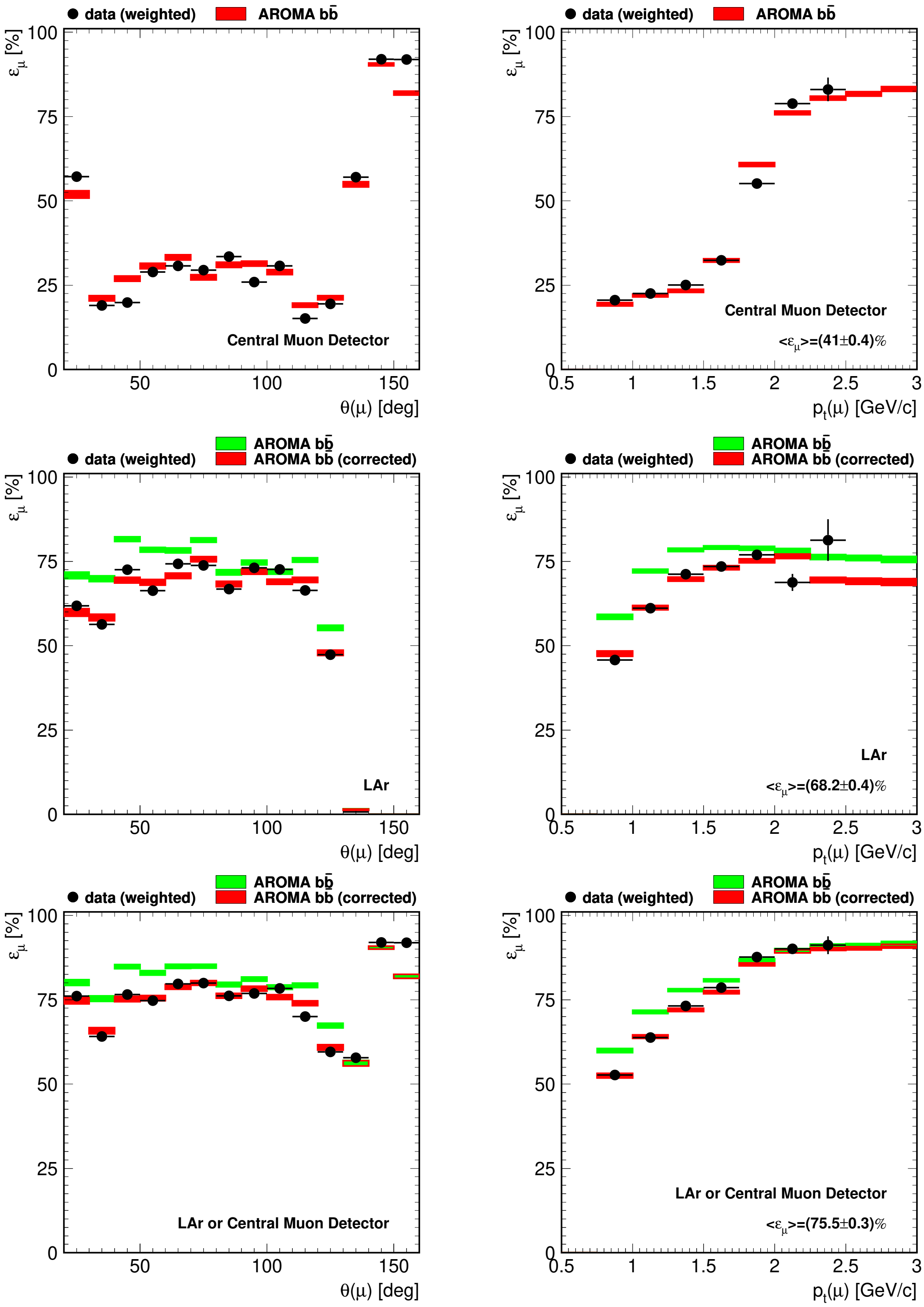

Figure 3.8: *Comparison of the muon identification efficiencies between the full data set (points) and the* AROMA $b\bar{b}$ *MC (dark shaded rectangles) displayed separately for the central muon system (upper row), the LAr calorimeter (middle row) and their combination (lower row) as a function of the muon candidate's polar angle $\theta(\mu)$ (left column) and its transverse momentum $p_t(\mu)$ (right column). The errors are the statistical uncertainties. Since the LAr efficiency has been corrected in the simulation, the uncorrected information is also shown (light shaded rectangles).*

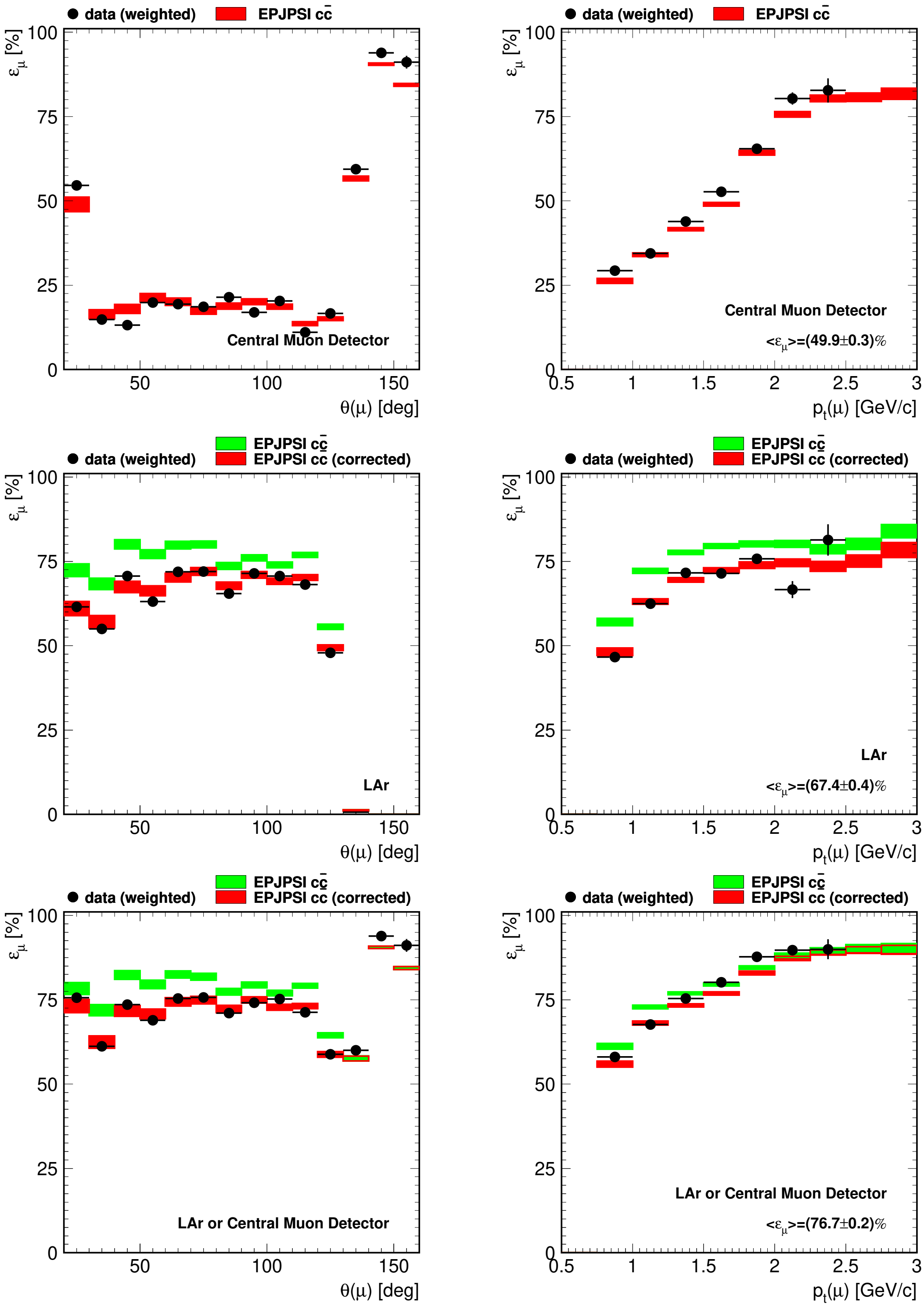

Figure 3.9: *Comparison of the muon identification efficiencies between the full data set (points) and the* EPJPSI $c\bar{c}$ *MC (dark shaded rectangles) displayed separately for the central muon system (upper row), the LAr calorimeter (middle row) and their combination (lower row) as a function of the muon candidate's polar angle* $\theta(\mu)$ *(left column) and its transverse momentum* $p_t(\mu)$ *(right column). The errors are the statistical uncertainties. Since the LAr efficiency has been corrected in the simulation, the uncorrected information is also shown (light shaded rectangles).*

The remaining differences in the efficiency distributions between data and each Monte Carlo simulation determine the relative systematic error σ/ϵ of the muon identification efficiency. It is calculated using the weighted quadratic average of half of the differences of the efficiencies in data ϵ_{data} and in the simulation ϵ_{MC}:

$$\frac{\sigma}{\epsilon} = \frac{1}{\epsilon} \cdot \sqrt{\sum_{\mathrm{bins}} N_i \cdot \left(\frac{\epsilon_{\mathrm{data},i} - \epsilon_{\mathrm{MC},i}}{2} \right)^2 \Big/ \sum_{\mathrm{bins}} N_i}. \tag{3.7}$$

The average efficiency is labeled ϵ and N_i denotes the number of events in data of bin i. The relative systematic error is calculated to be 5.3 % for beauty production (`AROMA` $b\bar{b}$ MC) and 3.8 % in the case of direct J/ψ production (`EPJPSI` $c\bar{c}$ MC).

3.5.2 Track Reconstruction Efficiency

The reconstruction efficiency of non–vertex fitted tracks has been determined elsewhere [95, 132]. In both cases, muon candidates as detected with the central muon system during the year 1997 have been utilized. The analysis of e^+p data gave a reconstruction efficiency of (97.8 ± 0.4) % [95], whilst the study of cosmic ray shower muons with high transverse momenta ($p_t \geq 3\,\mathrm{GeV/c}$) resulted in a value of 99.6 % [132]. The uncertainty in the track reconstruction is (as in previous analyses) conservatively estimated to be 2 % per track. The (relative) systematic error is thus 4 % for at least two (muon) tracks.

3.5.3 Determination of the Selection Efficiency

The selection efficiency considers all basic kinematical cuts, e.g. the requirement of photoproduction events (cf. Section 3.2), the selection of events with at least two well–defined tracks and a primary vertex near the nominal interaction point, the identification of two muons in the LAr calorimeter or the central muon system (cf. Section 3.3) and their combination into a J/ψ meson candidate with an invariant mass around the nominal J/ψ meson mass. The full listing of all selection cuts (in addition to the requirements listed in Table 3.1) is given in Table 3.5. Since all subtriggers used in this analysis (cf. Section 3.6) depend on a muon signature in the instrumented iron, at least one muon candidate in the central muon detector is needed. The subtrigger requirements themselves are treated separately in the trigger efficiency.

The selection efficiency after all requirements (excluding subtriggers) is shown in Figure 3.10. If the muons, however, are allowed to be identified in either the LAr calorimeter or the central muon detector, both Monte Carlo simulations agree very nicely (cf. Figure 3.10, top row). A rise at large polar angles $\theta(\mu\mu)$ reflects the higher muon identification efficiency in the backward end–cap. The average selection efficiency of about $\epsilon_{\mathrm{sel}} = 40\,\%$ is — as previously stated — dominated by the muon identification efficiency squared $\epsilon^2_{\mathrm{any}\ \mu} = 58\,\%$.

The efficiency distributions drastically change if at least one muon is required to be identified in the central muon detector (cf. Figure 3.10, middle and lower row). Since

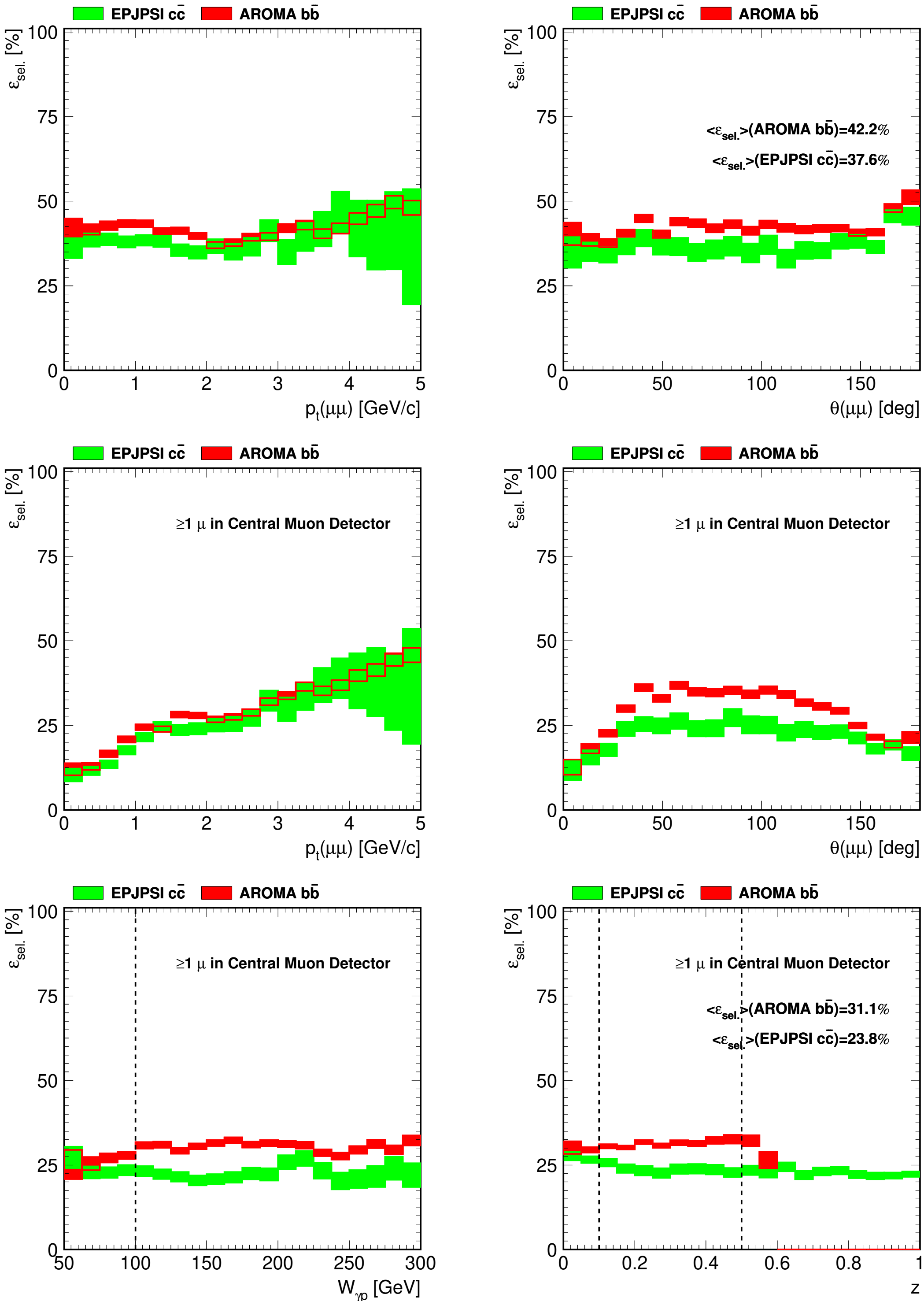

Figure 3.10: *Selection efficiency as a function of the J/ψ meson's transverse momentum $p_t(\mu\mu)$ and polar angle $\theta(\mu\mu)$ (top left and right corner, respectively). Here muons are allowed to be identified in either the LAr calorimeter or the central muon detector. The requirement of at least one muon candidate in the latter changes these efficiency distributions dramatically (middle row). The efficiency as a function of $W_{\gamma p}$ and of z is shown in the lower left and right corner respectively. The light (dark) shaded rectangles correspond to the* `AROMA` *$b\bar{b}$ (*`EPJPSI` *$c\bar{c}$) MC simulation.*

Event Selection	
Photoproduction	$E_{\mathrm{clu}} < 8\,\mathrm{GeV}$
	$E_{\mathrm{veto}} < 1\,\mathrm{GeV}$
γp center–of–mass energy	$W_{\gamma p} > 100\,\mathrm{GeV}$
Vertex position	$-35\,\mathrm{cm} < z_{1\mathrm{st}} < 35\,\mathrm{cm}$
J/ψ Meson Selection	
	two identified muons
	≥ 1 candidate in Central Muon Detector
Invariant mass	$2.1\,\mathrm{GeV/c^2} < m_{\mu\mu} < 4.1\,\mathrm{GeV/c^2}$
Cosmic cut	$R > 1$
Inelasticity	$0.1 < z < 0.5$
Trigger Condition	
Subtriggers	`S15 || S19 || S22`

Table 3.5: *Summary of all data selection cuts applied after the run selection has been performed (cf. Section 3.1). For completeness the subtrigger requirements are also listed. These will be described in Section 3.6.*

the transverse momenta of the muons are higher in the `AROMA` $b\bar{b}$ Monte Carlo simulation than in the `EPJPSI` $c\bar{c}$ MC (cf. Figure 1.18, left), the muon identification efficiency for the former is also higher in the barrel region. This has a direct impact on the overall efficiency as a function of the transverse momenta and polar angle of the J/ψ meson candidate. The efficiency, however, is nearly independent in both Monte Carlo simulations of the photon–proton center–of–mass energy $W_{\gamma p}$ and the inelasticity z. The average efficiency value is finally $(31.1 \pm 2.1)\,\%$ for the `AROMA` $b\bar{b}$ MC and $(23.8 \pm 1.3)\,\%$ for the `EPJPSI` $c\bar{c}$ MC. The quoted errors are the systematical uncertainties.

3.6 The Analysis Triggers

Subtriggers accept events which fulfill specific physics signatures, e.g. events with a muon candidate in the final state. To achieve a maximum total trigger efficiency several subtriggers are combined. The different analysis subtriggers (`Snn`, where `nn` denotes the subtrigger number) and their conditions are listed here[4]. The individual trigger elements have been explained in Section 2.2.5.

```
S15 == DCRPh_THig && zVtx_sig && (Mu_Bar || Mu_ECQ)
       where Mu_ECQ==Mu_FOEC || Mu_BOEC || Mu_2_BIoOEC.
```

[4]The convention for the logical operators used is "&&" for logical "AND", "||" for logical "OR", and "==" for logical equivalence.

Subtrigger `S15` is a universal muon trigger, which requires a muon candidate in either the barrel or in the outer end–caps of the instrumented iron. Since it uses relaxed track and vertex requirements, S15 is validated from run 193433 onwards by an L2 neural net to keep the rates at an acceptable level [133]. This net uses input quantities from the z–vertex and DC$r\phi$ trigger, the LAr calorimeter and the central muon system. The training of the net has been performed with an inelastic J/ψ meson candidate data sample from 1995 and 1996 triggered by `S19 || S22`.

`S19 || S22 == DCRPh_CNH && zVtx_sig>1 && (Mu_Bar || Mu_ECQ)`
where `DCRPh_CNH==DCRPh_Tc && DCRPh_THig && DCRPh_TNeg`.

Subtriggers `S19` and `S22` cover muon detection in the barrel region and in the outer end–caps respectively. Since their muon trigger conditions are completely orthogonal (`S19`: `Mu_Bar` and `S22`: `Mu_ECQ`), only their combination is considered. The vertex significance and the track multiplicity conditions are slightly tighter than for `S15`.

Different TOF veto conditions are assigned to each subtrigger. These conditions were mainly stable during the data periods 1997, 1999 and 2000 and do not affect the trigger efficiency. These veto conditions were, therefore, not listed here.

L1 Prescales

Since the trigger conditions of subtriggers `S15`, `S19` and `S22` were stable during each data period, the level 1 prescales have been already considered as global weights to the corresponding integrated luminosities. During trigger phases 2 to 4 the deviation of the weights from unity is always less than 5 %.

3.6.1 The Trigger Efficiency

The trigger efficiency is determined for those events which have passed the selection criteria described in Section 3.5 (unless stated otherwise). Since all used subtriggers rely on the central muon system, at least one muon candidate must be identified in the barrel region or in the outer end–caps of the instrumented iron. In addition at least one track with a transverse momentum of at least 400 MeV/c is required.

The H1 trigger system consists of three different levels. The trigger efficiency is a product of the single level efficiencies $\epsilon_{\mathtt{S}nn} = \epsilon_{\mathrm{L1}} \cdot \epsilon_{\mathrm{L2}} \cdot \epsilon_{\mathrm{L4}}$. The single subtrigger efficiency for each trigger level in data is shown to agree with the simulation. The combined efficiency of all three subtriggers can, therefore, be determined from Monte Carlo simulation.

Level 1 Trigger Efficiencies

Usually the L1 trigger efficiency is determined from events triggered by an independent subtrigger or subtrigger combination. Since no independent subtrigger (combination) with sufficient statistics exists, the efficiencies of the individual trigger elements are determined. The composition of each subtrigger from trigger elements is equal in simulation and data. Therefore an agreement between all the individual trigger element efficiencies in data and Monte Carlo simulation implies a correct description of the corresponding subtrigger efficiency in the simulation.

The subtriggers depend on trigger elements (`TE`) from three different detector systems, namely trigger elements from the DC$r\phi$ trigger derived from CJC information, from the z–vertex trigger based on the multiwire proportional chambers and from the central muon system. All other H1 subtriggers are sorted according to their trigger element assignment: only those subtriggers which do not contain trigger elements of one of the three specific subdetectors are used to determine the efficiency of trigger elements of *this subdetector*. Since most subtriggers which do not contain DC$r\phi$ or z–vertex trigger conditions are based on an energy deposition in the LAr calorimeter or in the SpaCal, the restriction to the photoproduction domain has to be suspended. The efficiency of the trigger elements of concern are expected to be independent of the virtuality Q^2. Only the low inelasticity region was studied, $0.1 < z < 0.5$, and invariant mass of a J/ψ meson candidate has been restricted to $200\,\mathrm{MeV/c^2}$ around the nominal J/ψ meson mass.

The full data set from 1997, 1999 and 2000 has been used for the efficiency determination. The efficiencies show, within statistical errors, no variations between these years where the errors are calculated according to the binomial distribution corrected for entries with very few statistics:

$$\sigma(\epsilon) = \max\left(\sqrt{\frac{\epsilon\cdot(1-\epsilon)}{N_{\text{events}}}}, \frac{1}{N_{\text{events}}}\right) \tag{3.8}$$

The efficiencies for the individual trigger elements are shown in Figures 3.11–3.13. The comparison between data, the `AROMA` $b\bar{b}$ and `EPJPSI` $c\bar{c}$ Monte Carlo simulations show good agreement:

Muon System Trigger Elements: In order to determine the efficiency of the muon system trigger elements only events with exactly one identified muon candidate in the central muon system are selected. The candidate must lie in the geometric acceptance of the studied detector part. The efficiency of the combined trigger element `Mu_Bar || Mu_ECQ` is analyzed as function of the transverse momentum $p_t(\mu)$ and polar angle $\theta(\mu)$ of this selected muon candidate, of z and of $W_{\gamma p}$ (Figure 3.11). At low inelasticities, the average efficiency for the combination `Mu_Bar || Mu_ECQ` in data is $(75.3\pm1.0)\,\%$ and in agreement with both Monte Carlo simulations. The error is the statistical uncertainty in data according to Equation (3.8).

DC$r\phi$ Trigger Elements: These depend mainly on the track multiplicity N_{track}. Since only tracks with at least a transverse momentum of $400\,\mathrm{MeV/c}$ are

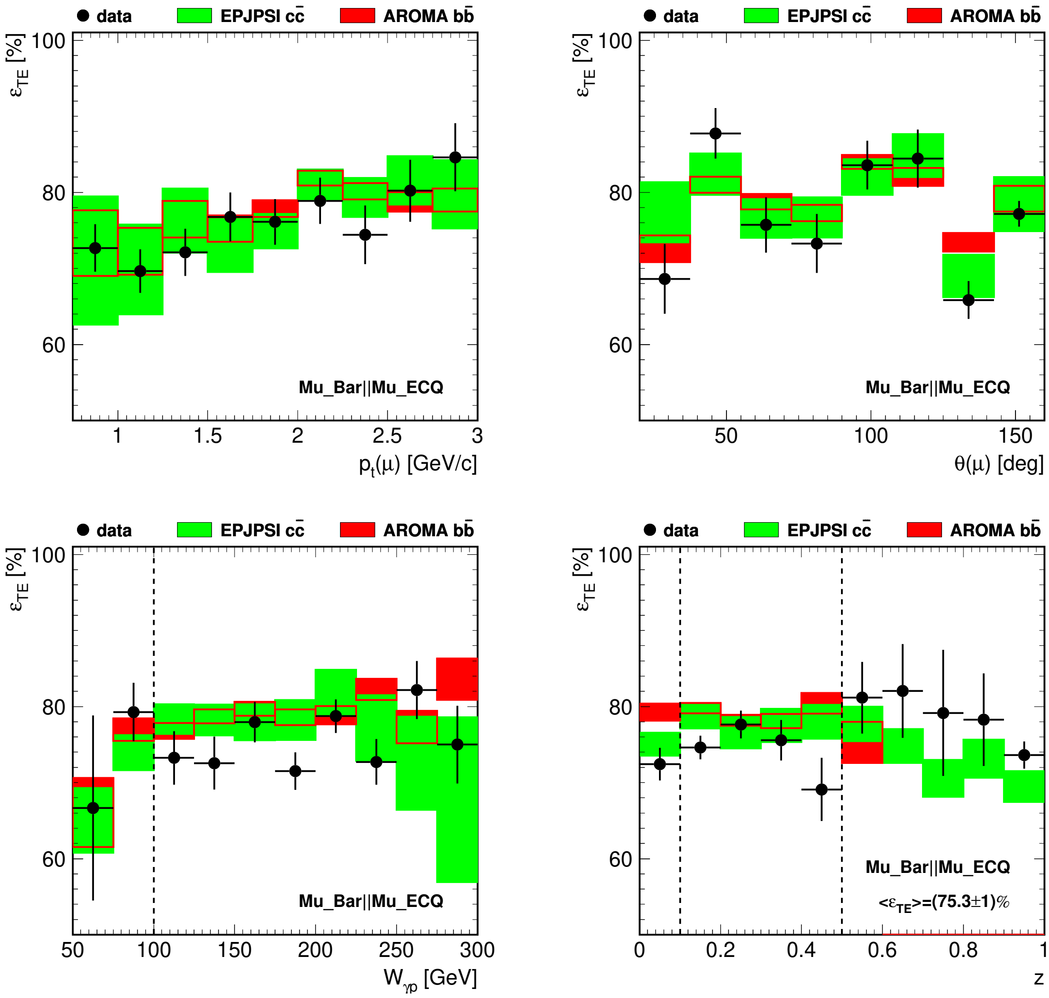

Figure 3.11: *Efficiencies for the muon trigger element combination* `Mu_Bar||Mu_ECQ` *as a function of the muon candidate's transverse momentum $p_t(\mu)$ and polar angle $\theta(\mu)$ (top left and right corner respectively), of the photon–proton center–of–mass energy $W_{\gamma p}$ (lower left corner) and of the inelasticity z (lower right corner). The points correspond to the full data set, while the light (dark) shaded rectangles display the* `AROMA` *$b\bar{b}$ (*`EPJPSI` *$c\bar{c}$) MC.*

capable of validating DC$r\phi$ masks, only tracks above this threshold are considered. The efficiencies of the elements `DCRPh_THig` and `DCRPh_CNH` as functions of N_{tracks}, the inelasticity z and the photon–proton center–of–mass energy $W_{\gamma p}$ are shown in Figure 3.12. The average efficiencies in data $\langle\epsilon_{\text{TE}}\rangle$ in the region $0.1 < z < 0.5$ are (99.5 ± 0.3) % for the `DCRPh_THig` trigger element and (95.5 ± 0.9) % for the `DCRPh_CNH` trigger elements respectively. The quoted errors are the statistical uncertainties. Both Monte Carlo simulations describe the efficiencies well.

z–Vertex Trigger Elements: Both used trigger elements differ in their significance condition. More tracks are needed to set the `zVtx_Sig>1` trigger element than `zVtx_Sig`. The former is, therefore, less efficient, especially at higher z (Figure 3.13). At low inelasticities, $0.1 < z < 0.5$, the average

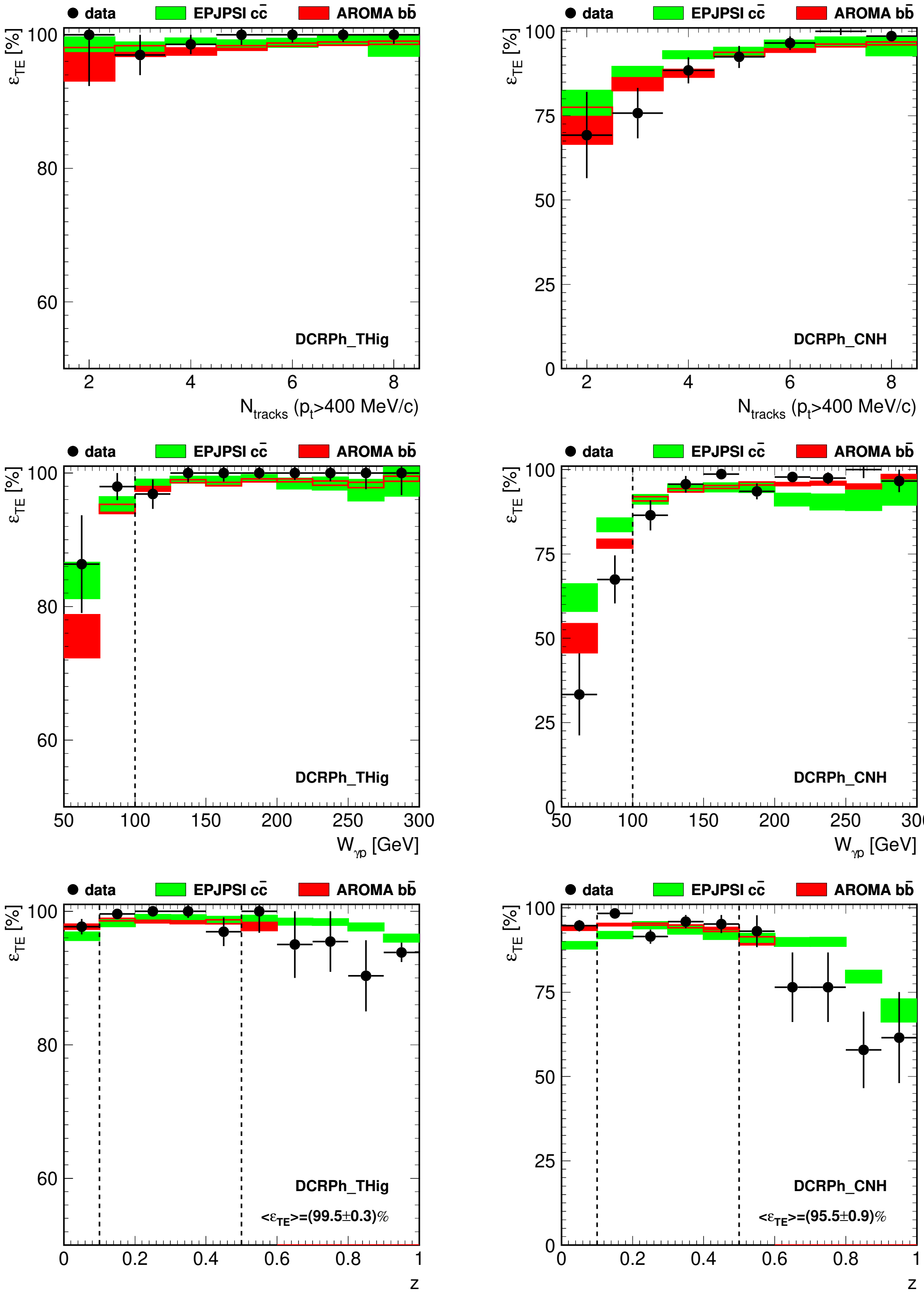

Figure 3.12: *Efficiencies for the DCrϕ trigger elements* DCRPh_THig *(left) and* DCRPh_CNH *(right) as a function of the number of tracks with at least* 400 *MeV/c transverse momentum (upper row), of the photon–proton center–of–mass energy $W_{\gamma p}$ (middle row) and of the inelasticity z (lower row). The points correspond to the full data set, while the light (dark) shaded rectangles display the* AROMA $b\bar{b}$ (EPJPSI $c\bar{c}$) *MC. Note the different scales for both trigger elements.*

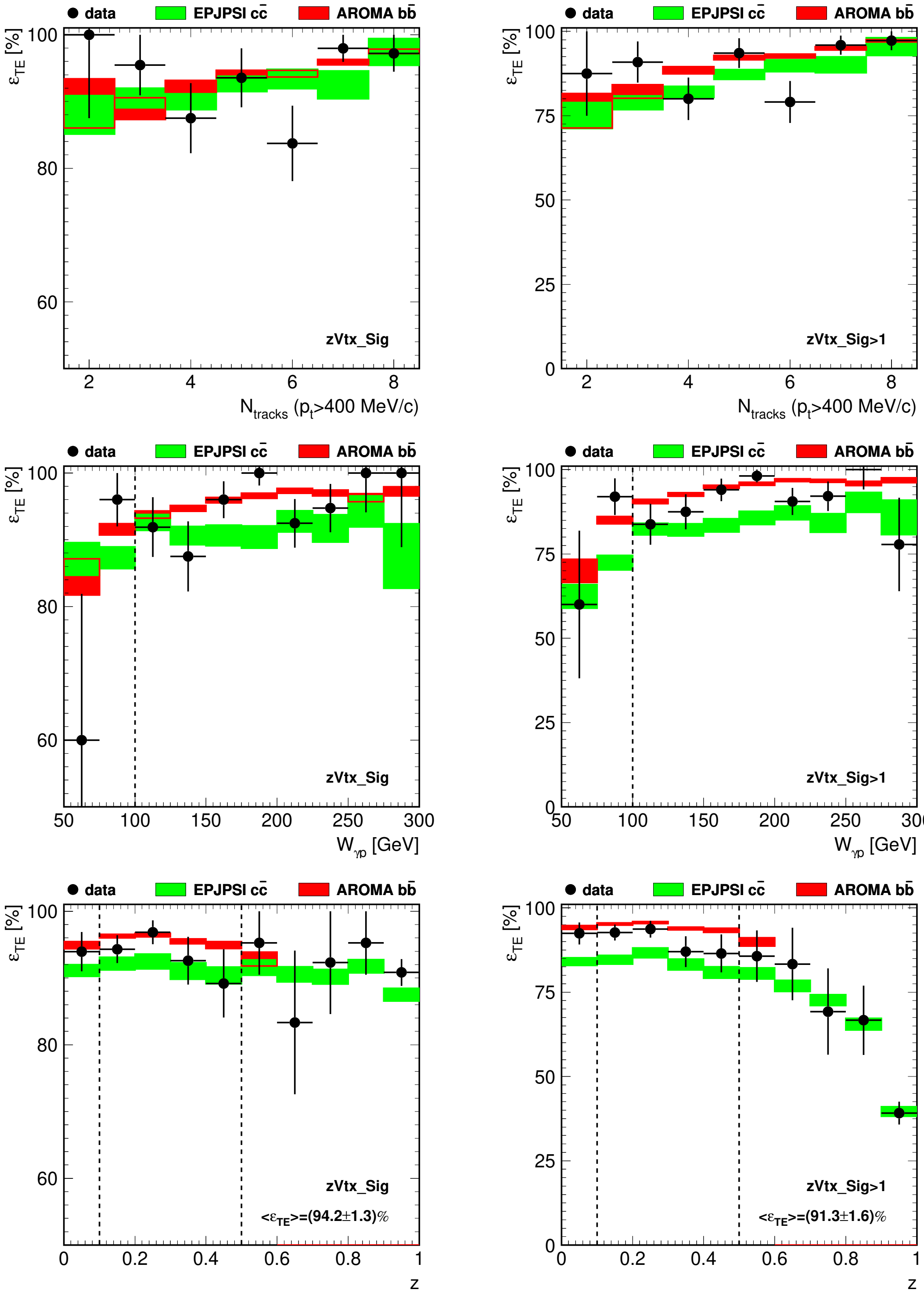

Figure 3.13: *Efficiencies for the z–vertex trigger elements* `zVtx_Sig` *(left) and* `zVtx_Sig>1` *(right) as a function of the number of tracks with at least* 400 *MeV/c transverse momentum (upper row), of the photon–proton center–of–mass energy* $W_{\gamma p}$ *(middle row) and of the inelasticity* z *(lower row). The points correspond to the full data set, while the light (dark) shaded rectangles display the* AROMA $b\bar{b}$ (EPJPSI $c\bar{c}$) *MC. Note the different scales for both trigger elements.*

efficiencies in data of the `zVtx_Sig` and `zVtx_Sig>1` trigger elements are reasonably high, i.e. $(94.2 \pm 1.3)\,\%$ and $(91.3 \pm 1.6)\,\%$ respectively. Since track multiplicities are fairly well described in the `AROMA` $b\bar{b}$ and `EPJPSI` $c\bar{c}$ Monte Carlo simulations, the former tends to reproduce a slightly higher `zVtx_Sig>1` efficiency than the data, while the latter is significantly below.

The difference in the efficiency distributions between data and Monte Carlo simulations determines the relative systematic error of the trigger element efficiency according to Equation (3.7). With a comparison to the `AROMA` $b\bar{b}$ MC simulation, it yields 4.3 % for the track–based (DC$r\phi$ and z–vertex) trigger elements and 3.8 % for the muon trigger elements. In the case of the `EPJPSI` $c\bar{c}$ MC these values are 4.5 % and 3.5 % respectively.

The average trigger efficiencies result from the product of the single trigger element efficiencies according to the subtrigger definitions (cf. listing on page 69). The values are listed in Table 3.6. The distributions of both Monte Carlo simulations agree reasonably well with the data. In the case of the `S19 || S22` subtrigger combination the discrepancy is a consequence of the reasonably described `zVtx_Sig>1` trigger element.

	ϵ_{L1}(`S15`) [%]	ϵ_{L1}(`S19` || `S22`) [%]
1997, 1999, 2000 e^+p data	70.6 ± 1.4(stat.)	65.7 ± 1.5
`AROMA` $b\bar{b}$ MC	74.7 ± 0.4(stat.) $\pm$ 4.3(syst.)	71.0 ± 0.4(stat.) $\pm$ 4.0(syst.)
`EPJPSI` $c\bar{c}$ MC	70.3 ± 1.0(stat.) $\pm$ 4.1(syst.)	60.7 ± 1.0(stat.) $\pm$ 3.5(syst.)

Table 3.6: *Comparison of the L1 trigger efficiencies between data, the* `AROMA` $b\bar{b}$ *and the* `EPJPSI` $c\bar{c}$ *Monte Carlo simulation. The first error quotes the statistical uncertainty, the second the systematical uncertainty.*

L2 Trigger Efficiency

Subtrigger `S15` is validated by a neural network condition on level 2. Its efficiency has been determined from those events which met the level 1 trigger conditions of `S15` and were also triggered by the subtrigger combination `S19 || S22`. The fraction of events which pass the L2 trigger condition is $\epsilon_{\mathrm{L2NN}}(\texttt{S15}) = (90.8 \pm 1.0)\,\%$ (Figure 3.14).

The training of the neural net has been performed with events from 1997 triggered by `S19 || S22`, which do not depend on a level 2 validation. At large inelasticity values, $z > 0.4$, the agreement between the data and the `EPJPSI` $c\bar{c}$ Monte Carlo simulation is reasonably good. Below $z \approx 0.4$ the background contribution due to mis–identified muons increases and influences the neural net decision. Obviously, the `AROMA` $b\bar{b}$ MC is not very well modelled. The discrepancy of about 15 % with the data leads to a relative change in the overall trigger efficiency (cf. below) by about 3.3 %. This will be incorporated into the systematic error. The relative systematic error for the `EPJPSI` $c\bar{c}$ MC is 1.9 %.

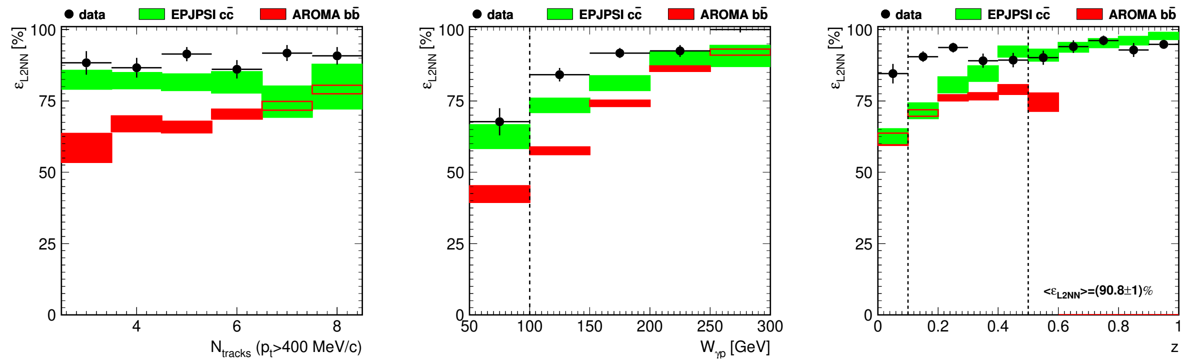

Figure 3.14: *L2 efficiency for the neural net validation of* `S15` *as a function of the number of tracks with more than 400 MeV/c transverse momentum (left), the photon–proton center–of–mass energy $W_{\gamma p}$ (middle) and the inelasticity z (right). The light shaded rectangles correspond to the* `AROMA` *$b\bar{b}$ Monte Carlo simulation, while the dark shaded rectangles are the* `EPJPSI` *$c\bar{c}$ MC.*

L4 Trigger Efficiency

Until 1997 a trigger verification was performed on L4 which mimicked the L1 subtrigger conditions. For the DC$r\phi$ and z–vertex trigger elements a “good” track in the CJC was demanded. The trigger elements of the instrumented iron were validated by a match between iron and central tracks. This restriction causes an inefficiency especially for subtriggers containing the `Mu_Bar` trigger element, such as `S19`. Since the events had in addition to fulfill an L4 hard–scale algorithm, at least one track per event with $p_t > 2\,\mathrm{GeV/c}$ is required.

The L4 efficiency is determined from those events which fulfilled the L1 and L2 trigger conditions of the studied subtrigger and are in addition triggered by a non–iron–dependent L4 verified subtrigger. The resulting efficiencies for the L4 trigger verification in 1997 data are $\epsilon_{\mathrm{L4}}(\texttt{S15}) = (98.5 \pm 1.0)\,\%$, $\epsilon_{\mathrm{L4}}(\texttt{S19}) = (90.6 \pm 2.4)\,\%$ and $\epsilon_{\mathrm{L4}}(\texttt{S22}) = (97.5 \pm 1.8)\,\%$. The quoted errors are the statistical uncertainties.

In 1998 the L4 scheme was completely changed. The trigger verification in its original sense was dropped and the classification done was replaced by the hard–scales and final–state finders (cf. Section 2.2.5). One of these finders is the *high mass finder* [134] which uses the full CJC track reconstruction similar to that described in Section 3.3.1. The invariant mass of each pair of central tracks is calculated and the event is accepted if a combination is found with at least $2\,\mathrm{GeV/c^2}$. The efficiency was determined for J/ψ meson production using 1999 positron data [94] and was $(98.5 \pm 1.5)\,\%$.

The fourth trigger level is not simulated in the Monte Carlo simulation. Since the luminosity for the years 1999 and 2000 dominates, a L4 efficiency factor of 98 % has been applied to the simulation. A relative systematic error of 2 % will be considered in the results.

Overall Trigger Efficiency

Since the agreement of the L1 trigger elements between data and Monte Carlo simulation is good and the L2 decision is reasonably understood, the overall trigger efficiency for the subtrigger combination `S15 || S19 || S22` is determined from the Monte Carlo simulations (Figure 3.15). The overall efficiency yielded $(75.8 \pm 5.2)\,\%$ for the `AROMA` $b\bar{b}$ Monte Carlo simulation and $(68.5 \pm 4.3)\,\%$ for the `EPJPSI` $c\bar{c}$ MC. The given errors are the overall systematical uncertainties.

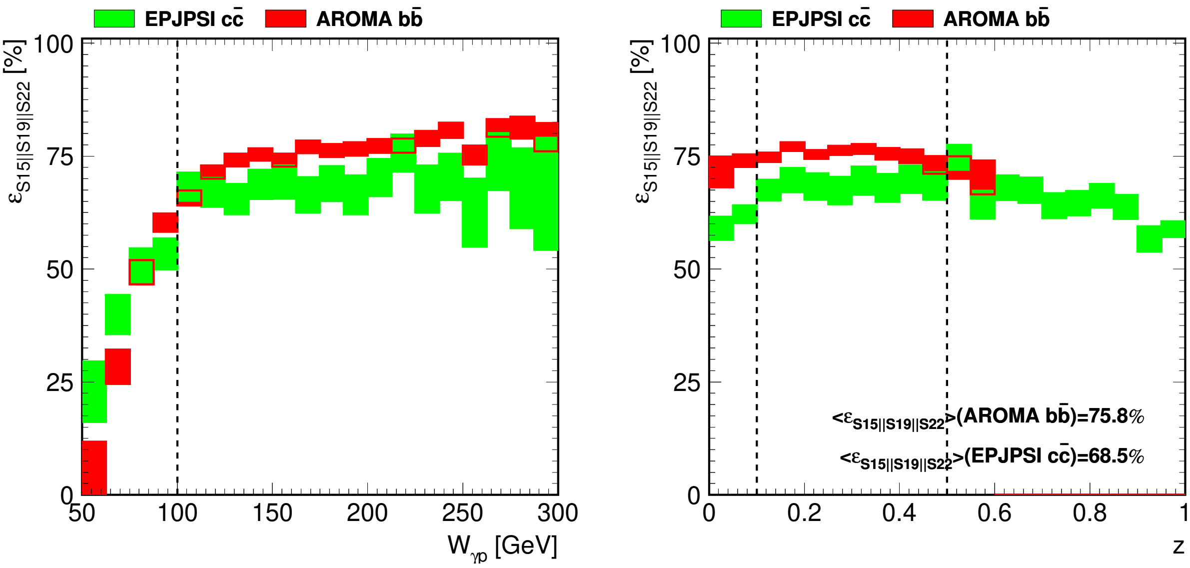

Figure 3.15: *The overall trigger efficiencies for the subtrigger combination* `S15 || S19 || S22` *after L2 and L4 conditions as a function of the photon–proton center–of–mass energy $W_{\gamma p}$ (left) and of the inelasticity z (right). The* `AROMA` *$b\bar{b}$ MC (light shaded rectangles) is about $10\,\%$ more efficient than the* `EPJPSI` *$c\bar{c}$ MC (dark shaded rectangles).*

Chapter 4

Determination of the Decay Length

Beauty–flavoured hadrons have lifetimes which are large enough to lead to measurable decay lengths (cf. Chapter 1). Since J/ψ mesons decay immediately, a J/ψ meson candidate resulting from a b–flavoured hadron decay appears after some distance compared to the directly produced "prompt" J/ψ mesons. Consequently an excess at larger decay lengths will make it possible to separate these event classes.

The decay length is the measure of the distance between primary and decay vertex. Whilst the determination of the primary vertex is a standard task in the H1 track reconstruction, the reconstruction of the decay vertex of heavy quarks is not. Since 1997 the CST has provided the precision necessary to resolve vertices from heavy quark decays. Based on the J/ψ meson candidate sample selected in Chapter 3, the heavy quark decay vertex is reconstructed from the muon candidate pair. To achieve a sufficient precision, both candidates are combined with CST hit information. From the remaining tracks in the event, which are also linked to CST hits, the primary vertex is determined (Figure 4.1).

The usual standard procedure for finding CST hits and linking them to CJC non–vertex fitted tracks is described in Section 4.1. The performance of this linking is quite optimal in the $r\phi$–plane but suffers from several problems in the z–direction. A multi–hypothesis ansatz improves the standard CST linking here and enhances the accuracy of the muon candidates' track parameters along the z–direction (Section 4.2) by including the common decay vertex as an additional constraint;

$$\chi^2 \equiv \chi^2_{\mathrm{vtx}} + \sum_{\mathrm{tracks}\ i} \chi^2_{\mathrm{link},i}.$$

The decay vertex for each J/ψ meson candidate is determined by means of two implementations of such an ansatz (Section 4.3). The resulting J/ψ samples are studied in Section 4.4. From the remaining tracks, the primary vertex position is determined (Section 4.5). Finally the decay length is calculated (Section 4.6).

4.1 Standard CST Linking

Since the hit resolution of the CST exceeds that of the central drift chambers by about a factor of ten, the combination of central tracks with CST hits will significantly im-

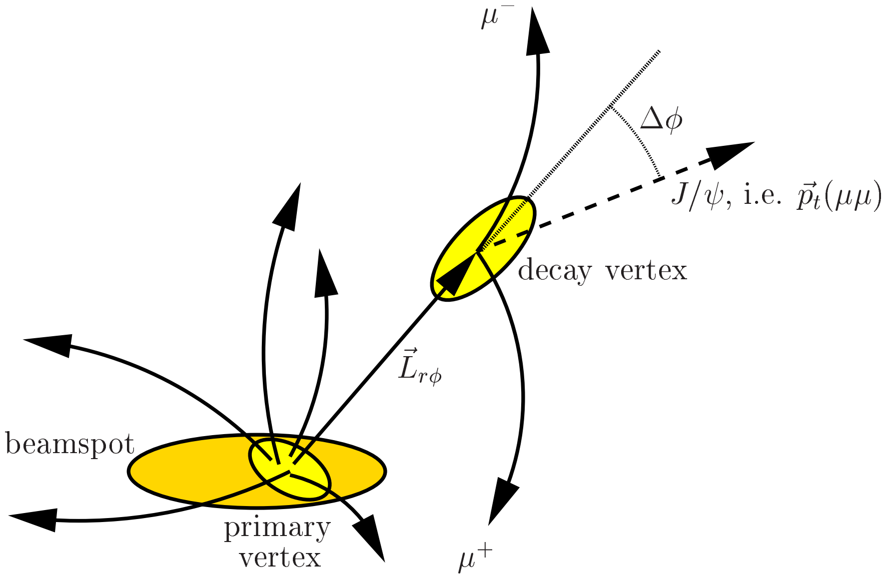

Figure 4.1: *Topology of the decay chain $B \to J/\psi X \to \mu^+\mu^- X$. The decay vertex is reconstructed from both muons. All other tracks in the event determine the primary vertex, where the beam spot position is taken as a further constraint. The indicated variables are defined in Section 4.6, e.g. $\vec{L}_{r\phi}$ denotes the decay length.*

prove the accuracy of the track parameters. Instead of fitting CJC / CIZ / COZ and CST hits simultaneously, a *linking* procedure combines already reconstructed central tracks (cf. Section 3.3.1) with the hit information of the CST. This reduces computing time considerably and can be performed on the DSTs which do not contain CJC hits.

Before the details, the advantages and disadvantages, of the standard CST linking are discussed, the achieved improvements in the track parameter resolutions with respect to the CJC central tracks alone are presented.

The resolution of the helix parameterization $(\kappa, \phi_0, d_{ca}, \theta_0, z_0)$ of the *CST improved tracks* is compared to CJC central tracks with and without primary vertex constraint using the 1999 `AROMA` $b\bar{b}$ Monte Carlo simulation (Table 4.1). Only those tracks which fulfilled the muon selection criteria described in Chapter 3 and passed the active volume of the CST detector are considered. In the case of the transverse track parameters, the azimuthal angle ϕ_0 and the distance of closest approach d_{ca} (here with respect to the experiment's origin) are improved by either the primary vertex constraint or even more by two linked hits of the CST ("CST standard linking" and "CST multi–hypothesis linking", respectively). The resolution of the curvature $\sigma(\kappa)$ depends strongly on the multiplicity of the CJC hits, their distribution along the track and on the *sagitta*, i.e. the deviation of the track circle from a straight line between the first and last hit [135]. The CST information and also the primary vertex constraint move the lever arm to smaller radii and, therefore, improve the resolution of the curvature to some extent. Along the z–axis, the CJC resolution is bad. Thus CIZ / COZ information, the primary vertex anchor or CST hit information are needed to constrain the polar angle θ_0 and the z–coordinate z_0 at the distance of closest approach.

	$\sigma(\kappa)$ [cm^{-1}]	$\sigma(\phi_0)$ [mrad]	$\sigma(d_{ca})$ [μm]	$\sigma(\theta_0)$ [mrad]	$\sigma(z_0)$ [mm]
central tracks (non–vertex fitted)	$3.6 \cdot 10^{-5}$	1.88	372.5	11.21	20.3
central tracks (primary vertex fitted)	$2.9 \cdot 10^{-5}$	1.13	91.1	1.04	0.75
CST standard linking (non–vertex fitted)	$2.4 \cdot 10^{-5}$	0.74	47.0	0.92	0.10
CST multi–hypothesis linking					
cluster method	$2.5 \cdot 10^{-5}$	0.67	43.6	0.81	0.08
spacepoint method	$2.4 \cdot 10^{-5}$	0.65	43.6	0.92	0.09

Table 4.1: *Resolutions of the CST improved track parameters compared to central tracks without and with additional primary vertex constraint. For the sake of completeness, the results of the new multi–hypothesis (cluster and spacepoint) methods are also listed and will be introduced in the next section. All values are taken from the width of a best–fit Gaussian curve to the difference of the generated and measured muon candidates' track parameters in the 1999* `AROMA` *$b\bar{b}$ MC.*

4.1.1 CST Acceptance

The active volume of the CST is restricted to the central region of the H1 experiment (cf. Table 2.1). The verification of the acceptance has been performed with the selected J/ψ data sample of Chapter 3 and compared to the Monte Carlo simulations (Figure 4.2). Each muon candidate must have crossed both CST layers, and, therefore, the acceptance depends strongly on the underlying polar angular distribution of the particles and the z–coordinate of the primary vertex $z_{1\mathrm{st}}$. The average acceptance for one candidate is about $(79.0 \pm 0.2)\,\%$ in data and $83.1\,\%$ ($79.5\,\%$) for the `AROMA` $b\bar{b}$ (`EPJPSI` $c\bar{c}$) Monte Carlo simulation. Monte Carlo simulations and data agree very well.

The combined acceptance for finding two muon candidates inside the active volume of the CST has been determined to be $(69.6 \pm 3.1)\,\%$ using the `AROMA` $b\bar{b}$ MC simulation and $(63.3 \pm 3.1)\,\%$ in the case of the `EPJPSI` $c\bar{c}$ MC. The denoted errors are deduced from the spread between both simulations and contribute to the systematic uncertainty.

4.1.2 Standard CST Linking Procedure

The standard linking method proceeds in two steps [136]: Starting with the $r\phi$–plane, the non–vertex fitted CJC tracks are matched with p–side clusters. If this is successful, the n–side clusters are linked. The $r\phi$– and the z–linking are, therefore, completely decoupled. Since all hits of one particle are correlated in their position, the clusters from each layer are linked simultaneously.

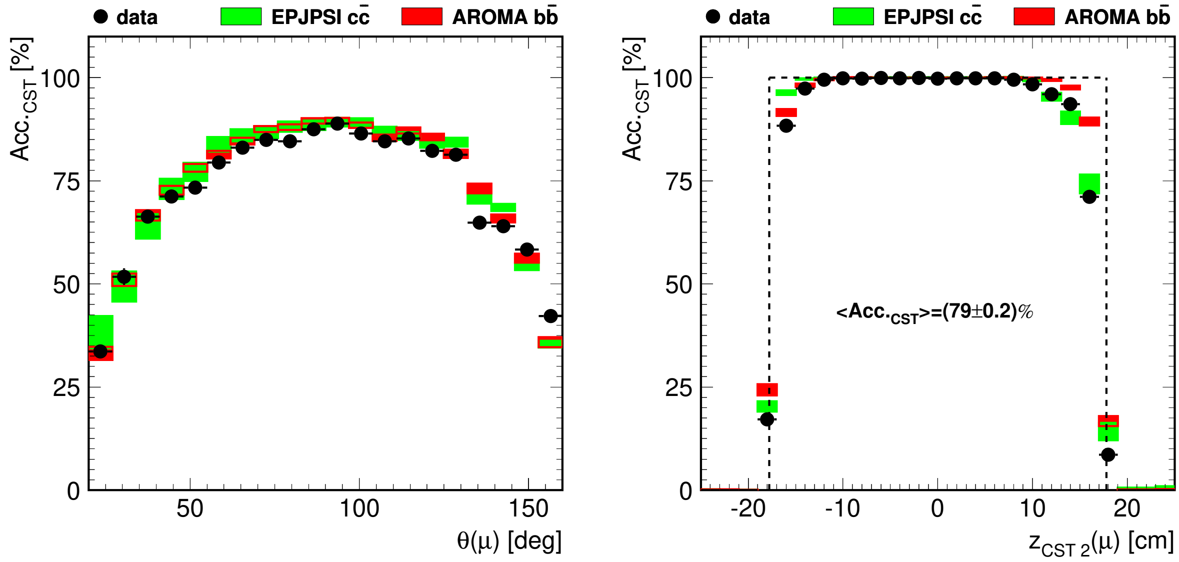

Figure 4.2: *The acceptance of the CST as a function of the polar angle $\theta(\mu)$ of the muon candidate is shown on the left. The acceptance is a result of the muon candidate's polar angular distribution convoluted with the Gaussian distributed z–coordinate of the primary vertex $z_{1\mathrm{st}}$. Their combination gives the z–coordinate of the crossing of a muon candidate with the outer layer of the CST, $z_{\mathrm{CST}\,2}(\mu) = z_{1\mathrm{st}} + r_{\mathrm{CST}\,2} \cdot \cot\theta(\mu)$ (right). The width of the CST is indicated by the dashed line; deviations at the edges are due to the limited track and vertex resolutions.*

The tracks are then extrapolated to the surfaces of the CST, beginning with those tracks which have the lowest error on their distance of closest approach. These are typically tracks with higher momenta for which multiple–scattering contributes less. The crossings are calculated from the CJC track parameters $\vec{T}_{\mathrm{CJC}}$. The error is taken from their covariance $C_{\vec{T}_{\mathrm{CJC}}}$ which also accounts for multiple scattering and energy loss [137]. The track extrapolation error defines a certain window on each layer, in which p–side clusters are searched for. The p–side clusters of both layers are considered simultaneously. Overlap regions are taken into account. The chi–squared is given by

$$\chi^2_{\mathrm{link},r\phi} \equiv \left(\vec{T} - \vec{T}_{\mathrm{CJC}}\right)^T \cdot C^{-1}_{\vec{T}_{\mathrm{CJC}}} \cdot \left(\vec{T} - \vec{T}_{\mathrm{CJC}}\right) + \sum_{\substack{\text{inner / outer}\\ p\text{–cluster } i}} \left(\frac{d(\vec{T}, i)}{\sigma(d)}\right)^2, \qquad (4.2)$$

where $d(\vec{T}, \text{cluster})$ denotes the Euclidean distance between the crossing of track $\vec{T}$ and a p–side cluster and $\sigma(d)$ is the corresponding error. All combinations of clusters from both layers within the search windows are tried. A CST improved set of track parameters in the $r\phi$–plane $\vec{T} = (\kappa, \phi_0, d_{ca})$ and the linked p–side clusters are obtained by maximizing the probability $\mathcal{P}(\chi^2_{\mathrm{link},r\phi})$. The lower limit is given by $\mathcal{P} > 0.01$. Solutions with a maximum number of p–side clusters are preferred. When no reasonable solution with hits in both layers has been found, a solution with clusters from one layer is tried. All linked clusters are locked afterwards to avoid double counting.

If an $r\phi$–link is successful, the non–vertex fitted track is matched with the n–side cluster. Only those n–side clusters are considered which lie within the search windows and on half ladders which also provided a linked p–side cluster. In addition, the z–information from the CJC, CIZ and COZ are added to the χ^2–function, viz.

$$\chi^2_{\text{link,z}} \equiv \sum_{\substack{\text{inner / outer CST } n-\text{cluster} \\ \text{CIZ / COZ hits } i}} \left(\frac{z_i - (z_0 + S_{r\phi} \cdot \cot\theta_0)}{\sigma(\Delta z)} \right)^2 \tag{4.3}$$

where $S_{r\phi}$ is the arc–length from the point of closest approach to the origin to the cluster in the CST or to a hit in the CIZ / COZ. The CST improved track parameters are defined by θ_0 and z_0; the error of the denominator is $\sigma(\Delta z)$. As before, all cluster combinations within the search windows are tried. The combination which maximizes the probability $\mathcal{P}(\chi^2_{\text{link,z}})$ is finally taken. Solutions with the maximum number of n–side cluster are preferred.

4.2 Multi–Hypothesis Ansatz for Three–Dimensional Linking

In the standard CST linking procedure, the combined efficiency and purity for matching CJC tracks with p–side hits has been optimized for an accurate measurement of the *transverse* track parameters.

In z–direction, however, the linking suffers from several problems. Firstly, the lower signal–to–noise ratio on the n–side compared to the p–side (cf. Figure 2.6), i.e. the higher noise level (on an average every 16 mm a noise hit) and the threefold ambiguity of the CST half ladders lead to a large number of n–side clusters, from which only few are true signal hits. Secondly, the high extrapolation error of the non–vertex fitted CJC tracks in the z–direction (cf. Table 4.1, corresponding values for θ_0 and z_0) and the poor performance of the CIZ since the year 1999 (Table 4.2) provide only a coarse search window on the faces of the CST for the true signal hit. Thus the n–side purity will be rather low.

Date	Run	z [mm]		θ [°]	
		min	max	min	max
05.03.1997	178322	480	600	18	23
18.08.1999	250680	-120	480	23	121
21.08.1999	251301	0	360	29	90
23.10.1999	257620	0	480	23	90

Table 4.2: *Regions of inefficiency of the CIZ during the years 1997 to 2000. Only periods affecting the selected data (cf. Table 3.1) are listed. Unfortunately, the major efficiency holes overlap with the CST acceptance, especially in the forward region.*

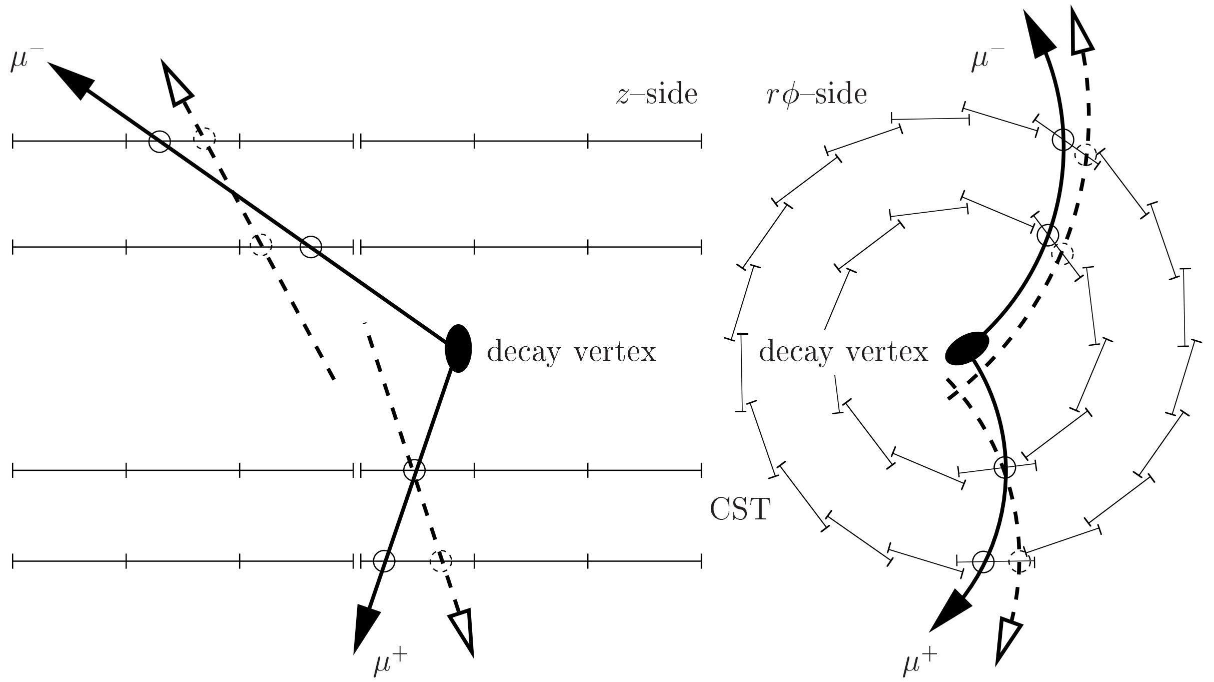

Figure 4.3: *Schematic illustration of the three–dimensional multi–hypothesis linking. Only one muon candidate pair (solid lines) can be linked to CST hits and combined to a three–dimension vertex, while wrong links (dashed lines), e.g. with noise hits, do not cross in three dimensions.*

Usually, the primary event vertex is taken for all tracks as a further constraint to improve purity. This, however, biases lifetime analyses, because tracks originating from decay vertices are forced to come from the primary vertex. More recent studies have shown that even the primary vertex determination is spoiled for low track multiplicity events [138], where wrongly linked noise hits lead to misplaced vertex positions.

More information is, therefore, needed to disentangle the true CST z–clusters.

4.2.1 The Multi–Hypothesis Ansatz

Certain tracks are related by their common origin, e.g. the primary or decay vertex. If these tracks can be assigned to one origin due to a reconstructed decay chain, i.e. $J/\psi \to \mu^+\mu^-$, this additional information provides a further constraint for the CST linking (Figure 4.3). Neglecting correlations of the measured track parameters of different tracks, the expression to be evaluated can be written as

$$\chi^2 \equiv \chi^2_{\mathrm{vtx}} + \sum_{\mathrm{tracks}\ i} \chi^2_{\mathrm{link},i}, \tag{4.4}$$

where χ^2_{vtx} and χ^2_{link} are the chi–squared contributions of a three–dimensional vertex fit and of the CST linking respectively. Maximizing the overall probability $\mathcal{P}(\chi^2)$ gives the three–dimensional (decay) vertex and the linked p– and n–side clusters of all participating tracks.

In order to be unbiased with respect to lifetime information, the non–vertex fitted CJC track parameterization of the selected muon candidates is taken as seed for two different linking methods used. In the *cluster linking* method, the p– and n–side clusters are linked independently, while their combination is considered in the *spacepoint linking* method. In both cases, all different hypotheses of track–to–cluster assignments are kept (the *multi–hypothesis* ansatz). The final combination of hypotheses from both muon candidates is determined from the maximization of $\mathcal{P}(\chi^2)$.

Both methods are described below. The determination of the decay vertex is described afterwards in Section 4.3.

4.2.2 Combined Cluster Linking

The cluster linking method is an extension of the standard CST linking. Due to the optimization of the transverse track parameters which is performed and due to the aforementioned major inefficiencies in z–direction only the z–linking step is modified.

Instead of maximizing the probability $\mathcal{P}(\chi^2_{\rm link,z})$ in order to make a decision on the final cluster combination immediately, all hypotheses for track / n–side cluster matches are kept. The hypotheses are sorted in ascending number of hits assigned in the linking and by a descending overall chi–squared, which is given by

$$\chi^2_{\rm link} \equiv \chi^2_{\rm link,r\phi} + \chi^2_{\rm link,z}. \tag{4.5}$$

Only hypotheses which have a very small probability, $\mathcal{P}(\chi^2_{\rm link}) < 5 \cdot 10^{-4}$, are discarded. The most likely hypothesis is determined simultaneously for both tracks together with the three–dimensional vertex by minimizing the chi–squared given in Equation (4.4).

The linking probability for these finally selected hypotheses is shown in Figure 4.4 and compared to all hypotheses. The probabilities for the $r\phi$– and z–linking mainly depend upon the quality of the CJC track parameters, since the chi–squared contributions from

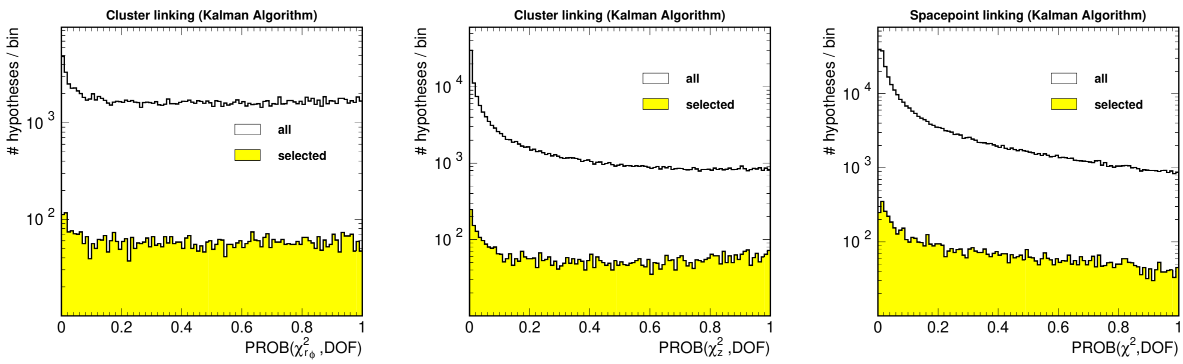

Figure 4.4: *Chi–squared probability distributions for the cluster linking, separately for $r\phi$– (left) and z–linking (middle), and for the spacepoint linking (right). The open histograms display all corresponding hypotheses; the shaded distributions show the finally selected hypotheses.*

the CST clusters to the sum in Equations (4.2) and (4.3) are low due to the high accuracy of the CST hits. The flatness of the probability distribution indicates a good control over errors and covariances. The peak at very low values stems from wrongly assigned clusters; the influence of the requirement $\mathcal{P}(\chi^2_{\text{link}}) < 5 \cdot 10^{-4}$ is visible in the very first bin.

4.2.3 Spacepoint Linking

In contrast to the cluster linking, where the p– and n–side information is decoupled, the spacepoint linking uses their combination. Each central track $\vec{T}_{\text{CJC}}$ is compared with spacepoints in each layer simultaneously:

$$\begin{aligned}\chi^2_{\text{link}} \equiv & \left(\vec{T} - \vec{T}_{\text{CJC}}\right)^T \cdot C^{-1}_{\vec{T}_{\text{CJC}}} \cdot \left(\vec{T} - \vec{T}_{\text{CJC}}\right) \\ & + \sum_{\text{spacepoint } i} \left(\vec{d}(\vec{T}_{\text{CJC}}, i)\right)^T \cdot C^{-1}_{\vec{d}} \cdot \vec{d}(\vec{T}_{\text{CJC}}, i)\Big),\end{aligned} \tag{4.6}$$

where $\vec{d}(\vec{T}_{\text{CJC}}, i)$ denotes the Euclidean distance between the two–dimensional coordinates (ϕ, z) of a spacepoint i and the intersection of an extrapolated track with the corresponding half ladder of the CST. The covariance is given by $C_{\vec{d}}$. Information from the z–chambers is not used.

The hypotheses for all doublets are kept (apart from those which have a negligibly low probability $\mathcal{P}(\chi^2_{\text{link}}) < 5 \cdot 10^{-4}$) and, again, the most probable hypothesis for each track is determined simultaneously together with the three–dimensional vertex. The linking probability is shown in Figure 4.4 (right).

4.3 Three–Dimensional Vertexing

For systematical cross checks, two different means to calculate the three–dimensional vertex are used. Both vertexing algorithms should finally give the same result. The first algorithm is based on a least–squares fitting method using a linearization ansatz to obtain the vertex position and final track parameters. This algorithm is also used for the CST improved primary event vertex determination (cf. Section 4.5). The second one uses a Kalman filtering algorithm (cf. Section 4.3.2). In both cases, the initial track parameters are varied within their errors.

4.3.1 Vertex Determination with Least–Squares Fitting

An initial set of measured helix track parameters $\vec{T}^i_0 = (\kappa, \phi_0, \theta, d_{ca}, z_0)^i$ are fitted to the most probable common origin point, i.e. to the vertex $\vec{V} = (x, y, z)_{\text{vtx}}$. For this purpose the tracks are transformed as $\vec{Q}^i = (p_t, \phi', \theta')^i$, i.e. the transverse momentum and two angles describing the flight direction at the vertex [139], such that the helix parameterization $\vec{T}^i(\vec{V},\vec{Q}^i)$ can be recovered from the vertex coordinates $\vec{V}$ and the track parameters $\vec{Q}^i$. The values $(\vec{V},\vec{Q}^i)$ are determined by minimizing simultaneously for all tracks the weighted distances between the initial track parameters $\vec{T}_0^i$ and the calculated helix parameters $\vec{T}^i(\vec{V},\vec{Q}^i)$:

$$\begin{aligned}\chi^2_{\rm vtx} \quad \equiv \quad & \left(\vec{V}_0-\vec{V}\right)^T \cdot C^{-1}_{\vec{V}_0} \cdot \left(\vec{V}_0-\vec{V}\right) \\ & + \sum_{\text{track } i} \left(\vec{T}_0^i - \vec{T}^i(\vec{V},\vec{Q}^i)\right)^T \cdot C^{-1}_{\vec{T}_0^i} \cdot \left(\vec{T}_0^i - \vec{T}^i(\vec{V},\vec{Q}^i)\right). \end{aligned} \tag{4.7}$$

$C_{\vec{T}_0^i}$ denotes the covariance of the track parameters $\vec{T}_0^i$. The first part makes it possible to include an independent measurement of the vertex $\vec{V}_0$ (e.g. the beam spot position) with covariance $C_{\vec{V}_0}$ and is only used in the primary vertex fit (cf. Section 4.5).

The minimization is performed using an iterative normal equation solver, i.e. via a linearization ansatz [140], where the solution for the fit–parameter vector $\vec{x} = (\vec{V},\vec{Q}^1,\ldots,\vec{Q}^n)$ after the $(k+1)^{\rm th}$ fit–iteration is given by a multi–dimensional Newton approximation:

$$\vec{x}_{k+1} = \vec{x}_k - \left(\vec{\nabla}\cdot\vec{\nabla}\chi^2\right)^{-1} \cdot \left(\vec{\nabla}\chi^2\right). \tag{4.8}$$

The derivatives are taken at $\vec{x}_k$. The linearization used in the first and second derivatives of the χ^2 are of the form

$$\vec{T}^i_{k+1} = \vec{T}^i_k + A\cdot d\vec{V} + B\cdot d\vec{Q}^i, \tag{4.9}$$

with $d\vec{V} = \vec{V}_{k+1} - \vec{V}_k$, $d\vec{Q}^i = \vec{Q}^i_{k+1} - \vec{Q}^i_k$ and the corresponding Jacobian matrices A and B.

4.3.2 Kalman–Filter Method

In the standard least–squares fit formalism *all tracks* are fitted *simultaneously* to the vertex. It is in this sense a *global* method. The Kalman filter method uses the information of different tracks about the vertex *consecutively* — a *local* technique [141].

The algorithm proceeds in two parts. In the *filtering* step, the vertex position $\vec{V}_k$ is calculated from the measured track parameters $\vec{T}_0^i$ of the $i^{\rm th}$ given track and compared to the vertex position $\vec{V}_{k-1}$ as determined with the previous track. Each track measurement $\vec{T}_0^i$ is described by a *mapping function* $\vec{T}_t^i$ of the true vertex position $\vec{V}_t$ and the true track parameters $\vec{Q}_t^i$ at this point distorted by the measurement noise ν^i:

$$\vec{T}_0^i = \vec{T}_t^i(\vec{V}_t,\vec{Q}_t^i) + \nu^i. \tag{4.10}$$

In the application of Kalman filtering, this *measurement equation* must be linear, i.e.

$$\vec{T}_t^i(\vec{V}_t,\vec{Q}_t^i) \approx \vec{T}_k^i(\vec{V}_k,\vec{Q}_k^i) + A\cdot d\vec{V}_k + B\cdot d\vec{Q}_k^i, \tag{4.11}$$

where $d\vec{V}_k = \vec{V}_t - \vec{V}_k$ and $d\vec{Q}_k^i = \vec{Q}_t^i - \vec{Q}_k^i$. The subscript denotes the estimate for the vertex coordinates $\vec{V}_k$ and the track parameterization $\vec{Q}_k^i$ at this point after filtering the $k^{\rm th}$ track. A and B are the corresponding Jacobian matrices.

Initially, a start value for the vertex position $\vec{V}_0$ is chosen, e.g. the origin of the coordinate system or the beam spot position. The comparison is accomplished through a weighted addition of the vertex information from the measured track to the chi–squared of the previous estimate for the vertex position

$$\chi_k^2 = \chi_{k-1}^2 + \left(\vec{V}_k - \vec{V}_{k-1}\right)^T \cdot C_{\vec{V}_{k-1}}^{-1} \cdot \left(\vec{V}_k - \vec{V}_{k-1}\right) + (r^i)^T \cdot C_{\vec{T}_0^i}^{-1} \cdot (r^i), \tag{4.12}$$

with the covariances $C_{\vec{V}_{k-1}}$ and $C_{\vec{T}_0^i}$ for the current vertex position and the track measurement respectively. The residua r^i are defined as

$$r^i \equiv \vec{T}_0^i - \vec{T}_{k-1}^i(\vec{V}_{k-1}, \vec{Q}_{k-1}^i) - A^i \cdot \left(\vec{V}_k - \vec{V}_{k-1}\right) - B^i \cdot \left(\vec{Q}_k^i - \vec{Q}_{k-1}^i\right). \tag{4.13}$$

Based on the minimization of this chi–squared, the new track parameters $\vec{Q}_k^i$ and the corresponding vertex coordinates $\vec{V}_k$ are obtained. The latter serves as a guess as this procedure is repeated for the next track. Finally, in the *smoothing* step the momenta of all tracks are re–calculated at the final vertex position.

4.3.3 Application in the Multi–Hypothesis Linking

Both vertexing algorithms have been applied to the muon candidate pairs using both multi–hypothesis linking methods (cf. Equation 4.4). The error calculations of both algorithms have been verified in the Monte Carlo simulations. For Gaussian distributed errors, the *pull distribution*,

$$\chi \equiv \frac{x_{\text{measured}} - x_{\text{true}}}{\sigma(x_{\text{measured}})}, \tag{4.14}$$

should have mean values of zero and a width of unity. Independent of the Monte Carlo simulation (`AROMA` $b\bar{b}$ or `EPJPSI` $c\bar{c}$) and independent of the three–dimensional vertexing method, the pull distributions of the cluster–linking shows a tendency to slightly broader widths (+5 %), while the spacepoint linking is 10 % broader. Thus the error is slightly underestimated. The mean values are — within errors — compatible with zero.

The error calculation is reasonably well understood. In contrast to the probability values of the linking methods, the probability of the three–dimensional vertex fit is sensitive to the CST resolution. The chi–squared probability $\mathcal{P}(\chi^2_{\text{vtx}})$ must exceed 5 % in order to reject badly reconstructed vertices, independent of the linking method. Its distribution is nearly flat (Figure 4.5).

If not stated otherwise, the Kalman algorithm will be used in the following.

4.4 CST Improved J/ψ Meson Reconstruction

Both multi–hypothesis methods, the cluster linking and the spacepoint linking, have been applied to the two muon candidates, which are combined into a J/ψ meson candidate.

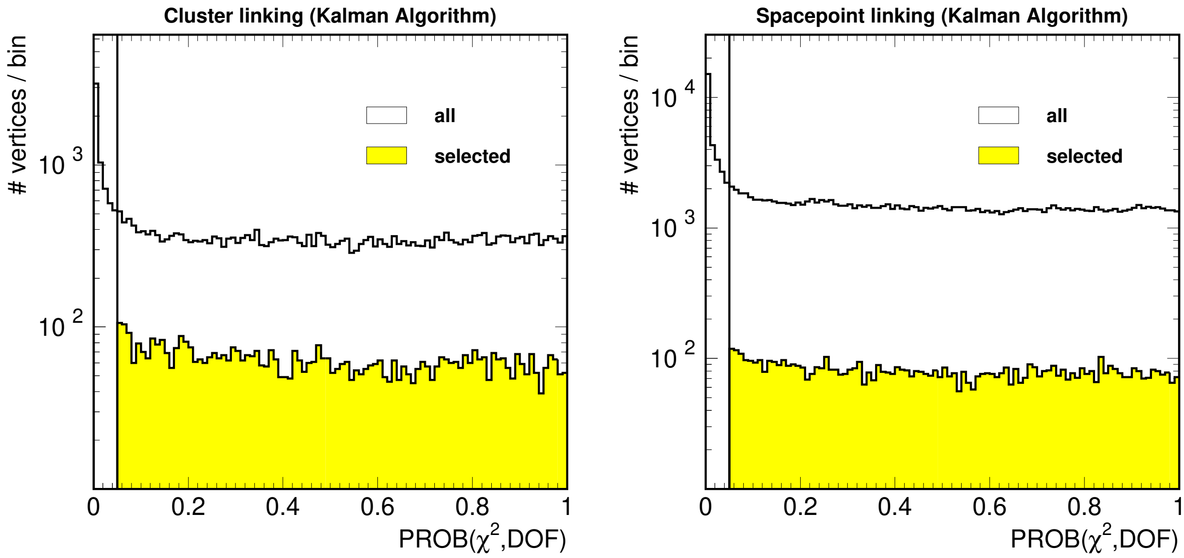

Figure 4.5: *Chi–squared probability distribution of the three–dimensional secondary vertex fit using the cluster–linking method (left) and the spacepoint linking method (right) both together with the Kalman vertex fit. The open histograms display all corresponding vertices; the shaded distributions show the finally used vertex. Vertices with a probability below* 5 % *have been discarded as indicated by the vertical line.*

The resolutions of the muon track parameters $(\kappa, \phi_0, d_{ca}, \theta_0, z_0)$ agree with the values of the standard CST reconstruction and are improved compared to the non–CST track reconstruction (cf. Table 4.1). Consequently, the mass resolution of the J/ψ meson candidates also improves (Figures 4.6 and 4.7).

The invariant mass distributions can be compared to those determined from the central tracks (cf. Figure 3.7). The restriction of the central tracks to the CST acceptance region improves the mass resolutions in the medium–z and elastic region by 5 to 8 %. Due to the multi–hypothesis linking the width is further improved by another 7 %. At low z the determination of the width suffers from low statistics. The resolution values agree within the relatively large errors.

From the number of J/ψ meson candidates within the peak region, however, a first estimate on the overall CST efficiency (including the CST acceptance) can be deduced:

$$\mathcal{A}_{\mathrm{CST}} \cdot \epsilon_{4/4} = \frac{N_{J/\psi}(\mathrm{CST})}{N_{J/\psi}(\mathrm{CJC})}, \tag{4.15}$$

where $\epsilon_{4/4}$ gives the efficiency of having measured and linked two muon candidates with two CST hits each. The number of candidates obtained with any of the two multi–hypothesis linking methods (cf. Figures 4.6 or 4.7) is denoted with $N_{J/\psi}(\mathrm{CST})$ and $N_{J/\psi}(\mathrm{CJC})$ gives the candidate yield from the standard track reconstruction without any CST information (cf. Figure 3.7). In the CST acceptance $\mathcal{A}_{\mathrm{CST}}$ for two muon candidates (approximately 70 %) the 4–of–4 efficiency $\epsilon_{4/4}$ is around 25 to 28 % for the cluster linking and 27 to 35 % for the spacepoint method. A more detailed study will follow in Section 4.4.2.

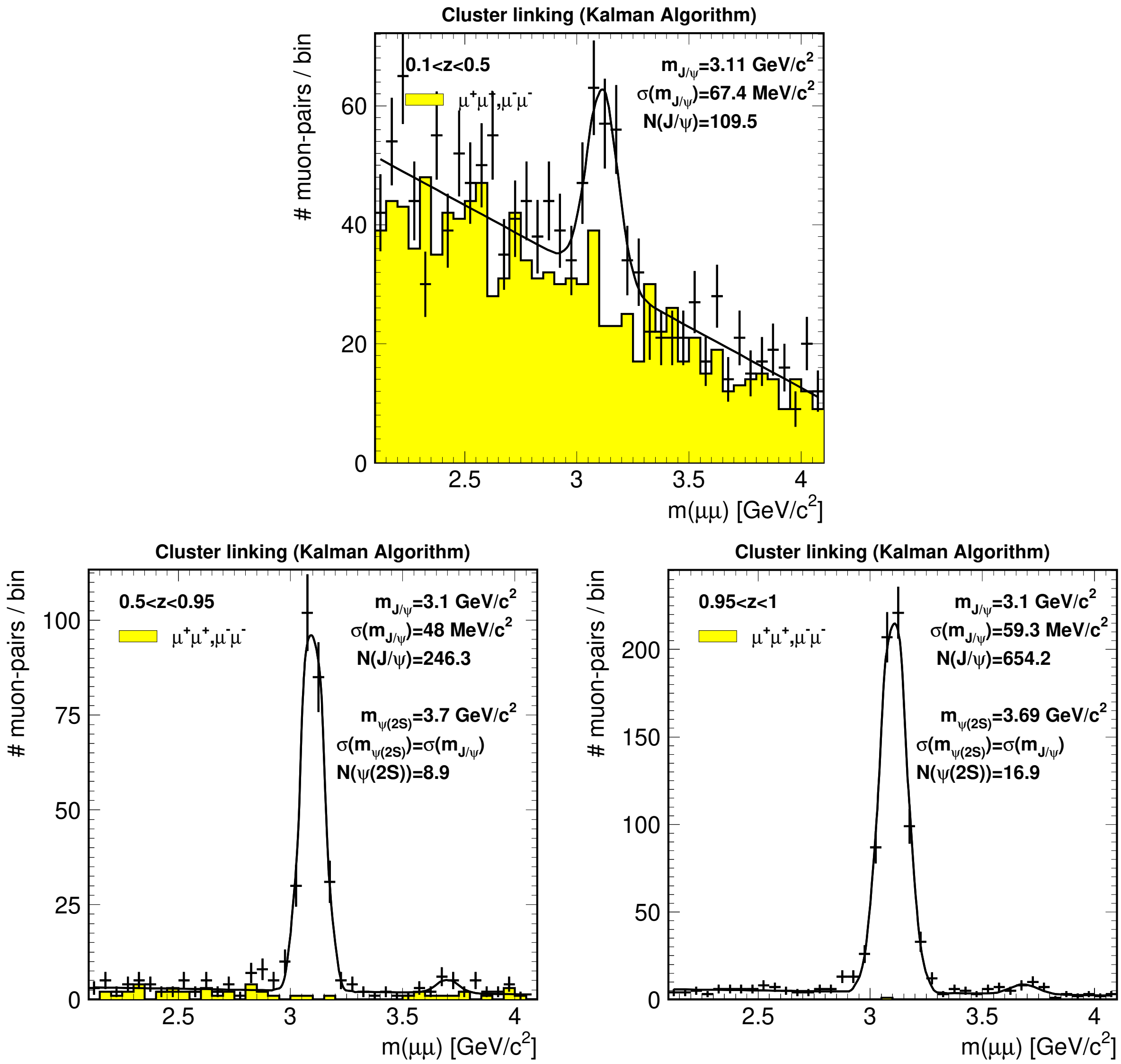

Figure 4.6: *Invariant mass distribution of the CST improved J/ψ meson candidates (1997, 1999 and 2000 e^+p data, without trigger requirements) using the* <u>*cluster linking method*</u>*. The low–z region, $0.1 < z < 0.5$, is shown on the top, while the cross–check samples with candidates at medium–z ($0.5 < z < 0.95$) and high–z ($0.95 < z$) are shown in the lower row, left and right, respectively. A best–fit curve of a Gaussian plus a straight line describes the mass distributions very well. Like–sign muon combinations are indicated by the shaded histograms.*

4.4.1 Hit Purities

The new multi–hypothesis methods agree in the track parameter resolution with the standard CST linking. Nevertheless, not only an accurate measurement of these parameters is required, but also the coordinates of the decay vertex need to be determined precisely. A wrong hit assignment in the linking does not necessarily worsen the track resolution, but will surely spoil the decay vertex position. A strong argument for the cluster and space-point linking methods will be, therefore, deduced from the *hit purity*, i.e. the fraction of

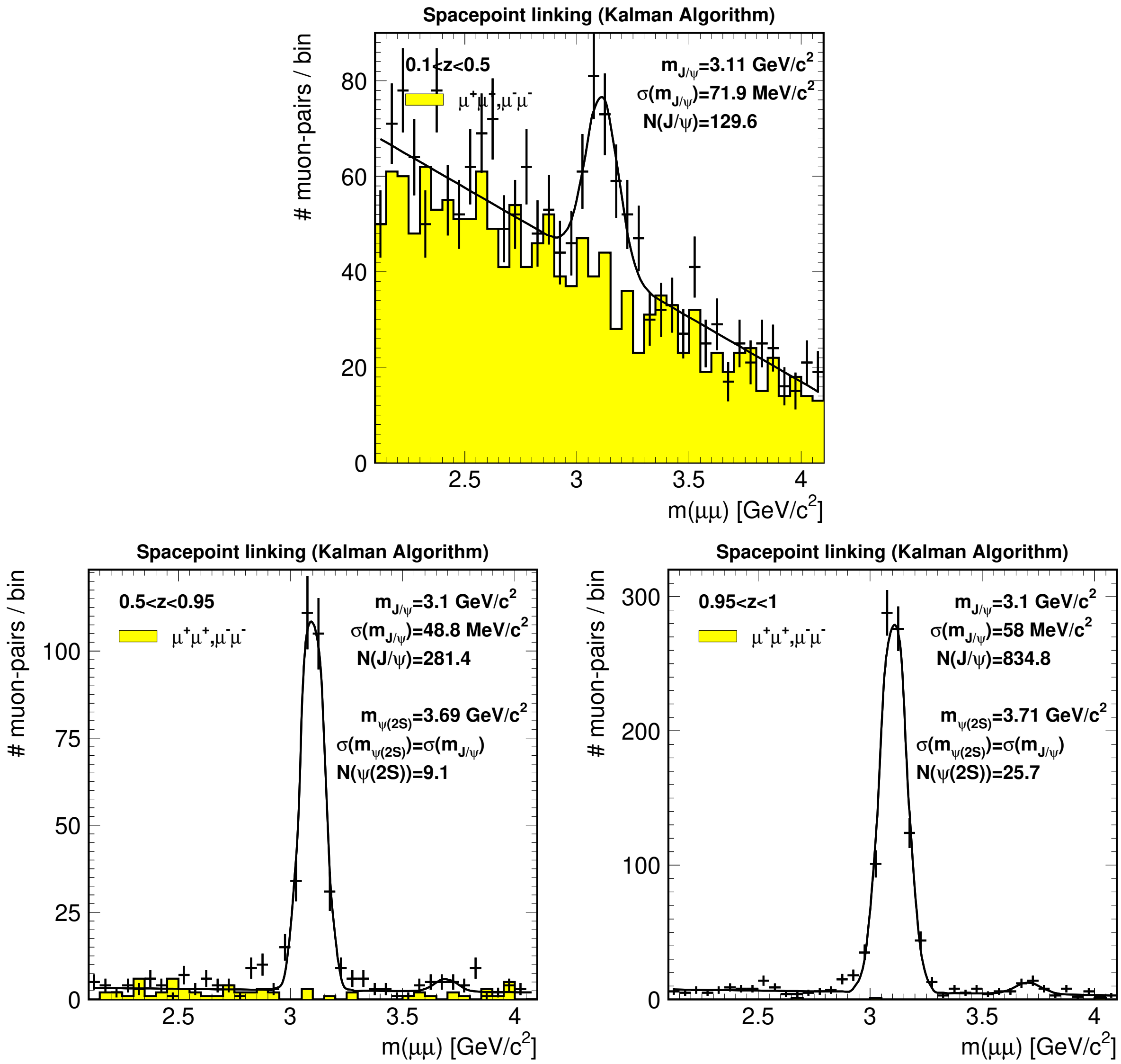

Figure 4.7: *Invariant mass distribution of the CST improved J/ψ meson candidates (1997, 1999 and 2000 e^+p data, without trigger requirements) using the spacepoint linking method. The low–z region, $0.1 < z < 0.5$, is shown on the top, while the cross–check samples with candidates at medium–z ($0.5 < z < 0.95$) and high–z ($0.95 < z$) are shown in the lower row, left and right, respectively. A best–fit curve of a Gaussian plus a straight line describes the mass distributions very well. Like–sign muon combinations are indicated by the shaded histograms.*

correct linked p– and n–side clusters of all (i.e. *4–of–4*) p– and n–side clusters.

For a sub–sample of the 1997 `AROMA` $b\bar{b}$ Monte Carlo, the simulated (true) p– and n–side hits are available. For every muon candidate the true hits are compared to those used by each linking method (i.e. standard CST linking, the cluster and the spacepoint linking). The purities $\mathcal{P}$, that both p– or n–side hits are the correct ones, are given in Table 4.3. The values are independent of the used vertexing method (i.e. Kalman– or least–squares vertexing).

		Standard CST [%]	Cluster [%]	Spacepoint [%]
p–side		97.4 ± 0.4	97.7 ± 0.6	97.4 ± 0.6
n–side	without CIZ / COZ	53.9 ± 1.0	84.4 ± 1.4	83.9 ± 1.4
	with CIZ / COZ	79.4 ± 1.0	92.3 ± 1.1	

Table 4.3: *Purity of the p– and n–side compared for the standard CST linking, the cluster linking and the spacepoint linking methods. The spacepoint linking uses per definition no CIZ / COZ hits. All values are determined from the 1997* `AROMA` *$b\bar{b}$ Monte Carlo simulation. The quoted errors are the statistical uncertainties.*

Because the p–side's signal–to–noise ratio is reasonably good, the cluster and spacepoint linking methods do not improve here — as expected. This differs drastically on the n-side. Since the spacepoint linking does not use CIZ / COZ hits, the purity for the standard CST and cluster linking are determined twice, with and without additional hits from the CIZ / COZ. Without consideration of the CIZ / COZ, the purities of the spacepoint and cluster linking methods are equal within errors ($\sim 84\,\%$). The purity of the standard linking is significantly smaller and approximately $54\,\%$. The addition of the CIZ / COZ raises the cluster linking purity by about $8\,\%$, while the standard linking reaches with $79\,\%$ nearly the purity of the spacepoint linking (which uses *no* CIZ / COZ hits). Thus the n–side purity for the standard CST linking is improved by about $13\,\%$ by utilizing the cluster linking.

On the n–side, a noise hit is present on average every 16 mm and the track resolution in z using the CIZ / COZ is of the order $\mathcal{O}(380\,\mu\text{m})$, therefore the probability to link a noise hit is about $\frac{380}{16000} \approx 2.5\,\%$. The probability to link no noise hit is $(1 - 2.5\,\%)^4 \approx 90\,\%$. Although this is a coarse calculation which does not make use of a linking method itself, nor a vertex constraint, it gives an estimate on the maximum purity value attainable. The high purity gained with the cluster linking method including CIZ / COZ hits is, therefore, a very good result.

During mid–1999 large parts of the CIZ degraded due to broken sense wires (cf. Table 4.2). The necessity of an improved CST linking becomes then even more important.

4.4.2 Linking Efficiencies

The fraction of events, where a specific multi–hypothesis linking method succeeded, i.e. where both muon candidates were linked to two p– and two n–side clusters, define the *4–of–4 hit efficiency*. Both muons must already lie in the CST acceptance, i.e. have crossed the active volume of the CST (cf. Section 4.1), viz.

$$\epsilon_{4/4} = \frac{\text{both muons linked and vertexed}}{\text{both muons in CST acceptance}}. \tag{4.16}$$

Only those events are considered which passed the event selection described in Chapter 3. In addition, since the 4–of–4 hit efficiency does not depend on the trigger requirements, these have been omitted here to increase the statistics.

The combined efficiency is shown in Figures 4.8 and 4.9. The 4–of–4 efficiency as a function of the azimuthal angle varies slightly since the single hit efficiency compared between individual half ladders is not equal [142]. The combined value for all years is calculated by weighting the efficiencies for individual years with the corresponding luminosities. The result is $\epsilon_{4/4} = (28.9 \pm 0.5)\,\%$ for the cluster linking using the Kalman vertexing algorithm and $(35.9 \pm 0.6)\,\%$ for the spacepoint linking. Using instead the least–squares vertexing algorithm, the 4–of–4 efficiencies are slightly higher, i.e. $(32.3 \pm 0.6)\,\%$ for the cluster linking method and $(39.3 \pm 0.6)\,\%$ for the spacepoint linking. The errors denote the statistical uncertainty. These efficiency values will later be used for the determination of the cross sections. The relative variation of about 15.3 % will be included in the systematic error.

The difference between the 1997 and 1999 / 2000 efficiencies requires some more discussion. During electron running in the year 1998, the CST readout chips on the half ladders suffered from very high synchrotron radiation rates. This radiation deteriorated their performance in such a manner, that the internal capacitors lost their stored charge (i.e. the hit information) faster than in 1997 [143]. The corresponding CST simulation in the Monte Carlo has been tuned to agree with the data by randomly discarding hits.

The efficiency displayed here is usually named "effective efficiency", because the purity $\mathcal{P}$ has not been corrected for. Since the spacepoint linking method does not use CIZ / COZ hits, the effective efficiency is higher than for the cluster linking. If the CIZ / COZ hits are discarded in the latter method, its efficiency agrees within errors with the spacepoint linking. The true efficiency is given by $\epsilon_{\mathrm{true}} = \epsilon_{\mathrm{effective}} \cdot \mathcal{P}$. For 1997 the purity values of the cluster linking method are known to be $\mathcal{P} = (92.3 \pm 1.1)\,\%$ (cf. Table 4.3), giving together with the 1997 values of the effective efficiency (cf. Figure 4.8) a true efficiency of $\epsilon_{\mathrm{true}} = (36.4 \pm 1.4)\,\%$. This translates to a single hit efficiency of $(77.7 \pm 2.9)\,\%$ for one combined p– and n–side cluster, where the error results from the statistical uncertainty. For the spacepoint linking method the single hit efficiency is deduced to be $(78.6 \pm 2.7)\,\%$. Both values is quite close to the value of $(73.2 \pm 1.2)\,\%$ determined by a more detailed study [142]. From 1999 onwards, the CIZ was more unstable (cf. Table 4.2) and the purities changed.

4.4.3 Conclusions

Both CST linking methods discussed here, the cluster linking and the spacepoint linking, improve the track parameters with respect to the standard track reconstruction and to the standard CST linking. By definition these new methods reconstruct a decay vertex which serves as an anchor for the track determination. This anchor replaces the usual primary vertex or beamspot constraint. The purity on n–side half ladders is considerably increased with respect to the standard CST linking, which suffers from the low signal–to–noise ratio on the n–side and which relies strongly on the CIZ / COZ information.

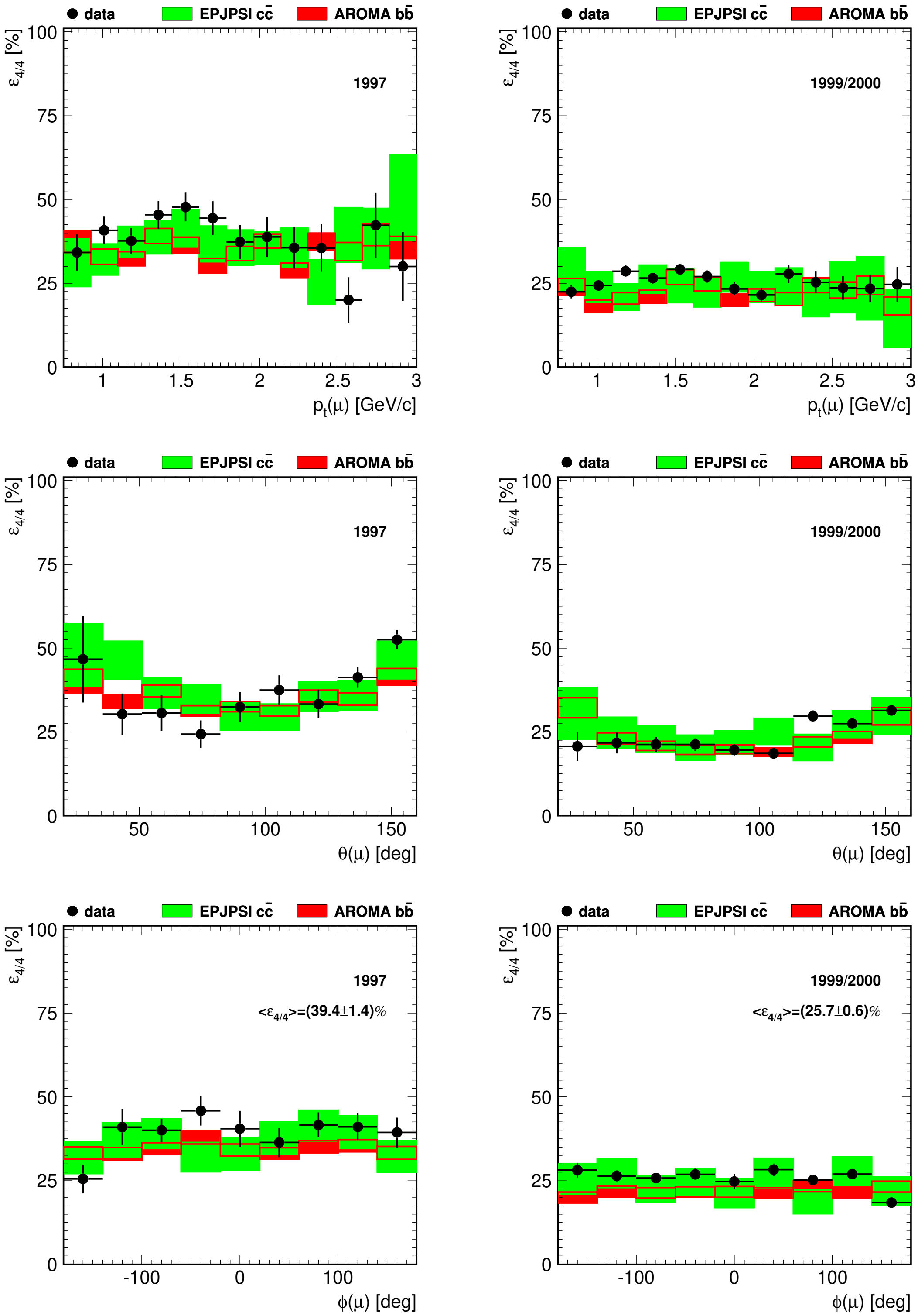

Figure 4.8: *4–of–4 hit efficiency for the* <u>*cluster linking*</u> *(using the Kalman vertexing algorithm) for the e^+p data of the years 1997 (left) and 1999/2000 (right) as a function of the muon candidate's transverse momentum $p_t(\mu)$ (upper row), its polar angle $\theta(\mu)$ (middle row) and its azimuthal angle $\phi(\mu)$ (lower row). The points correspond to the data (without trigger requirements), while the light (dark) shaded rectangles display the* AROMA *$b\bar{b}$ (*EPJPSI *$c\bar{c}$) MC simulations.*

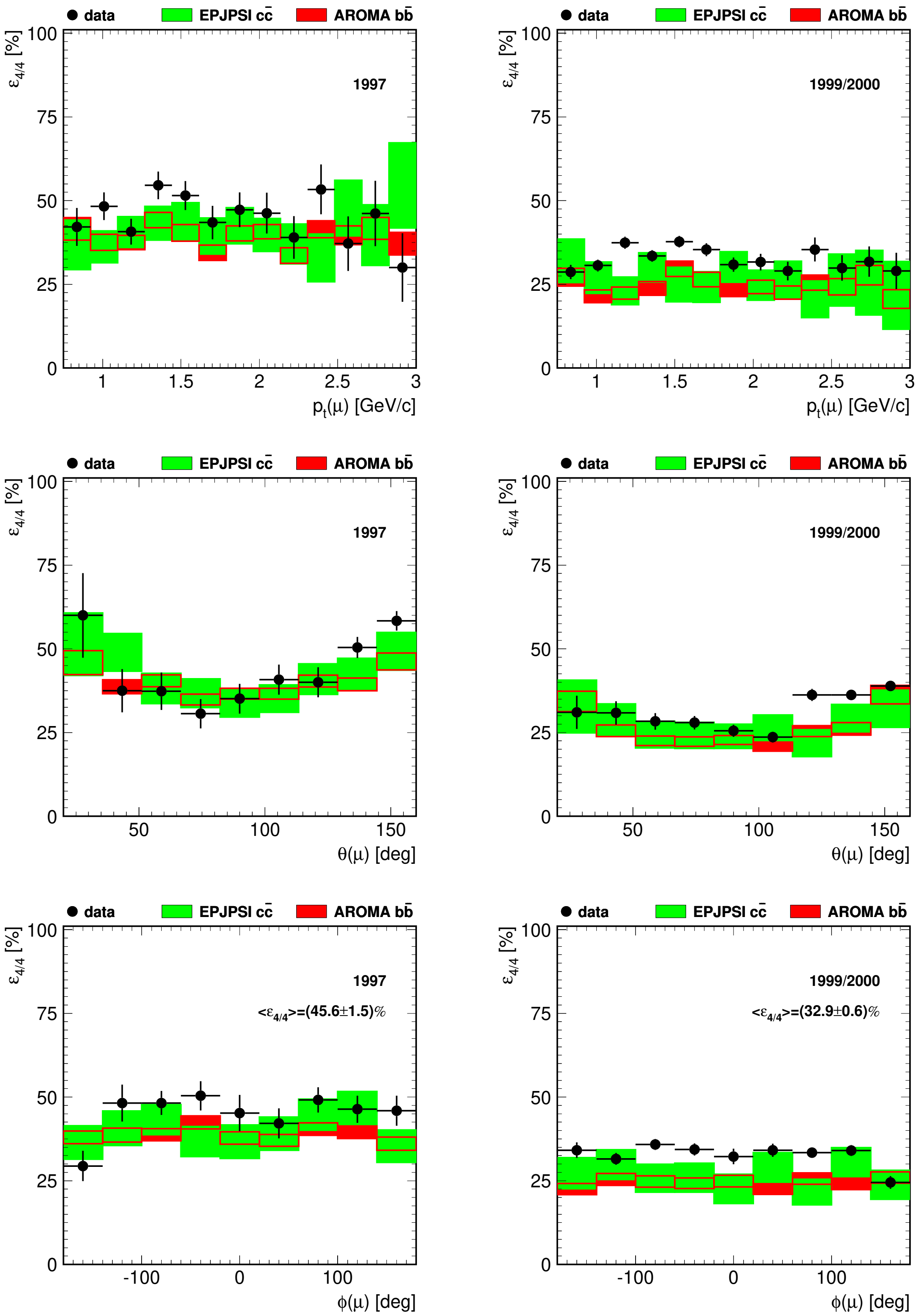

Figure 4.9: *4–of–4 hit efficiency for the spacepoint linking (using the Kalman vertexing algorithm) for the* e^+p *data of the years 1997 (left) and 1999/2000 (right) as a function of the muon candidate's transverse momentum* $p_t(\mu)$ *(upper row), its polar angle* $\theta(\mu)$ *(middle row) and its azimuthal angle* $\phi(\mu)$ *(lower row). The points correspond to data (without trigger requirements), while the light (dark) shaded rectangles display the* `AROMA` $b\bar{b}$ *(*`EPJPSI` $c\bar{c}$*) Monte Carlo simulations.*

4.5 The Primary Vertex

The standard procedure for the determination of the primary vertex [144] uses both the CST improved run vertex (cf. Section 4.5.1) and selected non–vertex fitted CST improved tracks as derived from the standard CST linking procedure. It proceeds in two steps.

In the first step, a track selection is applied to obtain a set of good quality tracks (similar to the requirements discussed in Section 3.3.1). To avoid any bias, the tracks of the muon candidates used in the decay vertex fit are excluded. By using the two–dimensional version of the least–squares fitting algorithm (cf. Section 4.3.1), all remaining tracks are fitted first in the $r\phi$–plane. The CST run vertex (cf. below) taken at the average z_0 of all tracks is added as an additional independent measurement. The algorithm is repeated as long as outlayers with a too high contribution, $\Delta\chi^2_{\mathrm{vtx}} \approx 3$, to the total chi–squared can be excluded. The tracks are refitted only after the final iteration.

In the second step, the $r\phi$–fitted tracks are used to determine the z–coordinate of the vertex. The mean distance of each track i to all others j,

$$d_i = \frac{1}{n-1} \sum_{j=1}^{n} \frac{|z_{0,i} - z_{0,j}|}{\sigma_{\Delta z_0}}, \tag{4.17}$$

is calculated and outlayers are rejected. With the initial track parameters in the Sz–plane, $\vec{T}_0^i = (z_0, \theta)^i$, and their covariance $C_{\vec{T}_0^i}$, the minimum of the function

$$\chi^2_{\mathrm{vtx}} = \sum_{\text{tracks } i} \left(\vec{T}_0^i - \vec{T}^i\right)^T \cdot C^{-1}_{\vec{T}_0^i} \cdot \left(\vec{T}_0^i - \vec{T}^i\right) \tag{4.18}$$

determines the z–coordinate of the primary vertex and the fitted polar angle at the vertex $\vec{T}^i = (z_{\mathrm{vtx}}, \theta')^i$. Again, tracks with a too high contribution to the chi–squared, $\Delta\chi^2_{\mathrm{vtx}} \approx 3$, are excluded and the fit is repeated.

Alternatively, the multi–hypothesis ansatz can also be applied to determine the primary vertex. Since the combinatorics increase as fast as $n_1 \cdot n_2 \cdot \ldots \cdot n_m$, where m and n are the number of tracks and hypotheses respectively, this requires too much computing power.

4.5.1 Determination of the Run Vertex

The CST improved run vertex is defined and calculated in analogy to the CJC run vertex (cf. Section 3.3.1). During the offline reconstruction, i.e. before the primary vertex has been calculated, a set of well measured CST improved tracks with high transverse momenta are selected from the events of a run. Instead of using the whole run as for the CJC run vertex, intervals of approximately 300 useful events are taken[1]. For each of the intervals, the CST run vertex coordinates, x_{beam} and y_{beam}, and tilts, α_x and α_y, are determined by a least–squares fit minimizing the overall distance of closest approach. The result is written to the database.

[1] This corresponds to approximately 20 minutes of data taking.

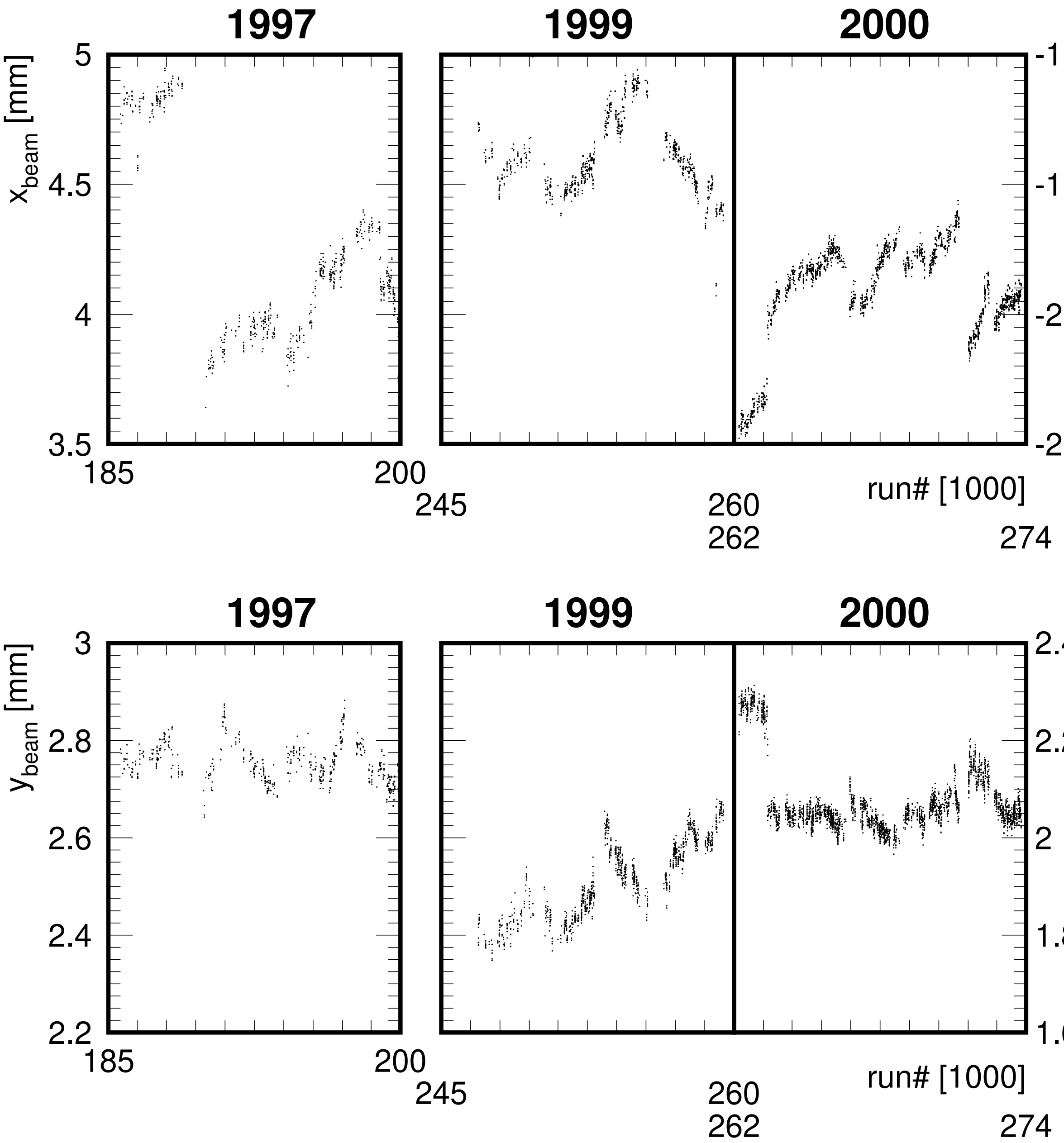

Figure 4.10: *Movement of the beam in the x– (upper row) and the y–directions (lower row) as a function of the run number and separately for the e^+p data of the periods 1997, 1999 and 2000. Note the different absolute scales for the movement in x.*

The position of the beamspot has been determined with high precision by this short–term run vertex. The mean error on the position is about $10\,\mu$m in both directions. The movement of the beam is illustrated in Figure 4.10. The drift during a run is approximately $50\,\mu$m in the x– and $20\,\mu$m in the y–directions.

Since the beam position is exactly known, the maximum inaccuracy of the primary vertex coordinates is given by the beamspot size. However, using the primary vertex determination, the resolution along the x–axis can be significantly improved in multi–track events,

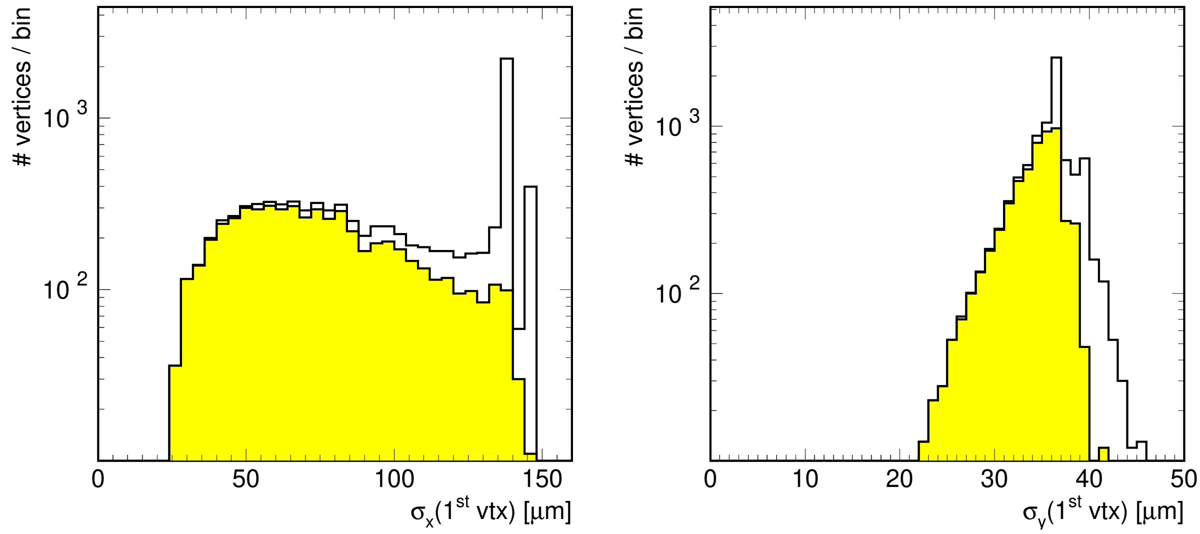

Figure 4.11: *Error distribution for the primary vertex coordinates in the x– (left) and the y–directions (1997, 1999 and 2000 e^+p data, without trigger requirements). Multi–track events (e.g. at low inelasticities $0.1 < z < 0.5$, shaded histograms) significantly improve the vertex resolution down from the initial size of the beamspot. The upper edges correspond to the beam spot size $\sigma(x_{\text{beam}}) = 138\ \mu m$ (since 1999; $145\ \mu m$ for 1997), where no further improvement has been achieved, e.g. in events with low track multiplicities like elastic J/ψ meson samples. The error in y experiences hardly any improvement beyond the beam spot size $\sigma(y_{\text{beam}}) = 36\ \mu m$ ($39\ \mu m$ for 1997). The tails towards higher values are due to very short run periods, where the statistics to determine the run vertex are small.*

e.g. events at low inelasticities $0.1 < z < 0.5$ (Figure 4.11). An improvement in the y–direction on the other hand is unlikely, because of the small vertical beamspot size.

In the Monte Carlo simulations, the beamspot position is generated according to two Gaussian distributions with fixed average positions, i.e. $x_{\text{beam}} \approx 4\,\text{mm}$ and $y_{\text{beam}} \approx 3\,\text{mm}$ respectively. The corresponding widths are taken from data.

4.5.2 Verification of the Error Calculation

As for the decay vertex determination, the error calculation has been verified using Monte Carlo events (Figure 4.12). The comparison between the `AROMA` $b\bar{b}$ and `EPJPSI` $c\bar{c}$ MC simulations reveal the influence of the rather large lifetimes of heavy quarks. Since the primary vertex algorithm is not capable of distinguishing decay and primary vertices, particles from decay vertices spoil the primary vertex determination. This is the case especially in x–direction, where the beamspot constraint is rather weak, while in y–direction this constraint nearly fixes the primary vertex coordinates. Due to the outlayer rejection performed (cf. Equation 4.17), the width of the pull distribution in z is smaller than unity.

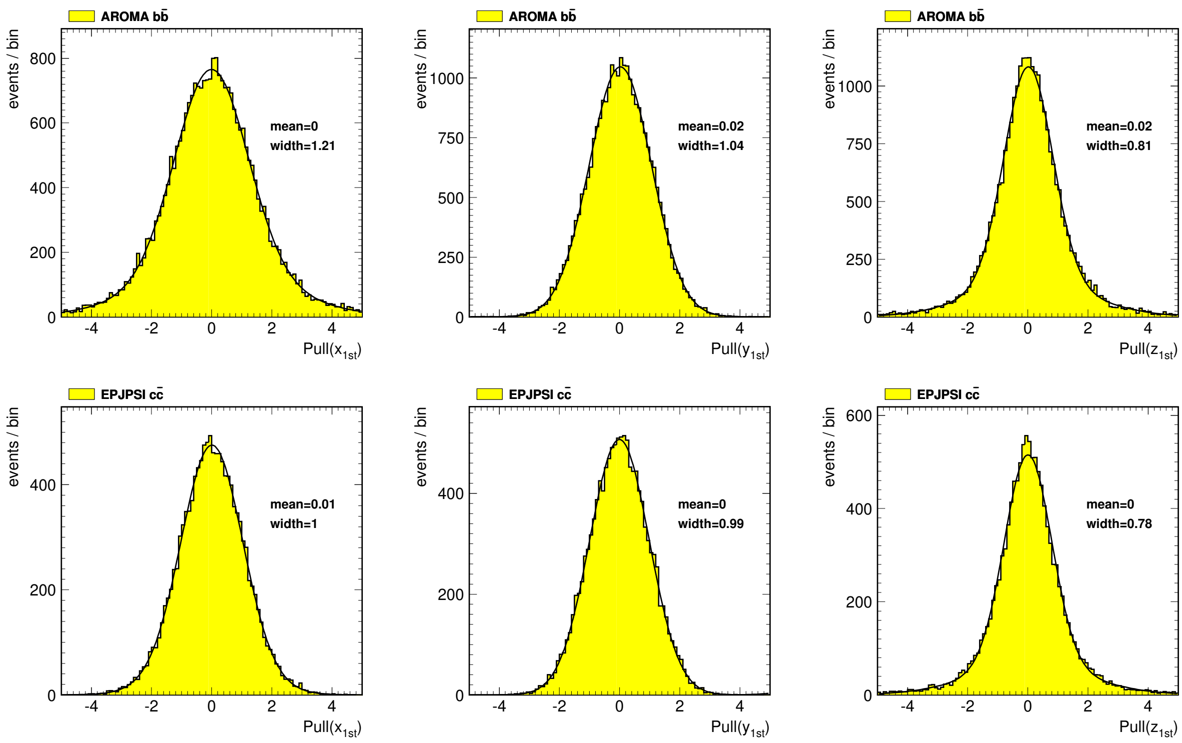

Figure 4.12: *Pull distributions of the primary vertex coordinates for the* `AROMA` $b\bar{b}$ *MC simulation (upper row) and* `EPJPSI` $c\bar{c}$ *MC (lower low). The three coordinates* x_{1st}, y_{1st} *and* z_{1st} *are displayed from left to right. All mean values are compatible with zero. Due to the intrinsic lifetime in the* `AROMA` $b\bar{b}$ *MC, particles from separated decay vertices spoil the primary vertex determination along the* x*–axis. This results in a larger width than unity. In the case of the* `EPJPSI` $c\bar{c}$ *MC, the width in* x *is nearly compatible with unity. In the* y*–direction the widths are compatible with unity, whilst along the* z*–direction the outlayer rejection of the primary vertex algorithm biases the pull distribution*

4.6 The Decay Length

The decay length is the measure of the distance between the primary (*1st*) and the decay vertex and is calculated in the $r\phi$–plane only: $\vec{L}_{r\phi} = \vec{V}_{\mathrm{1st}} - \vec{V}_{\mathrm{decay}}$. The coordinates of the decay vertex $\vec{V}_{\mathrm{decay}} = (x, y)_{\mathrm{decay}}$ are taken from the corresponding result of the three–dimensional linking. The primary vertex coordinates $\vec{V}_{\mathrm{1st}} = (x, y)_{\mathrm{1st}}$ are calculated event–wise as described in Section 4.5.

Due to the finite detector resolution, the one–dimensional distances $\Delta x = x_{\mathrm{1st}} - x_{\mathrm{decay}}$ and $\Delta y = y_{\mathrm{1st}} - y_{\mathrm{decay}}$ are not necessarily exactly zero for a zero–lifetime sample (Figure 4.13). Since the detector acceptance and the physics involved are invariant under rotations about the z–axis, they must be compatible with zero within errors. This is indeed the case as can be seen from the small values of the enclosing Gaussian best–fit. Two different and independent vertices give on average the same result. No systematical shift is observed which might bias the overall decay length calculation. The width of this distribution gives an estimate for the resolutions along the x– and y–directions of $\sigma(\Delta x) = 150\,\mu$m

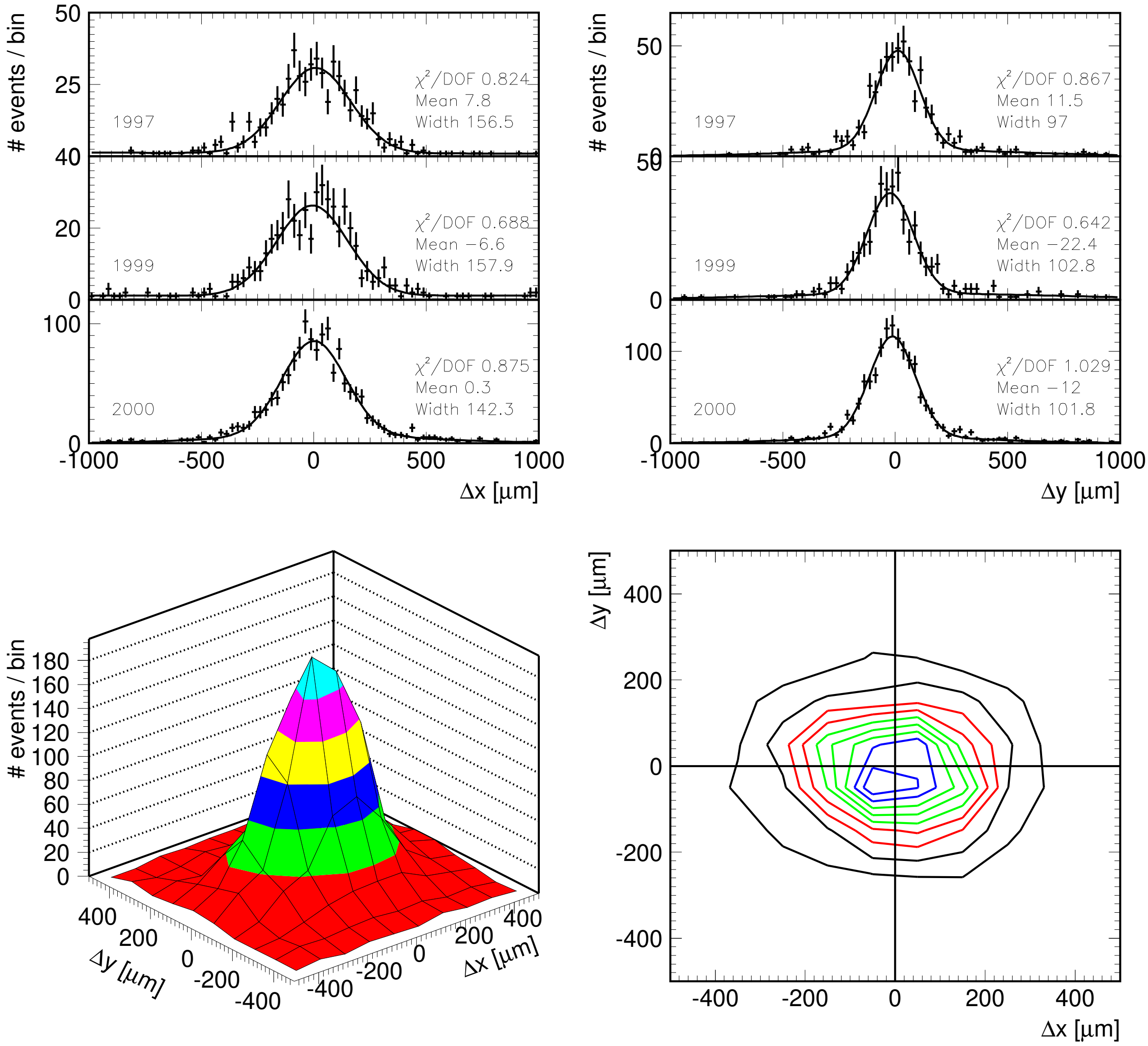

Figure 4.13: *Shown in the upper row are the one–dimensional distances between primary and decay vertices, Δx (left) and Δy (right), separately for the e^+p data of 1997, 1999 and 2000 (without trigger requirements). The values for the decay vertex are taken from the cluster linking method using the Kalman vertexing algorithm. A best–fit of a double–Gaussian curve is indicated by the solid line, where the $\chi^2/D.O.F$, mean and width values are from the tighter Gaussian. Both distributions are — within the precision of the CST — compatible with zero. The two–dimensional correlation of Δx and Δy is shown in the lower row in 3D (left) and as a contour plot (right).*

		x–direction [μm]	y–direction [μm]
One–dimensional distance	$\langle\Delta\rangle$	150	101
Primary vertex error	$\langle\sigma(1^{\mathrm{st}})\rangle$	97	35
Squared difference	$\sqrt{\langle\Delta\rangle^2 - \langle\sigma(1^{\mathrm{st}})\rangle^2}$	114	95
Decay vertex error	$\langle\sigma(\mathrm{decay})\rangle$	~ 105	

Table 4.4: *Validation of the vertex reconstruction. The squared difference of the mean primary vertex error (cf. Figure 4.11, open histogram) and of the averaged one–dimensional distance (cf. Figure 4.13, top row) agrees with the average decay vertex resolution. The remaining deviation is due to the limited precision of the vertex determination (cf. mean values of Figure 4.13, top row). The values are given for the cluster linking method using the Kalman vertexing algorithm. In the case of the other linking / vertexing combinations, the values are comparable.*

and $\sigma(\Delta y) = 100\,\mu$m respectively. Since the beam spot is much narrower in y, $\sigma(\Delta y)$ reflects essentially the decay vertex resolution, while $\sigma(\Delta x)$ is a squared sum of the decay and primary vertex resolutions (Table 4.4).

From the combination of the decay topology and the kinematics (cf. Figure 4.1), the signed decay length can be defined as

$$L_{r\phi} \equiv |\vec{L}_{r\phi}| \cdot \mathrm{sign}(L_{r\phi}) = \sqrt{\Delta x^2 + \Delta y^2} \cdot \mathrm{sign}(L_{r\phi}), \tag{4.19}$$

with the sign

$$\mathrm{sign}(L_{r\phi}) \equiv \mathrm{sign}\left[\frac{\vec{L}_{r\phi} \cdot \vec{p}_{t,J/\psi}}{|\vec{L}_{r\phi}||\vec{p}_{t,J/\psi}|}\right] = \mathrm{sign}\Big[\cos\left(\phi_{\vec{L}_{r\phi}} - \phi_{J/\psi}\right)\Big] \tag{4.20}$$

and $\vec{p}_{t,J/\psi} = (p_t, \phi)_{J/\psi}$ denotes the transverse track parameters of the J/ψ candidate.

For a zero–lifetime sample, the signed decay length reproduces the detector resolution as in the one–dimensional cases mentioned above. The reconstructed decay length distribution is described by two Gaussian distributions, $G(\Delta x)$ and $G(\Delta y)$, and the phase–space factor $2\pi L_{r\phi}$. The probability $d\mathcal{P}$ of finding an event within $[L_{r\phi}, L_{r\phi} + dL_{r\phi}]$ is given by

$$\frac{d\mathcal{P}}{dL_{r\phi}} = 2\pi L_{r\phi} \cdot \frac{d^2\mathcal{P}}{dx\,dy} \tag{4.21}$$

$$= 2\pi L_{r\phi} \cdot G(\Delta x) \cdot G(\Delta y) \tag{4.22}$$

$$\approx 2\pi L_{r\phi} \cdot G(L_{r\phi}), \tag{4.23}$$

where the resulting Gaussian distribution is defined as

$$G(L_{r\phi}) = \frac{1}{\sqrt{2\pi} \cdot \sigma(L_{r\phi})} \cdot \exp\left(-\frac{1}{2}\left[\frac{L_{r\phi}}{\sigma(L_{r\phi})}\right]^2\right). \tag{4.24}$$

As long as $\sigma(\Delta x) \approx \sigma(\Delta y)$, Equation (4.23) is valid and the error $\sigma(L_{r\phi})$ is equal to $\sigma(\Delta x, y)$. The argument of the exponential function defines the *significance* $S = L_{r\phi}/\sigma(L_{r\phi})$.

A deviation at positive significances from the symmetry of this distribution $d\mathcal{P}/dL_{r\phi}$ indicates events with lifetime, e.g. with beauty–flavour. Since the average values for the transverse boost in photoproduction and the lifetime are $\beta_t\gamma \approx 0.7$ and $c\tau = 466\,\mu$m (cf. Section 1.2.4) the average decay length is $\langle L_{r\phi}\rangle = \beta_t\gamma \cdot c\tau \approx 326\,\mu$m. The experimental decay length resolution is better than $150\,\mu$m. Dominant contributions from the decay of b–flavoured hadrons are, therefore, expected at significances around $S \approx 2$. At higher significances the available statistics decreases, since the decay length is exponentially distributed and the main fraction of events are expected at low decay lengths.

The decay length has been calculated for those events which passed the event and trigger selection (cf. Chapter 3) and where an improved linking method succeeded (Figure 4.14, data points). Neither the decay length nor the significance distribution shows a significant asymmetry (cf. Figure 4.14, left column). After restricting the sample to the régime where beauty–flavoured events are expected, i.e. at low inelasticities $0.1 < z < 0.5$ and within the invariant mass window $2.9\,\mathrm{GeV/c^2} < m_{\mu\mu} < 3.3\,\mathrm{GeV/c^2}$, an excess at positive decay lengths (or significances) becomes clearly visible (dark shaded histogram; scaled up for comparison in the light shaded histogram). This corresponds to an excess at positive signs (cf. Figure 4.14, lower right corner). The error on the decay length is of order $\mathcal{O}(130\,\mu\mathrm{m})$ (cf. Figure 4.14, upper right corner) as expected from the one–dimensional distributions in Figure 4.13.

A quantitative evaluation follows in the next chapter.

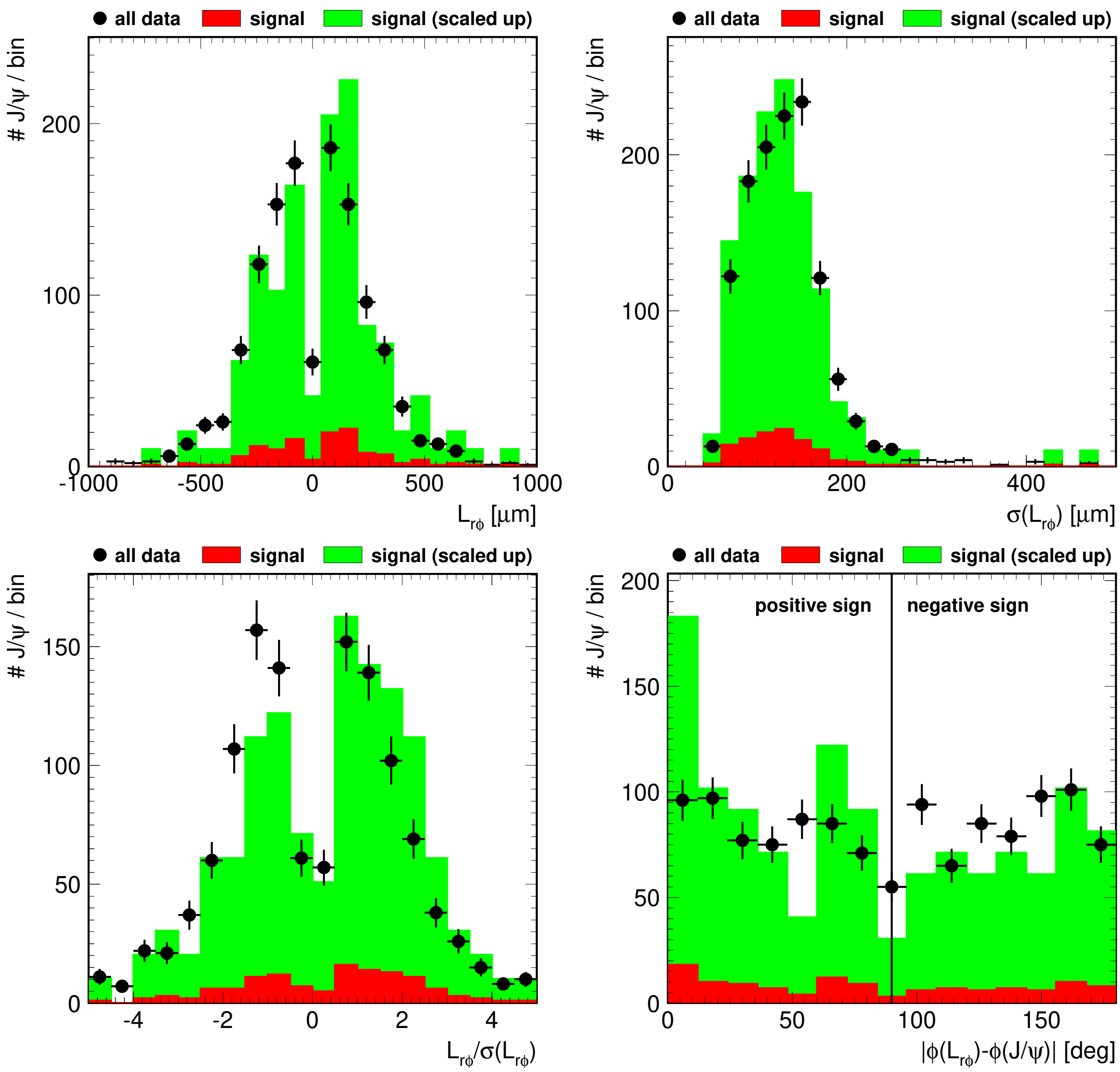

Figure 4.14: *The decay length has been calculated for the e^+p data from 1997, 1999 and 2000. The events must have fulfilled the selection and trigger criteria described in Chapter 3 and, here, the cluster linking method using the Kalman vertexing algorithm must have been succeeded. The distribution shows no asymmetry (upper left corner). The dark shaded histogram represents only J/ψ candidates at low–z, within $2.9\ GeV/c^2 < m_{\mu\mu} < 3.3\ GeV/c^2$ and with a combination of unlike charged muons. For comparison, the shaded histograms have been scaled up (light shaded histogram). An asymmetry is evident. The dip at $L_{r\phi} = 0$ is a consequence of the phase–space factor. The error of the decay length is displayed in the upper right corner. The significance $S = L_{r\phi}/\sigma(L_{r\phi})$ shows the same features as the plain decay length distribution: symmetric for the whole sample and asymmetric for the selected J/ψ candidates (lower left corner). The correlation between the decay length vector $\vec{L}_{r\phi}$ and the J/ψ candidate in the azimuthal angle is shown in the lower right corner.*

Chapter 5

Determination of the Beauty Production Cross Section

Beauty–flavoured hadrons have relatively large lifetimes, which produce an asymmetric decay length distribution in the event decay topology (Chapter 4). Since only events with beauty–flavour can lead to such an asymmetry, the fraction of J/ψ mesons from the decay of b–flavoured hadrons to all the produced J/ψ mesons is proportional to the ratio of the beauty cross section to the summed J/ψ meson production cross sections.

A log–likelihood fit to nine of twelve possible kinematical regions is performed to extract the number of b–flavoured events (Section 5.1). Eight regions are used to control the background distribution and to determine the resolution function. Events with an excess at positive significances are only expected in the region at low z, with an unlike charge combination of the muon candidates, and with an invariant mass near the nominal J/ψ meson's mass. The fraction of b–flavoured events is derived in Section 5.2. From their number the beauty production cross section is calculated and the systematic error is estimated (Section 5.3). Finally, in Section 5.4, the b–subtracted, i.e. *direct* J/ψ production cross section is determined and compared to the predictions of the Colour–Singlet and Colour–Octet calculations. The contribution from $B\bar{B} \to J/\psi X$ is discussed.

5.1 Tagging Events with Beauty–Flavour

The J/ψ mesons arising from a b–flavoured meson decay are kinematically restricted to contribute to J/ψ production only at low inelasticities, i.e. at $0.1 < z < 0.5$ (cf. Section 1.2.4). At higher inelasticities, at $0.5 < z < 0.95$, and in the elastic domain, J/ψ mesons decay promptly nearly without exception. Furthermore, neither non–resonant background (*mass sidebands*) nor like–sign charge combinations should contain any lifetime information. Consequently only events at low–z, with invariant masses inside a certain window around the nominal J/ψ meson's mass, i.e. $3 \cdot \sigma(m_{\mu\mu})$, and with two unlike–sign charged muons contribute to the *signal region*. The remaining regions define the *background* regions.

All events which have fulfilled the selection criteria and the trigger conditions (cf. Chapter 3) and where an improved linking method succeeded (cf. Chapter 4) are divided into twelve samples according to these three criteria;

Inelasticity: The inelasticity is separated into three regions, i.e. $0.1 < z < 0.5$, $0.5 < z < 0.95$ and the elastic domain.

Mass: The invariant mass distribution is divided into two regions, within three standard deviations of the mass resolution around the nominal J/ψ meson mass, i.e. $2.9\,\mathrm{GeV/c^2} < m_{\mu\mu} < 3.3\,\mathrm{GeV/c^2}$, and outside this window in the two *sidebands* of equal widths.

Charge: Depending on the charge combination of both muons, two regions are defined: unlike–sign and like–sign charge combinations.

Usually these criteria are applied in the form of one–dimensional cuts to the data set in order to enrich the signal–to–background ratio. The most powerful additional cut — the requirement of large positive significances — can, however, not be made, since the major contribution is expected to be around $S \approx 2$ (cf. Section 4.6) and the statistics fade out very quickly towards higher significances (cf. Figures 5.6).

Instead a log–likelihood fit will be performed simultaneously to the significance distributions of all twelve samples. Only in the signal sample will an asymmetry towards positive significances be evident, while in the background samples the significance distributions should be strictly symmetric. Thus, the latter can be used to fix the background contribution to the signal region.

5.1.1 The Method of Minimum Log–Likelihood

Suppose a measurement of a random variable yields values x_i which are distributed according to some a–priori known probability function $\mathcal{P}(x_i|\vec{a})$. This probability function depends on some free parameters $\vec{a} = (a_1, \ldots, a_n)$.

The *method of maximum likelihood* is a technique for estimating the values of the parameters given a finite sample of data. One of the main advantages of this method is that no binning is necessary. The likelihood function is a product of the single probabilities of each measurement i,

$$L(\vec{a}) \equiv \prod_i \mathcal{P}(x_i|\vec{a}), \tag{5.1}$$

where its maxima with respect to the free parameters,

$$\frac{\partial L(\vec{a})}{\partial a_k} = 0 \quad \text{and} \quad \frac{\partial^2 L(\vec{a})}{\partial a_k^2} < 0 \quad \text{for all } k \in [1, n], \tag{5.2}$$

determine the best estimate for the parameters $\vec{a}$. A wrong assumption for the probability distribution will lead to incorrect results in the likelihood calculation. Usually, for simplicity, the minimum of the *log–likelihood* $[-\ln L(\vec{a})]$ is calculated, since the logarithm is a monotone function and does not move the positions of the maxima.

In the actual application for this analysis the global log–likelihood is defined as

$$-\ln L \equiv \sum_{\text{samples}} \sum_{i} \Big[-\ln \mathcal{P}(S_i) \Big], \tag{5.3}$$

where the sum runs over all twelve samples and S_i is a significance measure within the sample. To reject outlayers, only measurements with $|S_i| < 5$ are considered. Two ansätze for the probability function $\mathcal{P}(S_i)$ are made; $\mathcal{P}_{\text{res}}$ is assumed to describe the CST resolution, while the signal parameterization $\mathcal{P}_{\text{xs+res}}$ includes the excess at positive significances due to lifetime. Both parameterizations are normalized such that $\int_{-\infty}^{\infty} \mathcal{P}_{\text{xs+res}}(S)\ dS = 1$ and $\int_{-\infty}^{\infty} \mathcal{P}_{\text{res}}(S)\ dS = 1$.

The Resolution Function

The background distribution of the signed decay length is a result of the finite resolution of the CST and thus determines the *resolution function.* A symmetrical distribution is expected around zero, which is confirmed by the measurement (cf. open histograms of Figure 4.14). In addition a Kolmogorov–Smirnov(KS)–Test [145] supports equal distributions for positive and negative significances. The probabilities that positive and negative values of each sample obey the same distribution are at reasonably high values, i.e. above 5 %.

Consequently, the resolution function $\mathcal{P}_{\text{res}}$ is parameterized with two Gaussian distributions G_a and G_b, whereby the second Gaussian copes with the non–Gaussian distributed tails of the former, viz.

$$\mathcal{P}_{\text{res}}(S_i) \equiv |S_i| \cdot \Big[f_a \cdot G_a(S_i) + f_b \cdot G_b(S_i) \Big], \tag{5.4}$$

where

$$G_{a,b}(S_i) = \frac{1}{2 \cdot \sigma_{a,b}^2} \cdot \exp\left(-\frac{1}{2} \cdot \left[\frac{S_i}{\sigma_{a,b}} \right]^2 \right) \tag{5.5}$$

and f_a and $f_b = 1 - f_a$ are the fractions of the Gaussian contributions with $\sigma_{a,b}$ the corresponding widths. The leading factor $|S_i|$ is a phase space factor (cf. Equation 4.21). The mean values are fixed to zero. Altogether three free parameters f_a, σ_a and σ_b are used to describe the resolution function in the minimization procedure.

The Signal Parameterization

In the signal sample, an additional term is needed to take care of the exponential lifetime distribution at positive significances $S_i > 0$

$$\mathcal{P}_{\text{xs+res}}(S_i) \equiv \underbrace{f_{\text{res}}^{\text{bkg}} \cdot \mathcal{P}_{\text{res}}^{\text{bkg}}(S_i) + f_{\text{res}}^{\text{sig}} \cdot \mathcal{P}_{\text{res}}^{\text{sig}}(S_i)} + f_{\text{xs}} \cdot |S_i| \cdot \mu^2 \cdot \exp\left(-\mu \cdot S_i\right) \tag{5.6}$$

$$\mathcal{P}_{\text{xs+res}}(S_i) = f_{\text{res}} \cdot \mathcal{P}_{\text{res}}(S_i) + f_{\text{xs}} \cdot |S_i| \cdot \mu^2 \cdot \exp\left(-\mu \cdot S_i\right) \tag{5.7}$$

The second line holds under the assumption, that both resolution functions, those for the background and for the signal samples, are equal. This will be validated in Section 5.2.2.

For negative significances $S_i < 0$ only resolution effects should take place:

$$\mathcal{P}_{\text{xs+res}}(S_i) \equiv f_{\text{res}} \cdot \mathcal{P}_{\text{res}}(S_i) + 0. \tag{5.8}$$

The visible fraction of b–flavoured events (the *excess*) $f_{\text{xs}}=1 - f_{\text{res}}$ and the effective reciprocal significance μ give two more free parameters.

5.1.2 Result of the Log–Likelihood Minimization

The fraction of b–flavoured events in the signal sample is determined by minimizing the log–likelihood expression with respect to the aforementioned five free parameters. The results for both multi–hypothesis linking methods using each vertexing algorithm are listed in the upper half of Table 5.1. All methods are treated independently.

Within the errors from the fit procedure all methods are in reasonable agreement. A slight tendency to a smaller excess is obtained by the spacepoint linking. The average excess of $(17.6 \pm 8.3)\,\%$ is about two standard deviations away from a zero excess. The resulting signal functions give a reasonable description of the signal sample data points (Figure 5.1).

Method	$\boldsymbol{f_{\text{xs}}}$ [%]	μ	σ_a	σ_b	f_a [%]
Cluster +					
Kalman	**17.5 ± 8.7**	1.12 ± 0.23	0.90 ± 0.04	1.72 ± 0.08	0.59 ± 0.06
Least–Squares	**20.2 ± 8.1**	1.04 ± 0.18	0.89 ± 0.04	1.72 ± 0.07	0.55 ± 0.06
Spacepoint +					
Kalman	**15.8 ± 8.4**	1.11 ± 0.25	0.84 ± 0.04	1.71 ± 0.06	0.49 ± 0.05
Least–Squares	**16.9 ± 7.8**	1.05 ± 0.20	0.86 ± 0.04	1.73 ± 0.06	0.49 ± 0.05
w/o trigger selection					
Cluster +					
Kalman	**14.7 ± 5.4**	1.19 ± 0.17	0.89 ± 0.03	1.64 ± 0.04	0.57 ± 0.04
Least–Squares	**16.6 ± 5.0**	1.09 ± 0.14	0.89 ± 0.03	1.65 ± 0.04	0.54 ± 0.05
Spacepoint +					
Kalman	**12.7 ± 5.0**	1.17 ± 0.19	0.87 ± 0.03	1.72 ± 0.03	0.49 ± 0.03
Least–Squares	**11.7 ± 4.7**	1.07 ± 0.16	0.88 ± 0.03	1.71 ± 0.03	0.48 ± 0.03

Table 5.1: *The results for the free parameters of the log–likelihood fit separately for both linking methods using both vertexing algorithms. The log–likelihood minimization has been repeated discarding the trigger requirements (cf. lower half). These results are also given.*

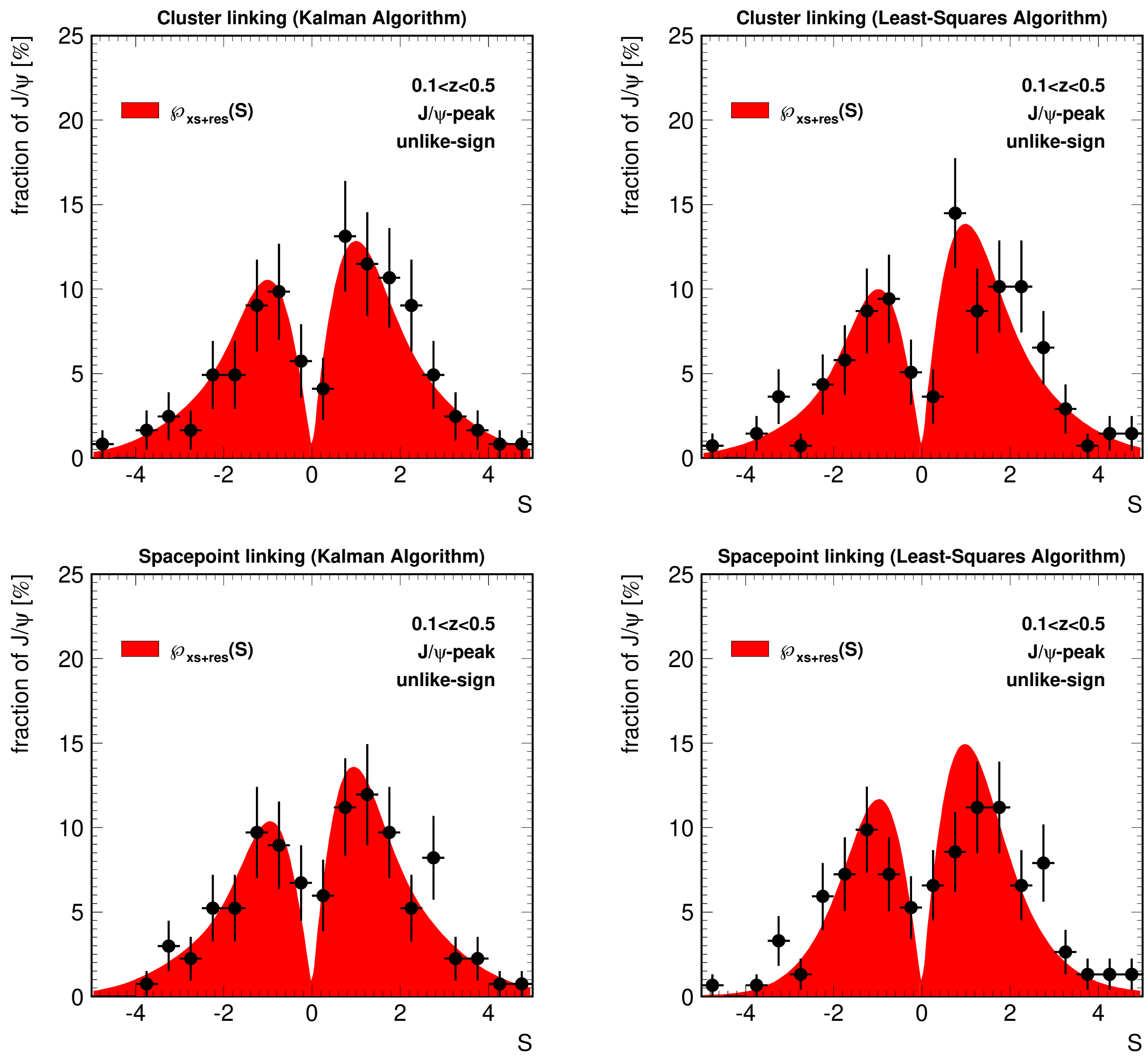

Figure 5.1: *Results of the log–likelihood fit for the cluster (top row) and space-point linking methods (lower row), separately for the Kalman (left column) and the least–squares vertexing algorithm (right column). The significance distribution in the signal sample (unlike–sign charge combination of the muon candidates, invariant mass of the J/ψ candidate within 2.9 GeV/c^2 $< m_{\mu\mu} <$ 3.3 GeV/c^2 and $0.1 < z < 0.5$) matches well with a result assuming an additional excess at positive significances to the resolution function, $\mathcal{P}_{\rm xs+res}$, (dark shaded).*

To decide whether this value is simply an upward fluctuation, the log–likelihood has been repeated under omission of the trigger requirements (Table 5.1, lower half). This increases the statistics slightly. The excess remains at an average value of $(13.9 \pm 5.0)\,\%$ — about three standard deviations above zero — and thus establishes the observation of a non–zero excess (Figure 5.2).

Performing the log–likelihood fit using the `AROMA` $b\bar{b}$ Monte Carlo simulation, the values for the excess are $(57.2 \pm 2.4)\,\%$ for the cluster linking method using the Kalman vertexing

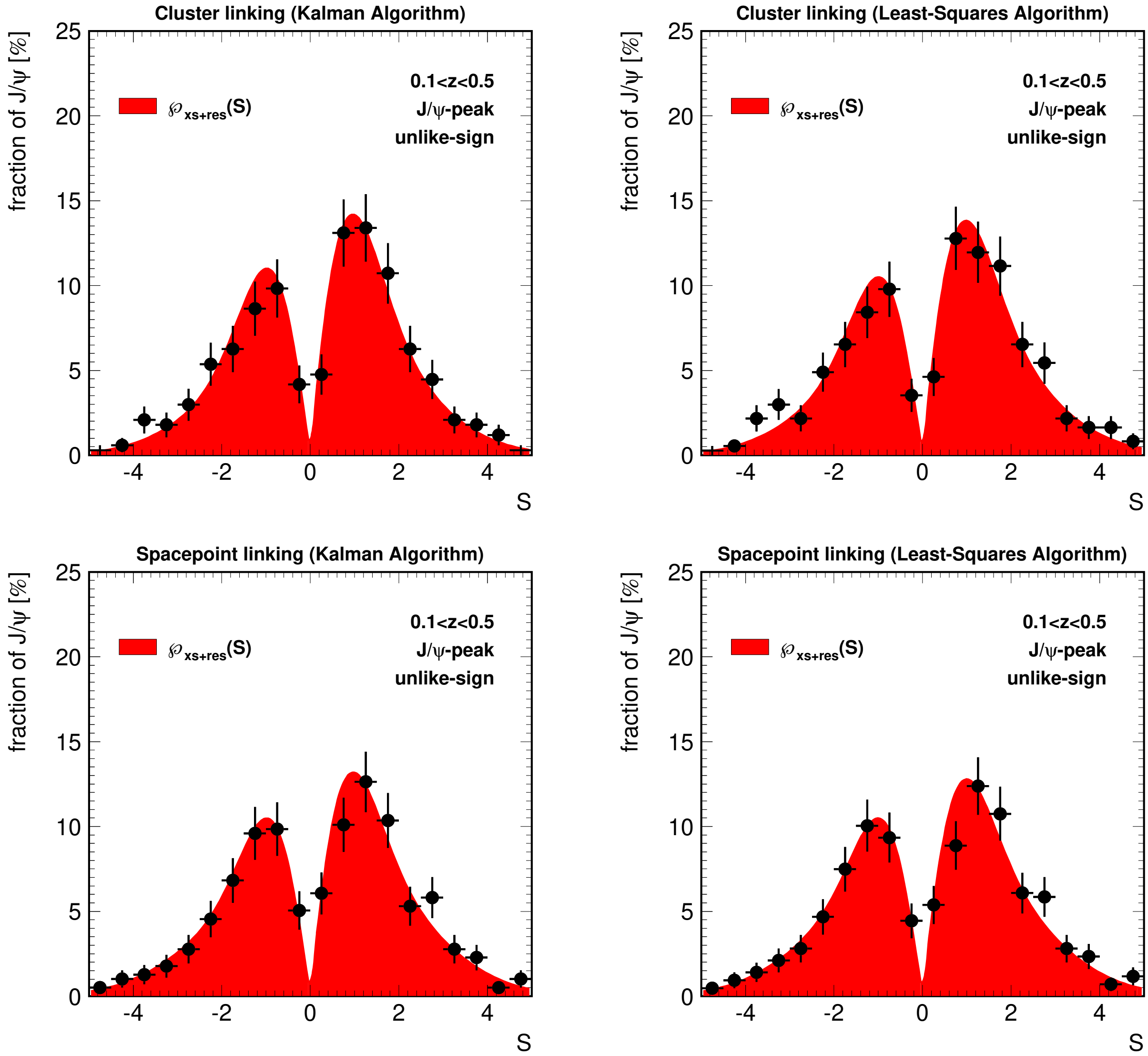

Figure 5.2: *Results of the log–likelihood fit for the cluster (top row) and spacepoint linking methods (lower row), separately for the Kalman (left column) and the least–squares vertexing algorithm (right column). In contrast to Figure 5.1 the trigger requirements have been discarded. The significance distribution in the signal sample matches well with a result assuming an additional excess at positive significances to the resolution function, $\mathcal{P}_{\rm xs+res}$, (dark shaded).*

algorithm and $(56.7 \pm 2.4)\,\%$ using the least–squares algorithm. For the spacepoint linking method, the results are $(57.2 \pm 2.3)\,\%$ and $(55.4 \pm 2.3)\,\%$ respectively. Their overall $2.2\,\%$ relative spread contributes to the systematic error. Since none of the methods is more sensitive than the others, their averaged result will be used to determine the fraction of beauty–flavoured events and, finally, the beauty production cross section.

5.1.3 Cross–Check with Prompt J/ψ Candidate Samples

The assumption of the behaviour of the probability function has a critical influence on the log–likelihood result. The resolution function $\mathcal{P}_{\rm res}$ and the signal parameterization $\mathcal{P}_{\rm xs+res}$ are therefore compared to the measurement using the cluster linking with the Kalman vertexing method. The five fit values are taken now and in the following from the log–likelihood minimization using the standard event selection (i.e. including the trigger selection). A good agreement in shape and normalization between the resolution function and eight of the eleven background samples is obtained (Figures 5.3 and 5.4). For the sake of completeness, the signal sample has (again) been displayed (Figure 5.3, top left corner). Neither of the background samples prefer an asymmetric distribution, however the statistics in the like–sign samples at higher inelasticities ($z > 0.5$) is rather low. Some samples have therefore been omitted.

More quantitatively, the compatibility of each data sample with any of the two distributions, $\mathcal{P}_{\rm xs+res}$ and $\mathcal{P}_{\rm res}$, has been determined using a χ^2–test. The compatibility with the signal distribution $\chi^2_{\rm xs+res}$/D.O.F. is better than with the background $\chi^2_{\rm res}$/D.O.F. only in the signal sample, i.e. values of 0.56 versus 0.90. The χ^2–test applied to each background sample and compared with the resolution function $\mathcal{P}_{\rm res}$ gave $\chi^2_{\rm res}$/D.O.F. –values of about unity.

Skipping some background samples in the log–likelihood fit, e.g. those with like–sign charge combinations or the elastic samples, does not change or remove the excess within the spread given in Table 5.1. An omission, however, reduces the accuracy of background determination. Furthermore, in a "blind–test", each of the eleven background samples has been assigned to the signal parameterization, while the signal sample is considered as background and, therefore, is only used in the determination of the resolution function. Thus every background sample is treated once as "signal". No excess was produced which was not compatible with zero within errors. In most of the cases, the minimization ignored the signal parameters $f_{\rm xs}$ and μ and converged using only the three background parameters.

5.2 The Fraction of Beauty–Flavoured Events

Since no background sample shows an excess, e.g. neither the mass sidebands nor the higher inelasticity regions, $z \gtrsim 0.5$, nor the like–sign charge combinations, the excess is interpreted as a genuine property — the beauty–flavoured fraction of the J/ψ candidates in the signal sample.

5.2.1 Number of Beauty–Flavoured Events

From the measured excess, the number of visible beauty–flavoured events can be calculated,

$$N^{\rm xs}_{b\bar{b}} = f_{\rm xs} \cdot N_{\rm events}\,, \tag{5.9}$$

where $N_{\rm events}$ denotes the number of events in the signal sample.

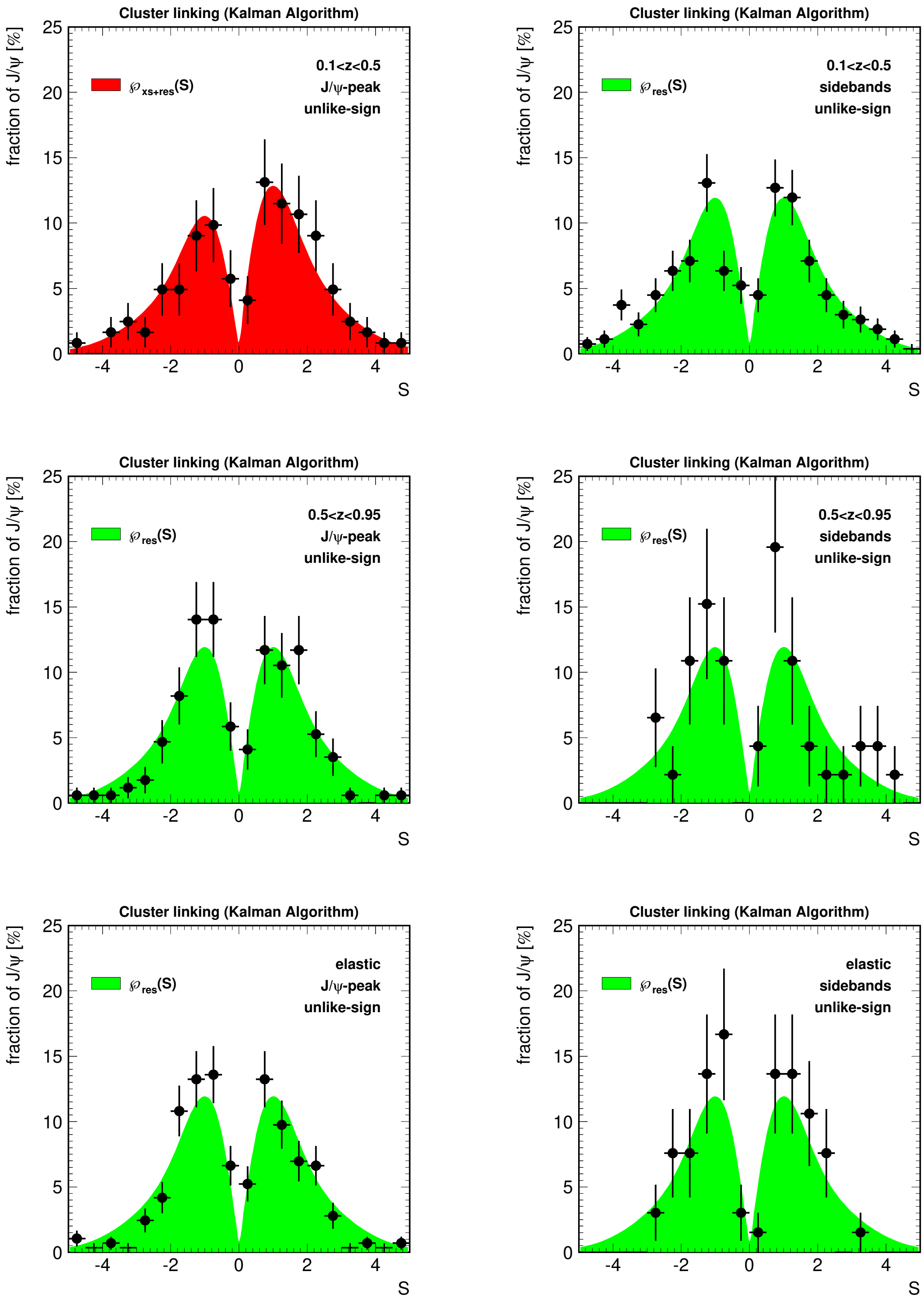

Figure 5.3: *Result of the log–likelihood fit for the samples with an unlike–sign charge combination of the muon candidates. Here the cluster linking method with the Kalman vertexing algorithm has been used. The three inelasticity regions are displayed from the upper row to lower row, $0.1 < z < 0.5$, $0.5 < z < 0.95$, and the elastic régime. The left (right) column represents the samples of J/ψ candidates with an invariant mass inside (outside) the interval $[2.9, 3.3]$ GeV/c^2. The distributions are compared to the log–likelihood fit results $\mathcal{P}_{\mathrm{xs+res}}$ (dark shaded) and $\mathcal{P}_{\mathrm{res}}$ (light shaded) respectively.*

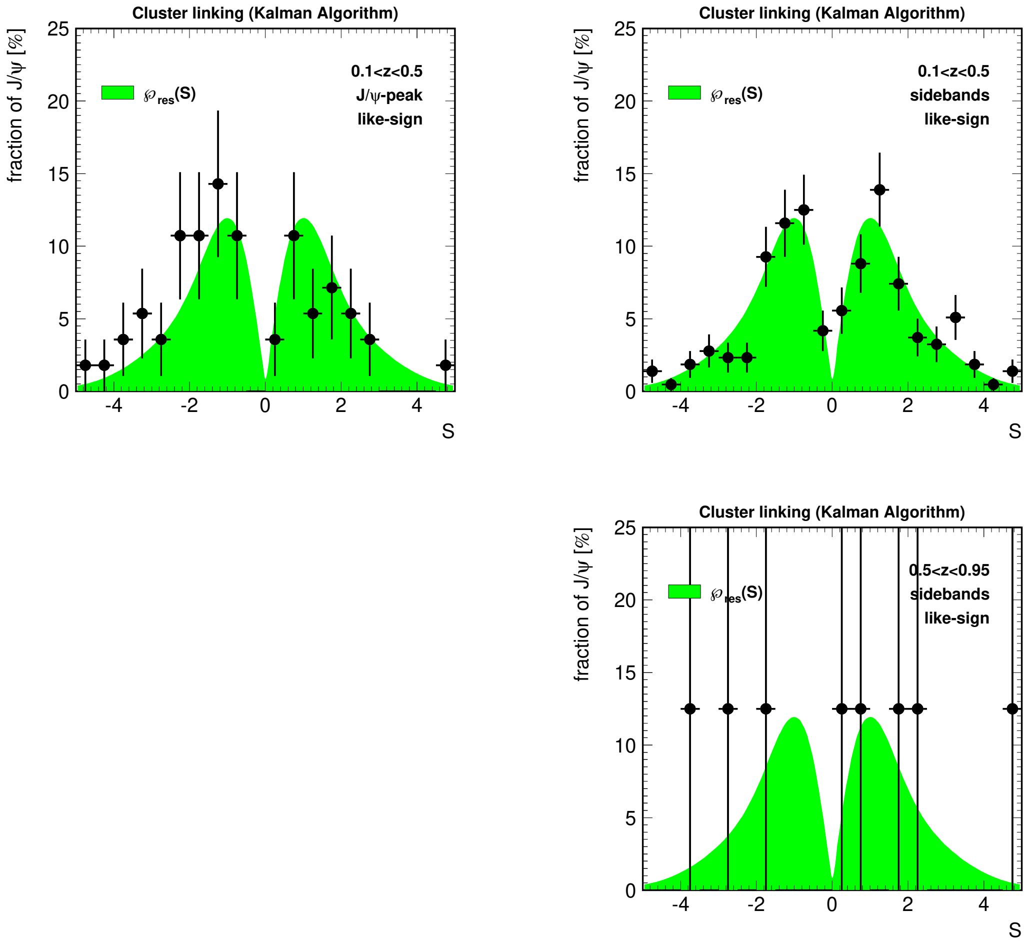

Figure 5.4: *Result of the log–likelihood fit for the samples with a like–sign charge combination of the muon candidates. Here the cluster linking method with the Kalman vertexing algorithm has been used. Only the inelasticity regions at* $0.1 < z < 0.5$ *(upper row) and at* $0.5 < z < 0.95$ *(lower row) are displayed. The left (right) column represents the samples of* J/ψ *candidates with an invariant mass inside (outside) the interval* $[2.9, 3.3]$ *GeV/*c^2*. The distributions are compared to the resolution function* $\mathcal{P}_{\mathrm{res}}$ *resulting from the log–likelihood fit (light shaded). Histograms without statistics are omitted.*

Alternatively, the number of visible beauty–flavoured events can be deduced from the number of J/ψ mesons with significances above $N_+ \equiv N\big|_{S_i>0}$ and below $N_- \equiv N\big|_{S_i<0}$ zero (Figure 5.5). The difference $N_+ - N_-$ in the numbers of J/ψ mesons obtained from a best–fit Gaussian curve to the invariant mass spectra agrees within errors with the number of b–flavoured events (Table 5.2) obtained from the log–likelihood minimization. Their sum gives about the same total number of J/ψ mesons as found in the signal sample (cf. Table 5.3). Due to the low statistics the fits to the invariant mass distributions must be handled with care. The peak position and the mass resolution, therefore, have been taken from the fit to all events at low z (Figures 4.6 and 4.7). The log–likelihood fit, however, slightly improves the result in terms of the error. In the following the number of beauty–flavoured events determined with the log–likelihood minimization is used.

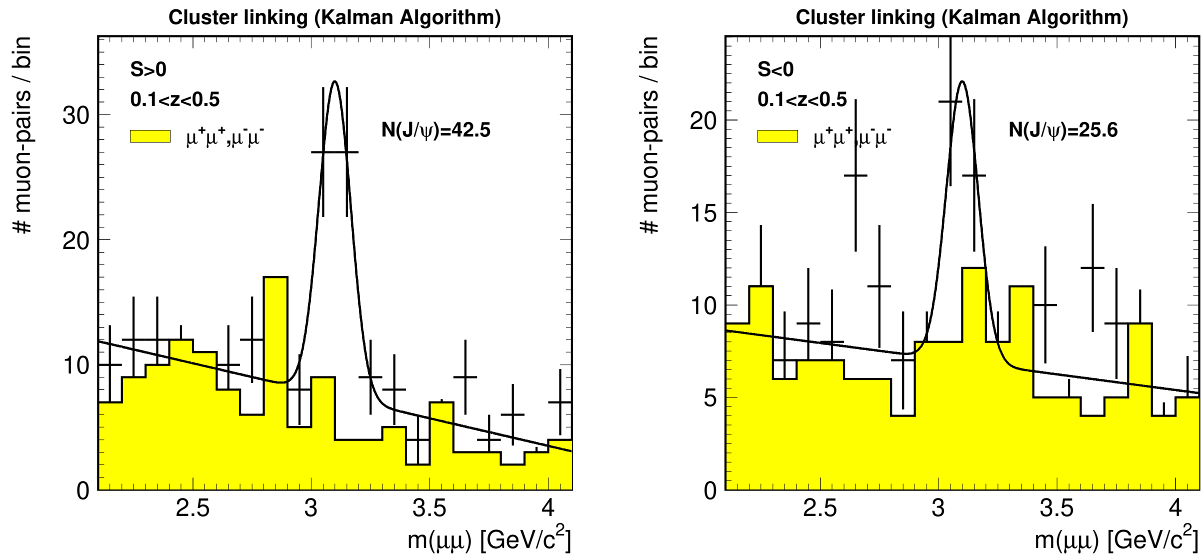

Figure 5.5: *Invariant mass distributions of J/ψ meson candidates with positive (left) and negative significances (right). Here, the cluster linking method with the Kalman vertexing algorithm has been used. A best–fit curve of a Gaussian, where the peak position and the width have been fixed according to the fit results at low–z from Figure 4.6, plus a straight line determines the number of J/ψ mesons. Like–sign muon combinations are indicated by the shaded histograms.*

5.2.2 Total Fraction of Beauty–Flavoured Events

The fraction of beauty–flavoured events to all J/ψ mesons in the signal sample is calculated as follows;

$$f_{b\bar{b}} \equiv \frac{N_{b\bar{b}}}{N_{J/\psi}}, \qquad \text{where} \qquad N_{b\bar{b}} = \frac{N_{b\bar{b}}^{\mathrm{xs}}}{(1 - 2 \cdot \mathcal{M}_S)}. \tag{5.10}$$

The number of J/ψ meson candidates $N_{J/\psi}$ are obtained from a Gaussian fit to the invariant mass spectrum at low inelasticity values (cf. Figures 4.6 and 4.7, but with additional trigger requirements).

Method	N_+	N_-	$N_+ + N_-$	$N_+ - N_-$	$N_{b\bar{b}}^{\mathrm{xs}}$
Cluster +					
Kalman	42.5 ± 8.2	25.6 ± 6.9	68.1 ± 10.7	16.9 ± 10.7	21.4 ± 10.8
Least–Squares	46.8 ± 8.6	23.5 ± 6.9	70.3 ± 11.0	23.3 ± 11.0	27.9 ± 11.5
Spacepoint +					
Kalman	44.9 ± 8.7	24.0 ± 7.2	68.9 ± 11.3	20.9 ± 11.3	21.2 ± 11.4
Least–Squares	51.6 ± 9.2	26.6 ± 7.4	78.2 ± 11.8	25.0 ± 11.8	25.7 ± 12.1

Table 5.2: *Number of beauty–flavoured events as deduced from the invariant mass spectra of J/ψ mesons with positive (N_+) and negative significances (N_+) and from the log–likelihood fit.*

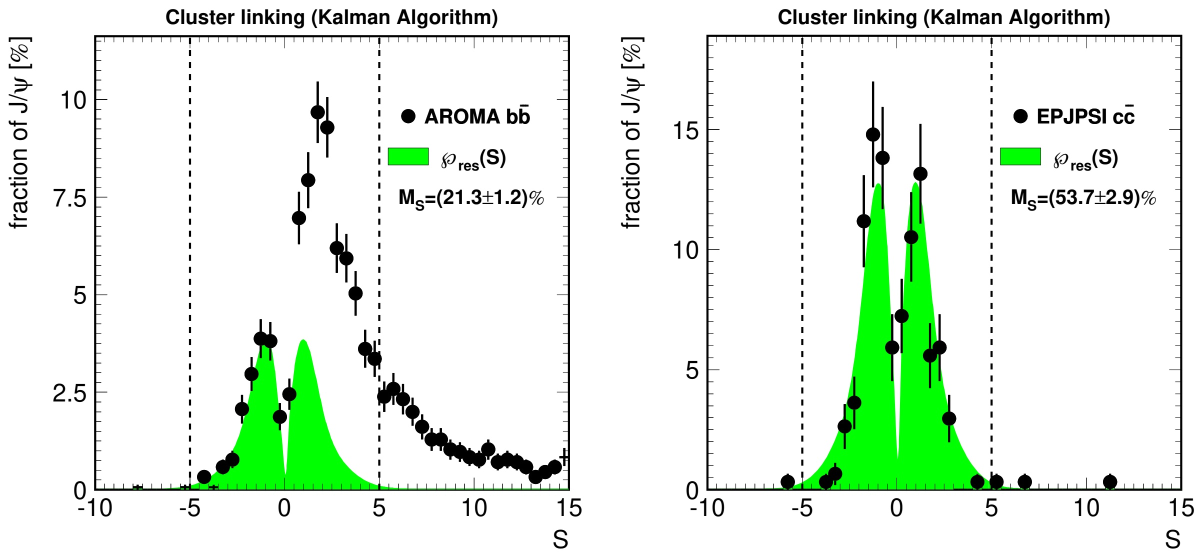

Figure 5.6: *Significance distribution for all selected events of the* `AROMA` $b\bar{b}$ *Monte Carlo simulation (left) and* `EPJPSI` $c\bar{c}$ *MC (right). Both simulations are normalized to unity and compared to the resolution function* $\mathcal{P}_{\rm res}$ *taken from data. The fraction of MC events with* $S < 0$ *of all events within* $|S| < 5$ *is given as a migration factor. The window is indicated by the vertical line.*

Due to the finite detector resolution, some b–flavoured events with small genuine decay lengths can appear at negative significances (as accounted for in Equation 5.6). The factor $\mathcal{M}_S$ considers those events which migrated to negative significances and contributed, therefore, to the background distribution. The background function therefore also includes a fraction $2 \cdot \mathcal{M}_S$ of beauty–flavoured events. This fraction is determined using the `AROMA` $b\bar{b}$ Monte Carlo simulation. The significance distributions after all selection requirements are shown in Figure 5.6 for both Monte Carlo simulations. Only in the `AROMA` $b\bar{b}$ MC simulation does an excess due to inherent lifetime becomes visible at positive significances, whilst in the case of the prompt J/ψ production (`EPJPSI` $c\bar{c}$ MC) the significance distribution is clearly symmetric.

Both distributions are normalized to unity and compared to the resolution function $\mathcal{P}_{\rm res}$, which has been obtained from data (cf. Section 5.1.2). The fit functions are adjusted such that the integral $\int_{-\infty}^{0} \mathcal{P}_{\rm res}\, dS$ equals the fraction of Monte Carlo events with $S < 0$. The agreement using the `EPJPSI` $c\bar{c}$ Monte Carlo simulation is very good, despite the discrepancies in the tails. Here non–Gaussian distributed resolution effects take place which are not included in the simulations. A similar agreement is found with the `AROMA` $b\bar{b}$ MC at negative significances. Thus the assumption of a consistent description of the resolutions in the `AROMA` $b\bar{b}$ and `EPJPSI` $c\bar{c}$ Monte Carlo simulations used to derive Equation (5.7) is reasonable. The shape of the CST resolution function in the simulations is confirmed by those obtained from genuine background.

The average fraction of beauty–flavoured events which migrated to negative significances to all b–flavoured events inside the significance window of $-5 < S < 5$ is $\mathcal{M}_S = (21.5 \pm 1.2)\,\%$ for the `AROMA` $b\bar{b}$ Monte Carlo simulation. In the case of the `EPJPSI` $c\bar{c}$ MC this value is $(52.1 \pm 2.8)\,\%$ and, since no excess is evident, in agreement with the expectation of 50 %. These fractions are — within the statistical errors — independent of the linking methods and the vertexing algorithms.

The Measured Fraction of Beauty–Flavoured Events

The resulting values for the total fraction of beauty–flavoured events selected from 1997 to 2000 e^+p data are shown in Table 5.3 for both linking methods and both vertexing

Method	f_{xs} [%]	N_{events}	$N_{J/\psi}$	$f_{b\bar{b}}$ [%]
Cluster + Kalman	17.5 ± 8.7	122	67.6 ± 11.0	55.1 ± 29.4
+ Least–Squares	20.2 ± 8.1	138	75.4 ± 12.0	64.8 ± 28.6
Spacepoint + Kalman	15.8 ± 8.4	134	88.0 ± 14.5	42.0 ± 23.8
+ Least–Squares	16.9 ± 7.8	152	100.0 ± 15.7	45.9 ± 22.8
Mean				$\mathbf{52.0 \pm 26.2 \pm 7.7}$

Table 5.3: *Fraction of b–flavoured events $f_{b\bar{b}}$ in the signal region together with their statistical errors. The mean values are given in the last row, where the first error denotes the statistical and the second the systematical uncertainty.*

algorithms. The average value for the fraction of b–flavoured events from all inelastically $(0.1 < z < 0.5)$ produced J/ψ mesons is

$$\boxed{f_{b\bar{b}} = \left[52.0 \pm 26.2(\text{stat.}) \pm 7.7(\text{syst.})\right]\,\%}$$

where the first error gives the statistical uncertainty and the second, systematic error is obtained from the spread of the results of the single methods. The number of J/ψ mesons $N_{J/\psi}$ agrees with those determined in Section 5.2.1 (cf. Table 5.2).

Within the large uncertainties, the resulting fraction $f_{b\bar{b}}$ is in agreement with a previously performed Monte–Carlo estimation of 28.2 % [94][1]. It should be stressed, however, that this fraction strongly depends on the basic event and J/ψ meson selection. The presented data selection (cf. Chapter 3) follows generally the standard procedure for inelastic J/ψ meson analyses within the H1 collaboration. Nevertheless any remaining differences of the selection in detail, i.e. the requirement of CST hits, might lead to larger fractions. Note that the aim of this analysis is the determination of the beauty production cross section.

[1] The here underlying beauty production cross section has been taken from [17]. The corresponding erratum [65] has scaled up the cross section by a factor of 2.1. This has been corrected for.

5.2.3 Discussion of Other Sources for an Excess

Measurable decay lengths at HERA are only expected for strange and heavy hadron decays. In addition to the already discussed b–flavoured hadron decays into J/ψ mesons, any of these hadrons might contribute to an excess at positive decay lengths.

Strange hadrons, e.g. kaons, are produced in various processes outnumbering events with J/ψ mesons (from b–flavoured decays). Any accidental reconstruction of kaons as muon candidates giving fake J/ψ mesons is expected to be independent of the reconstructed invariant mass. Since no excess in the significance distribution is observed in the case of the mass sideband samples, it is very unlikely that strange hadron decays contribute to the excess in the signal region.

Heavy quarks, precisely the semi–muonic decays of heavy hadrons $Q \to \mu X$, $Q \in \{c, b\}$, have branching ratios of the order of 10 % — one magnitude larger than the beauty–flavoured decay into a J/ψ meson. Heavy quark decays into a muon of minimum transverse momentum $p_t(\mu) > 1.6\,\mathrm{GeV/c}$ are studied using the `AROMA 2.2` event generator (cf. Section 1.4.1). At least one heavy quark must decay semi–muonically. Direct decays into a J/ψ meson are discarded. The momentum requirement enriches events with larger genuine decay lengths. Samples of about $1983\,\mathrm{pb}^{-1}$ and $19.5\,\mathrm{pb}^{-1}$ integrated luminosity from the $b \to \mu X$ and $c \to \mu X$ decay channels, respectively, were analyzed.

After applying the full data selection no indication of a J/ψ meson resonance has been found. All J/ψ meson candidates turn out to be fake. The significance distributions in

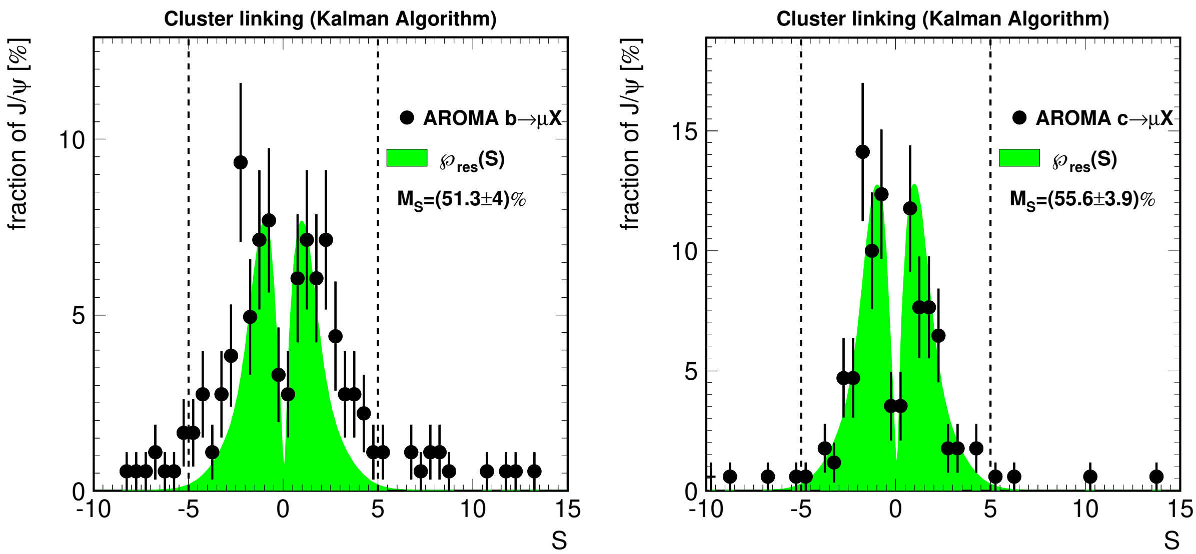

Figure 5.7: *Significance distribution for all selected events of two* `AROMA` *Monte Carlo simulations producing events with semi–muonic decays of heavy quarks, $b \to \mu X$ (left) and $c \to \mu X$ (right). Both simulations are normalized to unity and compared to the resolution function $\mathcal{P}_{\mathrm{res}}$ taken from data. The fraction of MC events with $S < 0$ of all events within $|S| < 5$ is given as a migration factor. The window is indicated by the vertical line.*

the signal region do not show any evidence for an excess at positive values (Figure 5.7). Both migration factors are compatible with a symmetric distribution (i.e. 50 %).

The distribution of the semi–muonic b–flavoured hadron decay (cf. Section 5.7, left) is somewhat broader than the resolution function $\mathcal{P}_{\mathrm{res}}$, which indicates the presence of a genuine life–time. At least one muon stems from a b–flavoured hadron, which might decay a measurable distance away from the primary vertex. The combination of this muon with any other particle mis–identified as a muon and thus leading to a wrongly reconstructed J/ψ meson candidate still gives a well separated decay vertex, independent of the origin of the second particle. The measured decay length is, therefore, on average larger than for zero–lifetime samples. Since the fake J/ψ candidate and the decay length are uncorrelated, no asymmetry in the decay length distribution is, however, expected — and observed.

Only about five events from the semi–muonic beauty–flavoured hadron decay per 56.1 pb^{-1} have passed the data selection and emerge in the signal region, while about 30 events contribute at low z to the background samples. Thus a general bias to the log–likelihood result can be neglected.

5.3 The Beauty Production Cross Section

From the number of beauty–flavoured events, the beauty production cross section in photoproduction can be determined. Firstly the visible cross section is determined and afterwards extrapolated to the full phase space. Beforehand, the systematic errors are reviewed and completed.

5.3.1 Systematic Errors

The major errors come from the statistical uncertainty. Throughout the analysis chain, however, several systematical uncertainties enter, which are listed in Table 5.4. Most uncertainties have been determined in the previous sections and chapters, therefore only their reference is given. Since the extrapolation to the full phase space depends strongly on the underlying theoretical model, i.e. on the Monte Carlo simulation, and on the branching ratio, the uncertainties arising due to this are treated in an additional *extrapolation* error (Table 5.5).

The error on the luminosity and on the branching ratio only affect the normalization. Their relative uncertainties are taken from [34] and [125] respectively. The beam energies differ for the 1997 and 1999 / 2000 data periods. Since the luminosity comes mainly from the latter period, the cross sections are given for a center–of–mass energy of $\sqrt{s} \approx 318\,\mathrm{GeV}$. The error entering through this is 2.6 % and results from the luminosity weighted beam energies, the cross sections scaling linearly with the beam energies.

The uncertainty in the extrapolation to the full phase space has been estimated from the prediction of the `AROMA` $b\bar{b}$ and `CASCADE` $b\bar{b}$ Monte Carlo simulations. The acceptance

Source	$ep \to b\bar{b}X$ [%]	$ep \to J/\psi X$ [%]	Reference
Luminosity	1.5	1.5	[125]
Different beam energies	+2.6	+2.6	Section 5.3.1
Muon identification	5.3	3.8	Section 3.5.1
Track reconstruction	4.0	4.0	Section 3.5.2
L1 track trigger efficiency	4.3	4.5	Section 3.6.1
L1 muon trigger efficiency	3.8	3.5	Section 3.6.1
L2 neural net efficiency	3.3	1.9	Section 3.6.1
L4 efficiency	2.0	2.0	Section 3.6.1
Subtotal (w/o CST)	10.0	8.9	
CST acceptance	4.5	4.9	Section 4.1.1
CST 4/4 efficiency (incl. 3D vertex fit)	15.3	15.3	Section 4.4.2
Variation of the excess f_{xs}	2.2	2.2	Section 5.1.2
Total systematic error	18.9	18.5	

Table 5.4: *Sources of systematic errors. The corresponding references are given in the last column. The total errors result from the quadratic sum.*

deduced from the `AROMA` $b\bar{b}$ MC was 49.2 % (cf. Section 1.4.3). The visible and total cross section predictions from the `CASCADE` MC of 3.95 pb and 5.73 nb [146] respectively lead to an acceptance of 50.8 % (cf. Equation 5.12). The relative deviation of 3.3 % is treated in an extra term to the systematic error, the *extrapolation error*, which also includes the uncertainty in the branching ratios. This uncertainty might be larger, if more extreme choices of the free parameters (e.g. parton densities, scales or quark masses; cf. Section 1.2.2) are applied to determine the extrapolation factor.

In the case of the `EPJPSI` $c\bar{c}$ Monte Carlo simulation, the uncertainty due to the extrapolation has been estimated by studying different parton density functions for the direct and resolved processes [94]. This gives a contribution to the extrapolation error of 5 %.

All systematic errors are treated independently of each other. The quadratic sum of all relative errors determines the relative uncertainties in the measured cross sections.

Source	$ep \to b\bar{b}X$ [%]	$ep \to J/\psi X$ [%]	Reference
Branching ratio	8.7	1.7	[34]
Acceptance	3.3	5.0	Section 5.3.1
Extrapolation error	9.3	5.3	

Table 5.5: *Sources for the extrapolation error. The corresponding references are given in the last column. The total errors result from the quadratic sum.*

5.3.2 The Visible Beauty Production Cross Section

The visible range comprises photoproduction events ($Q^2 < 1\,\mathrm{GeV}^2$) with photon–proton center–of–mass energies $W_{\gamma p} > 100\,\mathrm{GeV}$, inelasticity $0.1 < z < 0.5$ and both muons within the central region of the H1 experiment, i.e. $20° < \theta(\mu_{1,2}) < 160°$ (cf. Section 1.4.3). The cross section is calculated according to

$$\sigma_{\mathrm{vis}}(ep \to b\bar{b}X \to J/\psi X' \to \mu^+\mu^- X'') \equiv \frac{N_{J/\psi} \cdot f_{b\bar{b}}}{\int \mathcal{L}\, dt \cdot \mathcal{A}_{\mathrm{CST}} \cdot \epsilon \cdot (1 + \mathcal{M}_{\overline{\mathrm{vis}}})}, \tag{5.11}$$

where $\int \mathcal{L}\, dt$ denotes the underlying integrated luminosity for the e^+p data periods 1997 to 2000, i.e. $\int \mathcal{L}\, dt = (56.1 \pm 0.8)\,\mathrm{pb}^{-1}$ (cf. Section 3.1). $\mathcal{A}_{\mathrm{CST}} = (69.6 \pm 3.1)\,\%$ is the acceptance of the central silicon detector (cf. Section 4.1.1). The efficiency ϵ is factorized into the trigger efficiency $\epsilon_{\mathrm{trigger}} = (75.8 \pm 5.2)\,\%$ (cf. Section 3.6.1), the selection efficiency $\epsilon_{\mathrm{sel}} = (31.1 \pm 2.1)\,\%$ (cf. Section 3.5) and the efficiency for linking both muon candidates with CST information, i.e. $\epsilon_{4/4}$ (cf. Table 5.6 and Section 4.4.2). The latter depends on the linking and vertexing algorithms used and is, therefore, treated specially in the cross section calculation. All quoted errors are the corresponding systematical uncertainties. The last factor $(1 + \mathcal{M}_{\overline{\mathrm{vis}}})$ considers the migration from outside[2] the visible region to the selected sample. $\mathcal{M}_{\overline{\mathrm{vis}}}$ has been estimated to be 4.6 % using the `AROMA` $b\bar{b}$ Monte Carlo simulation.

The cross section is calculated separately for both multi–hypothesis linking methods using each of the vertexing algorithms (Table 5.6). Since none of the methods is preferred (cf. Section 5.1.2), their average value gives finally the result for the visible cross section:

$$\boxed{\sigma_{\mathrm{vis}}(ep \to b\bar{b}X \to J/\psi X' \to \mu^+\mu^- X'') = \left[13.0 \pm 6.2(\mathrm{stat.}) \pm 2.5(\mathrm{syst.})\right]\,\mathrm{pb}}$$

where the first error denotes the statistical and the second the systematical uncertainty. This and all following cross sections are quoted for a center–of–mass energy of $\sqrt{s} \approx 318\,\mathrm{GeV}$. The uncertainty in this central value has been included in the systematic error.

[2]The migration out of the visible region is already included in the selection efficiency.

Method	$N_{b\bar{b}}$ ($= N_{J/\psi} \cdot f_{b\bar{b}}$)	$\epsilon_{4/4}$ [%]	σ_{vis} [pb]
Cluster + Kalman	37.3 ± 18.9	28.9 ± 4.4	$13.4 \pm 6.8 \pm 2.4$
+ Least–Squares	48.8 ± 20.1	32.3 ± 4.9	$15.7 \pm 6.5 \pm 3.0$
Spacepoint + Kalman	37.0 ± 20.0	35.9 ± 5.5	$10.7 \pm 5.8 \pm 2.0$
+ Least–Squares	45.9 ± 21.7	39.3 ± 6.0	$12.1 \pm 5.7 \pm 2.3$
Mean			$\mathbf{13.0 \pm 6.2 \pm 2.5}$

Table 5.6: *Results for the visible beauty production cross section in photoproduction $\sigma_{\mathrm{vis}}(ep \to b\bar{b}X \to J/\psi X' \to \mu^+\mu^- X'')$. The first error quotes the statistical uncertainty and the second the systematical uncertainty.*

Comparison with NLO QCD Predictions

This result can be compared to a recent theoretical calculation [71] based on the extraction of the unintegrated gluon density from HERA F_2 measurements and which uses CCFM evolution equations [72] rather than DGLAP [9]. The CASCADE Monte Carlo generator, which implements these calculations, predicts a visible cross section of 3.95 pb [146] — about a factor 3.3 below the central value of this measurement. Here the beauty mass is set to 4.75 GeV/c^2, while all other scale–dependent parameters are fixed by the F_2 measurement. Nevertheless, due to the large statistical uncertainty of the presented measurement, this difference corresponds to only about 1.35 standard deviations.

Further comparisons between theory and data for several measurements performed so far at HERA (cf. Section 1.2.5) are shown in Figure 5.8. The result here agrees with previous HERA measurements [17]–[20], [147]. The systematical uncertainties are compatible, however the statistical error of the measurement presented in this thesis is significantly larger.

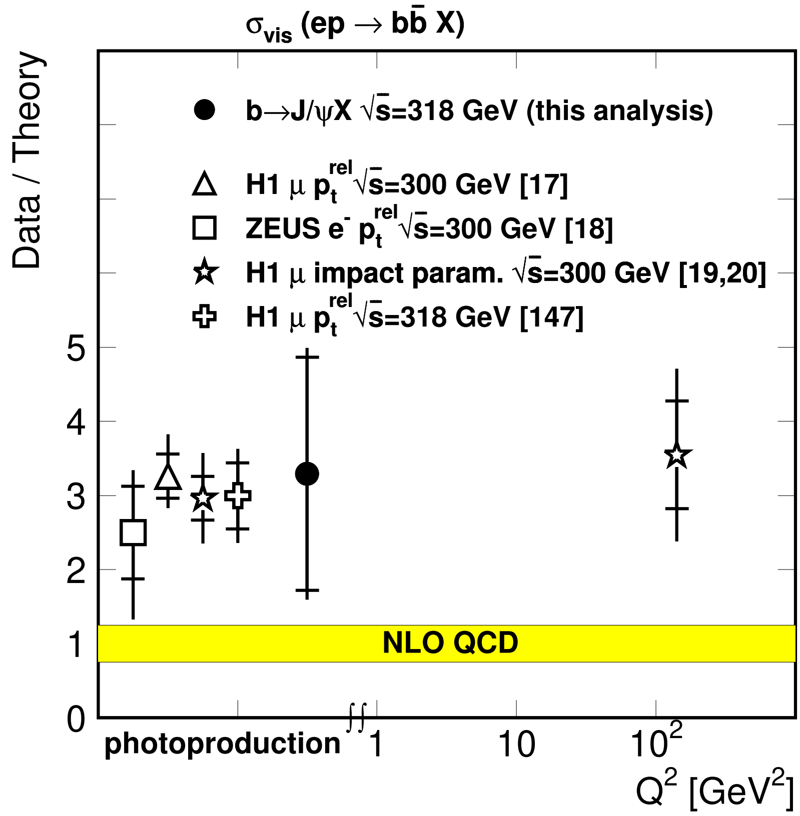

Figure 5.8: *Comparison of the measurement of beauty production cross section to other measurements performed at HERA [17]–[20], [147]. Displayed is the ratio data over NLO QCD prediction for the visible cross sections. The inner error bars indicate the statistical uncertainties, while the outer bars include the statistical and systematic uncertainties added in quadrature. The theoretical values are taken from the corresponding references (cf. Section 1.2.5). A global 20 % theoretical error is assumed (light shaded band).*

5.3.3 The Beauty Production Cross Section in Photoproduction

The visible cross section is extrapolated to the full phase space using the AROMA $b\bar{b}$ Monte Carlo simulation. The extrapolation factor is given by the acceptance $\mathcal{A} = (49.2 \pm 1.6)\,\%$ (cf. Section 1.4.3). The stated error is the systematic uncertainty. The beauty production cross section is determined according to

$$\sigma(ep \to b\bar{b}X) \equiv \frac{\sigma_{\rm vis}}{BR \cdot \mathcal{A}}, \tag{5.12}$$

where BR denotes the total branching ratio, $BR(B\bar{B} \to J/\psi X) \cdot BR(J/\psi \to \mu^+\mu^-)$.

Any of the two beauty–flavoured hadrons ($B\bar{B}$) can decay into a J/ψ meson. Their combined branching ratio can be deduced from the single branching ratio for a b–flavoured hadron decaying into a J/ψ meson,

$$BR(B\bar{B} \to J/\psi X) = 1 - \Big[1 - BR\big(B(\bar{B}) \to J/\psi X\big)\Big]^2. \tag{5.13}$$

The latter term $BR\big(B(\bar{B}) \to J/\psi X\big) \equiv BR\big(B^+/B^0/B^0_s/b\text{–baryon} \to J/\psi X\big)$ is $(1.16 \pm 0.10)\,\%$, while $BR(J/\psi \to \mu^+\mu^-) = (5.88 \pm 0.10)\,\%$ [34].

The beauty production cross section in photoproduction is, therefore,

$$\boxed{\sigma(ep \to b\bar{b}X) = \big[19.5 \pm 9.3(\text{stat.}) \pm 3.7(\text{syst.}) \pm 1.8(\text{ext.})\big]\ \text{nb}}$$

The last error denotes the uncertainty due to the extrapolation to the full phase space. The results for both multi–hypothesis linking methods using each of the vertexing algorithms are listed separately in Table 5.7.

Method	$\sigma(ep \to b\bar{b}X)$ [nb]
Cluster + Kalman	$20.1 \pm 10.2 \pm 3.7 \pm 1.9$
+ Least–Squares	$23.5 \pm 9.7 \pm 4.4 \pm 2.2$
Spacepoint + Kalman	$16.1 \pm 8.7 \pm 3.0 \pm 1.5$
+ Least–Squares	$18.2 \pm 8.6 \pm 3.4 \pm 1.7$
Mean	$\mathbf{19.5 \pm 9.3 \pm 3.7 \pm 1.8}$

Table 5.7: *Results for the total beauty production cross section $\sigma_{\rm tot}(ep \to b\bar{b}X)$. The first error quotes the statistical uncertainty, the second the systematical uncertainty and the third the uncertainty due to the extrapolation.*

Comparison with NLO QCD Predictions and Recent HERA Measurements

An early calculation of the total cross section for beauty–flavoured hadrons decaying into J/ψ mesons $\sigma(ep \to b\bar{b}X \to J/\psi X')$ predicted a value of 90 pb [53] per beauty quark. The total beauty production cross section is obtained by dividing by the branching ratio $BR\big(B(\bar{B}) \to J/\psi X\big) = (1.16 \pm 0.10)\,\%$ [34] and is predicted to be about 7.75 nb. Since this calculation provides only the total cross section, a factor of about 0.8 has been deduced from [19, 20] to estimate the photoproduction contribution[3]. In addition, the prediction has been increased by a factor of 1.1 to account for the higher center–of–mass energy in 1999 / 2000 than in 1997. The result of 6.8 pb is below the central value of this measurement by about a factor of 2.9.

More recent NLO QCD calculations by Frixione et al. [46, 148] predict a value of 5.10 nb for $\sqrt{s} \approx 318$ GeV (4.52 nb at $\sqrt{s} \approx 300$ GeV). These calculations use a beauty quark mass of 4.75 GeV/c^2 and the MRS(G) [63] and GRV-HO [64] structure functions for the proton and photon respectively. The prediction underestimates the central value for the beauty production cross section presented in this thesis by a factor of 3.8. Theoretical calculations utilizing the `CASCADE` Monte Carlo generator give a cross section of 5.73 nb [146], which lies approximately a factor of 3.4 below the measurement.

Since the combined branching ratio $BR(B(\bar{B}) \to J/\psi X)\cdot BR(J/\psi \to \mu^+\mu^-)$ is rather low, the presented cross sections suffer from the large statistical error at the given luminosity. Thus the differences to the aforementioned theoretical calculations correspond to only about 1.35 standard deviations. No significant agreement or disagreement is therefore found with the present NLO QCD predictions.

5.3.4 The Photon–Proton Cross Section

Using the Weizsäcker–Williams Approximation (cf. Section 1.1.2), the photon–proton (γp) cross section for beauty production can be unfolded

$$\sigma(ep \to b\bar{b}X) = \mathcal{F}_{\gamma/e} \cdot \langle \sigma(\gamma p \to b\bar{b}X) \rangle. \tag{5.15}$$

In the kinematical range of the proton–photon center–of–mass energy $W_{\gamma p} > 100$ GeV, the evaluation of Equation 1.19 gives a flux factor of $\mathcal{F}_{\gamma/e} = 0.063$. The beauty production γp cross section at an average photon–proton center–of–mass energy of $\langle W_{\gamma p} \rangle = 168$ GeV is, therefore,

$$\boxed{\langle \sigma(\gamma p \to b\bar{b}X) \rangle = \big[310 \pm 150(\text{stat.}) \pm 60(\text{syst.}) \pm 40(\text{ext.})\big]\ \text{nb}}$$

[3] From the previously measured beauty production cross sections (cf. Section 1.2.5) in photoproduction $\sigma_{\text{vis}}(ep \to b\bar{b}X \to \mu X) = 160$ pb [19] and in DIS, $\sigma_{\text{vis}}(ep \to b\bar{b}e'X \to \mu e'X) = 39$ pb [20], this factor results from

$$\frac{\sigma_{\text{vis}}(ep \to b\bar{b}X \to \mu X)}{\sigma_{\text{vis}}(ep \to b\bar{b}X \to \mu X) + \sigma_{\text{vis}}(ep \to b\bar{b}e'X \to \mu e'X)} = 0.804.$$

5.4 The J/ψ Meson Production Cross Section

At low inelasticities $0.1 < z < 0.5$ about 52 % of the J/ψ mesons are produced in beauty–flavoured hadron decays as discussed in Section 5.1.2. The remaining fraction of J/ψ mesons must be produced in a direct process. This beauty–subtracted direct J/ψ meson production cross section is defined by

$$\sigma(ep \to c\bar{c}X \to J/\psi X') = \frac{N_{J/\psi} \cdot (1 - f_{b\bar{b}})}{\int \mathcal{L}\, dt \cdot \mathcal{A}'_{\mathrm{CST}} \cdot \epsilon' \cdot BR \cdot \mathcal{A}'} \quad , \tag{5.16}$$

with the branching ratio $BR(J/\psi \to \mu^+\mu^-)$. The value for $\int \mathcal{L}\, dt$ is the same as in Section 5.3, while the values for ϵ', $\mathcal{A}'_{\mathrm{CST}}$ and $\mathcal{A}'$ depend on the underlying process and thus are different. The acceptances are determined with the `EPJPSI` $c\bar{c}$ Monte Carlo simulation and is $\mathcal{A}'_{\mathrm{CST}} = (63.3 \pm 3.1)\,\%$ (cf. Section 4.1.1) and $\mathcal{A}' = (36.2 \pm 1.8)\,\%$ (cf. Section 4.1). The efficiency ϵ' is the product of the trigger efficiency $\epsilon_{\mathrm{trigger}}(68.5 \pm 4.3)\,\%$ (cf. Section 3.6.1), the selection efficiency $\epsilon_{\mathrm{sel}} = (23.8 \pm 1.3)\,\%$ (cf. Section 3.5) and $\epsilon_{4/4}$ (cf. Table 5.6 and Section 4.4.2).

The resulting cross sections in photoproduction for the kinematical range $0.1 < z < 0.5$ and $W_{\gamma p} > 100$ GeV are listed in Table 5.8 separately for both linking methods and both vertexing algorithms. The average result

$$\boxed{\sigma(ep \to c\bar{c}X \to J/\psi X') = \big[950 \pm 540(\mathrm{stat.}) \pm 180(\mathrm{syst.}) \pm 50(\mathrm{ext.})\big]\ \mathrm{pb}}$$

is in agreement with the cross section obtained without any use of the CST, $\sigma(ep \to c\bar{c}X \to J/\psi X') = \big[990 \pm 540(\mathrm{stat.}) \pm 90(\mathrm{syst.}) \pm 50(\mathrm{ext.})\big]$ pb assuming an average beauty–fraction of 52.0 % (cf. Section 5.2.2).

This result can also be compared with a theoretical prediction [87] and a recently performed analysis [94]. Both determine the J/ψ meson production cross section as a function

Method	$\sigma(ep \to c\bar{c}X \to J/\psi X')$ [pb]
Cluster + Kalman	$850 \pm 580 \pm 160 \pm 40$
+ Least–Squares	$670 \pm 550 \pm 120 \pm 30$
Spacepoint + Kalman	$1150 \pm 510 \pm 210 \pm 60$
+ Least–Squares	$1120 \pm 500 \pm 200 \pm 60$
Mean	$\mathbf{950 \pm 540 \pm 180 \pm 50}$
w/o CST	$990 \pm 540 \pm 90 \pm 50$

Table 5.8: *Results for the direct J/ψ meson production cross section in photoproduction $\sigma(ep \to c\bar{c}X \to J/\psi X')$. The first error quotes the statistical uncertainty, the second the systematical uncertainty and the third the uncertainty due to the extrapolation.*

of the inelasticity z. Since the obtained statistics using any of the linking methods are too low to determine a differential cross section, the use of the CST is suspended in the following. Thus *all* events which passed the data selection of J/ψ mesons (cf. Chapter 3) are analyzed.

The influence of the b–flavoured contribution $B\bar{B} \to J/\psi X$ is discussed afterwards.

5.4.1 Comparison with Colour–Singlet / –Octet Calculations

The theoretical prediction [87] includes Colour–Singlet and Colour–Octet calculations (cf. Section 1.3.3) for the direct as well as for the resolved processes. The Colour–Octet contributions are roughly estimated from CDF data. To ensure the presence of a hard scale, a minimum transverse momentum of the J/ψ meson candidate of $p_t(\mu\mu) > 1\,\mathrm{GeV/c}$ has been required. The kinematical range is restricted to a window of $130\,\mathrm{GeV} < W_{\gamma p} < 250\,\mathrm{GeV}$. The photon flux factor for this $W_{\gamma p}$ interval is $\mathcal{F}_{\gamma/e} = 0.043$. For comparison, both requirements have been additionally applied to the basic J/ψ meson selection of Chapter 3.

The γp cross section for the *inclusive*[4] J/ψ meson production process at an average photon–proton center–of–mass energy of $\langle W_{\gamma p} \rangle = 172\,\mathrm{GeV}$ and inside a window $0.1 < z < 0.5$ is

$$\boxed{\sigma(\gamma p \to J/\psi X) = \left[40.0 \pm 4.1(\mathrm{stat.}) \pm 3.6(\mathrm{syst.}) \pm 2.0(\mathrm{ext.})\right]\,\mathrm{nb}}$$

The differential γp cross section in four inelasticity bins z is compared to the Colour–Singlet and Colour–Octet calculations (Figure 5.9). The measured values are also listed in Table 5.9.

A good agreement with Colour–Singlet (dotted line) and Colour–Octet (dashed line) predictions is achieved if a normalization of approximately $k = 3$ is applied to the predictions.

[4] This value also includes J/ψ mesons originating from beauty–flavoured hadron decays.

	$d\sigma(\gamma p \to J/\psi X)/dz$ [nb]
$0.1 < z < 0.2$	$53.9 \pm 9.5 \pm 4.8 \pm 2.7$
$0.2 < z < 0.3$	$28.3 \pm 6.5 \pm 2.5 \pm 1.4$
$0.3 < z < 0.4$	$33.5 \pm 7.1 \pm 3.0 \pm 1.7$
$0.4 < z < 0.5$	$51.8 \pm 6.9 \pm 4.6 \pm 2.6$

Table 5.9: *Results for the differential inclusive J/ψ meson production cross section as a function of the inelasticity z. The first error quotes the statistical uncertainty, the second the systematical uncertainty and the third the uncertainty due to the extrapolation.*

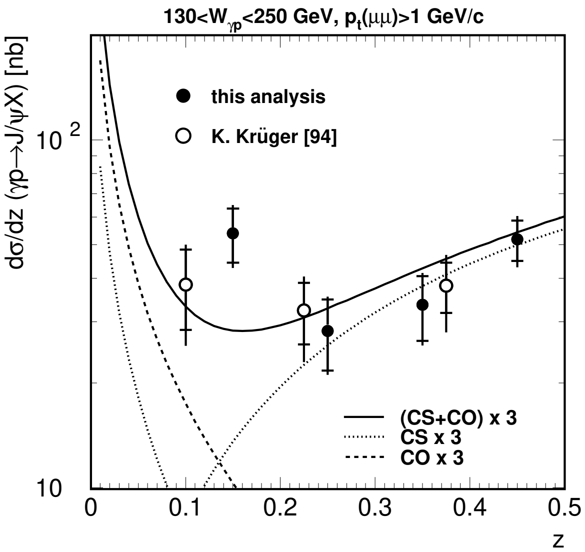

Figure 5.9: *Comparison of the measurement of the direct J/ψ meson production cross section (1997, 1999 and 2000 e^+p data) to the theoretical Colour–Singlet (CS) and Colour–Octet (CO) calculations [87] and to a more detailed measurement [94]. The inner error bars indicate the statistical uncertainties, while the outer bars include the statistical and systematic uncertainties added in quadrature. A normalization factor of $k = 3$ has been applied to the prediction to achieve a good agreement (left).*

This k–factor accounts for the missing NLO QCD contributions and includes generally the J/ψ mesons originating from b–flavoured hadron decays. The trend at low–z corresponds to the resolved contributions. In addition, the data are compared with a more detailed analysis of direct J/ψ meson production at low inelasticities [94]. Both measurements agree well. This lends reliability to the basic ("non–CST") analysis chain. As in [94], Colour–Octet contributions to the resolved process clearly improve the theoretical description of the measurement, although the first point lies towards higher values.

Neither this recent measurement nor the normalization factor k considers the beauty–flavoured fraction in detail. Thus *all* J/ψ meson candidates have been used to calculate the cross section and not only the beauty–subtracted fraction.

5.4.2 The Contribution from Beauty–Flavoured Hadron Decays

If the beauty–flavoured fraction of about 52 % (cf. Section 5.2.2) is subtracted, the γp cross section drops accordingly and gives the cross section for *direct* J/ψ meson production

$$\boxed{\sigma(\gamma p \to c\bar{c}X \to J/\psi X') = \left[19.2 \pm 10.7(\mathrm{stat.}) \pm 3.3(\mathrm{syst.}) \pm 1.0(\mathrm{ext.})\right] \mathrm{nb}}$$

This value is in agreement with the Colour–Singlet Model prediction plus Colour–Octet contributions, if a k–factor of only 1.5 is applied to these calculations (Figure 5.10, upper

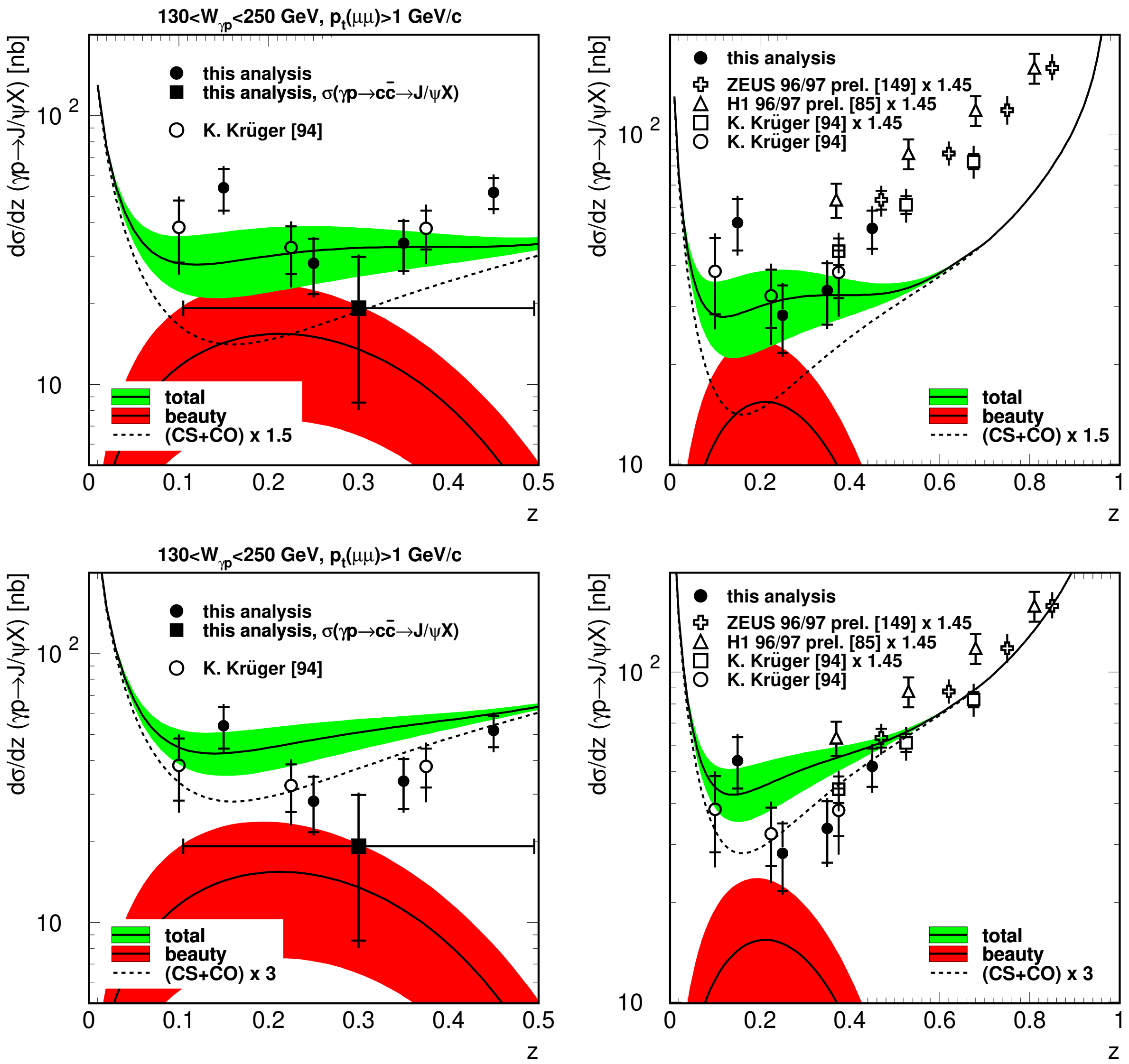

Figure 5.10: *Contribution of $B\bar{B} \to J/\psi X$ to the inclusive J/ψ meson production. The measurements of the inclusive (points) and direct (square) J/ψ meson production cross sections (1997, 1999 and 2000 e^+p data) are compared to a sum of Colour–Singlet (CS), Colour–Octet (CO) [87] and beauty–flavoured contributions. The normalization of the first two is chosen to be $k = 1.5$ (upper row) and $k = 3$ (lower row) respectively. The shape of the b–flavoured contribution is taken from the* `AROMA` *$b\bar{b}$ Monte Carlo simulation assuming a total beauty production cross section of* 19.5 nb *(cf. Section 5.3.3). The uncertainty in this measurement (dark shaded band) determines the width of the band for the total prediction (light shaded). In addition, several other measurements of the inclusive J/ψ meson production cross section at higher inelasticities [85, 94, 149] z are displayed (right column). A normalization factor of* 1.45 *has been applied to these measurements to account for the different average photon–proton center–of–mass energies (cf. text).*

left corner; dashed line). For a normalization of three, this cross section is about two standard deviations below the CS and CO prediction (cf. Figure 5.10, lower left corner).

The direct cross section $\sigma(\gamma p \to c\bar{c}X \to J/\psi X')$ in combination with those J/ψ mesons originating from b–flavoured hadron decays, i.e. $\sigma(\gamma p \to b\bar{b}X \to J/\psi X')$, should restore the inclusive J/ψ meson cross section $\sigma(\gamma p \to J/\psi X)$.

Both measurements of the inclusive and direct J/ψ meson production cross sections as a function of the inelasticity z can be compared to the CS / CO calculation together with a prediction of the differential beauty production cross section. The latter prediction is obtained using the `AROMA` $b\bar{b}$ Monte Carlo simulation under the assumption that the total beauty production cross section is 19.5 nb (cf. Section 5.3.3). The sum of this `AROMA` $b\bar{b}$ and the Colour–Singlet / Colour–Octet predictions agree well with the inclusive differential J/ψ meson production cross section $d\sigma(\gamma p \to J/\psi X)/dz$ of this analysis and with those of [94], if a normalization factor of $k = 1.5$ is applied to the Colour–Singlet and Colour–Octet calculations.

Towards medium inelasticity values $z > 0.5$, the k–factor of three, however, must be restored to match the results of the measurements there[5] [85, 94, 149] (cf. Figure 5.10, lower right corner). A value of $k = 1.5$ is not sufficient to describe the data (cf. Figure 5.10, upper right corner).

Conclusions

Due to the high observed beauty production cross section, the b–flavoured contribution has a significant impact on the inclusive J/ψ meson production cross section. The uncertainties in the beauty–flavoured fraction $f_{b\bar{b}}$, in the Colour–Singlet and Colour–Octet contributions, especially in their normalization, however, make it impossible to draw firm conclusions. The composition of J/ψ meson sources, taking also contributions from $\psi(2S)$ and χ_c decays into account, still needs further investigation.

[5] The average photon–proton center–of–mass energy at medium inelasticities is different to that used by the prediction [87], i.e. $\langle W_{\gamma p}\rangle_{\text{medium } z} = 100\,\text{GeV}$ and $\langle W_{\gamma p}\rangle_{\text{theory}} = 172\,\text{GeV}$. The functional dependence of the direct J/ψ meson production cross section is assumed to be $\sigma_{\gamma p} \propto W_{\gamma p}^{\delta}$, where $\delta = 0.68 \pm 0.10$ has been determined elsewhere [85]. The normalization for these measurements is, therefore, increased by a factor of

$$\left(\frac{\langle W_{\gamma p}\rangle_{\text{theory}}}{\langle W_{\gamma p}\rangle_{\text{medium } z}}\right)^{\delta} = 1.45. \tag{5.17}$$

Chapter 6

Summary

For the first time at HERA, beauty–flavoured hadrons decaying into J/ψ mesons, $b\bar{b} \rightarrow J/\psi X$, have been exploited to extract the beauty production cross section in photoproduction, i.e. at $Q^2 < 1\,\mathrm{GeV}^2$. The events were collected during the e^+p running years 1997, 1999 and 2000 by the H1 experiment and correspond to a total integrated luminosity of $56\,\mathrm{pb}^{-1}$. The muonic decay channel was used to select J/ψ mesons.

The central silicon detector (CST) of the H1 experiment has been proven to be capable of reconstructing the decay vertices of J/ψ mesons. Based on a newly introduced three–dimensional linking method (the *multi–hypothesis ansatz*), the track parameters of both muons were determined with high precision and combined into a three–dimensional J/ψ meson decay vertex. The achieved two–dimensional decay length resolution of about $150\,\mu$m is sufficient to distinguish between b–flavoured hadrons (having an average decay length of $326\,\mu$m) and directly produced J/ψ mesons (which decay instantaneously).

The finite resolution of the CST leads to a symmetric two–dimensional signed decay length distribution for directly produced or mis–identified J/ψ mesons. The sign is defined by the decay topology. Beauty–flavoured hadrons, however, mainly contribute to positive decay lengths. The fraction of J/ψ mesons originating from beauty–flavoured hadron decays extracted from the excess at positive decay length values using a log–likelihood minimization has been determined to be $\left[52.0 \pm 26.2(\mathrm{stat.}) \pm 7.7(\mathrm{syst.})\right]\%$ at low inelasticities $0.1 < z < 0.5$. It has been shown that neither kaons faking J/ψ meson candidates nor heavy quark decays other than into a J/ψ meson produce such an excess.

This fraction has been converted into a visible beauty production cross section of $\sigma_{\mathrm{vis}}(ep \rightarrow b\bar{b}X \rightarrow J/\psi X' \rightarrow \mu^+\mu^- X'') = \left[13.0 \pm 6.2(\mathrm{stat.}) \pm 2.5(\mathrm{syst.})\right]\,\mathrm{pb}$ at an ep center–of–mass energy of $\sqrt{s} \approx 318\,\mathrm{GeV}$. The visible range is defined by the inelasticity interval $0.1 < z < 0.5$, photon–proton center–of–mass energies $W_{\gamma p} > 100\,\mathrm{GeV}$ and two identified muons within the polar angular range $20^\circ < \theta_\mu < 160^\circ$. Due to the small overall branching ratio of the process $B\bar{B} \rightarrow J/\psi X \rightarrow \mu\mu X$ of $(0.136 \pm 0.012)\,\%$, the statistical error of this analysis is rather large. The systematical error is dominated by the uncertainties in the multi–hypothesis linking results.

The extrapolation to the full phase–space relies upon the implementation of the `AROMA` $b\bar{b}$ Monte Carlo simulation. The total beauty production cross section in photoproduction is

$\sigma(ep \to b\bar{b}X) = \big[19.5 \pm 9.3(\text{stat.}) \pm 3.7(\text{syst.}) \pm 1.8(\text{ext.})\big]$ nb, where the last error denotes the uncertainty due to the extrapolation to the full phase space. The photon flux factor calculated using the Weizsäcker–Williams approximation leads to a γp cross section at an average photon–proton center–of–mass energy of $\langle W_{\gamma p}\rangle = 168\,\text{GeV}$ of $\langle\sigma(\gamma p \to b\bar{b}X)\rangle = \big[310 \pm 150(\text{stat.}) \pm 60(\text{syst.}) \pm 40(\text{ext.})\big]$ nb.

Three different theoretical calculations in NLO QCD [46, 53, 146] have been compared to the results. The central values for both visible and total beauty production cross sections exceed these predictions by about a factor 3.5. These discrepancies, however, are in agreement with those observed by previous measurements performed at HERA [17]–[20], [147]. Due to the large statistical errors, the deviations correspond to only about 1.35 standard deviations.

Finally the b–subtracted, i.e. *direct*, J/ψ meson production cross section has been measured in photoproduction to be $\sigma(ep \to c\bar{c}X \to J/\psi X') = \big[950 \pm 540(\text{stat.}) \pm 180(\text{syst.}) \pm 50(\text{ext.})\big]$ pb for inelasticities of $0.1 < z < 0.5$ and $W_{\gamma p} > 100\,\text{GeV}$. By restricting the kinematic range to a photon–proton center–of–mass energy of $130\,\text{GeV} < W_{\gamma p} < 250\,\text{GeV}$ and requiring the minimum transverse momentum of the J/ψ candidate to be $p_t(\mu\mu) > 1\,\text{GeV/c}$, the direct J/ψ meson production cross section can be compared to the theoretical prediction [87] for the Colour–Singlet plus Colour–Octet contributions. An agreement is achieved, if a normalization ("k–factor") of 1.5 is applied to the prediction.

The *inclusive* J/ψ meson production cross section $\sigma(\gamma p \to J/\psi X)$, including the direct cross section and the fraction of beauty–flavoured events of about 50 %, is in agreement with previous measurements [94], but neither a normalization of $k = 1.5$ nor of three to the Colour–Singlet / Colour–Octet prediction is sufficient to describe all measurements simultaneously.

6.1 Outlook

This thesis has established the analysis of the decay $B \to J/\psi X$. This decay provides a wider field for further studies. In particular the constraints due to the mass of the beauty meson and due to the high generic track multiplicity remain to be exploited in the future. These might be used to improve the signal–to–background ratio by means of jet studies or isolation criteria on the J/ψ meson or on its decay muons. Furthermore, the electronic decay channel $J/\psi \to e^+e^-$ is open for further studies.

The lifetime information itself can also be re–analyzed in three–dimensions since the boost is larger ($\beta\gamma \approx 1.3$) than in two dimensions. Also alternative methods for lifetime tagging should be tried, e.g. the method of a topological vertex finder [150].

Two ongoing soft– and hardware projects will, in addition, make a direct improvement of this analysis possible. First, the reprocessing of the 1997, 1999 and 2000 data sets will lead to a further improvement of the CJC track parameters, of the alignment of the tracking detectors, and of the CST linking. After the machine and detector upgrade in the year 2001, a four–fold higher luminosity is anticipated. Since the design of the

CST has changed, new studies on its performance are necessary, but afterwards this will increase the available statistics. In addition, the installation of the forward silicon tracker in 2001 will extend precise track measurements to the forward region and the Fast Track Trigger [151] will provide a sophisticated J/ψ meson trigger.

The luminosity upgrade will finally open the field for a precise determination of the beauty production cross section in different kinematical régimes, e.g. in tagged photoproduction or in DIS. More dedicated measurements, e.g. of differential cross sections or of the beauty–flavoured contribution $F_2^{b\bar{b}}$ to the proton structure function, will provide new insights into the standard model of elementary physics.

List of Figures

List of Tables

Bibliography

[1] R. Feynman, *Very High–Energy Collisions of Hadrons*, Phys. Rev. Lett. **23** (1969) 1415.
J.D. Bjorken, *Asymptotic Sum Rules at Infinite Momentum*, Phys. Rev. **179** (1969) 1547.
J.D. Bjorken and E.A. Paschos, *Inelastic Electron Proton and Gamma Proton Scattering, and the Structure of the Nucleon*, Phys. Rev. **185** (1969) 1975.

[2] J.D. Bjorken, *Inequality for Backward Electron–Nucleon and Muon–Nucleon Scattering at High Momentum Transfer*, Phys. Rev. **163** (1967) 1767.
E.D. Bloom et al., *High–Energy Inelastic ep Scattering at 6° and 10°*, Phys. Rev. Lett. **23** (1969) 930.
M. Breidenbach et al., *Observed Behavior of Highly Inelastic Electron–Proton Scattering*, Phys. Rev. Lett. **23** (1969) 935.

[3] C.G. Callan and D.J. Gross, *High–Energy Electroproduction and the Constitution of the Electric Current*, Phys. Rev. Lett. **22** (1969) 156.

[4] M. Gell–Mann, *A Schematic Model of Baryons and Mesons*, Phys. Lett. **8** (1964) 214.
G. Zweig, *An SU(3) Model for Strong Interaction Symmetry and Its Breaking*, CERN Reports CERN-TH-401 and CERN-TH-412 (1964).

[5] D.H. Perkins, *Review of Neutrino Experiments*, in: "Proceedings of the 1975 International Symposium on Lepton and Photon Interactions at High Energy", ed. W.T. Kirk, SLAC (1975) 679.
H.L. Anderson, *Determination of the Quark and Gluon Moments of the Nucleon*, Phys. Rev. Lett. **40** (1978) 1061.

[6] D.J. Fox et al., *Early Tests of Scale Invariance in High–Energy Muon Scattering*, Phys. Rev. Lett. **35** (1974) 1504.
H1 Collaboration, *Measurement of Neutral and Charged Current Cross Sections in Electron–Proton Collisions at High Q^2*, Eur. Phys. J. **C19** (2001) 269; `hep-ex/0012052`.
H1 Collaboration, *Deep–Inelastic Inclusive ep Scattering at Low x and a Determination of α_s*, accepted by Eur. Phys. J. (2000); `hep-ex/0012053`.

[7] M.Y. Han and Y. Nambu, *Three–Triplet Model with Double SU(3) Symmetry*, Phys. Rev. **139** (1965) B1006.

[8] S. Bethke, *Determination of the QCD Coupling α_s*, J. Phys. **G26** (2000) R27; `hep-ex/0004021`.

[9] G. Altarelli and G. Parisi, *Asymptotic Freedom in Parton Language*, Nucl. Phys. **B126** (1977) 298.
V.N. Gribov and L.N. Lipatov, *Deep Inelastic ep Scattering in Perturbation Theory*, Sov. J. Nucl. Phys. **15** (1972) 438.
V.N. Gribov and L.N. Lipatov, *e^+e^- Pair Annihilation and Deep Inelastic ep Scattering in Perturbation Theory*, Sov. J. Nucl. Phys. **15** (1972) 675.
G. Ingelman et al., *Deep Inelastic Physics and Simulation*, in: "Proceedings of the HERA Workshop" Vol 1, ed. R.D. Peccei, DESY (1988) 3.

[10] F. Halzen and A.D. Martin, *Quarks and Leptons: An Introductory Course in Modern Particle Physics*, John Wiley & Sons Inc. (1984).
B.R. Martin and G. Shaw, *Particle Physics*, John Wiley & Sons Inc. (1992).
R.K. Ellis, W.J. Stirling and B.R. Webber, *QCD and Collider Physics*, University Press (1996).

[11] M.S. Chen and P. Zerwas, *Equivalent–Particle Approximation in Electron and Photon Processes of Higher Order QED*, Phys. Rev, **D12** (1976) 187.
V.M. Budnev, I.F. Ginzburg, G.V. Meledin and V.G. Serbo, *The Two Photon Particle Production Mechanism. Physical Problems. Applications. Equivalent Photon Approximation*, Phys. Rept. **15** (1974) 181.

[12] E. Fermi, *On the Theory of the Impact between Atoms and Electrically Charged Particles*, Z. Phys. **29** (1924) 315.
C.F. von Weizsäcker, *Radiation Emitted in Collisions of Very Fast Electrons*, Z. Phys. **88** (1934) 612.
E.J. William, *Nature of the High–Energy Particles of Penetrating Radiation and Status of Ionization and Radiation Formulae*, Phys. Rev. **45** (1934) 729.

[13] S. Frixione, M.L. Mangano, P. Nason and G. Ridolfi, *Improving the Weizsäcker–Williams Approximation in Electron–Proton Collisions*, Phys. Lett. **B319** (1993) 339; `hep-ph/9310350`.

[14] H1 Collaboration, *Photoproduction of $D^{*\pm}$ Mesons in Electron–Proton Collisions at HERA*, Nucl. Phys. **B472** (1996) 32; `hep-ex/9604005`.
H1 Collaboration, *Measurement of D^* Meson Cross Sections at HERA and Determination of the Gluon Density in the Proton Using NLO QCD*, Nucl. Phys. **B545** (1999) 21; `hep-ex/9812023`.
ZEUS Collaboration, *Measurement of Inclusive $D^{*\pm}$ and Associated Dijet Cross Sections in Photoproduction at HERA*, Eur. Phys. J. **C6** (1999) 67; `hep-ex/9807008`.

[15] H1 Collaboration, *Inclusive D^0 and $D^{*\pm}$ Production in Deep Inelastic ep Scattering at HERA*, Z. Phys. **C72** (1996) 593; `hep-ex/9607012`.

[16] U. Langenegger, *A Measurement of the Beauty and Charm Production Cross Section at the ep Collider HERA*, Ph.D. Thesis, ETH Zurich (1998).
M. Kander, *Bestimmung des ep–Wirkungsquerschnittes von Beauty–Quarks durch ihren semi–leptonischen Zerfall in Myonen mit dem H1–Detektor bei HERA*, Ph.D. Thesis, University of Hamburg (1998).

[17] H1 Collaboration, *Measurement of Open Beauty Production at HERA*, Phys. Lett. **B467** (1999) 156; `hep-ex/9909029`.

[18] ZEUS Collaboration, *Measurement of Open Beauty Production in Photoproduction at HERA*, Eur. Phys. J. **C18** (2001) 625; `hep-ex/0011081`.

[19] H1 Collaboration, *Measurement of the Beauty Production Cross Section at HERA Using Lifetime Information*, contributed paper to ICHEP2000, Osaka, Japan (2000).

[20] H1 Collaboration, *Beauty Production in Deep Inelastic ep Scattering*, contributed paper to EPS2001, Budapest, Hungary (2001).

[21] CDF Collaboration, *Measurement of the Bottom Quark Production Cross Section Using Semi–Leptonic Decay Electrons in $p\bar{p}$ Collisions at $\sqrt{s}$ =1.8 TeV*, Phys. Rev. Lett. **71** (1993) 500.

[22] CDF Collaboration, *Measurement of Bottom Quark Production in 1.8 TeV $p\bar{p}$ Collisions Using Muons from b–Quark Decays*, Phys. Rev. Lett. **71** (1993) 2396.
CDF Collaboration, *Inclusive χ_c and b Quark Production in $p\bar{p}$ Collisions at $\sqrt{s}$ =1.8 TeV*, Phys. Rev. Lett. **71** (1993) 2537.
D0 Collaboration, *Inclusive μ and b Quark Production Cross Sections in $p\bar{p}$ Collisions at $\sqrt{s}$ =1.8 TeV*, Phys. Rev. Lett. **74** (1995) 3548.

[23] D0 Collaboration, *The $b\bar{b}$ Production Cross Section and Angular Correlations in $p\bar{p}$ Collisions at $\sqrt{s}$ =1.8 TeV*, Phys. Lett. **B487** (2000) 264; `hep-ex/9905024`.

[24] D0 Collaboration, *Cross Section for b Jet Production in $p\bar{p}$ Collisions at $\sqrt{s}$ =1.8 TeV*, Phys. Rev. Lett. **85** (2000) 5068; `hep-ex/0008021`.

[25] CDF Collaboration, *Measurement of Correlated $\mu - \bar{b}$ Jet Cross Sections in $p\bar{p}$ Collisions at $\sqrt{s}$ =1.8 TeV*, Phys. Rev. **D53** (1996) 1051; `hep-ex/9508017`.
D0 Collaboration, *Small Angle Muon and Bottom Quark Production in $p\bar{p}$ Collisions at $\sqrt{s}$ =1.8 TeV*, Phys. Rev. Lett. **84** (2000) 5478; `hep-ex/9907029`.

[26] CDF Collaboration, *A Measurement of the B–Meson and b Quark Cross Section at $\sqrt{s}$ =1.8 TeV Using the Exclusive Decay $B^{\pm} \to J/\psi K^{\pm}$*, Phys. Rev. Lett. **68** (1992) 3403.

[27] CDF Collaboration, *Inclusive J/ψ, $\psi(2S)$, and b Quark Production in $p\bar{p}$ Collisions at $\sqrt{s}$=1.8 TeV*, Phys. Rev. Lett. **69** (1992) 3704.

[28] CDF Collaboration, *Measurement of the B Meson and b Quark Cross Sections at $\sqrt{s}$ =1.8 TeV Using the Exclusive Decay $B^0 \to J/\psi K^{*0}(892)$*, Phys. Rev. **D50** (1994) 4252.

[29] CDF Collaboration, *Measurement of the B Meson Differential Cross Section, $d\sigma/dp_t$, in $p\bar{p}$ Collisions at $\sqrt{s}$=1.8 TeV*, Phys. Rev. Lett. **75** (1995) 1451; hep-ex/9503013.

[30] D0 Collaboration, *J/ψ Production in $p\bar{p}$ Collisions at $\sqrt{s}$ =1.8 TeV*, Phys. Lett. **B370** (1996) 239.

[31] L3 Collaboration, *Measurement of the Cross Sections for Open Charm and Beauty Production in $\gamma\gamma$ Collisions at $\sqrt{s}$ =189-202 GeV*, Phys. Lett. **B503** (2001) 10; hep-ex/0011070.

[32] OPAL Collaboration, *Charm and Bottom Production in Two–Photon Collisions with OPAL*, contributed paper to PHOTON2000, Ambleside, UK (2000); hep-ex/0010060.

[33] R.K. Ellis, H. Georgi, M. Machacek, H.D. Politzer and G.G. Ross, *Perturbation Theory and the Parton Model in QCD*, Nucl. Phys. **B152** (1979) 285.

[34] Particle Data Group, *Review of Particle Physics*, Eur. Phys. J. **C15** (2000) 1.

[35] G. Levman, *Muon Pair Production by Two Photon Collisions at HERA*, in: "Physics at HERA. Proceedings of the Workshop" Vol. 1, eds. W. Buchmüller and G. Ingelman, DESY (1992) 623.

[36] H. Fritzsch and K.H. Streng, *Photoproduction of Heavy Quark Flavours*, Phys. Lett. **B72** (1978) 385.

[37] R.K. Ellis and P. Nason, *QCD Radiative Corrections to the Photoproduction of Heavy Quarks*, Nucl. Phys. **B312** (1989) 551.

[38] L.M. Jones and H.W. Wyld, *Charmed Particle Production by Photon–Gluon–Fusion*, Phys. Rev. **D17** (1978) 759.

[39] A. Ali and D. Wyler, *Heavy Quark Physics at HERA: Introduction and Overview*, in: "Physics at HERA. Proceedings of the Workshop" Vol. 2, eds. W. Buchmüller and G. Ingelman, DESY (1992) 669.

[40] J.J. Sakurai, *Theory of Strong Interactions*, Annals Phys. **11** (1960) 1.
J.J. Sakurai, *Vector Meson Dominance and High–Energy Electron Proton Inelastic Scattering*, Phys. Rev. Lett. **22** (1969) 981.
J.J. Sakurai and D. Schildtknecht, *Generalized Vector Dominance and Inelastic Electron–Proton Scattering*, Phys. Lett. **B40** (1972) 121.
T.H. Bauer, R.D. Spital, D.R. Yennie and F.M. Pipkin, *The Hadronic Properties of the Proton in High–Energy Interactions*, Rev. Mod. Phys. **50** (1978) 261; Erratum ibid. **51** (1979) 407.

[41] G.A. Schuler and T. Sjöstrand, *Towards a Complete Description of High–Energy Photoproduction*, Nucl. Phys. **B407** (1993) 539.

[42] R.J. DeWitt, L.M. Jones, J.D. Sullivan, D.E. Willen and H.D. Wyld, *Anomalous Components of the Photon Structure Functions*, Phys. Rev. **D19** (1979) 2046.

[43] S. Frixione, M.L. Mangano, P. Nason and G. Ridolfi, *Heavy–Quark Production*, in: "Heavy Flavours II", eds. A.J. Buras and M. Lindner, World Scientific Publishing Co. (1998) 609; `hep-ph/9702287`.

[44] L.E. Gordon and J.K. Storrow, *The Parton Distribution Functions of the Photon and the Structure Function* $F_2^\gamma(x, Q^2)$, Z. Phys. **C56** (1992) 307.

[45] M. Arpagaus, *Measuring the Partonic Structure of the Photon at the ep Collider HERA*, Ph.D. Thesis, ETH Zurich (1995).
H1 Collaboration, *Inclusive Parton Cross Sections in Photoproduction and Photon Structure*, Nucl. Phys. **B445** (1995) 195; `hep-ph/9504004`.

[46] S. Frixione, M.L. Mangano, P. Nason and G. Ridolfi, *Total Cross Sections for Heavy Flavour Production at HERA*, Phys. Rev. **B348** (1995) 633; `hep-ph/9412348`.

[47] ZEUS Collaboration, *Beauty Production in the Muon Semi–Leptonic Decay Mode at HERA*, contributed paper to EPS2001, Budapest, Hungary (2001).

[48] UA1 Collaboration, *Beauty Production at the CERN Proton–Antiproton Collider*, Phys. Lett. **B186** (1987) 237.
UA1 Collaboration, *Measurement of the Bottom Quark Production Cross Section in Proton–Antiproton Collisions at* $\sqrt{s}$*=0.63 TeV*, Phys. Lett. **B213** (1988) 405.

[49] UA1 Collaboration, *Beauty Production at the CERN* $p\bar{p}$ *Collider*, Phys. Lett. **B256** (1991) 121; Erratum ibid. **B262** (1991) 497.

[50] P. Nason, S. Dawson and R.K. Ellis, *The Total Cross Section for the Production of Heavy Quarks in Hadronic Collisions*, Nucl. Phys. **B303** (1988) 607.

[51] P. Nason, S. Dawson and R.K. Ellis, *The One Particle Inclusive Differential Cross Section for Heavy Quark Production in Hadronic Collisions*, Nucl. Phys. **B327** (1989) 49; Erratum ibid. **B335** (1990) 260.

[52] UA1 Collaboration, *Measurement of* $b\bar{b}$ *Correlations at the CERN* $p\bar{p}$ *Collider*, Z. Phys. **C61** (1994) 41.

[53] R.A. Eichler and Z. Kunzst, *Charm, Bottom and Top Production in High Energy Electron Proton Collisions*, Nucl. Phys. **B308** (1988) 791.

[54] J. Smith and W.L. van Neerven, *QCD Corrections to Heavy Flavour Photoproduction and Electroproduction*, Nucl. Phys. **B374** (1992) 36.

[55] G. Ingelman, J. Rathsman and G.A. Schuler, *AROMA 2.2: A Monte Carlo Generator for Heavy Flavour Events in ep Collisions*, Comp. Phys. Commun. **101** (1997) 135; `hep-ph/9605285`.

[56] W.A. Bardeen, A.J. Buras, D.W. Duke and T. Muta, *Deep–Inelastic Scattering beyond the Leading Order in Asymptotically Free Gauge Theories*, Phys. Rev. **D18** (1978) 3998.

[57] G. Altarelli, R.K. Ellis and G. Martinelli, *Leptoproduction and Drell–Yan Processes Beyond the Leading Approximation in Chromodynamics*, Nucl. Phys. **B143** (1978) 521; Erratum ibid. **B146** (1978) 544.
G. Altarelli, R.K. Ellis and G. Martinelli, *Large Perturbative Corrections to the Drell–Yan Process in QCD*, Nucl. Phys. **B157** (1979) 461.

[58] G. Ingelman and G.A. Schuler, *Characteristics of Heavy Flavour Production in ep Collisions*, Z. Phys. **C40** (1988) 299.

[59] B. Andersson, G. Gustafson, G. Ingelman and T. Sjöstrand, *Parton Fragmentation and String Dynamics*, Phys. Rept. **97** (1983) 31.
T. Sjöstrand, *Status of Fragmentation Models*, Int. J. Mod. Phys. **A3** (1988) 751.
T. Sjöstrand, *High–Energy Physics Event Generation with PYTHIA 5.7 and JETSET 7.4*, Comp. Phys. Commun. **82** (1994) 74.
T. Sjöstrand, *PYTHIA 5.7 and JETSET 7.4: Physics and Manual*, CERN Report CERN-TH-7112-REV (1995); `hep-ex/9508391`.

[60] E. Norrbin and T. Sjöstrand, *Production and Hadronization of Heavy Quarks*, Eur. Phys. J. **C17** (2000) 137.
OPAL Collaboration, *A Study on b Quark Fragmentation into B^0 and B^+ Mesons at LEP*, Phys. Lett. **B364** (1995) 93.

[61] N. Cabbibo, *Unitary Symmetry and Leptonic Decays*, Phys. Rev. Lett. **10** (1963) 531.
M. Kobayashi and T. Maskawa, *CP Violation in the Renormalizable Theory of Weak Interaction*, Prog. Theor. Phys. **49** (1973) 652.

[62] OPAL Collaboration, *Measurement of $|V_{ub}|$ Using B Hadron Semileptonic Decay*, to be submitted to Eur. Phys. J. **C**; `hep-ex/0107016`.

[63] A.D. Martin, R.G. Roberts and W.J. Stirling, *Pinning Down the Gluon in the Proton*, Phys. Lett. **B354** (1995) 155; `hep-ph/9502336`.

[64] M. Glück, E. Reya and A. Vogt, *Parton Structure of the Photon beyond the Leading Order*, Phys. Rev. **D45** (1992) 3986.
M. Glück, E. Reya and A. Vogt, *Photonic Parton Distributions*, Phys. Rev. **D46** (1992) 1973.

[65] H1 Collaboration, *Erratum to the Measurement of Open Beauty Production at HERA. Phys. Lett. B467 (1999) 156*, accepted by Phys. Lett. **B** (2001).

[66] B.W. Harris and J. Smith, *Charm Quark and $D^{*\pm}$ Cross Sections in Deeply Inelastic Scattering at HERA*, Phys. Rev. **D57** (1998) 2806; hep-ph/9706334.

[67] M.L. Mangano, P. Nason and G. Ridolfi, *Heavy Quark Correlations in Hadronic Collisions at Next–to–Leading Order*, Nucl. Phys. **B373** (1992) 295.

[68] P. Derwent, *Charm and Beauty Results from CDF and D0*, Fermilab Report FERMILAB-CONF-95/096-E (1995); hep-ph/9505009.

[69] S. Frixione, *Bottom Production in Hadronic Collisions*, in: "Hadron Collider Physics. Proceedings of the XI$^{\text{th}}$ Topical Workshop on $p\bar{p}$ Collider Physics", eds. D. Bisello, G. Busetto and L. Stanco, World Scientific Publishing Co. (1997); hep-ph/9607333.

[70] S. Frixione, M.L. Mangano, P. Nason and G. Ridolfi, *Charm and Bottom Production: Theoretical Results versus Experimental Data*, Nucl. Phys. **B431** (1994) 453.

[71] H. Jung and G.P. Salam, *Hadronic Final State Predictions from CCFM: The Hadron–Level Monte Carlo Generator CASCADE*, Eur. Phys. J **C19** (2001) 351; hep-ph/0012143.

[72] M. Ciafaloni, *Coherence Effects in Initial Jets at Small Q^2/S*, Nucl. Phys. **B296** (1988) 49.
S. Catani, F. Fiorani, G. Marchesini, *QCD Coherence in Initial State Radiation*, Phys. Lett. **B234** (1990) 339.
S. Catani, F. Fiorani, G. Marchesini, *Small x Behavior of Initial State Radiation in Perturbative QCD*, Nucl. Phys. **B336** (1990) 18.
G. Marchesini, *QCD Coherence in the Structure Function and Associated Distributions at Small x*, Nucl. Phys. **B445** (1995) 49; hep-ph/9412327.

[73] H. Jung, *Unintegrated Parton Densities Applied to Heavy Quark Production in the CCFM Approach*, Presented at "New Trends at HERA Physics 2001", Ringberg Castle, Germany (2001); hep-ph/0109146.

[74] J.J. Aubert et al., *Experimental Observation of a Heavy Particle J*, Phys. Rev. Lett. **33** (1974) 1404.

[75] J.E. Augustin et al., *Discovery of a Narrow Resonance in e^+e^- Annihilation*, Phys. Rev. Lett. **33** (1974) 1406.

[76] E. Leader and E. Predazzi, *An Introduction to Gauge Theories and Modern Particle Physics*, Cambridge University Press (1995).

[77] S. Okubo, *Phi Meson and Unitary Symmetry Model*, Phys. Lett. **5** (1963) 165.
J. Iizuka, *Systematics and Phenomenology of Meson Family*, Prog. Theor. Phys. Suppl. **37-38** (1966) 21.

[78] O. Nachtmann, *Elementary Particle Physics: Concepts and Phenomena*, Springer–Verlag (1990).

[79] T. Regge, *Introduction to Complex Orbital Moments*, Nuovo Cim. **14** (1959) 951.
T. Regge, *Bound States, Shadow States and Mandelstam Representation*, Nuovo Cim. **18** (1960) 947.
P.D.B. Collins, *An Introduction to Regge Theory and High–Energy Physics*, Cambridge University Press (1997).

[80] M.G. Ryskin, *Diffractive J/ψ Electroproduction in LLA QCD*, Z. Phys. **C57** (1993) 89.
L. Frankfurt, W. Koepf and M. Strikman, *Hard Diffractive Electroproduction of Vector Mesons in QCD*, Phys. Rev. **D54** (1996) 3194; `hep-ph/9509311`.

[81] E.L. Berger and D. Jones, *Inelastic Photoproduction of J/ψ and Y by Gluons*, Phys. Rev. **D23** (1981) 1521.

[82] E. Braaten, S. Fleming and T.C. Yuan, *Production of Heavy Quarkonium in High–Energy Colliders*, Ann. Rev. Nucl. Part. Sci. **46** (1996) 197.; `hep-ph/9602374`.
G.A. Schuler, *Quarkonium. Production and Decays*, CERN Report CERN-TH-7170/94 (1994); `hep-ph/9403387`.

[83] C.H. Chang, *Hadronic Production of J/ψ Associated with a Gluon*, Nucl. Phys. **B172** (1980) 425.
R. Baier and R. Rückl, *Hadronic Production of J/ψ and Y: Transverse Momentum Distributions*, Phys. Lett. **B102** (1981) 364.
R. Baier and R. Rückl, *On Inelastic Leptoproduction of Heavy Quarkonium States*, Nucl. Phys. **B201** (1982) 1.
R. Baier and R. Rückl, *Large $p(t)$ Quarkonium Production at Ultrahigh–Energies*, Nucl. Phys. **B208** (1982) 381.

[84] W. Kwong, P.B. Mackenzie, R. Rosenfeld and J.L. Rosner, *Quarkonium Annihilation Rates*, Phys. Rev. **D37** (1988) 3210.

[85] H1 Collaboration, *Inelastic Photoproduction of J/ψ and $\psi(2S)$*, in: "International Europhysics Conference on High–Energy Physics (EPS-HEP99)", eds. K. Huitu, H. Kurki–Suonio and J. Maalampi, IOP Publishing (2000).

[86] ZEUS Collaboration, *Measurement of Inelastic J/ψ Photoproduction at HERA*, in: "High–Energy Physics. Proceedings of the 29th International Conference, ICHEP'98", eds. A. Astbury, D. Axen and J. Robinson, World Scientific Publishing Co. (1998).

[87] B.A. Kniehl and G. Kramer, *Tevatron–HERA Colour–Octet Charmonium Anomaly Versus Higher–Order QCD Effects*, Eur. Phys. J. **C6** (1999) 493; `hep-ph/9803256`.

[88] M. Krämer, *QCD Corrections to Inelastic J/ψ Production*, Nucl. Phys. **B459** (1996) 3; `hep-ph/9508409`.

[89] M. Krämer, J. Zunft, J. Steegborn and P.M. Zerwas, *Inelastic J/ψ Production*, Phys. Lett. **B348** (1995) 657; `hep-ph/9411372`.

[90] CDF Collaboration, *Quarkonia Production at CDF*, Nucl. Phys. **A610** (1996) 373c.
CDF Collaboration, *J/ψ and $\psi(2S)$ Production in $p\bar{p}$ Collisions at $\sqrt{s}$=1.8 TeV*, Phys. Rev. Lett. **79** (1997) 572.
CDF Collaboration, *Production of J/ψ Mesons from χ_c Mesons Decays in $p\bar{p}$ Collisions at $\sqrt{s}$=1.8 TeV*, Phys. Rev. **79** (1997) 578.

[91] New Muon Collaboration, *Inelastic J/ψ Production in Deep Inelastic Scattering from Hydrogen and Deuterium and the Gluon Density Distributions of Free Nucleons*, Phys. Lett. **B258** (1991) 493.
European Muon Collaboration, *Muoproduction of J/ψ and the Gluon Distribution of the Nucleon*, Z. Phys. **C56** (1992) 21.

[92] G.T. Bodwin, E. Braaten and G.P. Lepage, *Rigorous QCD Predictions for Decays of P Wave Quarkonia*, Phys. Rev. **D46** (1992) 1914; `hep-lat/9205006`.
G.T. Bodwin, E. Braaten and G.P. Lepage, *Rigorous QCD Analysis of Inclusive Annihilation and Production of Heavy Quarkonium*, Phys. Rev. **D51** (1995) 1125; `hep-ph/9407339`; Erratum ibid. **D55** (1997) 5853.
E. Braaten and Y.Q. Chen, *Helicity Decomposition for Inclusive J/ψ Production*, Phys. Rev. **D54** (1996) 3216; `hep-ph/9604237`.

[93] A. Meyer, *Charmonium Production in Deep Inelastic Scattering at HERA*, Ph.D. Thesis, University of Hamburg (1998).
H1 Collaboration, *Charmonium Production in Deep Inelastic Scattering at HERA*, Eur. Phys. J. **C10** (1999) 373; `hep-ex/9903008`.

[94] K. Krüger, *Photoproduction of J/ψ Mesons at Medium and Low Elasticities at HERA*, Ph.D. Thesis, University of Hamburg (2001).

[95] S. Mohrdieck, *Inelastische J/ψ –Erzeugung in Elektroproduktion am H1 Experiment bei HERA*, Ph.D. Thesis, University of Hamburg (2000).

[96] M. Glück, E. Reya and A. Vogt, *Dynamical Parton Distributions of the Proton and Small–x Physics*, Z. Phys **C67** (1995) 433.

[97] H. Jung, *The Monte Carlo Generator EPJPSI for J/ψ Mesons in High Energy Electron Proton Collisions*, in: "Physics at HERA. Proceedings of the Workshop" Vol. 3, eds. W. Buchmüller and G. Ingelman, DESY (1992) 1488.

[98] H. Jung, D. Krücker, Ch. Greub and D. Wyler, *Relativistic Corrections to Photoproduction of J/ψ* , Z. Phys. **C60** (1993) 721.

[99] M. Bieler et al., *Recent and Past Experiences with Beam–Beam Effects at HERA*, in: "Proceedings of the Workshop on Beam–Beam Effects in Large Hadron Colliders (LHC99)", eds. J. Poole and F. Zimmermann, CERN SL-99-039-AP (1999).

[100] D. Pitzl et al., *The H1 Silicon Vertex Detector*, Nucl. Instr. Meth **A454** (2000) 334; `hep-ex/0002044`.

[101] H1 Collaboration, *The H1 Detector at HERA*, Nucl. Instr. Meth. **A386** (1997) 310.

[102] H1 Collaboration, *The Tracking, Calorimeter and Muon Detectors of the H1 Experiment at HERA*, Nucl. Instr. Meth. **A386** (1997) 348.

[103] W. Erdmann, *Untersuchung der Photoproduktion vom D^*–Mesonen am ep–Speicherring HERA*, Ph.D. Thesis, ETH Zurich (1996).

[104] M. Tluczykont, *z–Kalibration der zentralen Spurenkammer des H1–Detektors bei HERA*, Diploma Thesis, University of Hamburg (1999).

[105] K. Müller et al., *Construction and Performance of a Thin Cylindrical Multiwire Proportional Chamber with Cathode Pad Readout for the H1 Experiment*, Nucl. Instr. Meth. **A312** (1992) 457.

[106] P. Robmann et al., *Construction and Analysis of a Prototype Drift Chamber for the H1 Experiment*, Nucl. Instr. Meth. **A277** (1989) 368.
S. Egli et al., *The Central Inner z Drift Chamber of the H1 Experiment*, Nucl. Instr. Meth. **A283** (1989) 487.
P. Robmann, *The Central Inner z–Chamber of the H1 Experiment at HERA*, Ph.D. Thesis, University of Zurich (1994).
H. Bärwolff et al., *Performance of Prototypes of the H1 Outer z Drift Chamber*, Nucl. Instr. Meth. **A283** (1989) 467.

[107] M. Kausch–Blecken von Schmeling, *The H1 Silicon Microvertex Detector of the H1 Experiment: Read–out, Event Reconstruction, and Studies on Heavy Quark Decays*, Ph.D. Thesis, University of Hamburg (1998).

[108] J. Gassner, *Messung der Ortsauflösung des H1–Siliziumvertexdetektors*, Diploma Thesis, ETH Zurich (1996).

[109] H1 Calorimeter Group, *The H1 Liquid Argon Calorimeter System*, Nucl. Instr. Meth. **A336** (1993) 460.
H1 Calorimeter Group, *Electron / Pion Separation with the H1 LAr Calorimeter*, Nucl. Instr. Meth. **A344** (1994) 492.
H1 Calorimeter Group, *Beam Tests and Calibration of the H1 Liquid Argon Calorimeter with Electrons*, Nucl. Instr. Meth. **A350** (1994) 57.

[110] H1 Calorimeter Group, *Results from Pion Calibration Runs for the H1 Liquid Argon Calorimeter and Comparisons with Simulations*, Nucl. Instr. Meth. **A336** (1993) 499.

[111] M. Fleischer et al., *Performance and Upgrade of the H1 Calorimeters: LAr Calorimeter, SpaCal and VLQ*, DESY Report DESY-98-005 (1998).

[112] H1 SpaCal Group, *The H1 Lead / Scintillating Fiber Calorimeter*, Nucl. Instr. Meth. **A386** (1997) 397.
A. Meyer, *Measurement of the Structure Function $F_2(x, Q^2)$ of the Proton at Low*

Q^2 with the H1–Detector at HERA Using the New Detector Components SpaCal and BDC, Ph.D. Thesis, University of Hamburg (1997).

[113] H. Itterbeck, *Techniques and Physics of the Central–Muon–Trigger System of the H1–Detector at HERA*, Ph.D. Thesis, University of Aachen (1997).

[114] C. Kleinwort and U.-P. Krüger, *Track Reconstruction in the Iron*, H1 Software Note 35-08/92 (1992).
U.P. Krüger, *Untersuchung der Erzeugung schwerer Quarks durch ihren Zerfall in Myonen im H1 Detektor bei HERA*, Ph.D. Thesis, University of Hamburg (1994).

[115] C. Wissing, A. Beglarian, P. Biddulph and M. Fleischer, *The H1 ToF System in 1996 and 1997*, H1 Internal Note H1-01/98-533 (1998).

[116] E. Elsen, *The H1 Trigger and Data Acquisition System*, H1 Internal Note H1-01/93-262 (1993).

[117] F. Sefkow, *Experience with the First Level Trigger if H1*, IEEE Trans. Nucl. Sci. 42 (1995) 900.

[118] J. Fent et al., *A Neural Network Second Level Trigger for the H1–Experiment at HERA*, H1 Internal Note H1-10/95-457 (1995).
J. Köhne et al., *Realization of a Second Level Neural Network Trigger for the H1 Experiment at HERA*, H1 Internal Note H1-01/97-509 (1997).

[119] J.C. Bizot et al., *Proposal for a Topological L2–Trigger*, H1 Internal Note H1-06/91-181 (1991).
L. Goerlich et al., *Strategy Studies for the H1 Topological L2–Trigger (L2TT)*, H1 Internal Note H1-01/97-508 (1997).

[120] S. Eichenberger, *A Fast Pipelined Trigger for the H1 Experiment at HERA Based on Multiwire Proportional Chamber Signals*, Ph.D. Thesis, University of Zurich (1993).
H.P. Beck, *Measurement of the Total Photoproduction Cross Section at the Electron Proton Collider HERA at $W_{\gamma p}$ of 200 GeV*, Ph.D. Thesis, University of Zurich (1996).

[121] T. Wolff, *Entwicklung, Bau und erste Ergebnisse eines totzeitfreien Spurfinders als Trigger für das H1–Experiment am HERA Speicherring*, Ph.D. Thesis, ETH Zurich (1993).
R. Bernet, *Production of $D^{*\pm}$ Mesons Measured with the H1 Detector at HERA*, Ph.D. Thesis, ETH Zurich (1995).
J. Riedlberger, *The H1 Trigger with Emphasis on Tracking Triggers*, H1 Internal Note H1-01/95-419 (1995).

[122] H. Bethe and W. Heitler, *On the Stopping of Fast Particles and on the Creation of Positive Electrons*, Proc. Roy. Soc. Lond. **A146** (1934) 83.

[123] *GEANT — Detector Description and Simulation Tool*, CERN Program Library Long Writeup W5013.

[124] S. Peters, *Die Parametrisierte Simulation elektromagnetischer Schauer*, Ph.D. Thesis, Max–Planck–Institute Munich (1992).
M. Rudowics, *Hadronische Schauersimulation für den H1 Detektor*, Ph.D. Thesis, University of Hamburg (1992).

[125] S. Levonian, H1 internal information (2001).

[126] V. Karimäki, *Fast Code to Fit Circular Arcs*, University of Helsinki Report HU-SEFT-1991-10 (1991).

[127] B. Naroska, S. Schiek und G. Schmidt, *Lepton Identification in the H1 Detector at Low Momenta*, H1 Internal Note H1-05/97-518 (1997).
S. Schiek, *Untersuchung der inelastischen Photoproduktion von J/ψ Mesonen im H1 Detektor bei HERA*, Ph.D. Thesis, University of Hamburg (1997).

[128] G. Schmidt, *Untersuchung der diffraktiven Photoproduktion von J/ψ Mesonen im H1 Detektor bei HERA*, Ph.D. Thesis, University of Hamburg (1997).

[129] P. Laurikainen, *The JPATH Filter Algorithm for JADE Track Trigger*, JADE Note 112 (1984).

[130] F. Jacquet and A. Blondel, in: "Proceedings of the Study of an *ep* Facility for Europe", DESY Report DESY 79-048 (1979) 391.

[131] L. Wilden, *Inelastic Photoproduction of J/ψ Mesons at HERA*, Diploma Thesis, University of Hamburg (1998).

[132] A. Schwank, *Effizienzbestimmung von Detektorkomponenten des H1–Experiments mit Hilfe Kosmischer Strahlung*, Diploma Thesis, University of Hamburg (1998).

[133] S. Mohrdieck, *Neuronaler Netzwerk–Trigger für Myonen im H1–Detektor bei HERA*, Diplom Thesis, University of Hamburg (1997).

[134] D. Schmidt and P. Merkel, *HMASS Finder on L4 for 1999 e^+ running*, private note (1999).
P. Merkel, *Diffractive Photoproduction of Heavy Vector Mesons at HERA*, Ph.D. Thesis, University of Hamburg (1999).

[135] R.L. Gluckstern, *Uncertainties in Track Momentum and Direction due to Multiple Scattering and Measurement Errors*, Nucl. Instr. Meth. **24** (1963) 381.

[136] O. Behnke and J. Kroseberg, *CST Hit Linking CSTLIN goes to CSTREC. Inofficial Release Accompanying Inofficial Note*, private note (2001).
J. Kroseberg, *A Measurement of the Beauty Production Cross Section at HERA Using Lifetime Information*, Ph.D. Thesis in preparation, University of Zurich (2001).

[137] J. Gassner, *Measurement of D–Meson Production at HERA by Decay Vertex Identification*, Ph.D. Thesis in preparation, ETH Zurich (2001).

[138] O. Behnke, talk presented at the H1 Tracking Task Force Meeting (2001).

[139] O. Behnke, *3D–Vertex–Track Fit VFIT3DU*, private note (1998).
P. Billoir, R. Fruhwirth and M. Regler, *Track Element Merging Strategy and Vertex Fitting in Complex Modular Detectors*, Nucl. Instr. Meth. **A241** (1985) 115.
G. Lutz, *Topological Vertex Search in Collider Experiments*, Nucl. Instr. Meth. **A337** (1993) 66.

[140] S. Brandt, *Statistical and Computational Methods in Data Analysis*, North–Holland Publishing Co. (1970).

[141] R. Luchsinger and C. Grab, *Vertex Reconstruction by Means of the Method of Kalman Filtering*, Comp. Phys. Commun. 76 (1993) 263.

[142] W. Erdmann, private communication (2001).

[143] M. Hilgers and R. Horisberger, *Development of a Radiation Hard Version of the Analog Pipeline Chip APC128*, accepted by Nucl. Instr. Meth. **A** (2001); `hep-ex/0101023`.

[144] T. Kuhr and M. Kausch–Blecken von Schmeling, *CSPRIM: Primary Vertex Determination using CST Measurements*, private note (2000).

[145] W.T. Eadie, D. Drijard, F.E. James, M. Roos and B. Sadoulet, *Statistical Methods in Experimental Physics*, North–Holland Publishing Co. (1971).

[146] H. Jung, private communication (2001).
H. Jung, *The CCFM Monte Carlo Generator CASCADE*, DESY Report DESY 01-114 (2001); `hep-ph/0109102`.

[147] M. Hilgers, *Untersuchung von Beauty–Ereignissen bei HERA anhand ihres myonischen Zerfalls und Strahlenharte Ausleseelektronik für den Silizium–Vertex–Detektor des H1–Experimentes*, Ph.D. Thesis in preparation, ETH Zurich (2001).

[148] C. Grab, private communication (2001).

[149] ZEUS Collaboration, *Inelastic J/ψ Photoproduction at HERA*, contributed paper to ICHEP2000, Osaka, Japan (2000).

[150] A. Schöning, *Introduction to a Global Topological Log–Likelihood Vertex Fit*, private note (2000).

[151] A. Baird et al., *A Fast High Resolution Track Trigger for the H1 Experiment*, IEEE Trans. Nucl. Sci. 48 (2001) 1276; `hep-ex/0104010`.

[152] S. Lüders et al., *Compact Frontend–Electronics and Bidirectional 3.3 Gbps Optical Datalink for Fast Proportional Chamber Readout*, accepted by Nucl. Instr. Meth. **A** (2001); hep-ex/0107064.

Appendix A

Compact Frontend–Electronics and Bidirectional 3.3 Gbps Optical Datalink for Fast Proportional Chamber Readout

Paper [152] accepted by and to be published in
Nuclear Instruments and Methods in Physics Research
Section A: Nuclear Accelerators, Instrumentation and Techniques with Related Research in Physics.

Compact Frontend–Electronics and Bidirectional 3.3 Gbps Optical Datalink for Fast Proportional Chamber Readout

S. Lüders[a], R. Baldinger[a], D. Baumeister[b], K. Bösiger[c], R. Eichler[a*], M. Feuerstack–Raible[b], C. Grab[a], S. Löchner[b], B. Meier[a], P. Robmann[c], B.A. Schmid[c], U. Stange[b], S. Steiner[c], U. Straumann[c], S. Streuli[a], K. Szeker[a†] P. Truöl[c]

[a]Institute for Particle Physics, ETH Zurich, 5232 Villigen PSI, Switzerland

[b]ASIC–Laboratory, Kirchhoff–Institute for Physics, 69120 Heidelberg, Germany

[c]Physics Institute, University of Zurich, 8057 Zurich, Switzerland

The 9600 channels of the multi–wire proportional chamber of the H1 experiment at HERA have to be read out within 96 ns and made available to the trigger system. The tight spatial conditions at the rear end flange require a compact bidirectional readout electronics with minimal power consumption and dead material.
A solution using 40 identical optical link modules, each transferring the trigger information with a physical rate of 4×832 Mbps via optical fibers, has been developed and commisioned. The analog pulses from the chamber can be monitored and the synchronization to the global HERA clock signal is ensured.

1. Introduction

An optical link and frontend electronics has been developed to read out all 9600 channels of the H1 experiment's central inner multi–wire proportional chamber (*CIP*) within the time between two bunch crossings, i.e. 96 ns. The application requires a bidirectional multi–purpose link: the digitized chamber information has to be provided to the trigger system 40 m away, selected analog pulses should be accessible for monitoring purposes and the whole frontend electronics must be synchronized to the global HERA clock signal. Furthermore, the optical link and readout electronics must fit in the available space of a 130 mm long open cylinder with inner and outer radii of 152 mm and 198 mm. No commercial solution for optical links fulfill these requirements in one compact unit.

The custom–made solution is composed of forty identical *optical link modules*, where a 64–fold multiplexing reduces the number of data lines. Each module performs an optical transmission with a physical rate of 3.3 Gbps. Precisely aligned VCSEL and PIN diode arrays allow for bidirectionality. The bending of optical fibers by 90° within 2 mm minimizes the overall height of the design.

A short overview of the CIP upgrade is given in Section 2 and the general layout is discussed: Each of the optical link modules consists of an on–detector unit, two optical hybrids with optical cables and a receiver unit. Their functional designs are presented in Sections 3, 4 and 5, respectively. The performance of the optical link and frontend electronics is presented in Section 6.

2. CIP Upgrade and General Layout

With the year 2000 upgrade of the HERA electron–proton collider at DESY, an increase in luminosity by a factor of five is anticipated. The expected higher background rate, predominantly beam–wall and beam–gas reactions, necessitates an improvement of the CIP to provide high background rejection efficiency of the z–vertex trigger [1,2].

*Corresponding author. Phone: +41 1 633 2018, Fax: +41 1 633 1233, e–mail: eichler@particle.phys.ethz.ch
†Present address: Physics Institute, University of Zurich, 8057 Zurich, Switzerland

The redesigned CIP [3] is built of five concentrical cylinders (*layers*) with radii from 152 mm to 198 mm. In the azimuthal angle, each layer is equally subdivided into 16 *segments*, each consisting of 120 *pads*[1] along the symmetry axis (*z–axis*). Charged particles traversing the chamber are detected by the 9600 pads, which provide space points and timing information. The direction of tracks can be inferred from the pattern of hit pads. For electron–proton collisions intersections of tracks with the z–axis come mostly from the interaction region, while the dominating background originates from proton beam losses upstream of the experiment. Experience has shown, that such background tracks seen by the H1 experiment are typically intersecting the z–axis at 0.5 to 1.5 m upstream of the mean ep interaction position. A new trigger system based on the latest FPGA family will identify these upstream events and is presently being commissioned. According to simulations this new trigger will improve the background rejection capability of the first level trigger by an order of magnitude compare to the previous *z–vertex trigger* [4].

The decision has to be made for *every* bunch crossing. Thus all 9600 pads have to be read out within the time between two bunch crossings, i.e. within 96 ns, corresponding to the bunch crossing frequency of 10.4 MHz (*HERA clock*). From the timing information, the bunch crossing number can be deduced.

Each of the forty identical optical link modules is used to read out all 2×120 pads of two adjacent segments (a *double–segment*) of a layer with a rate of 10.4 MHz. The *on–detector electronics unit* amplifies and shapes the signals from the pads, discriminates and serializes them to 4×15 bit words. After a second level 16–fold multiplexing, this *trigger information* is transferred to the *receiver electronics unit* 40 m away, located outside the main detector. Thus the total digitized information per module sums up to a data rate[2] of 4×624 Mbps. The on–detector electronics component must be synchronized to the global HERA clock signal therefore the system requires bidirectionality. The receiver electronics provides the global HERA clock and retrieves the multiplexed trigger information, which is de–serialized and distributed to the *trigger system*. Additionally, analog signals from each pad are transmitted and accessible for monitoring purposes.

To retain high geometrical acceptances for the new CIP and neighbouring detectors in the H1 experiment, the available space for mechanical support structures and electronics is limited to a 130 mm long open cylinder with inner and outer radii of 152 mm and 198 mm, respectively, located at the backward end flange[3] of the CIP. This tight space has to be shared between on–detector electronics, their suspension and cooling, low and high voltage power cables and gas supply lines (Figure 1). The power consumption has to be minimized to avoid an excessive heat dissipation inside the H1 experiment due to limited cooling possibilities.

Only an optical transmission allows high serial data rates, suppresses crosstalk and decouples detector and trigger system, while reducing the number of cables and the power consumption to a minimum. A readout with copper cables as formerly done would increase that volume by a factor of ten, would require even more driving power and would produce an unwanted high contribution to the dead material. In addition, an electrical transmission at the required high rates will likely induce noise into the very sensitive liquid argon calorimeter of the H1 experiment.

The optical link between on–detector electronics and the receiver electronics is established by two *optical hybrids* which perform opto–electrical (re)conversion of all data lines, i.e. four digital channels for the trigger information, two analog channels and two channels for the HERA clock signal. Experience with opto–mechanics has already been collected in the ETH Zurich group. An analog optical readout for the H1 experiment

[1] In fact, the CIP uses a projective geometry requiring 119 pads on the innermost layer, and 112, 106, 99 and 93 pads on the following layers, respectively. But for symmetry reasons, each optical link module will be capable of handling 120 pads.

[2] In principle, each optical link module is capable to transmit at a data rate of 4×1000 Mbps at maximum.

[3] The term "backward" labels the $-z$ end of the H1 experiment pointing in the direction of the electron beam.

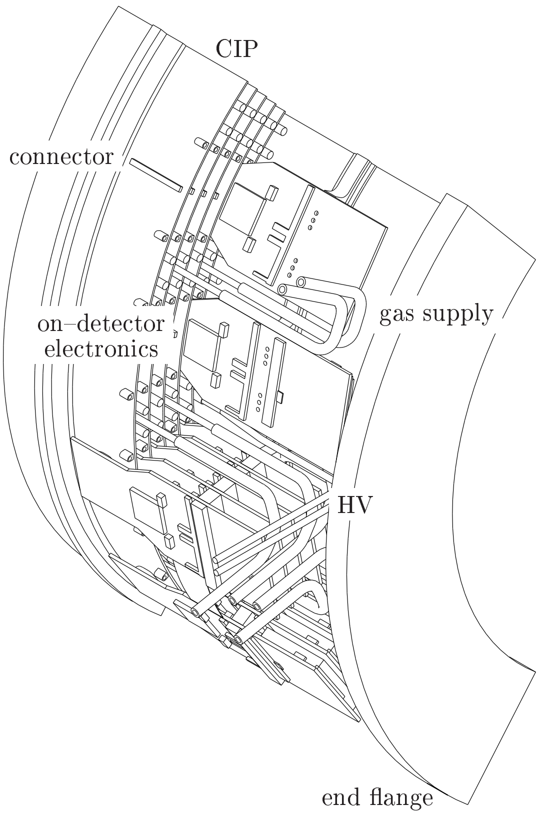

Figure 1. Illustration of the on–detector units mounted on the CIP. Four segments of the five layer CIP with gas tubes and HV cables are shown on the left. Five on–detector units stacked on top of each other and supported by cooling blocks are plugged on the lower segments; one unit is mounted on each of the upper segments. Their top sides face to the symmetry axis.

has been successfully operated since 1995 [5,6].

3. On–Detector Electronics Unit

Each on–detector unit collects the charge from 2×120 pads. Their charge is conducted via micro coax cables [7] to the rear end flange of the CIP. For each segment, a connector (Fujitsu FCN 298 [8], 120 contacts, 500 μm pitch, 2.5 mm height) passes the 120 channel pad information to a pair of analog readout (*CIPix*) chips. The CIPix chip amplifies, shapes, discriminates and four–fold multiplexes the signals. Further compression is done by two 16–fold multiplexers, each driving a differential high–speed data channel at 832 Mbps. After electro–optical conversion by the optical hybrid, the light pulses are transmitted to the receiver electronics unit. The overall synchronization is done with the global HERA clock signal received by the optical hybrid. A low jitter phase–locked–loop (*PLL*) unit [9] generates a 41.6 MHz clock signal, which is distributed to the multiplexer and — in addition to the HERA clock signal — to the CIPix chip. Furthermore, selected analog signals can be branched off before entering the CIPix discriminator to monitor the CIP. These *analog test signals* are also transmitted (Figure 2).

For compactness, one optical hybrid serves a double–segment and is mounted on one of the two separate halves of the on–detector unit. The other half holds the PLL unit and houses the voltage regulators. Due to the curvature of the CIP, a thin four layer flex–capton print bridges all signals via striplines to their destinations: The high–speed data channels and analog test signals are transferred from the other segment to the optical hybrid and, in return, the HERA clock signal is provided to the PLL unit. The flex–capton print is sandwiched between each of the halves. This *rigid–flex* print is produced by Dunkel & Schürholz [10]. It is implemented as an extremely high dense board with microstrip transmission lines and eight layers in total (Figure 3). Its outer dimensions are 130 mm in length, 2×49 mm in width and 9 mm in height. The open length of the capton print, i.e. the distance between both halves, increases proportional to the layer radii.

All on–detector units of one layer are connected via an I^2C bus daisy–chain [11]. This allows for a steering of every CIPix chip from a terminal, e.g. all CIPix chips can be initialized layer–wise. In addition, it performs a one–wire serialized temperature measurement [12].

3.1. CIPix IC

The CIPix analog readout chip is custom–made [13]. It amplifies, shapes, discriminates and multiplexes the incoming signals [14].

For each of the 64 analog input channels, it consists of a charge sensitive preamplifier with a gain of 20 mV per 10^5 electrons, a CR–RC semi Gaussian shaper with a peak time of 50 to 70 ns and a comparator. The discriminated signals are synchronized to the HERA clock signal and four adjacent pads are multiplexed (Figure 4). For monitoring and testing purposes, one of the analog signals can be selected and branched off to an analog output. Test pulses of user–defined pattern and frequency can be internally generated. Comparator thresholds, the selection of channels for analog output and test pulses are programmable via the I^2C bus. To protect the bond–wires and the surface, each CIPix chip is sealed ("glob–topped") with protective glue (Epoxy Technology H70S [15]).

The analog signals from 60 pads are processed by a single CIPix chip. Synchronously to the 41.6 MHz clock signal, the CIPix's 15 digital output channels give four successive words with 15 bits each. A *FirstWord bit* tags the first of these words and will make it possible to maintain the synchronization to the HERA clock signal in the trigger system. Together they form the 16 bit *data word*. An EmptyDataSet signal, generated in the case of missing inputs on all 60 input pads of the CIPix chip, serves as the *EmptyDataSet bit*. All 160 EmptyDataSet bits provide a coarse readout and will be used for a trigger decision whether an event is compatible with cosmic ray background or not.

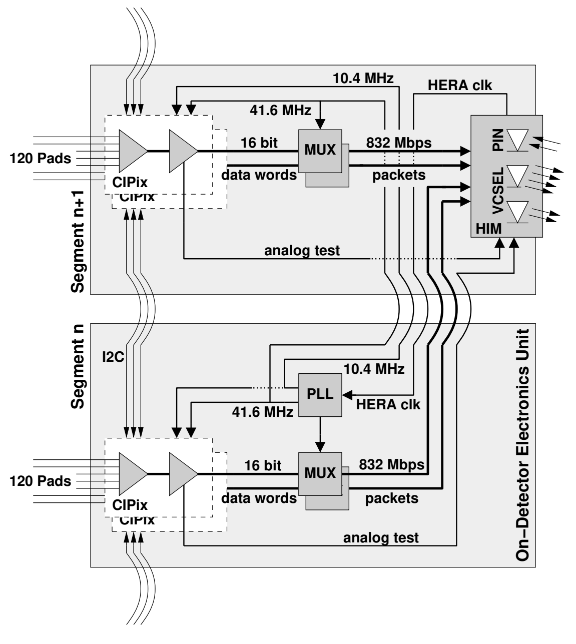

Figure 2. Signal flow of the on–detector electronics unit. A data word consists of the 15 bit trigger information plus the FirstWord bit. For details see text.

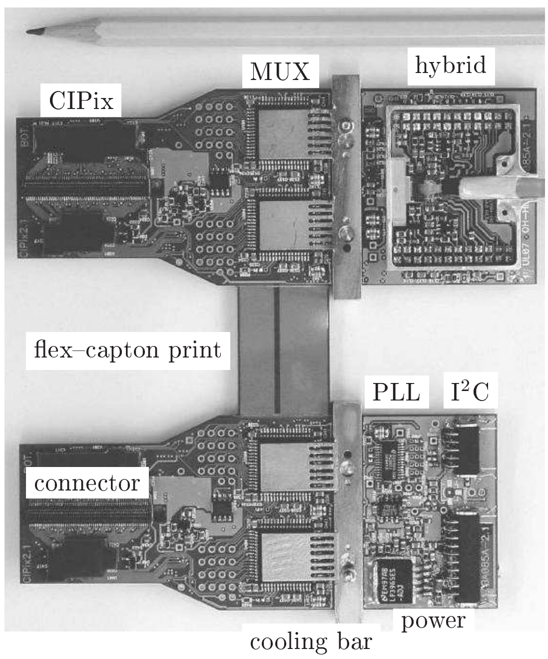

Figure 3. On–detector electronics rigid–flex print serving one double–segment.

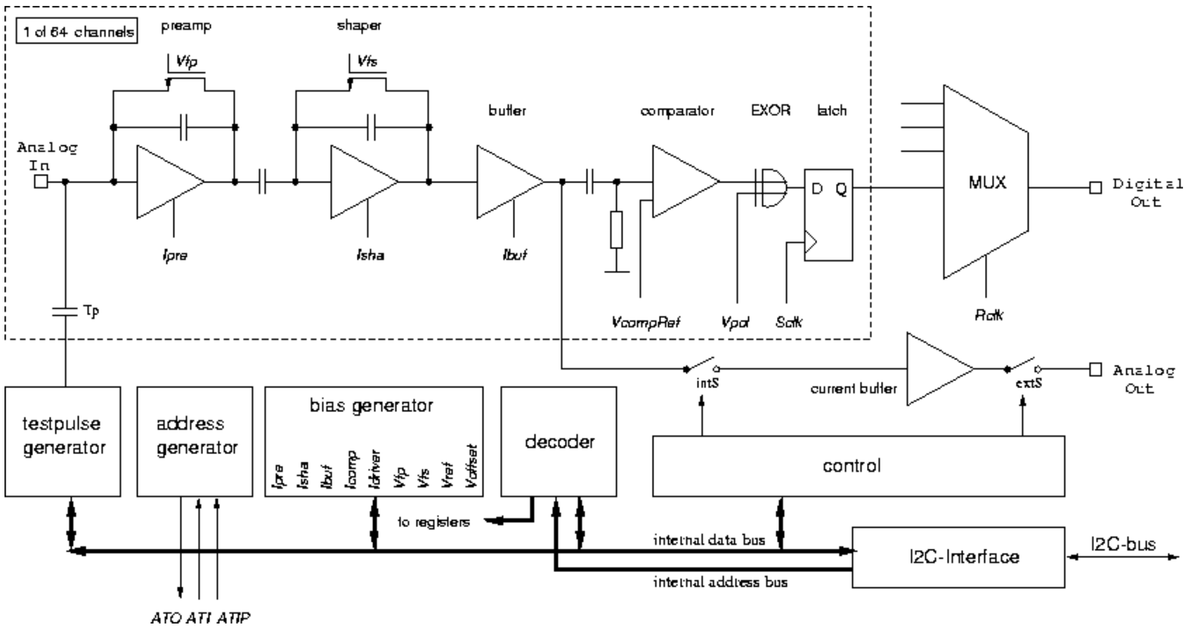

Figure 4. Block diagram of the CIPix chip.

3.2. Multiplexing / Demultiplexing

A further reduction of channels is achieved by building a differential high–speed data link for point–to–point communication between the Hewlett–Packard HDMP 1032 transmitter and the HDMP 1034 receiver [16].

Both bipolar chips provide the transmission of a 16 bit TTL data word plus one flag bit with a serial data rate of 221 to 1190 Mbps. The rate is chosen by an external reference clock signal synchronous with the incoming word. The HDMP 1032 PLL / clock generator locks onto the reference clock signal and multiplies it up to the high–speed serial clock signal. From the data word a special four bit encoding information is generated on the fly, proceeding the data word. Together they give a 20 bit *packet*. On the one hand, the encoding ensures the DC balance of the serial line. The disparity[4] of each data word is determined. Depending on the disparity of the previous data word, an inversion of the actual word is done to keep a 50 % duty cycle. Additionally, the encoding bits provide an error detection, tagging wrongly transmitted words, and include an user–controlled *flag bit*. On the other hand, the unique bit pattern of the encoding scheme incorporates the high–speed clock signal and thus saves an additional clock signal line between transmitter and receiver. The packet is serialized and leaves the HDMP 1032 as a differential 100 Ω terminated ECL compatible high–speed signal.

The HDMP 1034 receiver's Clock Data Recovery unit separates encoding bits and data word from the 20 bit packet, extracts the high–speed serial clock signal and locks to its phase. The data words are (eventually) inverted and then demultiplexed. The Parallel Automatic Synchronization System synchronizes these words to an external reference clock signal. A master–slave mode allows for a synchronization of several HDMP 1034 chips: A deviation of the relative phase of the data word and the reference clock signal generates

[4] The disparity is defined as the total number of "high" bits minus the total number of "low" bits.

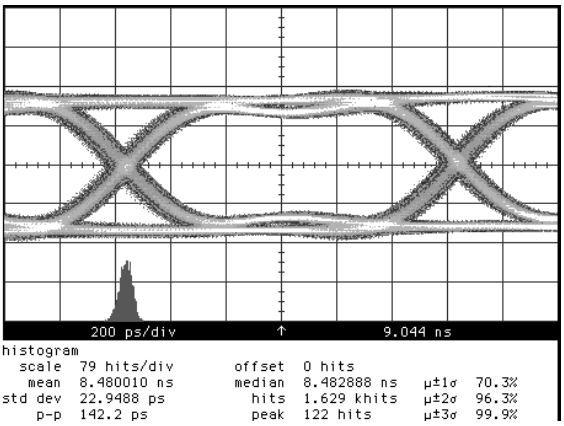

Figure 5. Eye–diagram accumulated from one digital channel and measured directly at the differential output of the 16–fold multiplexer. Shown is the digital level ("high" / "low") superimposed for all bits as a function of time. The small histogram gives the jitter. The signal density is given by the greyscale: the lighter the denser.

a shift request, passed to the master. The master controls the delay of all outputs of all slaves.

Each 16 bit data word is serialized by a HDMP 1032 chip. The EmptyDataSet bit is used as input for the flag bit; the 41.6 MHz clock signal provides the reference clock signal for both HDMP chips. Therefore the digitized trigger information from 60 pads is transmitted every 96 ns with a data rate of 624 Mbps. The overall physical rate includes in addition per 96 ns the four FirstWord bits and 4×4 bits of the encoding scheme (with the EmptyDataSet bit) and amounts to 832 Mbps. The receiver chip re–parallelizes the trigger information and extracts the FirstWord bit and EmptyDataSet bit. Four transmitter / receiver chip pairs — one for each CIPix chip — are used per module.

Bits of one high–speed digital channel have been superimposed for the eye–diagram (Figure 5). The rising and falling edges are well separated. The measurement of the zero–crossing of the rising edge results in a jitter of the data words of 23 ps before entering the optical hybrid.

4. Optical Hybrid

The optical hybrids constitute the interface between the electrical and the optical régime.

Following the signal flow from the CIP to the trigger system, the optical hybrid on the on–detector unit (*HIM*, High–Speed Interconnection Module) acts as a driver for the outgoing 20 bit packets and analog test signals and as a receiver for the incoming HERA clock signal. The optical hybrid on the receiver unit side (*DeHIM*) acts vice versa. The interfacing pins require or deliver differential CMOS logic signals for each data channel, respectively.

Each HIM / DeHIM pair serves one double–segment, i.e. transmits four multiplexed data channels with a physical rate of 4×832 Mbps, two analog test signal channels and two HERA clock signal channels via an optical fiber array with eight fibers.

The four data channels are driven by the Helix HXT 2000 [17] chip optimized for vertical cavity surface emitting laser (*VCSEL*) diodes. The VCSEL diodes convert the electrical signal to light pulses. After 40 m of optical fibers, conventional PIN diodes reconvert the optical to electrical signals. These are amplified by the Helix HXR 2004 receiver chip and produce four differential data signals. Because of the high data rates, the hybrid boards are impedance controlled and realized in four–layers with layer–to–layer blind–via connections [10].

For redundancy two HERA clock signals are transmitted in parallel. Standard SZ 125 drivers match their signal levels with respect to the VCSEL diode specifications. Conexant (formerly Microcosm) MC 2007 receivers [18] convert the PIN diode responses back to voltage–modulated signals. Its active gain control (*AGC*) ensures a stable output signal above the sensitivity limit at about -20 dBm. The two analog test signals are driven by Maxim MAX 4212 operation amplifiers [19] and received by Conexant MC 2011 (without AGC) chips. These differential analog signals and the HERA clock signal are finally amplified by Maxim MAX 4212 chips.

4.1. Driver and Receiver Circuits

The Helix HXT 2000 driver and the HXR 2004 receiver chips are designed for high–speed optical transmission up to 1.25 Gbps per channel; the HXT 2000 is optimized for VCSEL diodes at 800 to 1500 nm wavelength. The differential inputs to the HXT 2000 — four of them enabled — are amplified and current–modulated. External resistors allow to control the average and modulation current collectively for a VCSEL diode array. Thus the working range, i.e. the laser current, of an array of four VCSEL diodes can be optimized for maximum optical output.

The four channel HXR 2004, compatible to 0.6 pF photodiode arrays, converts the photocurrent from the PIN diodes to differential output voltages. In addition, the average photocurrents can be monitored.

4.2. Vertical Cavity Surface Emitting Laser Diodes

Laser diodes convert current–modulated signals into power–modulated light signals.

In a VCSEL diode the light propagates vertically through the structure (Figure 6). With this orientation the laser cavity can be grown to match the wavelength of the laser light, i.e. 850 nm. The total spectral width of the emission is generally less than 0.5 nm, which ensures a low coherence source. The beam divergence is typically below 12° FWHM. Alternating layers of AlAs and $Al_{0.15}Ga_{0.85}As$ provide the p– and. n–mirror stack surrounding the active region, respectively. With contact to the p–mirror, the VCSEL anode is bonded to the modulating current line, while the GaAs substrate holds the cathode i.e. ground potential [20]. Both, VCSEL and PIN diodes, are grouped in six– and two–diodes dies, respectively, from Truelight Corporation [21]. The specifications for the VCSEL and PIN diode arrays used are given in Table 1. The VCSEL diodes are specified as "class IIIb laser" in the safety standard ANSI Z136.1 [22] and have to be treated as a potential eye hazard.

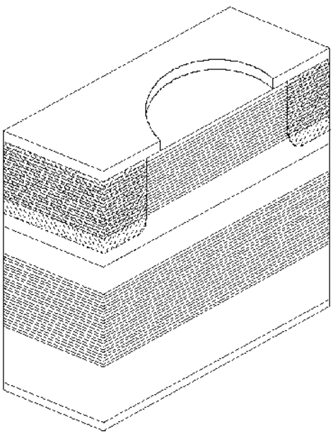

Figure 6. Sketch of a VCSEL diode.

Because of a delicate passivation, the softer ball–bond process using golden bond wires has been preferred to the wedge–wedge bonding and to the use of aluminum bond wires. Thus ultrasonic vibrations acting on the VCSEL diodes could be minimized and harm to the passivation could be prevented. Together with the required specifications of at least 1.5 mW at 12 mA laser current (i.e. to a slope efficiency of 0.125 W/A) and an uniform power gain over the VCSEL array, the yield has been tested to be about 31 %.

The lasering of the used VCSEL diodes typically starts at a current of 4.5 mA (Figure 7). With appropriate settings for the average and modulation current of the HXT 2000 ($V_{\mathrm{avg}} = 1.74 \pm 0.13$ V and $V_{\mathrm{mod}} = 1.38 \pm 0.08$ V, respectively) the working range has been optimized. The digital signal levels vary beween -49.1 ± 4.5 dBm for logical "low" and -3.7 ± 0.8 dBm for logical "high", leading to a dynamic range in optical output of approximately 45 dB. The uniformity over a VCSEL diode array is about 1.3 ± 0.7 dB.

4.3. Alignment and 90° Bending

In case of the HIM, the sixfold VCSEL and twofold PIN diode arrays are aligned with a precision of 5 μm with respect to each other and with respect to two guiding pins [23]. This provides a pitch of 250 μm in order to match the pitch of con-

Table 1
Specifications of the VCSEL and PIN diode arrays.

Optical specifications:	VCSEL	PIN
Wavelength	850 nm, multimode	850 nm
Beam profile and divergence	round, $< 12°$	
Active / Sense area diameter	$18\,\mu$m	$120\,\mu$m
Slope efficiency / Response at 850 nm	> 0.125 W/A	> 0.6 A/W ± 3 %
Electrical specifications:	**VCSEL**	**PIN**
$U_{\text{operating}}$	1.7..2.3 V	
U_{reverse}	> 10 V	> 10 V
Serial impedance	typ. 30 Ω	
I_{laser} / I_{dark}	4.5 mA	< 40 nA
C_{total}		< 0.9 pF @ 5 V
$\tau_{\text{rise / fall}}$	< 250 ps	100 ps
Crosstalk		> 30 dB
Mechanical specifications:	**VCSEL / PIN**	
Operating temperature	$< 85°$ C	
Chip thickness	$150\,\mu$m	
Pitch diode / diode	$250\,\mu$m	

ventional fiber ribbon connectors (*MTP connectors* [24]). The guiding pins adjust the connector to the diode arrays (Figure 8).

To obtain the desired precision, each diode array is positioned by a custom–made micro manipulator. The manipulator is mounted on an xy table, which makes it possible to perform an accurate position measurement and an optical survey. At its final position, the diode array is lowered and glued onto the hybrid. An optimal mechanical and optical performance has been achieved using a two component conductive glue (Epoxy Technology H21D [15]) with a resistivity of $3 \cdot 10^{-4}\,\Omega/\square$ and a bakeout time of 2 h. On the DeHIM side, sixfold PIN and twofold VCSEL diode dies are aligned with the same accuracy.

Since the distance between two CIP layers is less than 9 mm, it is not feasible to mount the MTP connector above the VCSEL / PIN array. Even if the connector is reduced to its inner core, namely the *ferrule*, adjusting the ferrule perpendicular to the hybrid leaves no space to properly fix the connector to the optical hybrid. In addition, it complicates the installation of the fibers at the end flange. Consequently the ferrule had to be mounted parallel to the optical hybrid, i.e. parallel to the z–axis. Since the diodes send the light perpendicular to the die, the light needs to be redirected. Therefore the $62.5\,/\,125\,\mu$m fibers are bent within 2 mm of height by modifying the ferrule and by using special fibers (GGP fibers from [25]). The performance of the transmission line has been measured to remain stable while the attenuation at each deflection lies below 2.1 ± 0.9 dB. On the DeHIM side, the fibers are conventionally bent within 10 mm.

Each optical hybrid is embedded in an aluminum casing to provide robustness and handiness, to avoid electrical induction from outside and to shield the VCSEL and PIN diodes from

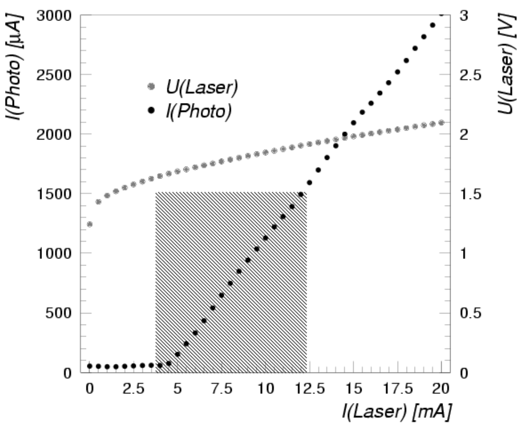

Figure 7. Output power ($\sim I_{\text{Photo}}$) and characteristic curve (U_{Laser}) of a VCSEL diode. The shaded area marks the working range.

dust. Its outer dimensions are $41 \times 33 \times 6\,\text{mm}^3$. Clamps at the aluminum casing give a proper mechanical connection of the hybrid with the fiber tails of 600 mm length (300 mm at the DeHIM) and prevents outside stress to affect the precise mechanical adjustment of the ferrules to the diodes.

4.4. Optical Cables

In guiding the optical fibers out of the main detector, several aspects have to be taken into account. Safety rules demand that all fibers and the sheathings be halogen–free and inflammable, space constraints require low bending radii of the cables, the CIP and parts of the on–detector electronics should be as easy to maintain as possible and all cables need to have a connection at the *cable distribution area* (CDA) at the backward end of the CIP. For these reasons, the optical transmission line is divided into four parts. Starting at the HIM, its fiber tail is plugged to a 3 m long fiber ribbon cable ending at the CDA. From there, a 36 m cable feeds the signals to the electronics cabin outside the main detector and is connected to the tail firmly attached to the DeHIM casing.

The 600 mm tails, including the 90° bending part, are produced by Schütten Optocommunication [26]. The long distance cables and 300 mm tails are made by Infineon [27]; the short distance cables are from Siecor [28]. The specifications of the cables are listed in Table 2. All cables are assembled with standard MTP connectors (except the ferrule end of the tails) with a typical attenuation of 0.3 to 0.5 dB at each MTP–MTP connection and three connectors per link. Adapters from AMP [29] attach two MTP connectors to another. To obtain a predictable timing between different modules, all cables of each type are chosen to have equal length. Measurements give an average length of 3.12 ± 0.05 m and 36.03 ± 0.15 m, respectively.

5. Receiver Electronics Unit

The receiver unit provides the signals of four adjacent pads, i.e. four successive data words

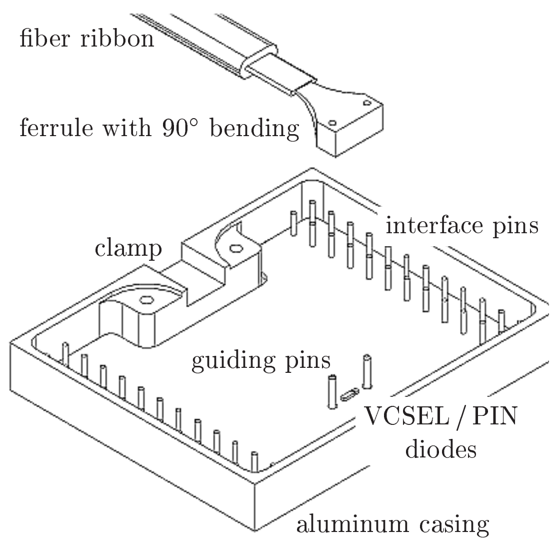

Figure 8. Exploded view of the aluminum casing. Between two guiding pins for the ferrule (enclosing the 90° fiber deflection) are the aligned sixfold VCSEL and twofold PIN diode arrays.

Table 2
Specifications of the fiber ribbons.

Mechanical specifications:	
Fiber count / type	$12 \times 62.5\,/\,125\,\mu$m
Flame resistance	UL-910 (Siecor)
	LSZH (Infineon)
Dimensions	$< 4.6 \times 2.1\,\mathrm{mm}^2$
Minimum bending radius (long term)	30 mm
Optical specifications:	
Maximum attenuation	4.0 dB/km
Minimum bandwidth	160 MHz $\times$ km
Numerical aperture	0.275 ± 0.020

and the EmptyDataSet bits, to the trigger system (Figure 9).

The DeHIM receives the high speed data signals and passes them to the four HDMP 1034 demultiplexers regaining the data words. The demultiplexers are used in the master–slave daisy–chain mode to maintain synchronization of all words, at which anyone of the HDMP 1034 can serve as master. Latches feed the four–fold multiplexed data words and the EmptyDataSet bit

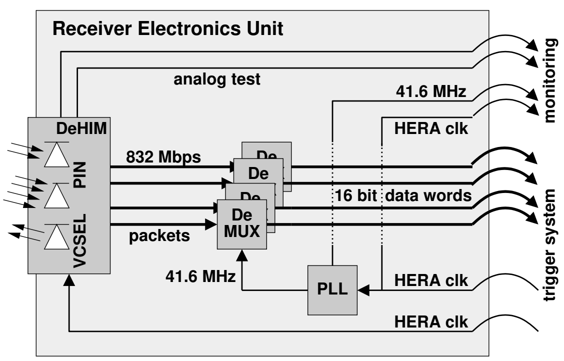

Figure 9. Signal flow of the receiver electronics unit.

with a rate of 41.6 MHz to the backplane that connects the trigger system and the receiver electronics. The incoming global HERA clock signal is received from the backplane and directed via the DeHIM to the on–detector PLL unit. It is also passed to the receiver board's low jitter PLL unit [9] producing the HDMP 1034 reference clock signal. This 41.6 MHz clock signal and the First-Word bit are used in the trigger system for the synchronization of different receiver units.

The receiver unit board is implemented as a six layer, high density and high speed board with microstrip transmission lines produced by Alwaprint [30]. At the receiver unit's frontplate, the following signals are available for monitoring purposes: the 16 bit data word, the EmptyDataSet bit, the differential analog test signals, the HERA– and the 41.6 MHz clock signal.

6. Performance

The optical link modules will be operated inside the H1 experiment in a 1.16 T magnetic field and only 15 to 20 cm away from the electron beam. Thus they will be exposed to synchrotron radiation and not be accessible from outside without major effort.

Therefore, the modules needed to be tested beforehand for long–term stability, reliability and robustness. Special attention has been paid to the bit–error rate, the transmission of the analog signals and the power dissipation.

Prototypes of the modules have been successfully operated since November 1999. Neither a break–down of any of the used components nor a decrease in the power output of the VCSEL diodes have been observed.

6.1. Link Performance

As soon as the global HERA clock signal is applied, each link module runs autonomously. The PLL unit of the on–detector electronics locks on the HERA clock signal and distributes the HERA– and 41.6 MHz clock signals to the CIPix chip and multiplexer. After 650 μs the multiplexer has been able to lock on the 41.6 MHz clock signal and the optical link is established. Frequency changes of the HERA clock signal within

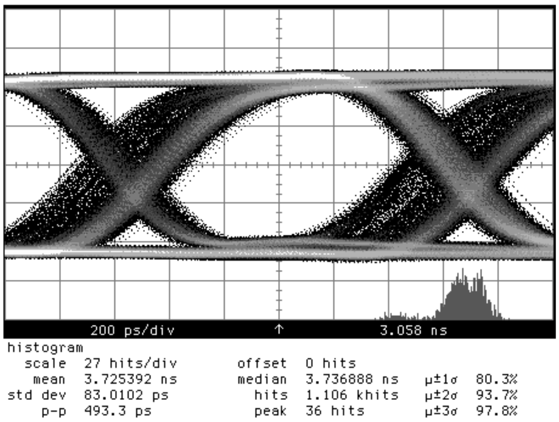

Figure 10. Eye–diagram accumulated from one digital channel and measured directly at the demultiplexer's input. Shown is the digital level ("high" / "low") superimposed for all bits as a function of time. The small histogram gives the jitter. The signal density is given by the greyscale: the lighter the denser.

a window of 8.6 to 11.4 MHz have been proven to be tolerable.

For random data words, i.e. words with 50 % duty cycle, the average light yield has been measured to be -8.7 ± 1.8 dBm at the DeHIM's end of the link after 40 m and three connector pairs. The PIN diodes' high response of typically 63 μA drives the HXR 2004 receiver into saturation, thus noise is suppressed. From the measurement of the bit–error–rate (see below), the lower limit has been estimated to be approximately 15 μA. An eye–diagram of the digital information directly at the demultiplexer's input is shown in Figure 10. The rising and falling edges are well separated. The jitter of the 20 bit packets is about 83 ps. A few percent of the entries shift to earlier crossings, as can be seen in the early sideband of the jitter histogram. The crosstalk between two digital channels and the crosstalk of digital to analog channels lies below -20 dB.

For quantitative tests 16 bit pseudo–random bit patterns were used to simulate the data words at the multiplexer's input. After transmission via the full 40 m link and after demultiplexing, these patterns have been compared with the original input to determine the bit–error–rate. Over a period of ten days, three errors occurred, corresponding to a bit–error–rate below 10^{-14}. This lies far below the tolerated rate of 10^{-9}, i.e. one error per second. All errors could be related to instabilities in the external power supply.

Problems with the synchronization between HDMP 1032 and HDMP 1034 have been seen if the data words imitate the bit pattern of the 16–fold multiplexer's encoding scheme for some hundred periods or if a bit next to an encoding bit is periodical in such a manner that a bit–shift results in another valid encoding bit pattern. In both cases the Clock Data Recovery unit locks on the fake bit pattern instead of the genuine encoding bits. In the operational mode of concern for the H1 experiment, this would require the same pattern of 60 pads of one segment (in a very special arrangement) repeated over many bunch–crossings. This is highly improbable and no reason for concern.

The transmission of the analog signals has been optimized to realize a one–to–one image of the chamber signals. Therefore the amplification of the CIPix chip and of the Maxim drivers in the optical hybrids have been fine–tuned. The peak–time of the analog signal is in the order of 50 ns. From the analog signals, a delay time between CIPix chip input pads and receiver electronics unit frontend of 230 ns has been measured. This is dominated by the delay in the optical fibers of 200 ns. A summary of the specifications of the optical link module is given in Table 3.

6.2. Mechanical Tests

The heat dissipation has been calculated from the measurement of the power consumption of one on–detector unit and gives 6.2 W per module. The total dissipation at the CIP end flange, i.e. the sum of all 40 modules, is about 250 W, sufficiently low for a water based cooling.

The on–detector electronics has been operated in a magnetic field from 0 to 2 T to simulate the impact of the H1 experiment's magnetic field. The optical output of the VCSEL

Table 3
Specifications of one optical link module.

Optical specifications:	
P_{out} (digital "high")	-3.7 ± 0.8 dBm
P_{out} (digital "low")	-49.1 ± 4.5 dBm
Dynamic range	45 dB
Att. at 90° bending	2.1 ± 0.9 dB
Att. per connector	0.3 . . . 0.5 dB
Crosstalk	< -20 dB
$\langle P \rangle$ after 40 m	-8.7 ± 1.8 dBm
Electrical specifications:	
Jitter HERA clock	43 ps
Jitter 41.6 MHz clk	49 ps
Jitter 20 bit packet	83 ps
	(before HIM: 23 ps)
Delay time	230 ns
	(fibers: 200 ns)
Bit–error–rate	$< 10^{-14}$
Power Dissipation per digital channel	(total 240 channels)
On–detector unit	20 mW @ +3.95 V
	4 mW @ −3.95 V
Receiver unit	13 mW @ +3.3 V
Power Dissipation per analog channel	(total 2 channels)
On–detector unit	110 mW @ +4.4 V
	110 mW @ −4.4 V
Receiver unit	135 mW @ +5 V
	384 mW @ −12 V

diodes, the threshold of the CIPix chip, the analog pulse heights, the noise level and the total power consumption of the on–detector electronics have shown no variations within the measurable precision. The jitter of the HERA clock signal remains stable, while jitter of the 41.6 MHz clock signal increases from 49 to 53 ps with a phase shift of 18 ps. Thus no losses in the performance of the optical link due to the magnetic field are expected.

The irradiation at the CIP end flange and thus at the on–detector electronics is estimated to be less than 50 Gy per year [6]. The VCSEL diodes have been irradiated to a flux of about 2×10^{14} neutrons/cm^2, with no measurable change in either threshold or efficiency [31]. After exposure to 200 Gy ± 4 % from a ^{60}Co source, the optical fiber tails and the short distance cables have shown no change in the optical behavior. The same is expected for the 36 m long cables.

6.3. Installation

Forty optical link modules have been successfully installed at the CIP rear end flange in April 2001. All spatial requirements are met. No additional noise has been induced into the liquid argon calorimeter. All modules run autonomously with bit–error–rates well below 10^{-9}. Due to contact problems of the chamber connectors and due to broken bonds at the CIPix chip inputs 0.8 % of all channels are lost. Another 0.9 % inefficiency results from the failure of two VCSEL diodes providing digital signals. For the same reason, one analog channel cannot be monitored.

7. Summary

A fast and compact frontend electronics has been developed to transfer $40 \times 4 \times 832$ Gbps trigger information from the H1 experiment's central inner multiwire proportional chamber to the corresponding trigger system. Forty identical modules have been successfully installed at the chambers end flange and fulfill the tight spatial constraints, while the power dissipation is only about 250 W. The optical transmission has been optimized and is functioning reliably. The bit–error–rate for each module is around 10^{-14}.

Acknowledgments

The optical link project has been supported by the Swiss National Science Foundation.

REFERENCES

1. H1 Collaboration, Nucl. Instr. and Meth. **A386** (1997) 310.
2. K. Müller et al., Nucl. Instr. and Meth. **A312** (1992) 457.
3. M. Cuje et al., "H1 High Luminosity Upgrade 2000 CIP and Level 1 Vertex Trigger" presented to the 44th DESY PRC (1998), DESY-PRC 98/02 and H1 internal note H1-IN-535(01/1998).
4. S. Eichenberger, "A Fast Pipelined Trigger for the H1 Experiment at HERA Based on Multiwire Proportional Chamber Signals", Ph.D. Thesis (1993), University of Zurich, unpublished.
5. W. Erdmann et al., Nucl. Instr. and Meth. **A372** (1996) 188.
6. D. Pitzl et al., Nucl. Instr. and Meth **A454** (2000) 334.
7. Axon Kabel GmbH, Postfach 1131, 71229 Leonberg, Germany.
8. Fujitsu Takamisawa Europe B.V., Diamantlaan 25, 2132 WV Hoofddorp, The Netherlands.
9. Quality Semiconductors Inc., now:
   IDT Inc., 2975 Stender Way, Santa Clara, CA 95054, USA,
10. Dunkel & Schürholz GmbH, Herbecke 12, 58579 Schalksmühle, Germany.
11. Philips Semiconductors, The Netherlands.
    A. Vollhardt, "Entwurf und Bau einer Frontend–Steuerung für das CIP–Upgrade Projekt für H1 bei HERA", Diploma Thesis (2001), University of Zurich, Switzerland, unpublished.
12. Dallas Semiconductor Corporation, 4401 South Beltwood Parkway, Dallas, TX 75244, USA.
13. ASIC Laboratory Heidelberg, Schröderstr. 90, 69120 Heidelberg, Germany.
14. S. Löchner, "Charakterisierung und Entwicklung eines CIP–Auslese–ASIC für das H1–Upgrade–Projekt 2000", Diploma Thesis (1998), University of Heidelberg, Germany, unpublished.
    D. Baumeister, "Entwicklung und Charakterisierung eines ASICs zur Kathodenauslese von MWPCs für das H1 Experiment bei HERA" Diploma Thesis (1999), University of Heidelberg, Germany, unpublished.
    U. Stange, "Charakterisierung und Weiterentwicklung des CIPix" Diploma Thesis (2000), University of Heidelberg, Germany, unpublished.
15. Epoxy Technology, 14 Fortune Drive, Billerica, MA 01821, USA.
16. Hewlett–Packard Company, 3000 Hanover Street, Palo Alto, CA 94304, USA.
17. Helix AG, Wolfenbachstr. 9, 8032 Zurich, Switzerland.
18. Conexant Systems Inc., Newport Beach, CA., USA.
19. Maxim Integrated Products Inc., 120 San Gabriel Drive, Sunnyvale, CA 94086, USA.
20. Honeywell Inc., USA.
21. Truelight Corporation, 2F–2, No. 21, Prosperity RD. I, Science–Based Industrial Park, Hsin–Chu, Taiwan.
22. American National Standards Institute, USA.
23. Diamond SA, Via dei Patrizi 5, 6616 Losone, Switzerland.
24. US Conec Ltd, USA.
25. 3M Corporate, 3M Center, St. Paul, MN 55144, USA.
26. S. Schütten Optocommunication, Hans–Bunte–Str. 20, 69123 Heidelberg, Germany.
27. Infineon Technologies AG, St.–Martin–Str. 53, 81541 Munich, Germany.
28. Corning Incorporated, One Riverfront Plaza, Corning, NY 14831, USA.
29. Tyco Electronics AMP Deutschland GmbH, Ampèrestr. 12–14, 64625 Bensheim, Germany.
30. Alwaprint AG, Siloring 8, 5606 Dintikon, Switzerland.
31. T. Weidberg, ATLAS STC Links Group at CERN (1998).

Danksagung

An dieser Stelle sollen diejenigen Erwähnung finden, die zum Gelingen dieser Dissertation beigetragen haben.

Prof. Dr. Ralph A. Eichler danke ich für das in mich gesetzte Vertrauen während der Planung und Realisierung des Hardware Projektes über die "Optische Link Elektronik" und für die damit gewonnenen Erfahrungen. Ganz besonders bedanke ich mich für die Freiheiten in der Wahl und Durchführung dieser Analyse, der Unterstützung dabei und für die Begutachtung dieser Dissertation. Prof. Dr. André Rubbia danke ich für die Übernahme des Zweit–Gutachtens.

Für die spannende Zeit während der Hardware–Entwicklung am Paul–Scherrer–Institut danke ich ganz herzlich

- Raphael Baldinger und Karoly Szeker, mit denen ich endlose Tage und Nächte (sic!) im E–Labor verbracht habe.
- Dr. Roland Horisberger, Beat Meier und Silvan Streuli, für die vielen Diskussionen über alle Belange unseres Hardware–Projektes.
- Carmen Büchli und Marta Sekolec für die Unterstützung in der Bürokratie und im Privaten.

Viele nette Menschen haben mich während dieser Analyse, der Seminare und Übungen am DESY und an der ETH Zürich begleitet und unterstützt:

- Johannes Gassner, für die tiefgehende Freundschaft — auch über die Distanz Hamburg–Zürich.
- Dr. Benno List und Dr. André Schöning, die mir hart zusetzten, um diese Arbeit voran zu treiben und deren exzessive Korrekturvorschläge zur Qualitätsverbesserung beigetragen haben. Alle eventuell verbliebenen Fehler liegen selbstverständlich allein bei mir.
- Dr. Duncan P. Brown, für die intensive Korrektur auf "native english", auch wenn ich trotzdem einige Amerikanismen beibehalten habe.
- Dr. Olaf Behnke, Dr. Wolfram Erdmann und Dr. Daniel Pitzl, die mir die Grundlagen des CSTs und dessen Datenanalyse, insbesondere des z–Seiten Linkings näherbrachten. Unvergessen bleiben die niemals endenden Iterationen zur Überprüfung des Repro2000++.

- Dr. Katja Krüger und Dr. Susanne Mohrdieck, deren Ratschläge über die Grundlagen der J/ψ Meson Selektion und der Effizienzbestimmung mir sehr hilfreich waren.
- Dr. Hannes Jung für die vielen kurzen und langen fruchtbaren Diskussionen über die Theorie im Allgemeinen, sowie "Heavy Flavour Production", "Heavy Flavour Excitations", "Small–x Effects" und NLO QCD Rechnungen im Speziellen.
- Rosa Bächli, Dr. Christophorus Grab, Michael Hilgers und David Meer, für die gemeinsamen Zeiten am Hönggerberg.
- Simon Baumgartner, Dr. Stefan Hengstmann, Dr. Oliver Karschnik, Jürgen Kroseberg und der Kaffee–Runde der Universität Hamburg für das freundschaftliche Arbeitsklima.

Diese subjektive Auswahl erhebt natürlich keinen Anspruch auf Vollständigkeit.

Letztendlich möchte ich von ganzem Herzen meiner Familie, meinem Sonnenschein Nea Sophie und meiner Liebe Tina, für die aufgebrachte Geduld — vor allem in den letzten Monaten — und Unterstützung danken. *Dito Yo 2!*

Curriculum Vitae

Personal Data

Name	Stefan Lüders
Date of Birth	October 24th, 1971
Place of Birth	Hamburg (Germany)
Nationality	German

Education

1978 – 1982	Primary School, Hamburg (Germany)
1982 – 1988	Secondary School, Hamburg (Germany)
1988	"Mittlere Reife"
1988 – 1991	Technical High School, Hamburg (Germany)
1991	Abitur
1991 – 1992	Military service
1992 – 1997	Study of physics at the University of Hamburg (Germany)
1997	Diploma with the H1 Collaboration at DESY on the "Identification of Semimuonic Decays of Heavy Quarks Using Neural Networks at the H1 Detector at HERA"
1997 – 2001	Graduate education in Experimental High Energy Physics at the Swiss Federal Institute of Technology (ETH) in Zurich (Switzerland)